Towards Electrochemically Triggered Disassembly of a Redox-Active Artificial Metalloenzyme Immobilised on Gold Electrodes

Natalia Gabriela Baranska

Doctor of Philosophy

University of York

Chemistry

June 2023

Abstract

In an era marked by escalating concerns surrounding increasing pollution levels, there is significant pressure on developing chemical processes which prioritise sustainability, while not compromising on output efficiency and quality. Artificial metalloenzymes (ArMs) represent an emerging field of biocatalysts, enabling chemical transformations which go beyond the scope of natural enzymes to be performed in mild conditions and aqueous environments with comparable activity and selectivity. The recent development of an ArM, based on an iron periplasmic binding protein and its cognate iron(III) siderophore complex, for the first time allowed redox-triggered disassembly. The chemical reduction of the iron(III) centre released the metal cofactor and facilitated the recycling of the protein scaffold. This thesis details the efforts towards optimising the disassembly process and transferring it onto a conductive surface to establish an immobilisation platform which offers electrochemical control over the ArM disassembly without adverse effects on the catalytic performance.

Initial work focused on the interrogation of the redox chemistry exhibited by the iron(III) siderophore complex at the centre of the redox-active anchor. The structural and voltammetric characterisation revealed its uncommon preference for the formation of the coordinatively unsaturated complex. The ArM was immobilised onto gold electrodes functionalised with nitriloacetic acid (NTA) through self-assembled monolayer (SAM) formation, exploiting the affinity between the protein's polyhistidine tag and nickel(II) NTA complex resulting in minimal non-specific binding. A direct electrochemical connection was not able to be established with the immobilised ArM, thus multiple approaches for indirect determination of the metal cofactor release were studied. A robust approach utilising native ESI-MS was implemented to successfully distinguish between the ArM and the corresponding apoprotein. The thesis concludes in preliminary work towards artificially wiring the non-electrochemically active ArM; the approach is envisioned to be of interest to the wider community for establishing a connection with other electrochemically silent proteins.

Contents

List of tables, figures, schemes, and equations

Acknowledgments

What a wild ride this project has been, and I have to admit I have never been a massive fan of rollercoasters in the first place. However, for every breakdown, tear and moment of doubt, there have been countless laughs, joys and feelings of overwhelming satisfaction. All this before mentioning the fact the pandemic outbreak happened within the first 6 months of me starting this project – if possible, I would recommend avoiding it.

I do not think I would have made it so far without the support and guidance of my supervisors, Prof. Anne-Kathrin Duhme-Klair and Prof. Alison Parkin. I have been extremely fortunate to work with two great female scientists, which have inspired me to always push further and pursue my own ideas and scientific curiosity. Anne, thank you for the wealth of knowledge you have shared with me and for ingraining in me the importance of always trying the simplest approach first. Your enthusiasm for the group hiking trips and home-baked goods will always be fondly remembered. Alison, thank you for always believing in me and supporting me when I needed it the most. Your encouragement and infectious enthusiasm for research have been a highlight of many meetings. I am still not sure how you have managed to convince me that pursuing a research career in bioelectrochemistry was not an inherently crazy idea.

A highlight of pursuing a PhD in electrochemistry is the wonderfully skilled team of technicians that you get the opportunity to work with, and without whom completing this project would have not been impossible. Abby Mortimer, Stuart Murray, and Chris Rhodes; thank you for all your patience, understanding and tireless work in materialising my extremely vague ideas as well as repairing my countless mistakes. Dr Adam Dowle receives my enormous gratitude for helping me in manoeuvring the mythical art of protein mass spectroscopy and coming to my aid after several months of

fruitless work. Julia Walton, all the work you put into keeping Chemical Biology together is a miracle, thank you for everything you have done over all these years.

Thank you to all the colleagues and friends I have made during my time, members of both research groups and also those in the rest of the department. Whether it was a 'mutual exchange of information' over prolonged coffee breaks, board game nights, much needed venting sessions or pub lunches, I will cherish them all.

Alice Hewson, you are a ray of sunshine in my life. We could not be more different from each other and yet I have the pleasure of calling you my best friend. Thank you for always being there, for all the highs and lows, regardless of whether we were at home or on the other side of the world.

Lloyd Murphy, no number of words would express how extremely grateful I am for everything you have done for me. Thank you for being the best friend and partner, and everything in between, I could have ever asked for. You are by far the best experiment I carried out during this PhD.

Tabitha, you have been my favourite writing companion while I was endlessly staring at blank pages. Gabi, your annoyance at my audacity to write this thesis while you were sat on my lap will be forever missed. Thank you both for all your feline love.

And thank you to those who have motivated me to finish this journey without knowing it. This is not for you; this is for me.

"Journey before destination..."

− Brandon Sanderson

But I am so glad that I do not have to do this journey ever again...

Declaration

I, Natalia Gabriela Baranska, declare that the research presented within this thesis is a presentation of original work and I am the sole author. The described work was performed under the supervision of Prof. Anne-Kathrin Duhme-Klair, Prof. Alison Parkin and Prof. Steven Johnson at the University of York. This work has not previously been presented for an award or other qualification at this University or elsewhere. All sources are acknowledged as references. Contribution to this work by other researchers is explicitly stated when relevant data are discussed and in the appropriate experimental sections.

Chapter 2 includes content from a previous publication:

Electrochemical and solution structural characterization of Fe(III) azotochelin complexes: Examining the coordination behavior of a tetradentate siderophore; N. G. Baranska, A. Parkin and A.-K. Duhme-Klair, *Inorg. Chem.*, 2022, **61**, 19172−19182

To my parents,

I know you would have been proud of me

***

Chapter 1 – Introduction

This thesis explores the development and optimisation of a recyclable biohybrid catalytic platform, comprising an immobilised redox-active artificial metalloenzyme. These biohybrid catalytic systems exemplify the next generation of biocatalysis, granting access to chemical transformations previously unknown to nature and biological systems. However, this biocatalytic novelty comes at a price. To guarantee high stability, strong binding motifs between the biological and chemical components are at the centre of artificial metalloenzyme design. Nonetheless, the utilisation of scarce noble metals necessitates these systems to be recyclable to combat the declining metal supplies and the environmental impact associated with their extraction. This creates the demand not only for ArM designs with inherent recyclability features but also for compatible platforms that facilitate the recycling process without an additional environmental burden. For redox-active systems, electrochemical-based approaches can offer an attractive solution.

1.1 The age of biocatalysis

The increasingly damaging impact of chemical industrial processes on the environment, and the rising concerns surrounding climate change have prompted researchers to look towards more sustainable approaches for the production of chemicals. Reports released by the United States Environmental Protection Agency (US EPA) highlight the chemical manufacturing industry as the largest producer of chemical waste, representing an increase of 18% since 2011 and the second largest sector contributing to the amount of waste released into the environment within the US, accounting for 216 388 tonnes in 2020.[1] It is thus not surprising that process adaptations that result in lower E-factors, defined as the mass ratio

of waste to product, have been the predominant focus of the 'sustainable chemical industry' movement over the last years.[2]

The application of enzymes, nature's catalysts, in organic synthesis offers the advantage of producing enantiopure products without the requisite for harsh conditions, multiple protection and deprotection strategies, and the consumption of scarce noble metals.[3] However, these features are the hallmark of inorganic catalysis. Small metal complexes outperform enzymes in the number of chemical transformations they can access and the extent of their substrate scope, nonetheless, they often possess inferior enantio- and regioselectivity and the associated environmental impact cannot be disregarded. Contrarily, biocatalysis conforms to 10 out of 12 principles of green chemistry (**Figure 1.1**); the two unfulfilled principles (design for safer chemicals and degradation) are a result of their applicability to the final product rather than the catalytic process itself. The principles are a set of guidelines described by Anastas and Warner in 1998 to guide the development of new chemical processes, allowing them to maintain the needs of modern-day society without having a detrimental effect on future generations.[4,5]

Subsequently, enzymatic synthesis has become the central focus of present-day research, particularly within the pharmaceutical industry where the attention has shifted towards the development of more complex structures, which often require strict chiral control and high enantiopurity.[6–9] The evolutionary adaptions of enzymes have optimised these catalysts to perform only very specific chemical reactions on a limited number of substrates in a well-defined biological environment consisting of a complex cellular matrix in physiological conditions.[10] However, revolutionary advances in enzyme discovery and protein engineering have allowed to significantly expand the number of their industrially-relevant applications.[11,12] Pioneering work, particularly by Frances Arnold and co-workers played a pivotal role in the development of a new generation of

biocatalysts; enzymes with improved solubility profiles, enhanced conversion rates, new reaction scopes and higher thermostability are no longer a distant aspiration.[13–17] Current research efforts focus on enzyme immobilisation, multi-enzymatic cascades and whole-cell biocatalysis amongst others, as novel strategies for increasing the versatility of biocatalysts for industrial processes.[18–20]
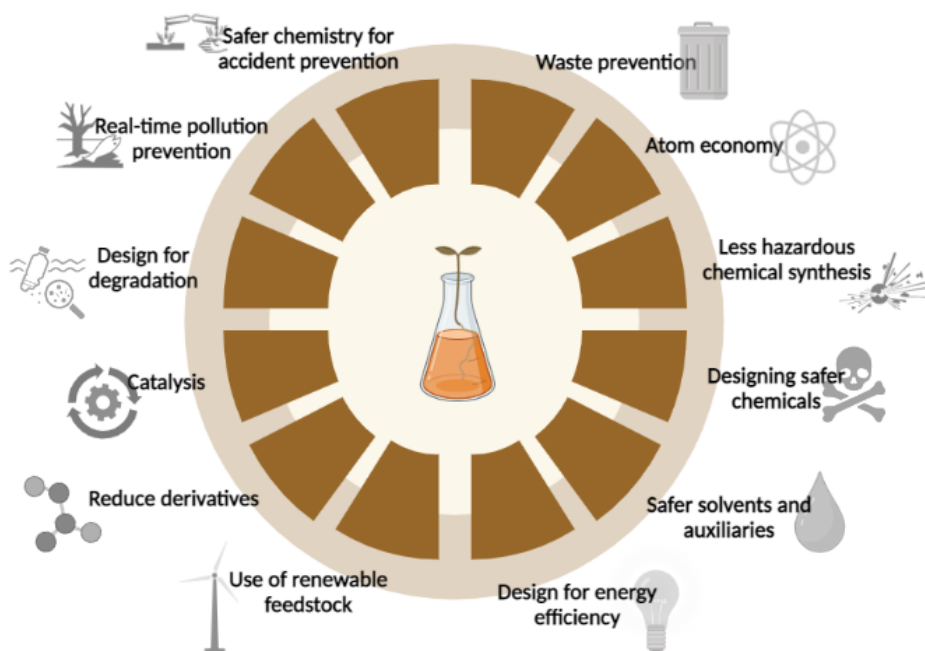
Figure 1.1 A graphic illustrating the twelve principles of green chemistry. Created with Biorender.com.

Nonetheless, the extent to which structural modifications can be performed without adversely affecting catalytic activity is limited, and thus the inability to access all chemical transformations invented within the laboratory remains one of the predominant challenges associated with the use of enzymes. Alternative systems have begun to emerge, including the development of artificial metalloenzymes (ArMs) which arise from the combination of enzymatic and small molecule inorganic catalysis.

1.2 Artificial metalloenzymes

The fundamentals of ArM design lie in the introduction of an abiotic metallic centre into a protein scaffold to manipulate its catalytic activity. This can be achieved either through the modification of the natural metal cofactor to influence the existing catalytic activity or the introduction of a synthetic metal catalyst into a non-catalytically active protein.[21,22] This hybrid approach enables harnessing the advantageous properties of both enzymes and homogenous organometallic catalysis (**Table 1.1**) simultaneously within one system.

Table 1.1 Summary of characteristics exhibited by enzymes and small inorganic catalysts; italicised properties are those conserved during the development of artificial metalloenzymes.

Biocatalysis	Organometallic catalysis
Narrow substrate scope	*Substrate promiscuity*
Specific reaction scope	*Diverse reaction scope*
High selectivity	Low selectivity
Aqueous solubility	Organic solvent solubility
Room temperature	High temperature
Air stability	Oxygen sensitivity

The resulting catalysts are capable of performing new-to-nature chemical transformations with remarkable regio- and enantioselectivity.[23–25] This is facilitated through the second coordination sphere of the ArM (**Figure 1.2**); a set of non-covalent interactions between the amino acids residues and the incoming substrate as well as the catalytic metal centre.[26–28] Their cumulative effect within the binding pocket is able to confer a discrete conformation on the substrate molecule and define catalytic transition states, resulting in a selective formation of a single product. The encapsulation of the catalytic centre within the protein scaffold additionally shields the metal cofactor from oxygen and water molecules, commonly

responsible for its degradation or deactivation, thus increasing catalyst stability in an aqueous environment.[29,30] The beneficial partnership between the two components yields a system which performs reactions previously restricted to organic solvents and elevated temperatures in significantly milder conditions − a crucial step towards more sustainable catalysis.

The hybrid nature of ArMs enables a dual approach to catalyst optimisation, allowing for independent modification of the cofactor and the protein scaffold, frequently referred to as chemogenetic optimisation.[31−33] Changes to the first coordination sphere, often through rational ligand design to manipulate the electronic effects around the metal centre and linker variations to adjust the position of the cofactor within the binding pocket can lead to the diversification of the catalytic repertoire of the ArM and improved activity.[34] Genetic modification of the biological component illustrates a far more challenging aspect of ArM optimisation. Many reports outline successful enhancements in enantioselectivity through rational design and site-directed mutagenesis, yet direct evolution approaches are often favoured, particularly with ArMs capable of self-assembly where their preparation times are minimised.[25,35] While the high-throughput screening requirements associated with the generation of a large library of random mutants, for example through error-prone PCR, are costly and highly time-consuming, accurate predictions of the intricate relationships within the protein scaffold remain difficult to foresee.[36] However, technological advances in computational modelling and structural predictions are capable of significantly accelerating the process, offering a deeper understanding of the secondary coordination sphere effects and their influence on the catalytic activity.[37−39]
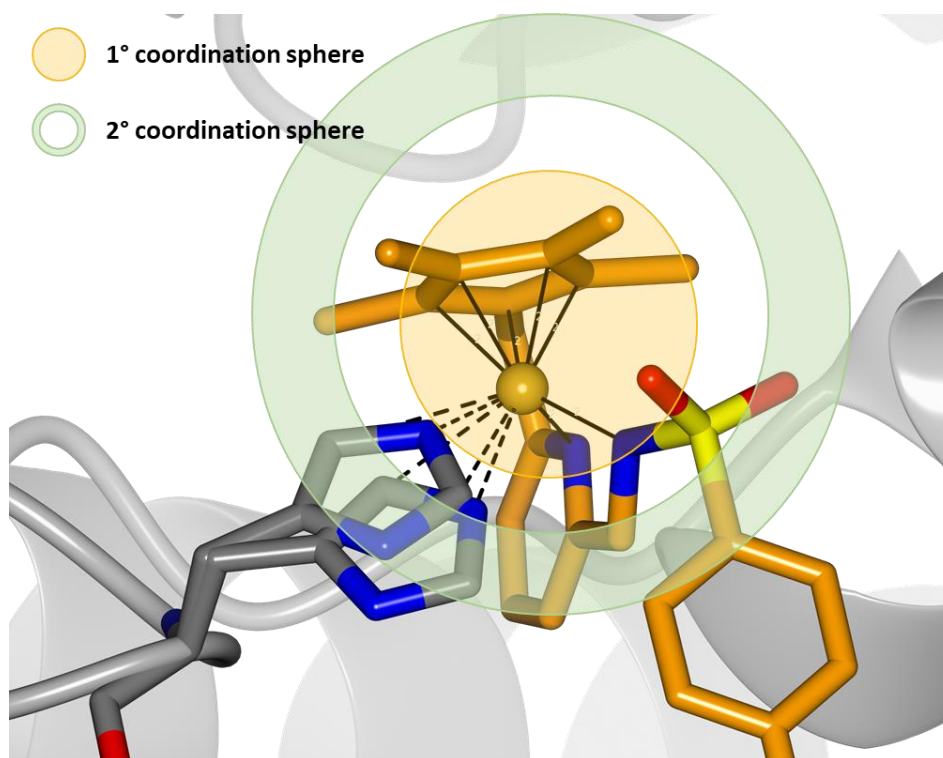
Figure 1.2 Schematic representation of the primary (1°) and secondary (2°) coordination spheres of the inorganic metal complex situated within the protein scaffold of the ArM. The 1° coordination sphere comprises atoms and ligands directly bonded (solid black lines) to the metal centre (yellow sphere). The 2° coordination sphere represents the interactions (dashed black lines) between the metal centre and the surrounding residues but may also include interactions of the amino acids with the substrate.

The attractive features of ArMs have inspired the creativity of researchers to develop multiple methods for their design, which can be classified into three main strategies – reconstitution of natural metalloproteins, de novo design and anchoring of a metal catalyst within a protein, either covalently or non-covalently (**Figure 1.3**). Several excellent reviews have been published comprehensively reviewing the field of artificial metalloenzymes and thus, the commentary below only provides a brief summary of the fundamental concepts.[21,40–43]

In the first approach, the exchange of the individual metal centre or the entire metal cofactor can confer a new catalytic activity onto the enzyme. In carbonic anhydrase (CA), which naturally catalyses the hydration of CO_2

to HCO_3^-, the replacement of the native histidine-coordinated zinc(II) ion with manganese(II) created a peroxidase for the epoxidation of *p*-chlorostyrene and styrene with an enantiomeric excess (*ee*) of 67% and 58%, respectively.[44] Substitution with rhodium(I) yielded a stereoselective catalyst for the hydrogenation of stilbene, with a 20-fold higher preference for the cis-isomer.[45] Examples of ArMs utilising myoglobin (Mb) as the protein scaffold include the exchange of the native iron(II) containing haem to manganese(III) porphycene which bestows the ability to catalyse $C(sp^3)$-H bond hydroxylation reactions onto the protein complex (**Figure 1.3 A**).[46] Taking advantage of pre-existing metalloprotein architectures offers a relatively straightforward pathway towards new functionalities. Nonetheless, the natural evolution process of proteins has resulted in strictly predefined binding pockets with minimum flexibility, thus severely limiting the breadth of metals and prosthetic groups that can be accommodated within.
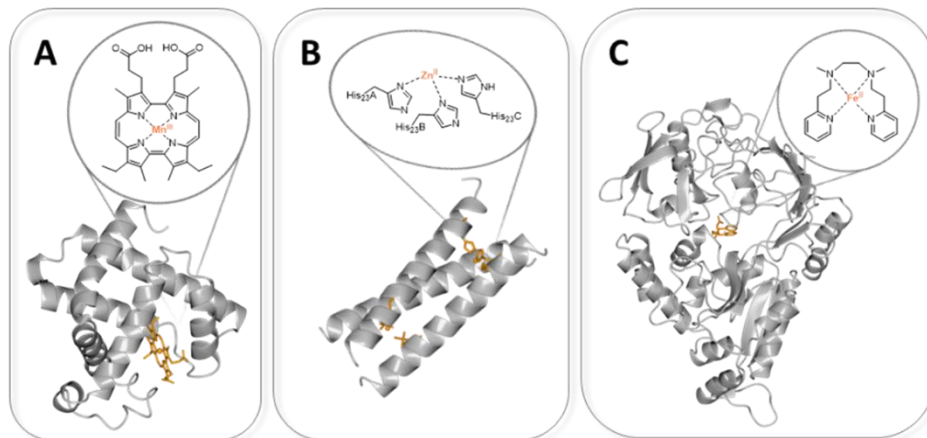
Figure 1.3 Crystal structures of prominent ArM examples developed through each of the strategies and their corresponding target reactions; protein scaffolds are depicted as grey ribbons and the metal cofactors as orange cylinders, with a zoomed-in chemical catalyst structure adjacent. **A** rMb(Mn(III)Pc), an artificial C-H hydroxylase comprising reconstituted myoglobin with an artificial manganese porphycene cofactor (PDB: **3WI8**);[46] **B** [Hg(II)]$_S$ [Zn(II)(OH$_2$)]$_N$(TRIL9CL23H)$_3$; a de novo artificial hydrolase based on a three-stranded coiled coil unit with a catalytic zinc(II) centre (PDB: **3PBJ**);[47] **C** Fe(L4D) $\subset$ NikA, an artificial oxygenase constituting an abiotic iron metal cofactor incorporated inside the pocket of a periplasmic nickel-binding protein (PDB: **4I9D**).[48]

The de novo design describes a 'from scratch' or 'bottom-up' route towards the development of new ArMs. Significant advancements in protein engineering and computational modelling are allowing researchers to develop protein scaffolds from individual peptide sequences which assemble into well-defined three-dimensional structures with engineered metal binding sites.[49] Most examples in the literature employ three-stranded coiled coil assemblies of alpha-helices, however, more recent works have successfully demonstrated the catalytic activity of β-sheet constructs.[50−52] The design of the first bimetallic ArM exploited a coiled peptide scaffold to incorporate a catalytic zinc(II) ion within a histidine binding site and at an independent location, a structural mercury(II) ion bound by three cysteine residues (**Figure 1.3 B**).[47] The authors demonstrated the capability of the system to catalyse the hydrolysis of p-nitrophenyl acetate with only 100-fold less efficiency at pH 9.5 in comparison to CA II at pH 8.0, a native hydrolase enzyme. While, in the absence of the catalytic metal centre the peptide complex still exhibited activity towards hydrolysis of the substrate, only in the presence of the zinc(II) ion, the ArM was capable of CO_2 hydration with a 500-fold efficiency over the natural equivalent. The flexibility of the de novo approach allows access to more diverse metalloprotein architectures, and thus a greater reaction scope. Nonetheless, replicating the intricacies of the interactions which exist within natural proteins, particularly those responsible for the secondary coordination sphere effects remains extremely challenging.

In order to fully exploit the utility of ArMs to perform new-to-nature reactions, the breath of metal cofactors needs to be expanded to those comprising metals either not natively associated with the protein scaffold of choice or not known to be found within living organisms at all. However, as natural protein scaffolds have evolved with discrete binding pockets, such an approach frequently necessitates additional anchoring motifs to be incorporated into the ArM design further limiting the choice of the scaffold.[53−56] Alternatively, and frequently supported through the

implementation of protein engineering methodologies, pre-existing biomacromolecules, with native functions unrelated to the one desired in the ArM can accommodate inorganic metal complexes to create new biohybrid catalysts.[57] NikA, a nickel periplasmic binding protein (PBP) from *Escherichia coli* (*E. coli*) has been shown to demonstrate catalytic activity towards sulfide oxidation after incorporation of an iron complex with N_2Py_2 ligands (**Figure 1.3 C**).[48,58] A sulfide containing a $4\text{-}AcNHC_6H_4$ aryl substituent was converted to its corresponding sulfoxide with a yield of 69%, turnover number (TON) of 173 and a turnover frequency (TOF) of 43 h^{-1}, thus exhibiting one of the highest TONs amongst artificial oxygenases. The rise in the number of ArM designs which exploit the above approach reflects its immense versatility, not only in the methodologies available for anchoring the abiotic cofactor inside the scaffold but also in its compatibility with multiple optimisation strategies, which allows the development of the most efficient catalytic systems.

Within these three main strategies, ArMs can be further classified based on the method utilised for the installation of the metallic cofactor within the protein scaffold – dative coordination, covalent immobilisation and non-covalent binding, also referred to as supramolecular anchoring (**Figure 1.4**). The development of systems which depend on the spontaneous self-assembly of the two components through non-covalent interactions has attracted significant attention. Their operational simplicity greatly facilitates optimisation attempts and eliminates challenges associated with covalent modification of the biomolecular scaffold, of which the results are sometimes difficult to anticipate. However, the successful exploitation of supramolecular anchoring motifs requires the use of complementary binding pairs which exhibit high affinity towards each other to ensure ArM stability.
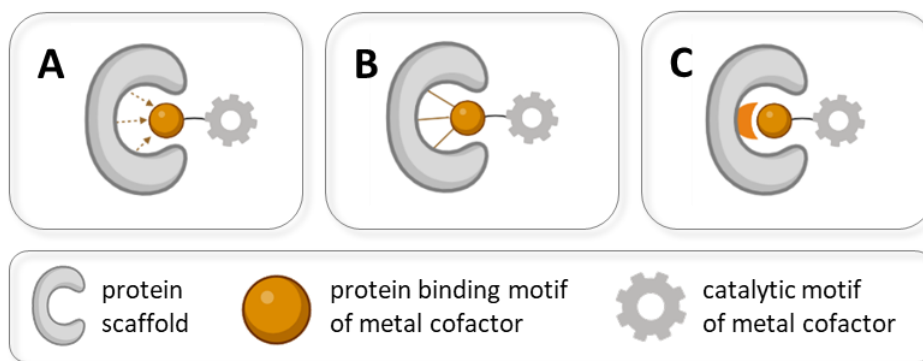
Figure 1.4 A summary of different methods for installing the metal cofactor within a protein scaffold for the assembly of ArMs. **A** Dative coordination; **B** covalent attachment; **C** supramolecular anchoring using high affinity-based pairing. Created with Biorender.com.

1.3 Supramolecular anchoring strategies for artificial metalloenzyme assemblies

1.3.1 Irreversibly bound ArMs based on the streptavidin-biotin motif

The binding between the proteins from the avidin family and biotin represents the strongest non-covalent interactions reported to date, with dissociation constant (K_d) values in the range of 10^{-15} M.[59] In 1978, Wilson and Whitesides exploited the remarkable affinity between avidin and its natural ligand for the development of the first reported ArM, targeting the reduction of C=C within an α-acetamidoacrylic acid molecule.[60] A rhodium(I) norbornadiene complex was chelated to a diphosphine modified biotin anchor allowing the incorporation of the inorganic catalyst within the protein scaffold which facilitated enantioselective catalysis. Despite the successful conversion of the substrate to *N*-acetylalanine with a 44% *ee* in favour of the (*S*) isomer, the authors concluded the catalytic system to be 'not a practical asymmetric catalyst' as the scaffold was 'expensive by the standards of transition metal catalysis' and the enantioselectivity was 'only modest'.[60] The system was revisited 25 years later when the Ward group performed chemogenetic optimisation to improve the localisation of the catalyst within the secondary coordination sphere of the protein. Through several rounds of optimisations, including the introduction of spacer

moieties, replacement of the avidin scaffold with streptavidin (another member of the avidin protein family which offers a deeper binding pocket for the catalyst with comparable binding affinity), and site-directed mutagenesis, a significant improvement in enantioselectivity of up to 96% *ee* with a preference for the (*R*) isomer of *N*-acetylalanine was achieved.[53,61] However, most revolutionary advances in the group have been made towards the development of artificial asymmetric transfer hydrogenase (ATHase) catalysts. The incorporation of biotinylated Noyori-type metal complexes, predominantly based on ruthenium and iridium, within the streptavidin scaffold (**Figure 1.5**) has led to the successful reduction of a range of substrates including imines, enones and ketones.[62−65]

Since, the Ward group has developed a vast library of ArMs based on the streptavidin-biotin technology capable of catalysing a range of chemical transformations, which have been expanded to operate in complex biological systems and participate in cascade reactions, illustrating the exemplary flexibility of the system.[66]
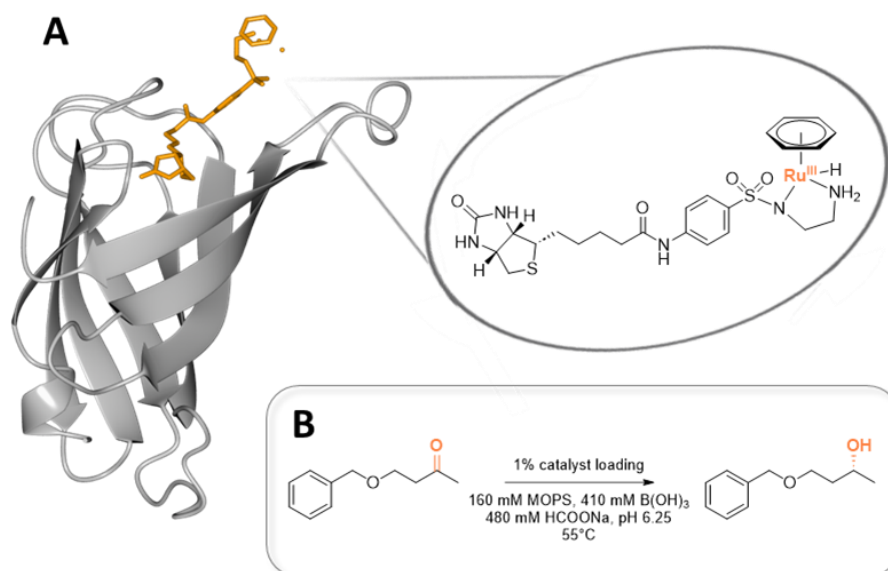
Figure 1.5 A The crystal structure of an asymmetric transfer hydrogenase based on the streptavidin scaffold (grey ribbon) with a biotinylated ruthenium(III) catalyst (orange cylinders) (PDB: **2QCB**); the chemical structure of the cofactor is shown for clarity. **B** Example ketone reduction reaction catalysed by the ArM.[65]

Nonetheless, despite their remarkable stability and functionality, ArMs based on the streptavidin-biotin motif are not exempt from limitations. The homotetrameric structure of the protein scaffold which arises from the assembly of a dimer of dimers poses challenges for catalyst design. In particular, efforts towards genetic optimisation and precise control of the secondary coordination sphere are complicated by the reflection of any mutations across all four subunits. The two subunits constituting the biotin binding pocket are related through the C_2 symmetry axis, thus any mutations to the two residues in its proximity are reflected in both monomers of a binding interface.[67] The proximity of the S112 and K121 residues to the anchored biotinylated catalyst (**Figure 1.6 A**) makes them excellent candidates for mutagenesis studies. However, this symmetry relation complicates an accurate evaluation of the correlation between the mutation's location and the catalytic performance. Subsequently, efforts
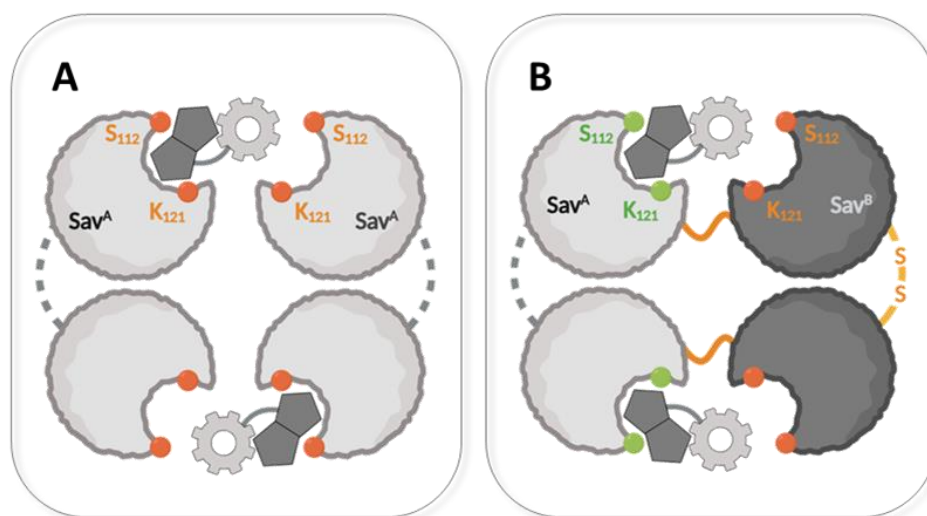
Figure 1.6 A Cartoon representation of the ArM based on a homotetrameric protein scaffold, highlighting the two symmetry-related residues, S112 and K121 and their location in relation to the biotinylated catalyst. **B** Schematic representation of the ArM mutant composed of two single-chain dimeric streptavidins, highlighting the two engineered linking units, the polypeptide linker between Sav^A and Sav^B units and the disulfide bond between the two chains.[67,68]

were made to engineer a streptavidin mutant exhibiting a dimeric quaternary structure which would enable independent mutagenesis of each subunit within the binding pocket. The fusion of Sav^A and Sav^B units (**Figure 1.6 B**) was achieved through the insertion of a short polypeptide linker, constituting 26 amino acids, between the C-terminus and N-terminus of the two subunits, respectively.[68] Additionally, the H127C mutation was engineered on the Sav^B unit to promote the formation of a disulfide bond between the two dimeric streptavidins, which alongside the π-π stacking between the H127 residues on the parallel faces facilitated the assembly of the correct quaternary structure.[69]

As outlined above, the remarkably high affinity between a biotinylated cofactor and the streptavidin scaffold creates an almost irreversible anchoring motif. The subsequent high stability of ArMs based on the streptavidin ⊂ biotin technology ensures a prolonged lifetime of these hybrid catalysts, however, simultaneously precludes the recycling of the protein scaffold upon poisoning or deactivation of the inorganic small molecule catalyst. Overcoming this design limitation necessitates reengineering the binding pocket to allow for a higher degree of flexibility without compromising on the binding affinity. Several reports in the literature have described their contributions to developing a streptavidin capable of reversible biotin binding, prominently introducing single-point mutations within and in the vicinity of the binding pocket, focusing on modifications of the flexible loops 3-4 and 7-8.[70,71] However, to date there are no reports which employ streptavidin mutants capable of reversible biotin binding as protein scaffolds for artificial metalloenzymes.

Thus, it remains unknown how feasible reversible binding is for ArMs based on the streptavidin ⊂ biotin technology as it has been shown that loop mutations, especially those situated close to the metal complex may significantly impact the activity and enantioselectivity of the catalyst.[61,63,72,73]

1.3.2 Reversibly bound ArMs based on the periplasmic binding protein-siderophore motif

The complementary binding between siderophores, small molecule iron(III) chelators secreted by microorganisms, and their cognate periplasmic binding proteins (PBPs) offers a viable platform for the development of recyclable ArMs. Within the bacterial iron uptake pathway, siderophores play a crucial role in the delivery of the metal ion from the environment into the cytoplasm. Iron chelation overcomes the metal's limited solubility and hence bioavailability and facilitates its uptake across the cellular membrane.[74] In Gram-negative bacteria, the periplasm features as an additional boundary for the iron(III) siderophore complexes to traverse; once inside, PBPs capture these complexes and transport them within the proximity of transporter proteins translocated across the inner membrane, which in turn aid their crossing into the cytoplasm.[75,76] The precise mechanism for the interaction between siderophore complexes and their PBPs remains unclear, as the pathway is not conserved across bacterial species further complicating its study.[77–79] Prior to the iron being incorporated into the intracellular machinery, the metal must be released from the strongly bound chelator. One of the proposed release mechanisms is dependent on the ability of siderophores to release the metal upon the reduction of iron(III) to iron(II).[80,81] Iron in its lower oxidation state possesses a larger ionic radius and lower charge density, thus resulting in an iron siderophore complex of much lower thermodynamic stability in comparison to the equivalent iron(III) species.[82] This discrepancy in stabilities facilitates the dissociation of the complex and the release of the metal without comprising the structure of the chelating ligand, subsequently allowing its recovery and recycling.[83,84]

The reductive iron release mechanism employed by bacteria has inspired the Duhme-Klair group to design an ArM capable of redox-triggered disassembly.[54] Azotochelin, a tetradentate catecholate siderophore secreted by *Azotobacter vinelandii* (*A. vinelandii*), when in complex with

iron(III), was found to be capable of binding to CeuE, a PBP found in *Campylobacter jejuni* (*C. jejuni*), with a high affinity (K_d = 4.9 ± 0.4 nM).[54,85] Within the protein binding pocket, two amino acid residues, Y288 and H227, coordinate to the metal centre, thus completing the coordination sphere of the coordinatively unsaturated iron(III) azotochelin complex and contributing to the notably low dissociation constant. The complementary pairing of iron(III) azotochelin complex and CeuE was subsequently used as the anchor and the protein scaffold, respectively, of the ArM.

Azotochelin bears a free carboxylic acid moiety on its lysine backbone which upon binding to CeuE points away from the binding pocket, making it an excellent candidate for functionalisation with catalytic metal complexes.[54,86] An iridium(III) Noyori-type catalyst was conjugated to the non-metallated siderophore anchor through an amide bond on the aryl sulfonamide ligand, yielding an AzotoCat complex. The incorporation of the iron(III) anchor-catalyst conjugate, SidCat (**Figure 1.7 A**) within the protein scaffold, resulted in the formation of an ATHase, capable of enantioselective imine reduction (**Figure 1.7 B**).[54] The secondary coordination sphere was shown to promote the formation of (*R*)-salsolidine with a 35.4 ± 0.1 *ee* in comparison to the free catalyst, albeit with a 20-fold lower TOF. Structural studies have led to suggest the considerable decrease in activity upon protein binding was a result of the H227 residue, which resides on a flexible loop, coordinating to the iridium centre.[54] This was hypothesised to restrict the binding of the hydride, although mutagenesis experiments in which the histidine residue was replaced by alanine, have revealed its presence to be essential for achieving enantioselectivity. However, the notable feature of the ArM is not its catalytic reactivity or enantioselectivity but its unprecedented ability to disassemble into individual constituents, the protein scaffold, and the anchor-catalyst conjugate, without any adverse structural changes to the former and thus enabling its recycling.
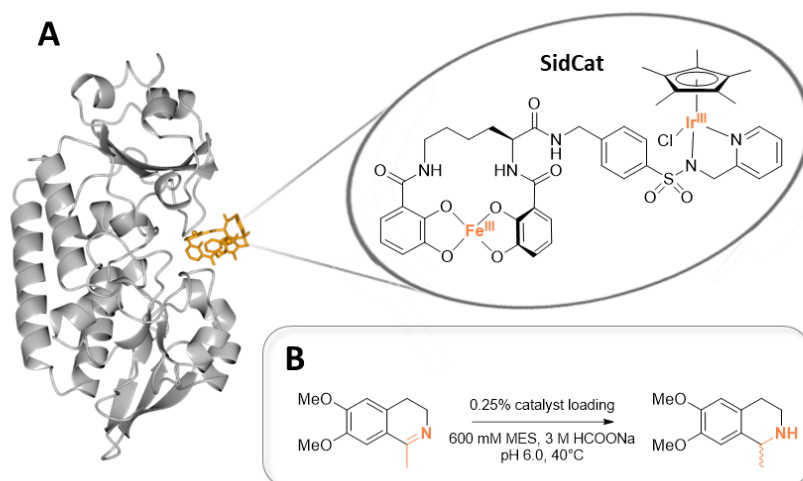
Figure 1.7 A The crystal structure of an asymmetric transfer hydrogenase based on the complementary pairing between a PBP (grey ribbon) and iron(III) azotochelin, with the latter, conjugated to iridium(III) Noyori-type catalyst (orange cylinders) (PDB: **5OD5**); the chemical structure of the metal cofactor is shown for clarity. **B** The benchmark imine reduction reaction used for validating the catalytic activity of the ArM.[54]

In a parallel manner to the hypothesised redox-triggered intracellular release of iron within the bacterial cytoplasm, as described above, the iron(III) centre of the azotochelin anchor can be reduced to iron(II) in the presence of a sodium dithionite, a strong reducing agent (**Figure 1.8**). The release of the anchor-catalyst conjugate allows the protein scaffold to be utilised in a subsequent ArM assembly with a new SidCat molecule. The change of the oxidation site within the binding pocket of CeuE was successfully followed using UV-vis spectroscopy. The bleaching of ligand-to-metal charge transfer (LMCT) band (λ_{max} = 547 nm) associated with iron(III) azotochelin was observed upon the addition of excess reducing agent and was shown to subsequently reform in an oxidised solution.[54] The formation of the iron(II) complex of SidCat triggers the release of the anchor-catalyst conjugate from the protein scaffold due to its significantly lower thermodynamic stability and in effect lower binding affinity towards CeuE (K_d ≤ 1 μM).[54] Following the separation of the two dissociated molecules, a fresh aliquot of SidCat was added to the recycled CeuE to assemble an ArM which despite a small loss in catalytic activity it displayed

comparable enantioselectivity (32% *ee*), confirming the incorporation of SidCat within the binding pocket.

Unfortunately, simultaneous recovery of both ArM components was not feasible as AzotoCat was found to adsorb to the membrane of the concentrating filters used for the isolation of the protein scaffold. Despite several limitations and drawbacks of the initial ArM design, the successful demonstration of redox-triggered disassembly symbolises a notable step forward towards the sustainable use of ArMs. Nonetheless, further optimisations are required to facilitate the separation and isolation of both disassembled components, achieving a fully recyclable system.
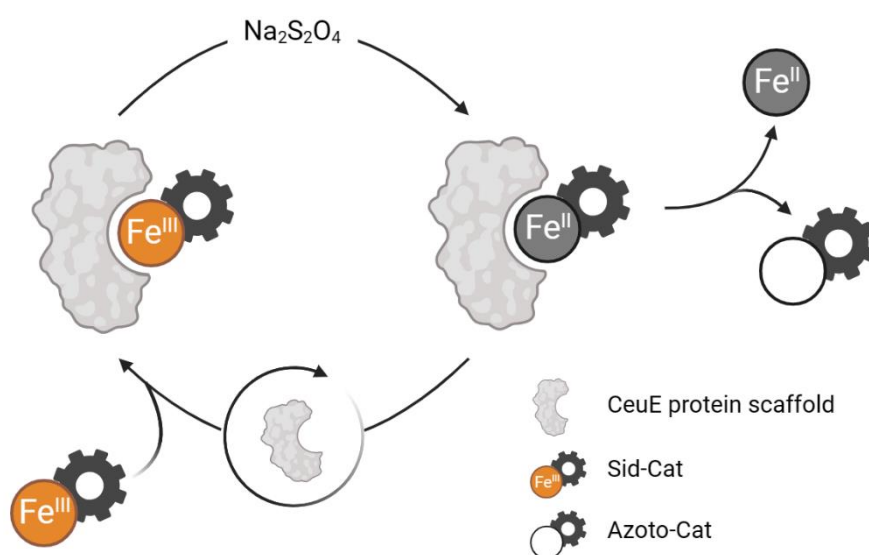
Figure 1.8 Schematic illustration of the redox-triggered disassembly for an ArM based on the reduction of the iron(III) to iron(II) and the recycling of the CeuE protein scaffold to reassemble the ArM.[54] Created with Biorender.com.
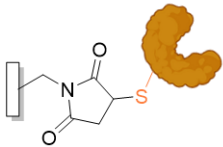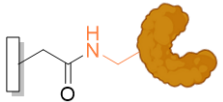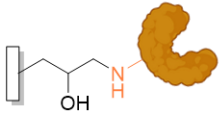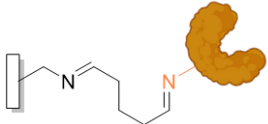
1.4 Artificial metalloenzyme immobilisation

Enzyme immobilisation has been a crucial driver in adapting biocatalysis for industrial applications. Carrier-tethered catalysts are able to be incorporated within fixed-bed flow reactors facilitating reaction scale-up
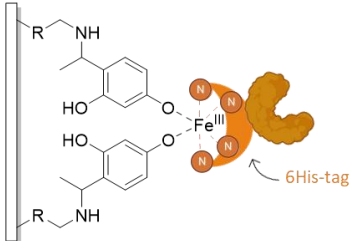
and have been shown to exhibit prolonged stability and higher tolerance towards organic solvents, as well as facilitate efficient product isolation for subsequent enzyme reusability; considerations which are at the centre of process development.[87–90] The portfolio of immobilisation chemistries as well as support materials which are compatible with multiple enzyme families has greatly expanded and diversified over the years (**Table 1.2**). Protein adsorption remains prevalent across the literature as an effective method for immobilising enzymes, however, the phenomenon of conformational changes exhibited upon contact with solid surfaces, often detrimental to their catalytic activity, has accelerated the research towards more elaborate approaches.[87,91–93] Covalent linkages exploit reactive amino acid residues in bioconjugation reactions to offer precise and site-specific immobilisation, however, these become challenging if multiple residues are accessible for the reaction.[94] Moreover, if the modified residue contributes to structural stability or enzymatic function, its chemical modification may have a detrimental impact.

Contrarily, the employment of affinity tags, further discussed in **Chapter 3**, offers site-specific immobilisation without the requisite for additional protein modification strategies, beyond those already necessary for protein expression. However, their dependency on non-covalent interactions can give rise to protein leaching during long-term usage.[94] In recent years, the employment of 'tag and catcher' pairs has evolved as a more promising immobilisation approach, offering a very precise bioconjugation methodology. In 2012, Howarth and co-workers have made a revolutionary discovery into the spontaneous and self-catalysed isopeptide bond formation between lysine and aspartic acid within the fibronectin-binding protein, FbaB of Streptococcus pyogenes which they have engineered into an efficient, yet irreversible, coupling pair, known as the SpyTag-SpyCatcher technology.[95] While this tag and catcher pair has found multiple applications, its employment in protein immobilisation has been limited and has yet to be translated into an industrial setting.[96–98]
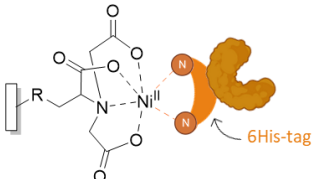
Table 1.2 Summary of most prevalent covalent (**1** – **4**) and non-covalent (**5** – **7**) immobilisation strategies used in tethering enzymes to solid supports.

Immobilisation strategy	Support	Enzyme	References
1 Maleimide-thiol bonding	MWCNTs[a]	dehydrogenase oxidase	99,100 101
	SiO$_2$	nitroreductase carbonic anhydrase β-glucosidase	102 103 104
2 Amide formation	Au	cytochrome c glycosyl transferase	105 106
	PSi[a]	acetylcholinesterase	107
	PEAA[a] film	peroxidase	108
	Au SiO$_2$	ribonuclease	109 18
3 Epoxide activation	Au	peroxidase	110
	dextran	dehydrogenase	111
	sepabeads	β-galactosidase acylase	112 113
4 Dialdehyde crosslinking	MWCNTs	lipase β-galactosidase	114 115
	chitosan	oxynitrilase lipase	116 117
5 Biotin-streptavidin binding	NPs[a]	oxidase	118
	MPS[a]	β-galactosidase	119
	SiO$_2$	peroxidase	120

6 EziG support

CPG[a]

lyase	121
peroxygenase	122
reductase	123
ω-transaminase	124

7 NTA/His-tag affinity

Au	laccase	125
carbon	peroxidase	126
MWCNTs	nitrogenase	127
	oxidase	128

[a] CPG, controlled porosity glass; MPS, modified polysulfone; MWCNTs, multi-walled carbon nanotubes; NPs, nanoparticles; PSi, porous silicon; PEAA, poly(ethylene-co-acrylic acid).

Despite the apparent advantages of protein immobilisation, its application in the field of ArMs has been very limited and only a few literature reports are available. Controlled site-specific immobilisation becomes a more critical consideration with ArMs as the accessibility of the exposed metal cofactor towards the substrate is essential for its catalytic function. And despite extensive advances, such precision remains one of the greatest challenges.

1.4.1 ArM immobilisation on non-conducting supports

The covalent immobilisation of a lipase-based ArM was the first literature report to describe the attachment of a biohybrid catalyst to a solid support. Published in 2015, Jose Palomo and co-workers evaluated multiple strategies for the immobilisation of lipase-based ArMs onto either functionalised Sepharose and Sepabead supports.[129] A palladium pincer ligand was selected as the metal cofactor and incorporated into the protein scaffold through a covalent bond formation between the OH group of a serine residue situated within the binding pocket and p-nitrophenyl

phosphonate moiety of the inorganic catalyst. Interestingly, the ArM assembly was performed following the tethering of the protein scaffold to the support. The authors did not comment on the efficiency of ArM assembly in comparison to the unbound lipase nor on the immobilisation yield of the assembled ArM versus the apo protein; both factors requiring consideration. The most successful iteration comprised a lipase from *Candida antarctica* B (CAL-B) tethered to a commercially available Sepabeads resin, functionalised with aldehyde groups which upon reaction with lysine residues yielded an immobilised strategy based on multi-point imine attachment; the non-reacted aldehyde groups were modified with alkyl chains (C8) to increase the hydrophobicity of the surrounding environment (**Figure 1.9**).[129] The resulting catalytic platform was tested in an asymmetric Heck coupling reaction between iodobenzene and 2,3-dihydrofuran; a yield of 95% with 96.6% *ee* was achieved in optimised conditions of 25% water in DMF at 120°C after 24 hours. Unfortunately, the free palladium cofactor was not evaluated for its capability to perform enantioselective conversion and as such it is not possible to confirm the effect of the secondary coordination sphere. The immobilised catalyst was able to be reused for two consecutive cycles illustrating a crucial step towards achieving industrially attractive heterogenous ArM systems.

Nanoparticles as a support for enzyme immobilisation offer favourable loading capacities due to their remarkably high surface area to volume ratio, subsequently minimising mass transfer limitations and thus exhibiting key attributes for achieving efficient biocatalysis.[130,131] An ArM based on the streptavidin-biotin motif described in **Section 1.3.1**, was anchored to amino-modified silica nanoparticles via glutaraldehyde, which served the role of a homobifunctional linker.[132] Imine bond formation between the aldehyde functionalities and the surface of the nanoparticles on one end and lysine residues on the streptavidin scaffold on the other end, was employed to promote stable immobilisation.[133]
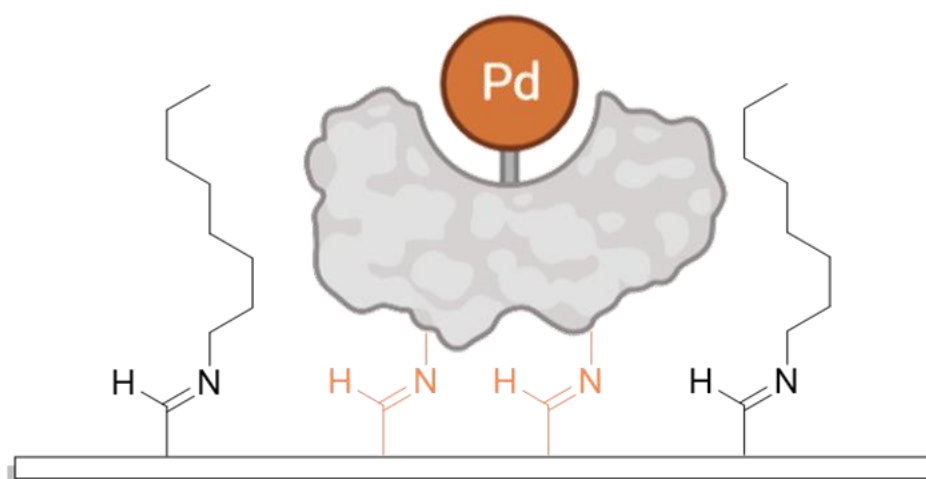
Figure 1.9 Schematic representation of the immobilised Pd-CALB ArM on a modified Sepabead resin through multi-point covalent linkages between aldehyde functionalised support and lysine residues on the protein scaffold.[129]

Moreover, the modified nanoparticles were further functionalised to incorporate an organosilica layer, within which the immobilised ArM was encased, offering a protective barrier against catalyst deactivation. The beneficial effect of immobilisation on the catalytic performance was demonstrated on a benchmark asymmetric imine reduction reaction, where the immobilised ATHase based on the S112A-K121A streptavidin scaffold was able to achieve a TON of 12 885 with a 97% conversion rate, as opposed to a TON of 2 513 and a conversion of 19% for the free catalyst.[132] The increase in catalytic activity was achieved at the expense of reaction selectivity with a 19% *ee* reduction upon immobilisation. The nanoparticles were able to be recycled successfully for two successive cycles with retention of enantioselectivity, albeit a two-fold decrease in conversion rate.[132] The individual contributions of immobilisation on silica nanoparticles versus the presence of the protective organosilica envelope on the catalytic activity remain unclear, however, the improved performance of immobilised ArMs over the free catalysts is unequivocal.

Universal methods for covalent tethering of proteins remain evasive and thus a change in the support material frequently necessitates a distinct approach. Methodologies employing gold nanoparticles commonly exploit the high affinity of alkanethiols towards gold and their ability to form self-assembled monolayers (SAM) for an efficient and straightforward functionalisation.[134] An azido-alkyl dithiolane bifunctional linker was developed to bind to the nanoparticle surface through SAM formation while simultaneously tethering a protein scaffold modified with a strained alkyne through strained-promoted azide-alkyne cycloaddition (SPAAC) reaction (**Figure 1.10**).[135] An iron(III) containing mimochrome, artificial haem metalloenzyme exhibiting peroxidase activity was selected as the model catalyst for examining the effect of immobilisation through the bifunctional linker.[136] The gold nanoparticles were decorated with azide functionalities through the formation of lipoic acid-based SAMs while the ArM was conjugated selectively to a pegylated aza-dibenzocyclooctyne linker via the only lysine residue on the protein scaffold, forming a 'clickable' ArM.[135] Bioconjugation through a lysine residue offers a versatile path towards protein modification, however, in only a few examples this promotes a site-selective reaction as frequently protein scaffolds comprise multiple primary amines on their surface. The immobilised mimochrome was successfully characterised through circular dichroism (CD) spectroscopy to confirm its structure did not undergo conformational changes upon tethering to gold nanoparticles.[135] The effect of immobilisation on the catalytic activity was evaluated against the oxidation of 2,2'-azino-bis-3-ethylbenzothiazoline-6-sulfonic acid in the presence of hydrogen peroxide. Control experiments on the bioconjugated versus unmodified ArM established a minimal effect of protein functionalisation on the catalytic reactivity.

However, subsequent immobilisation on gold nanoparticles resulted in a substantial decrease of the k_{cat} value from 58 x10^2 s^{-1} to 1.10 x10^2 s^{-1}; no details on the stereoselectivity of the reaction were documented.[135] Despite, the unsuccessful attempt to improve the catalytic performance of the

mimochrome upon immobilisation, the development of an efficient route for tethering proteins onto gold is a crucial example as it offers compatibility with other gold materials, such as electrodes.
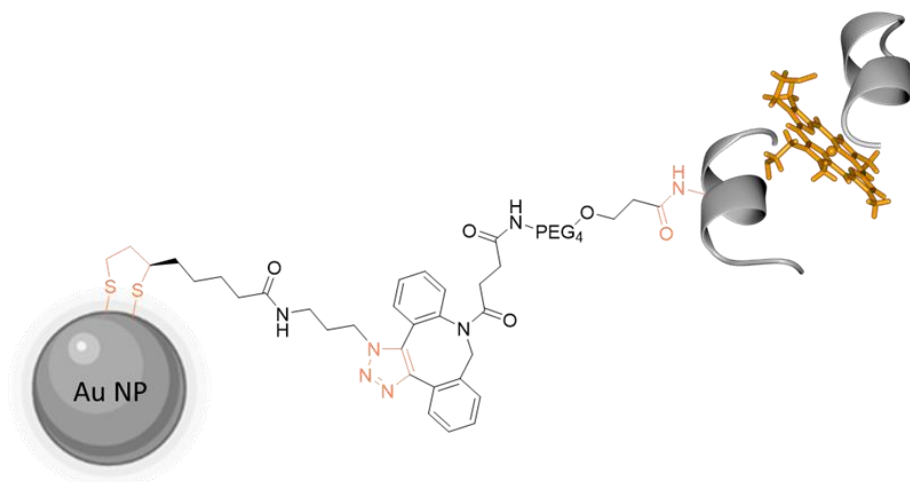
Figure 1.10 Schematic diagram of an immobilised ArM arising from the conjugation of the gold nanoparticle (Au NP) functionalised with a dithiol-based bifunctional SAM linker and a 'clickable' ArM, an iron(III) mimochrome tethered to a PEG chain with a strained alkyne handle resulting in the formation of a triazole.[135]

1.4.2 ArM immobilisation on conducting supports

The immobilisation of redox-active proteins on conducting surfaces, either for the study of their electron transfer properties or exploitation in redox catalytic reactions is associated with similar challenges as the immobilisation of non-redox enzymes. However, additional considerations are required to ensure an efficient electrochemical connection is established between the electrode and the redox centre of the protein. Detailed studies of metalloenzymes have revealed the distance of 14 Å as the upper length limit for facilitating electron tunnelling between redox active sites, imposing restrictions on the design of immobilisation approaches.[137,138] Alternative strategies are available including the employment of redox mediators, either in solution or tethered to proteins, allowing to circumvent the limitations of the distance between the electrode and the redox centre, as further discussed in **Section 4.1**.[139]

Protein adsorption exemplifies the simplest approach in the field of protein immobilisation, as no modifications of the electrode or the biomolecule are necessary. However, the lack of specificity in protein orientation upon contact with the surface may result in a layer comprising a heterogeneous population.[140,141] The presence of multiple environments and thus varying electron transfer properties across such layer give rise to broad Faradaic peaks in cyclic voltammograms, the phenomenon known as 'dispersion', making data analysis challenging.[142] Consequently, more elaborate approaches are necessary; the functionalisation of electrode surfaces to control protein orientation upon adsorption, frequently through electrostatic or hydrophobic-hydrophilic interactions, illustrates one example. Lombardi and co-workers modified the surface of a gold electrode with SAMs of decane-1-thiol for the immobilisation of mimochrome VI, an artificial haem oxidase.[136,143] The approach exploited the interaction between the non-polar SAM and the hydrophobic face of the ArM, immobilising the metalloenzyme in an electroactive conformation. Cyclic voltammetry (CV) was able to successfully distinguish between the two electrochemically active conformers of the ArM as the oxidised form, with no net charge, was stabilised over its reduced equivalent bearing a net charge of -1. Thus, two formal reduction potential values were observed; an ArM comprising an iron(III) haem centre exhibited a formal reduction potential ($E^{\circ\prime}$) of -106 mV vs saturated calomel electrode (SCE), whereas for the conformer constituting an iron(II) haem centre a value of -131 mV vs SCE was measured.[143] No fluctuations in the voltammogram shape were observed during repeated measurements in a temperature range of $5 - 35°C$, ascertaining the stability of the immobilisation method.[143] Electrochemical measurements in the presence of an increasing concentration of oxygen, demonstrated that the ability of the ArM to perform an electrocatalytic reduction of dioxygen was preserved upon adsorption.[143] However, the overall catalytic performance was limited by the loss of the protein from the electrode surface, highlighting the need for more stable immobilisation

approaches if the aim is to develop electrocatalytic platforms with long-term stability.

In a parallel approach to immobilising ArMs on gold nanoparticles, the utilisation of a bifunctional linker with a disulfide group on one end and an orthogonal bioconjugation functionality on the other enables the tethering of proteins to gold electrodes (**Figure 1.11**).[144–146] A mimochrome derivative, an artificial haem peroxidase was conjugated to an activated lipoic acid, a *N*-hydroxysuccinimide ester derivative (LA NHS) through amide bond formation between the carboxylic acid on the linker moiety and a single lysine residue on the protein scaffold in a site-selective manner.[147] Subsequently, the inherent affinity of sulfur atoms towards gold was exploited for the formation of mimochrome SAMs on the electrode, achieving a surface coverage comparable to one obtained through protein adsorption on decane-1-thiol SAMs, 20.4 pmol cm^{-2} and 23.5 pmol cm^{-2}, respectively.[143,147] Electrochemical characterisation revealed the retention of the protein's ability to exchange electrons with the electrode surface upon covalent attachment to the surface. A quasi-reversible electrochemical behaviour was observed with an $E°'$ value of -143 mV vs standard hydrogen electrode (SHE), in comparison to a freely diffusing ArM, which exhibited a one-electron reversible redox process with an $E°'$ value of -117 mV vs SHE.[147] The potential shift was hypothesised to have arisen from a change in the microenvironment surrounding the redox centre that occurred during the immobilisation process, resulting in slower electron transfer kinetics. While such small changes can be frequently overlooked in the immobilisation of non-redox enzymes, they have a significant impact on redox-active proteins as electron transfer properties influence the efficiency of electrocatalysis. Catalytic studies were not performed for the ArM tethered to the gold electrode; however, the stability of the immobilisation method was demonstrated through consecutive cycles of cyclic voltammetry during which the voltammograms did not exhibit significant changes.[147]
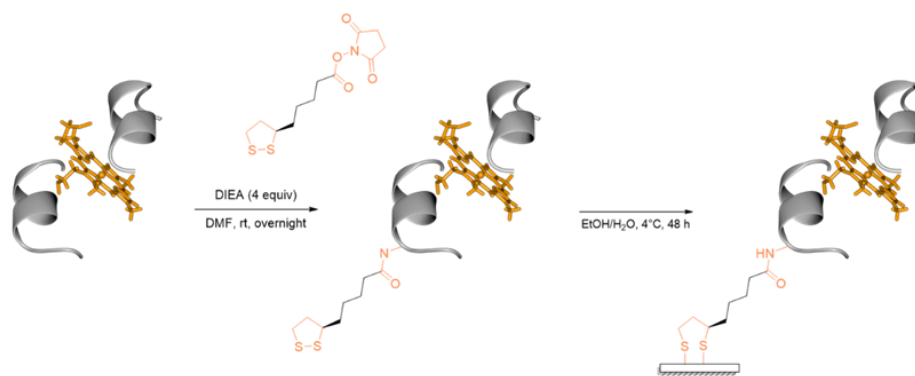
Figure 1.11 Stepwise methodology for the covalent tethering of an artificial haem enzyme onto a gold electrode surface through the SAM formation of a lipoic acid conjugated ArM.[147]

While gold electrodes are frequently the material of choice for the immobilisation of redox enzymes, predominantly due to the ease of their functionalisation in addition to gold's compatibility with a range of techniques and applications, they are not the sole choice. Pyrolytic graphite edge (PGE) electrodes have gained recognition in the field of bioelectrochemistry for their effectiveness in adsorbing proteins. Their reputation is attributed to vast surface heterogeneity which supports the immobilisation of redox proteins in electroactive conformations and the presence of carboxylate functionalities on the surface, facilitating the adsorption of proteins bearing positively-charged faces.[148–150] However, tethering of proteins with a dominating negative surface polarisation through simple adsorption becomes more challenging as electrostatic repulsions will become more prevalent accelerating protein desorption. Thus, there is a demand for stronger coupling approaches. A nickel-substituted rubredoxin (NiRd), an artificial hydrogenase, developed by metal substitution of the protein's native iron centre, was immobilised on PGE electrodes through both adsorption and direct covalent attachment, the latter exploiting carbodiimide cross-linker chemistry between carboxylates on the electrode surface and a surface primary amine of the ArM (**Figure 1.12**).[151] The electron transfer protein does not exhibit a typical redox couple traditionally observed for metalloenzymes, rather, cyclic voltammograms of the ArM exhibit a large cathodic current wave

associated with catalytic protein reduction process at an onset potential of −800 mV vs normal hydrogen electrode (NHE).[151,152] The immobilisation process did not impact the catalytic activity on the protein significantly, with the cyclic voltammogram remaining predominantly unchanged upon covalent attachment with a similar catalytic onset potential.
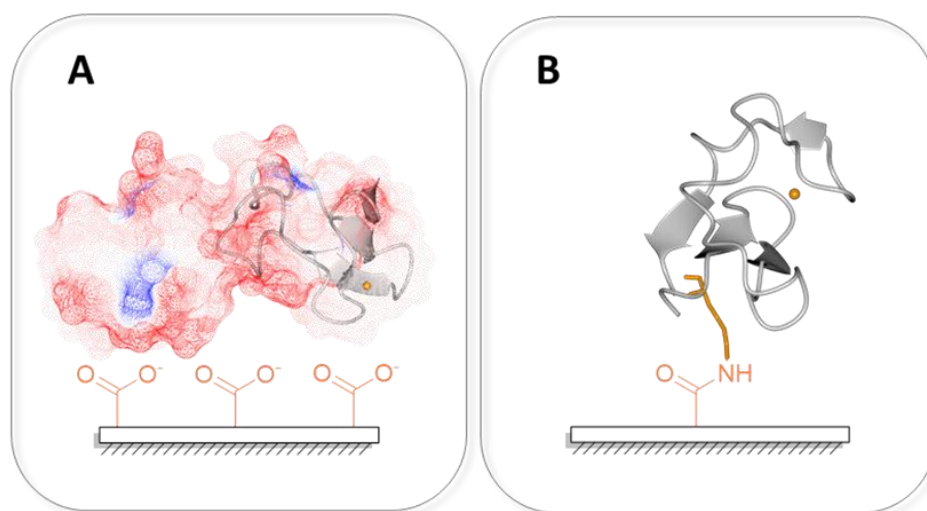
Figure 1.12 Comparison of two strategies for the immobilisation of a nickel(II) substituted rubredoxin, NiRd (PDB: **6NW0**) on pyrolytic graphic electrodes. **A** Electrostatic adsorption dependent on the interaction between negatively charged carboxylates on the electrode surface and the complementarily polarised surface of the protein; the electron density map is shown for information, where the red regions correlate to a positively charged surface. **B** Covalent tethering of the ArM onto the electrode through direct coupling of a carboxylate on the electrode surface and a primary amine on the protein scaffold, either from a lysine, asparagine, or glutamine residue; one of the surface lysine residues (orange cylinder) is shown as an example.[151,153]

However, a diminishing maximum current was detected at −1.00 V vs NHE, 250 µA and 150 µA for adsorbed and covalently immobilised ArM, respectively, denoting an almost three-fold reduced TOF, attributed to restricted flexibility of the protein scaffold upon covalent anchoring.[151] Despite the reduced catalytic performance of the immobilised ArM, the stability of the catalytic platform was enhanced upon covalent immobilisation as demonstrated through smaller decay constants, although the catalytic current density was reduced by 77% over a 25-day

period.[151] While the immobilised NiRd requires optimisation to improve its catalytic performance, the study illustrated a simple yet effective approach for covalent tethering which can be applied to other metalloenzymes bearing surface lysine residues.

1.5 Summary and conclusions

In response to the devastating effect of the chemical industry on the environment and the increasing concerns regarding its huge waste footprint, research into more sustainable processes has never been more important. While enzyme-catalysed reactions embody the premise of green chemistry, they remain limited in the number of different reactions they can be utilised for, despite remarkable advances in protein engineering methodologies. A plethora of literature is available highlighting the promise of artificial metalloenzymes for overcoming such limitations, as new-to-nature reactions are being performed in biocompatible conditions. Nonetheless, where advancements have been made in adapting enzymes for industrially relevant applications, ArMs remain in their infancy period. An increasing number of publications are available describing the incorporation of ArMs in multi-enzymatic cascades and whole-cell catalysis, however, the reports on their immobilisation are limited, despite its importance in obtaining long-term stability and recyclability. The few examples available describe the recyclability of the whole platform, enzyme and support included, yet to this date, there are no examples reporting surface regeneration for a fully recyclable system.

The development of ArMs which combine two individual components offers great potential for exploring an additional recycling point. However, the majority of ArM designs in the literature focus on an irreversible attachment of the metal catalyst within the protein scaffold to ensure high stability. The recent report on an Fe-PBP ArM capable of redox-triggered assembly exemplifies an appealing approach for the recycling of a protein scaffold if

poisoning or decomposition of the metal cofactor occurs; a problem often encountered by inorganic complexes in aqueous buffers utilised in ArM catalysed reactions. As the authors noted, method optimisation is required to ensure the simultaneous isolation of both components post-disassembly is possible.

Thus, there is a huge opportunity in combining the recyclability aspect of the redox-active ArM with immobilisation on a solid surface to explore the feasibility for recycling of each individual component, creating a fully recyclable catalytic platform. However, the proposed ArM recycling platform must have the potential for compatibility with a range of ArM designs to ensure it remains beneficial to a wider scientific community and particularly those within industrial settings.

1.6 Project aims

The overarching aim of this project is to harness the power of electrochemistry and exploit established approaches in protein immobilisation for a novel biotechnological application within the field of (artificial) biocatalysis. More specifically, the project will work towards the development of an immobilisation platform for the attachment of an Fe-PBP ArM, constituting a redox-reversible catalyst-protein anchor, onto a conducting surface (**Figure 1.13**).

This approach is anticipated to facilitate the electrochemical reduction of the anchor, resulting in the disassembly of the ArM into its individual elements and the separation of the anchor-catalyst conjugate from the immobilised protein scaffold, making the biological component available for recycling. This aims to address the issues previously encountered during the homogenous separation of the disassembled units which limited the recyclability aspect of the ArM design.[54] The use of an electrochemical switch is proposed to not only allow precise control over the disassembly

but also eliminate the by-products associated with the previously employed chemical reducing agents, increasing the green profile of the system. The complexity of the proposed immobilisation platform necessitates in the first instance the investigation of the individual components in closer detail prior to looking at the system as a whole. Thus, the first two chapters within this thesis explore the redox-active motif and the protein immobilisation approach independently before attempting to bring them together in a synergistic manner to achieve redox-triggered disassembly of an immobilised ArM.
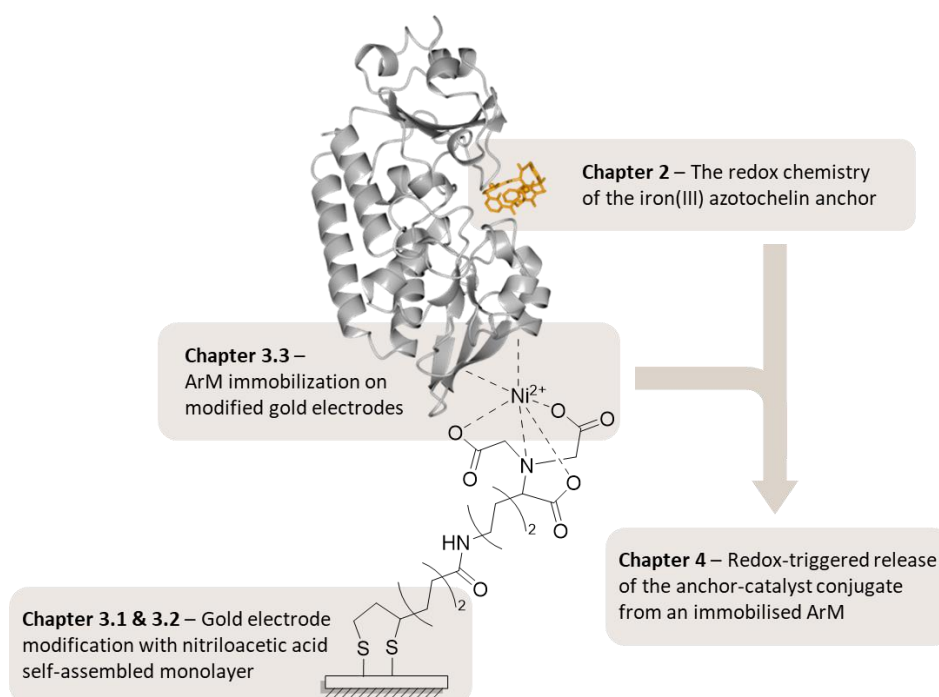
Figure 1.13 Schematic representation of the proposed ArM recycling platform constituting a highly conductive surface, a heterobifunctional linker allowing simultaneous attachment to the electrode and the proteins scaffold, and the Fe-PBP ArM with the highlighted redox anchor. The components which have been studied extensively within individual chapters of this thesis have been highlighted.

Chapter 2 investigates the redox properties of iron(III) azotochelin, the anchoring unit responsible for the redox reversibility of the biohybrid catalyst. As previously not studied, a detailed understanding of its redox behaviour was necessary before electrochemical control could be

established. Due to the diminishing availability of mercury-based electrodes, which are predominately used across literature for electrochemical studies of siderophore complexes, the experimental work within this chapter will explore the use of an boron-doped diamond (BDD) as an alternative working electrode material. Insight into the ability to modulate the redox potential of the anchor without comprising the stability of the ArM is crucial for facilitating a more facile release of the anchor-catalyst conjugate. Hence, the relationship between the redox potential values and the coordination sphere of the redox-active centre will be evaluated using voltammetry methods, supplemented with mass spectrometry and UV-vis spectroscopy to establish a link between function and structure.

Chapter 3 will shift focus to the electrode surface and its modification for the selective and site-oriented immobilisation of the protein scaffold. Synthetic modification of nitriloacetic acid (NTA), the chelating ligand underpinning the mechanism of affinity-based protein purification methods, will be explored to allow its incorporation onto the surface of gold electrodes. The employment of NTA functionalities should allow selective binding of proteins incorporating the polyhistidine-tag (6His-tag) with the potential for reversible binding of the protein scaffold to achieve a fully recyclable and thus a sustainable immobilisation platform.

Chapter 4 aims to unite the components discussed individually in the previous two chapters and critically assess the potential of the immobilisation platform to facilitate the electrochemical reduction of the iron(III) anchor. In the first instance, the feasibility of direct electron transfer (DET) between the iron centre and the electrode surface will be evaluated. However, it is anticipated that the length of the NTA linker may create challenges in achieving a facile electron transfer; alternative approaches to traditional voltammetry methods may be necessary to establish whether the disassembly process has occurred.

***

Chapter 2 – Interrogating the redox chemistry of the iron(III) azotochelin anchor

This chapter describes the electrochemical investigation into the redox chemistry of iron(III) azotochelin, the anchoring motif of the Fe-PBP ArM, building the foundation for achieving electrochemically triggered ArM disassembly. It describes the novel use of a boron-doped diamond (BDD) working electrode for studying the redox properties of iron(III) siderophores, in replacement of the widely employed across literature mercury-based electrodes. The implications of the developed electrochemical set-up extend to the wider research community and as such **in Section 2.2.4**, siderophores not employed in the ArM design are investigated electrochemically to demonstrate the extent of the electrode's versatility. The work presented herein was repurposed from "**Electrochemical and solution structural characterisation of Fe(III) azotochelin complexes: Examining the coordination behaviour of a tetradentate siderophore**", which was published in Inorganic Chemistry (2022) with me as the first author, and my supervisors as the only co-authors.[154]

2.1 Preliminary protein electrochemistry experiments

Since its discovery, protein film voltammetry (PFV) has become the default method of choice for interrogating the redox chemistry of metalloproteins. Extensively developed by Fraser Armstrong and his research group, the technique relies on the adsorption of proteins onto the electrode surface in an electroactive configuration, one which facilitates the direct electron transfer (DET) between the redox centre and the electrode surface.[141,150] The close interaction with the electrode surface minimises mass transport limitations by removing the requirement for protein diffusion which frequently acts as the rate-determining step in solution voltammetry.[155] However, as protein adsorption is not driven by covalent bond formation,

the orientation achieved upon attachment to the electrode may affect the structural integrity of the protein. In the case of catalytic redox enzymes, the absence of structural damage can be validated by measuring a flow of so-called 'turnover current' in the presence of a corresponding substrate.[156] However, for non-catalytic redox-active properties, comparison with spectroscopic data are frequently required to validate that the protein remains unaffected by the formation of a 'film' configuration.

The preliminary approach for investigating the electrochemical behaviour of the iron(III) azotochelin complex constituted PFV experiments of the P-Sid complex, comprising the isolated anchor bound to CeuE, the protein scaffold of the Fe-PBP ArM. The elimination of the catalyst moiety was anticipated to simplify data interpretation and ensure any redox activity was unambiguously associated with the Fe(III)/(II) redox couple. The P-Sid complex was subsequently immobilised on glassy carbon (GC) electrodes functionalised with MWCNTs. Both 6His-tagged and non-tagged CeuE variants were employed in the study to probe whether the presence of the tag, situated on the opposite face to the binding pocket, would facilitate the correct protein orientation upon adsorption. This was proposed to result from the π-π stacking interactions between the imidazole rings of the 6His-tag and the graphene sheets of the MWCNTs.[157,158] An identical voltammetric response was observed for both P-Sid and P(6His)-Sid samples with both cathodic and anodic peak present, however, upon further analysis with supporting data from the CV of the free Sid complex adsorbed onto the electrode, it was not possible to confidently assign the peaks to the Fe(III)/(II) redox pair. Thus, it was deemed necessary to first examine the solution redox chemistry of the isolated iron(III) complex of azotochelin, a tetradentate catecholate siderophore, which forms the premise of the data discussed in this chapter.

2.2 Introduction

2.2.1 The biological role of siderophores

Microorganisms secrete siderophores, low molecular weight iron(III) chelators to overcome the limited bioavailability of iron(III) arising from its extremely low solubility in aqueous aerobic environments at pH 7.0 (K_{sp} [Fe^{3+}][OH^-]^3 = $10^{-38.7}$ M). Upon metal chelation, siderophores aid the solubilisation of iron(III) from the environment and facilitate its transport across the cellular membrane, delivering the essential metal into either the cytoplasm or periplasm.[159,160] All siderophore families possess chelating groups comprising hard donor oxygen atoms (**Figure 2.1**) for selective coordination of the strongly Lewis acidic iron(III) with great affinity, giving rise to complexes exhibiting exceptionally high thermodynamic stability (log $K_f \cong 30 - 49$).[161] As the strong chelation of iron(III) by siderophores precludes its utilisation by the cell machinery, microorganisms have developed efficient mechanisms for the intracellular dissociation of the iron(III) siderophore complex, enabling the subsequent release of the metal ion.
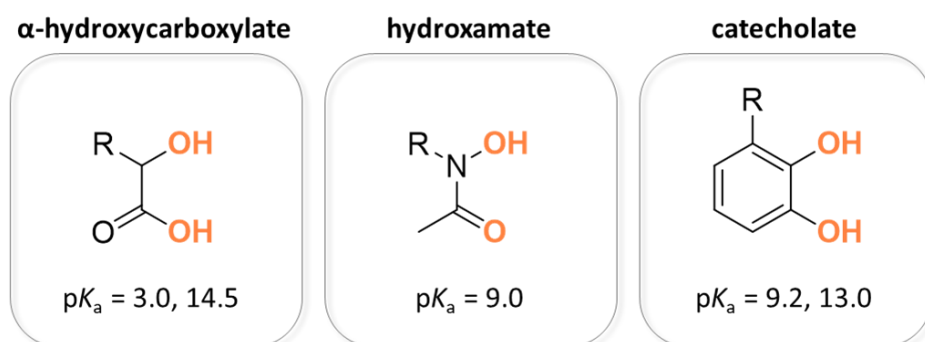
Figure 2.1 Chemical structures of the bidentate chelating ligands for the three most common families of siderophores, α-hydroxycarboxylates, hydroxamates and catecholates. The donor oxygen atoms for each group are highlighted and the pK_a values are displayed; a higher pK_a value indicates greater electron density on the hydroxy oxygen atoms and a stronger chelating power.

The redox-dependent release of iron from its siderophore complexes is frequently considered the most plausible mechanism for its dissociation into the intracellular matrix. The reduction of the iron(III) centre to iron(II) decreases the charge on the metal while simultaneously increasing the ionic radius, which subsequently lessens its Lewis acidity and gives rise to a reduced affinity between hard oxygen donor atoms and the now soft(er) Lewis acid iron(II) centre.[162] The consequence is an iron(II) siderophore complex with significantly lower thermodynamic stability in comparison to the iron(III) equivalents thus facilitating dissociation of the complex and the subsequent release of iron. The affinity of the oxygen atoms towards iron(III) and resulting high complex stability are directly associated with the Fe(III)/(II) redox potential, giving rise to very negative values (−82 mV to −750 mV vs NHE at pH 7.0), which are found to be outside the potential window attainable to majority of biologically relevant reducing agents under physiologically relevant conditions (**Figure 2.2**).[162] Thus, extensive research
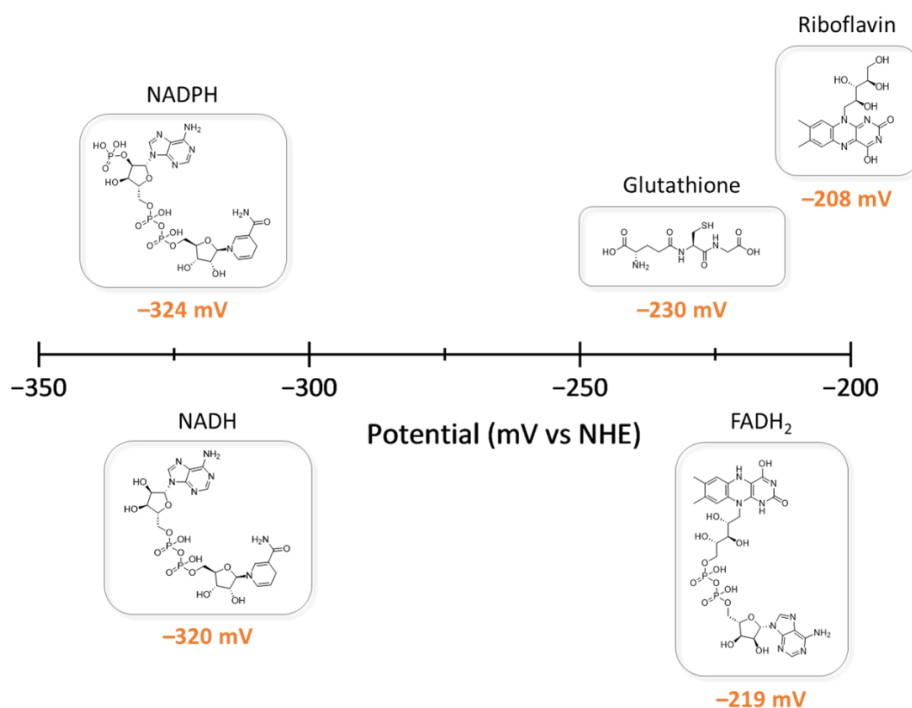
Figure 2.2 The midpoint potentials ($E_{1/2}$) of biological reducing agents (measured vs NHE at pH 7.0) within the range of reduction potentials exhibited by iron(III) siderophore complexes.[163]

has been conducted towards gaining a more in-depth understanding of the reductive mechanism for intracellular iron release and identification of species capable of modulating the reduction potential to bring it within the range of biological reducing agents.[164]

2.2.2 The reduction potential of iron(III) catecholate siderophores

Enterobactin, the chelating ligand shown in (**Figure 2.3**) has always been at the centre of siderophore research as it has the greatest affinity towards iron(III), demonstrated by its high pFe value, which describes the free iron concentration, $-\log [Fe^{3+}]$, at pH 7.4 in a solution where the total $[Fe^{3+}] = 10^{-6}$ M and total $[L] = 10^{-5}$ M.[165] This hexadentate siderophore constitutes three catecholate groups bound to a cyclic trilactone backbone; the preorganised structure and the strongly binding nature of the siderophore chelating groups both contribute to the large pFe value. The subsequent high thermodynamic stability of the iron(III) enterobactin complex is reflected by the very negative $E_{1/2}$ value of -790 mV vs. NHE (pH 7.4).[166] This has been experimentally measured by calculating the mean value of the cathodic (E_{pc}) and anodic (E_{pa}) peak potentials measured via solution CV at a hanging mercury drop electrode (HMDE). The reversible waveshape was assigned to the one-electron process for the Fe(III)/(II) redox pair.[166,167]

The relationship between the reduction potential of iron(III) enterobactin and pH has been extensively documented; upon increasing proton concentration from pH 11.4 to 6.0, a positive potential shift is observed which has not been reported to a similar extent in other families of siderophores.[166] Structural characterisation studies of the iron(III) enterobactin complex performed by K. N. Raymond and co-workers confirmed the protonation of the meta catecholate oxygens (pK_a 4.95, 3.52 and 2.50) under sufficiently acidic conditions; this gives rise to a salicylate-type bonding of the metal ion as shown in **Figure 2.4**.[166,168]
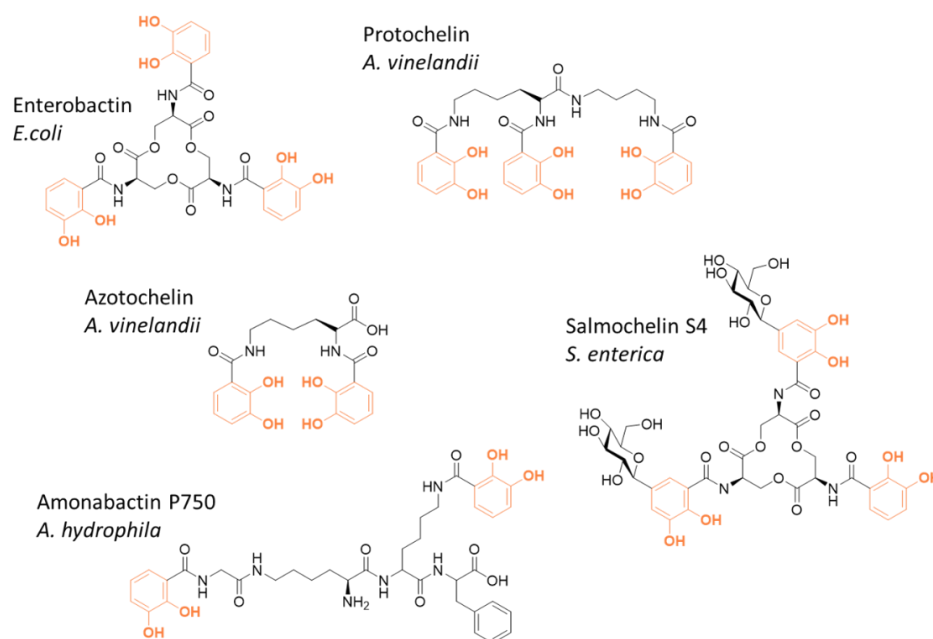
Figure 2.3 Chemical structures of most widely studied catecholate siderophores and the respective microorganisms they are secreted by; the chelating units of each siderophore are highlighted.

The reorganisation of the iron coordination sphere lowers the thermodynamic stability of the iron(III) siderophore complex which correlates to an increased reduction potential of the Fe(III)/(II) redox couple.[169] While fluctuations in $E_{1/2}$ values as a function of pH have been noted for all siderophores, the ability of catecholate siderophores to maintain their complex speciation in the presence of competing H⁺ ions is reflective of the high affinity the catechol units exhibit towards iron(III) and the subsequent complex stability of iron(III) catecholate sideropores.[164]
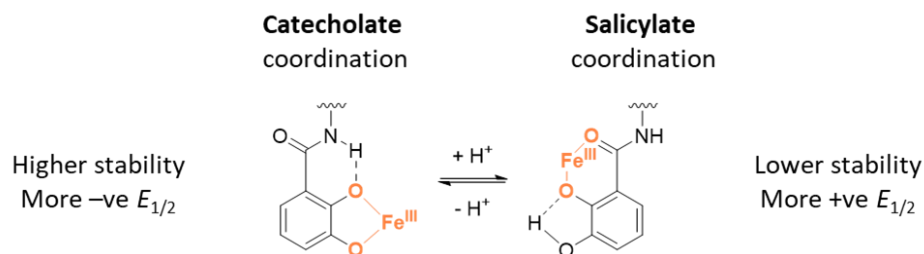
Figure 2.4 Skeletal structure of the iron(III) chelating catechol units in catecholamide siderophores illustrating the switch between the two coordination modes in response to the protonation of the phenolic meta oxygen in acidic conditions.

Ligand denticity has been proposed to be an additional factor contributing to the redox potential of iron(III) siderophores. Crumbliss and colleagues have investigated hydroxamate siderophores and shown a relationship between their $E_{1/2}$ and pFe values; this can be interpreted as a direct correlation between the number of chelating ligands and the thermodynamic stability of the complexes.[170] However, similar studies have not been explicitly performed for catecholate siderophores. In lieu, Taylor et al. used catechol (cat) ligands as simple models for catecholate siderophores and measured the $E_{1/2}$ values for solutions prepared in varying metal to ligand ratios (M:L) to mimic iron(III) catecholate siderophore complexes of varying denticities.[171] The data allowed the authors to propose a 'chelate scale' (**Figure 2.5**) which allows the prediction of the stability of an iron(III) catecholate complex from its Fe(III)/(II) reduction potential. The linear relationship highlights the differences in the thermodynamic stability of tetradentate and hexadentate ligands as illustrated by the E_p values of the tetracoordinate $[Fe(cat)_2]^-$ and hexacoordinate $[Fe(cat)_3]^{3-}$ complexes, −354 mV vs SCE (−110 vs NHE) and −680 mV vs SCE (−436 vs NHE), respectively.

The 'chelate scale' has been successfully utilised for determining the log K values for iron(III) complexes of marine siderophores comprising catechol binding units.[172] Control of the coordination environment to prepare iron(III) siderophore complexes of varying stabilities and subsequently kinetic lability is a valuable tool in coordination chemistry as well as in nature. A. vinelandii secretes three catecholate siderophores of varying denticities, tris(catecholate) protochelin, bis(catecholate) azotochelin and mono(catecholate) aminochelin, in response to changes in extracellular iron concentration.[173,174] This allows the bacteria to maximise the efficiency of its iron uptake mechanism.
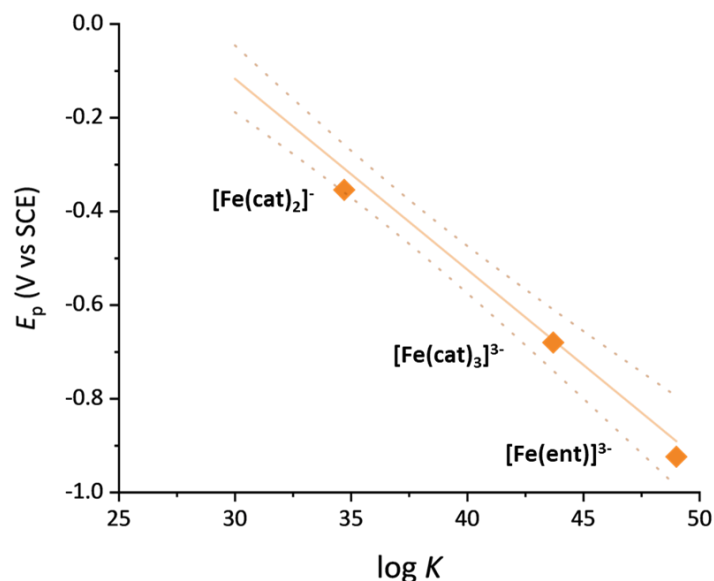
Figure 2.5 Simplified representation of the 'chelate scale' describing the negative linear relationship between the reduction potential (E_p) of the Fe(III)/(II) redox couple and the thermodynamic stability (log K) of iron(III) complexes with natural siderophore enterobactin (ent) and simple catechol (cat) ligands. The orange solid line and the dotted lines illustrate the linear regression and the 95% confidence interval.

2.2.3 Flexible speciation of coordinatively unsaturated iron(III) siderophore complexes

To date, iron(III) complexes of low denticity, bis(catecholate) siderophores such as azotochelin, amonabactin (**Figure 2.3**) and salmochelin S1 have not been investigated electrochemically. Instead, the information available on their coordination chemistries and thermodynamic stabilities have been predominantly acquired through MS and UV-vis experiments. Iron(III) amonabactins have been demonstrated to form tetracoordinate $\mathbf{M_1:L_1}$ species at neutral pH, which exhibit significant stability despite an unsaturated iron coordination sphere.[175] Studies on the effect of pH on the coordination environment were restricted due to the precipitation of the complex below pH 5.5 and thus no information is available on the shift from catecholate to salicylate-type coordination, characteristic of this siderophore family.

Voltammetric and structural studies of tetradentate siderophores alcaligin and rhodotorulic acid (**Figure 2.6**), cyclic and linear ligands bearing hydroxamate ligands, have shown a contrasting behaviour. Data obtained through electrospray ionisation-mass spectrometry (ESI-MS) provided evidence for both siderophores to preferentially form dimeric $M_2:L_3$ species (**Figure 2.6**) with fully saturated iron coordination spheres at neutral pH, even in stoichiometric solutions.[176] The $M_1:L_1$ species, observed readily for iron(III) amonabactins, have only been observed for the hydroxamate siderophores under acidic conditions where H^+ competition is more prevalent. This was reflected in the E°′ values of alcaligin and rhodotorulic acid iron(III) complexes, −422 mV vs NHE and −443 mV at pH 7.0, which were comparable to the value of −481 mV vs NHE obtained for ferrioxamine E, an iron(III) complex of a hydroxamate siderophore.[170] Therefore, it is plausible to hypothesise that the speciation pattern for iron(III) siderophores is dependent on the nature of the chelating groups rather than ligand denticity.
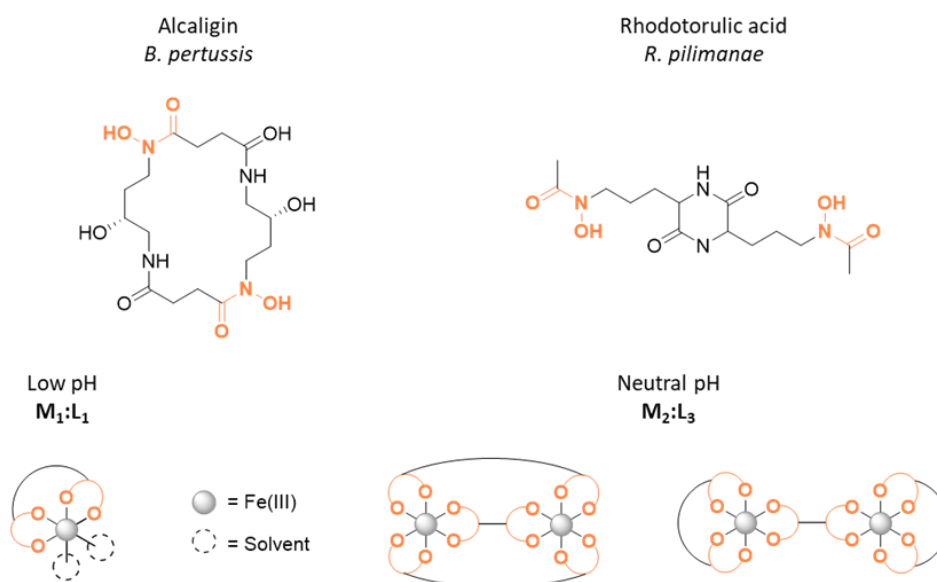
Figure 2.6 Chemical structures of alcaligin and rhodotorulic acid, low denticity dihydroxamate siderophores; the chelating groups have been highlighted in orange. The model representations underneath represent the two stoichiometries, $M_1:L_1$ and $M_2:L_3$ observed for their iron(III) complexes.

2.2.4 Aims

Prior to exploiting the redox sensitivity of the iron(III) azotochelin anchor (**Figure 2.7**) to facilitate ArM disassembly, its redox properties must be well understood. As achieving precise electrochemical control over the anchor necessitates establishing a narrow potential window and identification of factors which allow to manipulate the reduction potential without compromising the structural stability of the ArM to ensure scope for further optimisation.
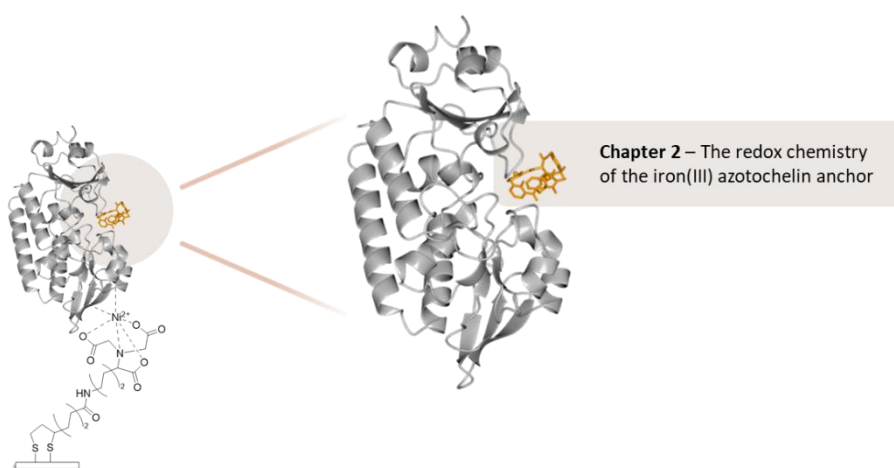
Figure 2.7 A scheme adapted from **Figure 1.13**, illustrating the redox-active anchor as the focus of the work described in **Chapter 2** and where it is situated within the proposed system.

Thus, the work in this chapter focuses exclusively on electrochemical and structural interrogation of the isolated iron(III) azotochelin complex , which can be summarised as following objectives:

- Identification of a suitable working electrode material for detecting the Fe(III)/(II) redox couple of an iron(III) siderophore complex, as an alternative to mercury-based working electrodes.
- Solution voltammetry measurements of iron(III) azotochelin complex at neutral pH to determine the reduction potential for the Fe(III)/(II) redox couple.

- Determination of the complex stoichiometry exhibited by the species responsible for the observed redox response.

- Identification of factors capable of shifting the reduction potential of the complex without altering the stoichiometry of the iron(III) azotochelin complex.

2.3 Results and discussion

2.3.1 Investigating the suitability of the BDD electrode for detecting the Fe(III)/(II) redox couple of iron(III) siderophores

Throughout this chapter, cyclic voltammetry was employed for the electrochemical characterisation of the iron(III) siderophore complex, with the measurements being performed in a conventional three-electrode electrochemical cell, as described in **Section 6.2.2**. During the CV, a linear sweep was applied to the working electrode, cycling between two potential extremes, 0 V and −1.0 V at a fixed rate of change, also referred to as scan rate (v).[177] The resulting voltammogram plot describes the current flowing through the working electrode (the y-axis) as a function of the fluctuating potential (the x-axis). The current response comprises both non-Faradaic and Faradaic signals; the former is associated with a background capacitive current resulting from the movement of ions at the electrode surface, whereas the latter corresponds to the transfer of electrons in a formal redox reaction depicted as peaks in the voltammogram. The reduction of the redox species, i.e. the transfer of electrons from the electrode to the analyte is represented as a negative (cathodic) current peak (i_{pc}), whereas the oxidation process, i.e. the transfer of electrons from the analyte to the electrode is illustrated as a positive (anodic) current peak (i_{pa}). More negative peak potential values, E_p indicate a redox species with a higher lowest unoccupied molecular orbital (LUMO) thus making it more difficult to accept an electron and vice versa, a lower level LUMO corresponds to a more positive E_p value (**Figure 2.8**). A similar theory applies to the reverse process, however, for the study of iron(III) siderophore we are

predominantly concerned with the reduction process. Subsequently, information from cyclic voltammetry experiments provides insight into the stability of the complex from its electrochemical reversibility and the reduction potential (E_{pc}) value, as the latter can be presumed to be proportional to the stability constant of the reduced species.
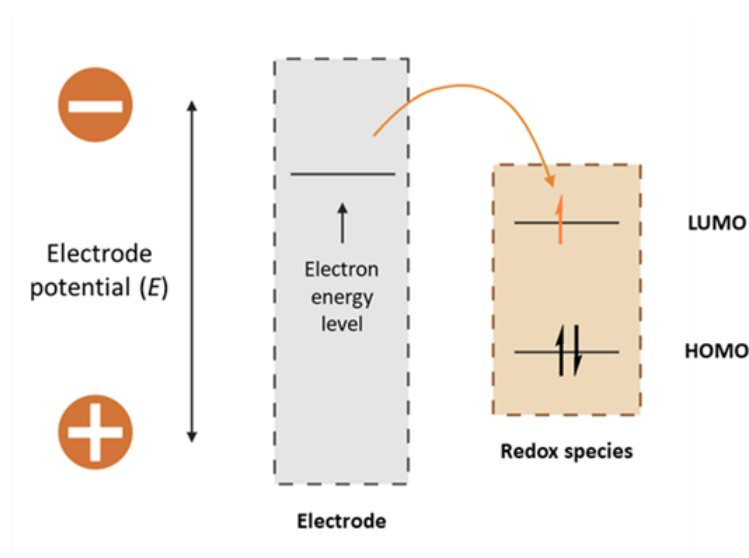
Figure 2.8 Simplified molecular orbital diagram representing the reduction process of a redox species in solution at the surface of an electrode. The energy of the LUMO indicates the potential energy required for the transfer of the electron from the electrode to the redox species, which is representative of the E_p value.

In pursuit of an alternative electrode material to the mercury-based working electrodes employed throughout the literature for the study of siderophores, three common electrode materials were investigated: Au, GC and BDD. Their suitability was evaluated against the detection of Fe(III)/(II) redox couple of an iron(III) catechol complex, employed as a simplified model for catecholate siderophores. The cyclic voltammograms were obtained after sequential additions of $FeCl_3$ and catechol stocks to a buffer solution (5 mM Bis-TRIS, 100 mM NaCl, pH 7.0), with an equilibration period of 5 minutes following each step to ensure a complete complex formation in situ. The solution under analysis comprised iron(III) and catechol in a 1:3 ratio, to facilitate the formation of a thermodynamically stable hexacoordinate

M₁:L₃ complex with a saturated coordination sphere. Successful detection of the electrochemical iron(III) reduction was only attainable using the BDD working electrode as shown in **Figure 2.9**.
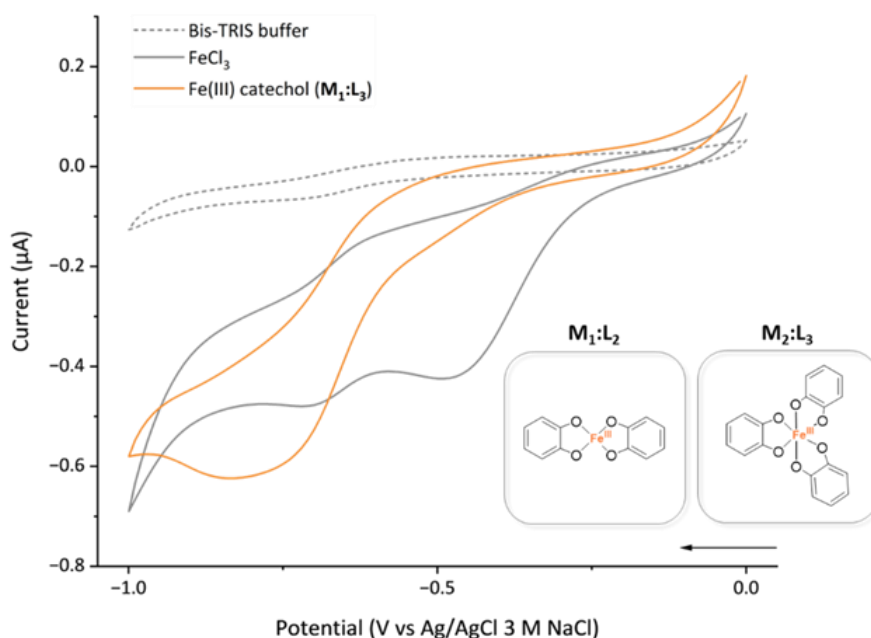
Figure 2.9 Cyclic voltammograms illustrating the in situ formation of an iron(III) catechol (orange solid line) complex after the addition of the catechol stock to a FeCl₃ (grey solid line) solution in 5 mM Bis-TRIS buffer, 100 mM NaCl at pH 7.0 (grey dashed line). Final analyte concentrations [Fe] = 0.48 mM, [Fe] : [cat] = 0.42 : 1.25 mM; v = 50 mV s^{-1}; third scans are shown (**Figure A.1** includes first scans for reference). The inset depicts the two possible structures of the iron(III) catechol complex, either with an **M₁:L₂** or an **M₁:L₃** stoichiometry.

Following the addition of the catechol stock to a FeCl₃ solution, a single irreversible cathodic peak with an E_p of −840 mV vs Ag/AgCl 3 M NaCl (−650 mV vs NHE) was observed. This waveshape was distinct from the reductive current measured for the iron(III) salt and thus was attributed to the Fe(III)/(II) reduction of the iron(III) catechol complex. It was not possible to assign the exact species responsible for the electrochemical behaviour as the coordination of iron(III) by catechol may occur to varying degrees, resulting in (mono)catecholate, (bis)catecholate or tris(catecholate)

species. As no anodic current was observed on the reverse scan, it can be proposed that the reduced species was unstable on the electrochemical timescale and dissociated before it could be reoxidised. A similar observation was made by Taylor et al., who studied iron(III) catechol complexes at a mercury drop electrode and only detected a cathodic current for a $[Fe(cat)_2]^-$ complex, prepared in an **$M_1:L_4$** ratio, with an E_{pc} of -354 mV vs SCE (-110 mV vs NHE).[171] However, the discrepancy in the reduction potentials across the two studies suggests that the species under analysis may exhibit higher thermodynamic stability than the $[Fe(cat)_2]^-$ complex as indicated by the more negative reduction potential.

Further characterisation of the BDD electrode was performed using a well-characterised redox species with a fast electron transfer, potassium ferricyanide, as described in **Section 6.4.1**. The data was compared to a GC working electrode, employed here as a reference standard, and analogous results were obtained, although the BDD electrode exhibited marginally slower electron transfer kinetics. Nonetheless, the BDD electrode was regarded to be a satisfactory replacement for the mercury electrode to study the electrochemical behaviour of an iron(III) complex of azotochelin.

2.3.2 Electrochemical behaviour of iron(III) azotochelin

An analogous procedure was employed for the electrochemical study of iron(III) azotochelin (Azoto). The siderophore azotochelin **[NGB-05]** was first synthesised according to the literature in a sufficiently high yield, as described in **Scheme 2.1**.[178–180] The catechol functionalities of 2,3-bis(benzyloxy)benzaldehyde were first protected using benzyl (Bn) groups to allow for selective modification of the aldehyde in subsequent steps; benzyl chloride was employed under basic conditions of potassium carbonate to yield **NGB-01**. The resulting product was used in the subsequent step without further purification, where sodium chlorite was utilised in a Pinnick oxidation to yield the corresponding carboxylic acid,

NGB-02. The reaction releases hypochlorite, HOCl as a byproduct which is known to inactivate the oxidising agent and thus sulfamic acid was added as a scavenger to hinder the side reaction; the acid has been reported to be effective in the presence of aromatic aldehydes.[181] However, the alternating addition of the reagents is suspected to have been too slow resulting in some of the oxidising agent being inactivated regardless, as the achieved yield was lower than the 75% quoted in the literature.[180] To facilitate a facile formation of **NGB-04**, the carboxylic was first converted into an activated ester derivative in an overnight reaction with *N*-hydroxysuccinimide (NHS) and dicyclohexylcarbodiimide (DCC) as the reactant and coupling reagent, respectively. For the formation of an azotochelin backbone in **NGB-04**, two equivalents of **NGB-03** were reacted with one lysine equivalent in the presence of triethylamine. The disubstituted molecule, **NGB-04** was formed preferentially in a 67% yield, and the small amounts of the monosubstituted byproduct were efficiently removed during column chromatography purification. Azotochelin was subsequently yielded in a hydrogenation reaction where all the benzyl protecting groups were cleaved revealing the catechol binding groups; a quantitative yield was achieved. To ensure that the siderophore was isolated in a metal-free state, all glassware used in the reaction and purification steps were firstly treated with 6 M HCl solution to remove any iron salts, followed by an aqueous wash.
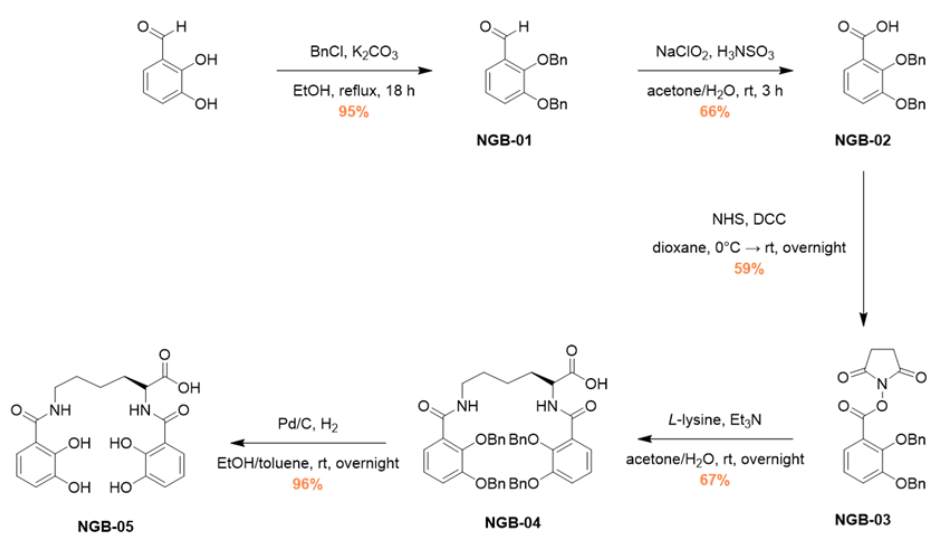
Scheme 2.1 Synthetic strategy for the preparation of **NGB-05**.

Aliquots of FeCl$_{3(aq)}$ and the synthesised **NGB-05**$_{(DMSO)}$ were added sequentially to a Bis-TRIS solution and in a parallel manner to the iron(III) catechol experiment described above, the solution was allowed to equilibrate for 5 minutes after each addition. The voltammogram of the solution prepared in an **M$_1$:L$_1$** ratio exhibited a single cathodic waveshape with a potential peak of −660 mV vs Ag/AgCl 3 M NaCl (−470 mV vs NHE), characteristic of an irreversible electrochemical process (**Figure 2.10**). The appearance of the peak only upon the addition of the siderophore allows us to attribute it to the Fe(III)/(II) reduction of the formed complex, with the latter being confirmed through the deep-purple colouration of the solution within the electrochemical cell, distinctive for iron(III) complexes of bis(catecholate) siderophores.
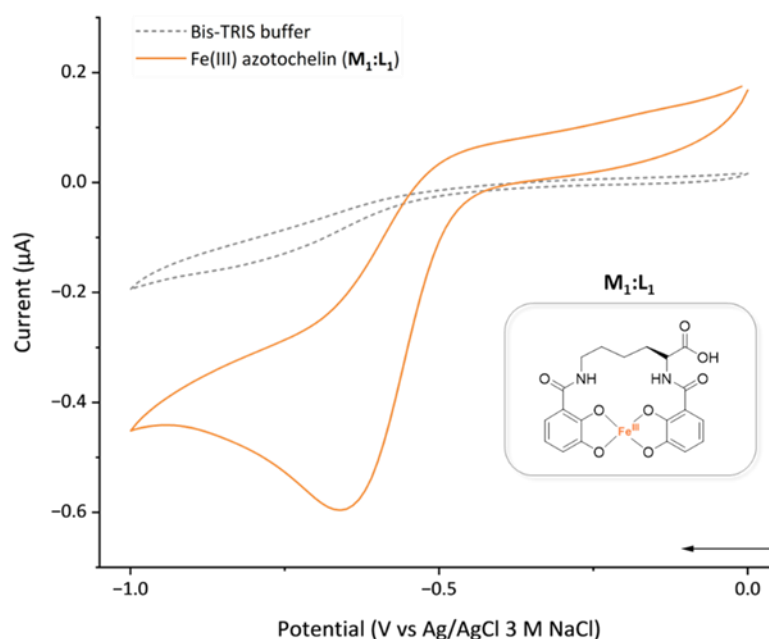
Figure 2.10 Cyclic voltammograms of an iron(III) azotochelin solution prepared in an equimolar ratio (orange solid line) and a blank buffer solution (grey dotted line). Buffer composition comprises 5 mM Bis-TRIS and 100 mM NaCl at pH 7.0; v = 10 mV s^{-1}; third scans are shown (**Figure A.2** includes first scans for reference). The structure of an **M$_1$:L$_1$** iron(III) azotochelin complex is shown in the indent.

To probe the speciation of the complex in solution, the concentrations of iron and azotochelin were varied throughout the experiment and the impact on the reduction potential and cathodic current values was investigated, as summarised in **Table 2.1**. The introduction of an additional equivalent of azotochelin, produced a negative potential shift of 10 mV for an $M_1:L_2$ solution, however, a further shift was not observed upon the addition of a third equivalent to form an $M_1:L_3$ solution. The observed decrease in cathodic current as the experiment progressed is expected for an irreversible system because the redox species is depleted at the surface of the electrode rather than replaced through reoxidation. This subsequently confirms that no new electroactive species was formed with further additions of the siderophore. An increase in iron concentration to yield an $M_2:L_3$ solution resulted in a further shift giving rise to a final potential of −680 mV vs Ag/AgCl 3 M NaCl (−490 mV vs NHE). The addition of iron generated a significant increase in current, although with no change in the shape of the voltammogram, implying the formation of the same species as the one present in an $M_1:L_1$ solution, a result of iron chelation by the excess ligand. The consistent electrochemical response throughout the whole range of M:L ratios allows us to conclude the high stability of the iron(III) azotochelin species under the experimental conditions employed, with no changes in speciation being observed.

Table 2.1 Tabulated values for the reduction potential (E_p) and cathodic current ($-i_{pc}$) extracted from solution cyclic voltammetry experiments investigating iron(III) azotochelin solution at different M:L ratios.

M:L	[Fe] / mM	[Azoto] / mM	E_p / mV[a]	$-i_{pc}$ / μA
1:1	0.45	0.45	−660	0.596
1:2	0.43	0.87	−670	0.472
1:3	0.42	1.25	−670	0.397
2:3	0.80	1.20	−680	0.556

[a] E_p vs Ag/AgCl 3 M NaCl; 5 mM Bis-TRIS buffer, 100 mM NaCl, pH 7.0; v = 10 mV s^{-1}

As described above, irreversible voltammograms are not commonly observed for iron(III) siderophore complexes at neutral pH, thus an iron(III) complex of bis(2,3-dihydroxybenzoyl-L-serine) (bisDHBS) [**NGB-06**], a tetradentate product of enterobactin hydrolysis was investigated to determine whether such electrochemical behaviour is characteristic of bis(catecholate) siderophores. bisDHBS is structurally analogous to azotochelin and was found to exhibit a similar irreversible cathodic waveshape under identical conditions in an **M$_1$:L$_1$** ratio (**Figure 2.11**).[182] The peak attributed to the Fe(III)/(II) reduction was observed at −670 mV vs Ag/AgCl 3 M NaCl (−480 mV vs NHE), only 10 mV more negative than E_p measured for iron(III) azotochelin.
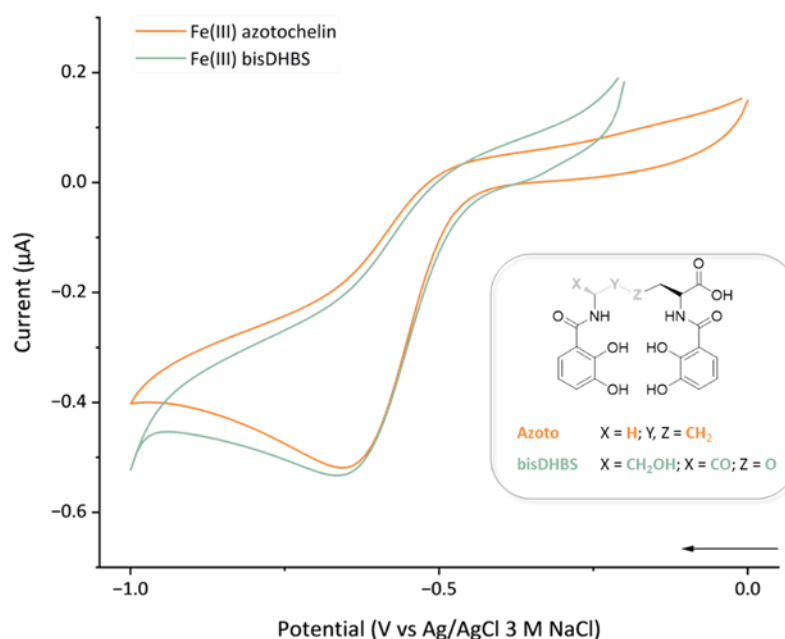
Figure 2.11 Cyclic voltammograms of iron(III) azotochelin and iron(III) bisDHBS solutions prepared in an **M$_1$:L$_1$** ratio. Experiments were performed in 5 mM Bis-TRIS buffer, containing 100 mM NaCl at pH 7.0 with the final analyte concentrations of [Fe] = 0.45 mM and [siderophore] = 0.45 mM; v = 10 mV s^{-1}; third scans are shown (**Figure A.3** includes first scans for reference). The inset shows the structure comparison between azotochelin and bisDHBS, two bis(catecholate) siderophores, with the differences between the lysine and serine backbone, respectively, being highlighted.

While the irreversible electrochemical behaviour exhibited by both bis(catecholate) siderophores is complimentary, it contrasts the reversible voltammograms observed for iron(III) complexes of other siderophores recorded at approximately pH 7.0.[167,183,184] The reversibility of voltammograms can be concluded from evaluating both the peak-to-peak separation (ΔE) between the cathodic and anodic peaks, and the ratio (i_{pa}/i_{pc}) of peak currents.[166] However, limited accounts of irreversible reductive waveshapes for iron(III) siderophore complexes can be found across the literature.[170,185] In studies with similar results to those presented in **Figure 2.11**, the data are frequently attributed to the presence of coordinatively unsaturated iron(III) siderophore complexes which have much lower thermodynamic stability than complexes comprising iron with a fully saturated coordination sphere. Thus, the proposed hypothesis is that such complexes are more susceptible to dissociation which results in the iron(II) oxidation peak not being observed on the reverse scan. The [Fe(cat)$_2$]$^-$ complex studied by Taylor et al., reported to produce a similar irreversible reductive waveshape, was further characterised through UV-vis spectroscopy and confirmed to be a coordinatively unsaturated species, exhibiting a λ_{max} value of 570 nm characteristic of bis(catecholate) siderophore complexes.[171]

Alcaligin, a naturally occurring tetradentate hydroxamate has been shown to preferentially form a dimeric hexacoordinate complex, Fe$_2$(alcaligin)$_3$, which exhibits characteristic reversible electrochemical behaviour at neutral pH.[170] However, at sufficiently low pH ($\leq$ pH 2), the iron(III) siderophore complex has been reported to exhibit an irreversible reductive waveshape at a peak potential 400 mV more positive than the one reported for the **M$_2$:L$_3$** complex; Spasojević and co-workers attributed the voltammogram shape to [Fe(alcaligin)(H$_2$O)$_2$]$^+$, an **M$_1$:L$_1$** species.[170] Hou et al. investigated the hydroxamate siderophore further; UV-vis spectroscopy was performed on its iron(III) complex and the authors were able to obtain a set of results complementary to the electrochemical study.

At pH 2.5, a λ_{max} value of 472 nm was observed confirming the presence of a tetracoordinated iron(III) alcaligin species under acidic conditions, while at physiologically relevant pH the predominant species in solution was shown to be a hexacoordinated **M$_2$:L$_3$** complex, exhibiting a λ_{max} value of 426 nm.[184] The formation of thermodynamically stable dimeric iron(III) complexes at neutral pH by dihydroxamate siderophores is therefore in agreement with the preference of iron(III) to exist as a 6-coordinate metal centre. Subsequently, a parallel speciation pattern can be expected of all other low denticity siderophores, including azotochelin and bisDHBS, however, the observed irreversible reductive waveforms do not support the formation of hexacoordinate **M$_2$:L$_3$** complexes by these bis(catecholate) siderophores.

2.3.3 Structural characterisation of iron(III) azotochelin

The ambiguity associated with the speciation of the iron(III) azotochelin complex at neutral pH prompted further structural studies of the bis(catecholate) siderophore. UV-vis and native ESI-MS experiments have been extensively utilised across the literature for elucidating the coordination environment of the metal centre in iron(III) siderophore complexes and thus have been chosen to supplement the voltammetric information obtained for azotochelin.[175,176,186,187] The absorbance of iron (III) azotochelin was measured in buffer conditions analogous to those employed in cyclic voltammetry studies (5 mM Bis-TRIS, 100 mM NaCl at pH 7.0) at varying M:L ratios (**Figure 2.12**). For an equimolar solution (**M$_1$:L$_1$**), the λ_{max} associated with the LMCT band was observed at 557 nm. The fluctuations of the λ_{max} value with the varying M:L ratio followed a similar pattern to the potential shifts observed during the CV measurements. The addition of one siderophore equivalent did not affect the position of the LMCT band, however, for an **M$_1$:L$_3$** ratio the λ_{max} was observed at 563 nm and an increase in the iron concentration which yielded an **M$_2$:L$_3$** solution shifted the λ_{max} value to 569 nm. Such minimal value variations are unlikely to have been a result of speciation changes and

rather arisen from shifts to the equilibrium position throughout the experiment as the concentration of each species has been varied. UV-vis studies performed by Duhme et al. and Cornish and Page report λ_{max} values (pH 7.0) within the 552 – 560 nm range, in agreement with the data obtained for all M:L ratios studied.[173,187] However, the proposed structure of the iron(III) species in these studies is contradictory, reporting the presence of a bis(catecholate) and tris(catecholate) complex, respectively. Across the literature, λ_{max} values between 480 and 495 nm have been shown to be characteristic of hexacoordinate catecholate complexes, and thus it is more probable that the azotochelin siderophore investigated in this study forms an $M_1{:}L_1$ complex upon iron(III) chelation.[165] Moreover, the consistency in the λ_{max} values throughout the time course of the experiment and the changing M:L ratios implies the stability of the species formed, conflicting with the inherent disposition of iron(III) to form hexacoordinate complexes.
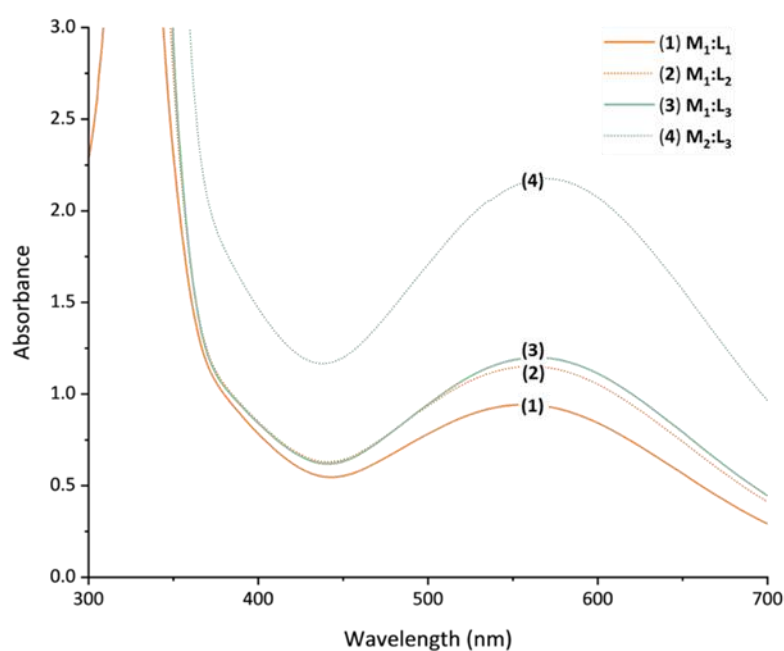
Figure 2.12 Comparison of UV-vis absorption spectra of iron(III) azotochelin at varying M:L ratios; 1:1 (**1**), 1:2 (**2**), 1:3 (**3**) and 2:3 (**4**). All measurements were obtained in 5 mM Bis-TRIS, 100 mM NaCl buffer at pH 7.0.

Native ESI-MS studies were performed to obtain additional structural evidence for the preferential formation of an **M_1:L_1** complex by iron(III) azotochelin at pH 7.0. To study non-covalently bound complexes, soft ionisation methods such as those employed in ESI-MS are imperative to preserving metal-ligand interactions and thus preventing complex dissociation upon its entry into the gas phase.[188] Successful utilisation of this technique for studying the speciation of iron(III) siderophore complexes has been widely documented across the literature including the study of catecholate siderophore-antibiotic conjugates.[176,186,189,190] Sample preparation for ESI-MS necessitates the employment of a volatile buffer such as ammonium acetate (NH_4OAc) to facilitate the vaporisation of the analyte upon injection. Thus, a supplementary solution CV experiment was performed to ensure the change in buffer composition from the initial studies in **Section 2.2.2** does not influence the coordination environment of the metal centre in the iron(III) siderophore complex. In a parallel manner to the studies in Bis-TRIS buffer, varying M:L ratios of iron(III) azotochelin were investigated and a comparable one-electron irreversible reductive waveshape was observed across all ratios (**Figure 2.13**). A small fluctuation of +30 mV was noted in comparison to the E_p values measured in the Bis-TRIS buffer, which can be ascribed to the presence of the positively charged ammonium ion and its interaction with the hypothesised negatively charged complex of iron(III) azotochelin, $[Fe^{3+} Azoto^{4-}]^-$. The positive potential shift indicates a more facile reduction of the iron(III) centre which is proposed to be a direct result of the ionic pairing between the two charged species. Nonetheless, this interaction does not comprise the chelation of the buffer ion to the metal centre, nor does it affect the speciation of the complex, the latter being confirmed with UV-Vis spectroscopy which yielded similar λ_{max} values as those obtained in measurements presented in **Figure 2.12**. Subsequently, NH_4OAc was regarded as a suitable buffer for employment in ESI-MS studies for allowing comparison of the generated data with the information obtained during solution CV experiments.
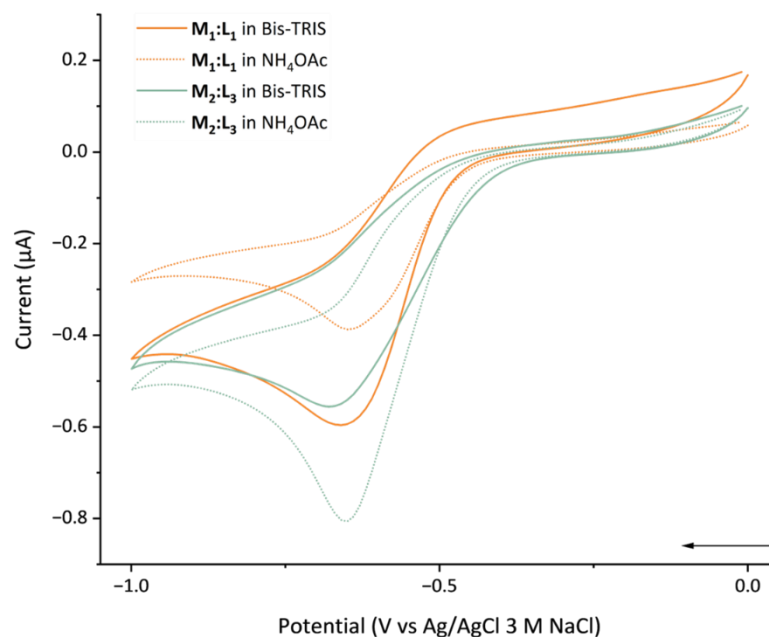
Figure 2.13 Cyclic voltammograms of iron(III) azotochelin solutions in two metal (M) to ligand (L) ratios, 1:1 and 2:3 for comparison of the electrochemical response in two different buffers, Bis-TRIS (electrochemistry buffer) and NH_4OAc (native ESI-MS buffer). All buffers contained 5 mM of the buffer salt and 100 mM NaCl as the supporting electrolyte at pH 7.0; experiments were performed at v = 10 mV s^{-1}; third scans are shown (**Figure A.4** includes first scans for reference). Analyte concentrations at M_1:L_1 ratio, [Fe] = 0.45 mM and [Azoto] = 0.45 mM; at M_2:L_3 ratio, [Fe] = 0.80 mM and [Azoto] = 1.20 mM.

Contrary to the in situ complex formation employed in solution CV and UV-vis studies, chelation of iron by azotochelin was performed prior to sample injection as described in **Section 6.4.1.3** for solutions constituting the metal and siderophore species in M_1:L_1 and M_2:L_3 ratios. Spectra recorded in the negative ionisation mode for both sample ratios (**Figure 2.14**) exhibited a peak at m/z 470.0425 with a 1- charge. The presence of the peaks supports the hypothesis for the preferred formation of a coordinatively unsaturated tetradentate complex by iron(III) azotochelin as the m/z value can be ascribed to the presence of a species with an M_1:L_1 composition, $[Fe^{3+} Azoto^{4-}]^-$. Close examination of the spectra did not yield any evidence for the formation of a hexacoordinate M_2:L_3 complex, $[(Fe^{3+})_2(Azoto^{4-})_3]^{6-}$, for either of the solution ratios.
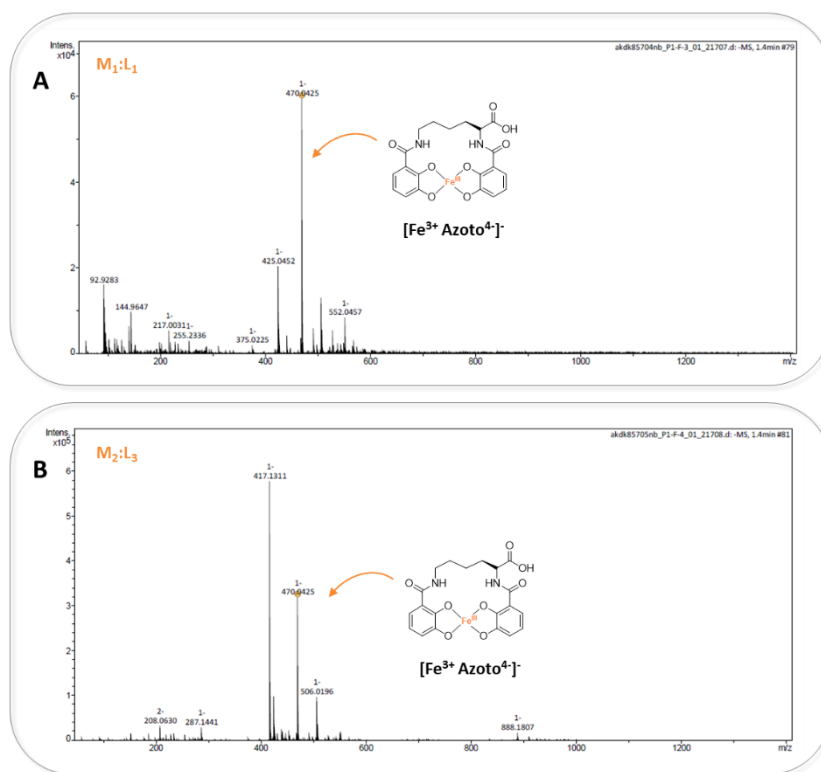
Figure 2.14 Native ESI mass spectra measured in the negative ionisation mode for iron(III) azotochelin solutions prepared in NH_4OAc buffer (pH 7.0) at two different M:L ratios. **A M$_1$:L$_1$**, [Fe] = 0.5 mM, [Azoto] = 0.5 mM; **B M$_2$:L$_3$**, [Fe] = 1.0 mM, [Azoto] = 1.5 mM. In both spectra only the presence of the **M$_1$:L$_1$** complex, [Fe^{3+} Azoto^{4-}]$^-$ was detected.

MS data was also acquired in the positive ionisation mode for both solution ratios (**Figure 2.15**), revealing singly charged peaks at m/z 472.0583 and 472.0573 in the **M$_1$:L$_1$** and **M$_2$:L$_3$** spectra, respectively. Both peaks illustrate an increase of 2.0 in comparison to the m/z values of the molecular ion peaks obtained in the negative ionisation mode. The protonation of an analyte in mass spectroscopy within the positive ionisation mode is not an unusual phenomenon; molecules are frequently observed in the mass spectrum at a m/z value corresponding to the [M+H]$^+$ species. However, the +1 charge associated with both peaks and the 2.0 increase in the m/z values implicates the protonation is not only of the carboxylic acid as one would expect. In **Section 2.1.2**, the susceptibility of catecholamide siderophores, such as azotochelin, to undergo protonation of the two meta catechol oxygens under sufficiently acidic conditions is described, which gives rise to a salicylate-type bonding in an iron(III) complex (**Figure 2.4**).

The literature reports acidification of the ammonium acetate buffer upon vaporisation in the positive ionisation mode of ESI-MIS, effectively lowering its pH to 4.75 ± 1, thus, creating an acidic environment.[191] Subsequently, it can be proposed, although with no certainty, that the observed peaks in the positive ionisation mode are associated with the addition of two protons to the $[Fe^{3+} Azoto^{4-}]^-$ ion observed in the negative ionisation mode, resulting in a $[Fe^{3+} H_2Azoto^{2-}]^+$ species.[191]
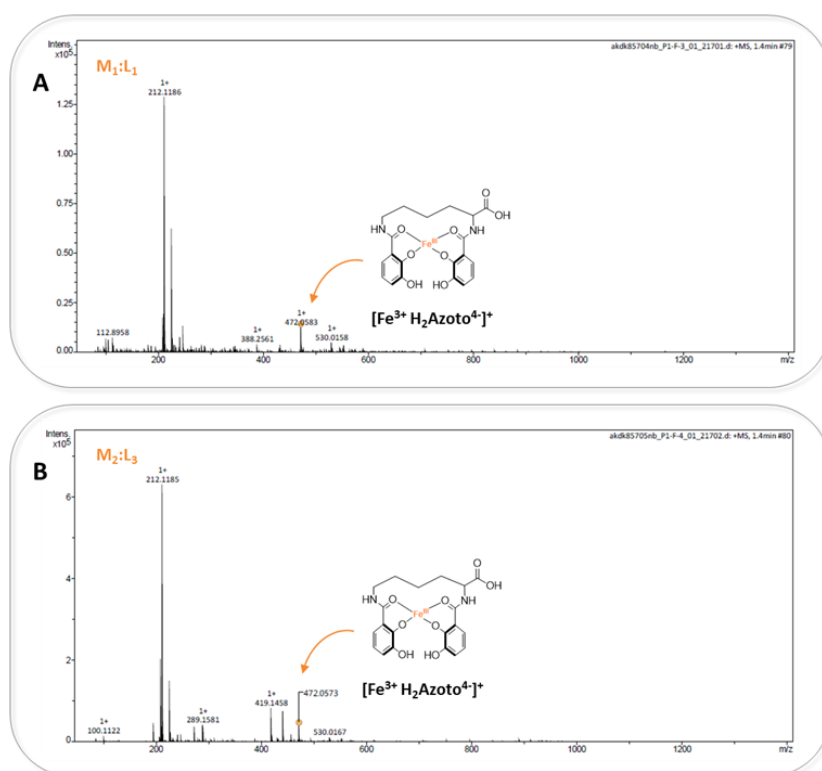
Figure 2.15 Native ESI mass spectra measured in the positive ionisation mode for iron(III) azotochelin solutions prepared in NH_4OAc buffer (pH 7.0) at two different M:L ratios. **A M_1:L_1**, [Fe] = 0.5 mM, [Azoto] = 0.5 mM; **B M_2:L_3**, [Fe] = 1.0 mM, [Azoto] = 1.5 mM. In both spectra only the presence of the **M_1:L_1** complex in a salicylate coordination mode, $[Fe^{3+} H_2Azoto^{2-}]^+$ was detected.

While the mass spectra in the positive ionisation mode cannot be assumed to be conclusive, combination of the mass spectra in the negative ionisation mode and the UV-vis absorption spectra, allows to assign the irreversible reductive waveshape observed in the CVs to the tetracoordinated $[Fe^{3+} Azoto^{4-}]^-$ complex. Nonetheless, despite conclusive evidence, the

predisposition of the tetradentate catecholate siderophore to favourably form an iron(III) complexes with an unsaturated coordination sphere remains contrasting to the tetradentate siderophores bearing hydroxamate groups which prefer to adopt iron(III) complexes with octahedral geometry. Limited structural studies are available for low denticity catecholate siderophores, however, a similar $M_1:L_1$ speciation pattern at pH 7.0 has been observed for (mono)catecholate and (bis)catecholate siderophores, chrysobactin and amonabactin (**Figure 2.3**), respectively, as confirmed through native ESI-MS studies.[175,192] There is an evident correlation between the identity of the chelating groups in low denticity siderophores and the complex stoichiometry of their iron(III) complexes, not described previously in the literature. Catechol groups comprise oxygen donor atoms with high electron density, arising from the neighbouring aromatic ring and the subsequent resonance stabilisation which enhances the affinity between the iron(III) ion and the catechol chelating functionalities.[193] The extensive resonance may offer enough stabilisation to balance the lower stability of tetracoordinated versus hexacoordinate complexes. Comparatively, the resonance stabilisation in hydroxamate siderophores emerges only from the lone pair on the nitrogen and thus the electron density on the donor atoms is not comparable.[193]

Moreover, the favourable formation of the iron(III) azotochelin complex in tetracoordinate coordination provides a plausible explanation for the presence of an irreversible reductive voltammogram. The significantly lower thermodynamic stability of the iron(II) complex is further decreased by the incomplete coordination sphere around the metal centre which concludes in the dissociation of the iron(III) azotochelin within the timescale of the experiment before the metal centre can be reoxidised. CV experiments were performed at higher scan rates (50, 100, and 500 mV s^{-1}) in an attempt to measure the potential for the oxidation of iron(III) before complex dissociation, however, the experiments did not yield successful results as high capacitive currents were observed.

2.3.4 Modulating the reduction potential of iron(III) azotochelin

The sensitivity of iron(III) siderophore complexes to solution pH offers a straightforward approach for controlling the thermodynamic stability and subsequently E_{pc} values of those complexes. It thus presents an opportunity for controlling the ease with which the SidCat dissociates from the protein scaffold, triggering the disassembly of the ArM. As described in **Sections 2.1.2** and **2.1.3**, the reorganisation of the metal coordination sphere takes place in iron(III) siderophores as a response to changes in pH, either through changes in complex stoichiometry or a shift in the coordination mode. For a parallel approach to be plausible for the SidCat conjugate, the change within the first coordination sphere must not hinder the binding of the iron(III) azotochelin anchor to the CeuE binding pocket.

The voltammetric investigation of iron(III) azotochelin was thus extended to encompass the pH range relevant for either catalytic or immobilisation studies of the Fe-PBP ArM; pH 6.0 − 8.5 at 0.25 and 0.5 increments. In a parallel approach to the initial study, CVs were recorded in 5 mM Bis-TRIS, 100 mM NaCl buffer with complex preparation occurring in situ, upon addition of the azotochelin stock to a solution containing an iron(III) salt and an equilibration time of 5 minutes. The investigation of iron(III) azotochelin complexes prepared in an **M$_1$:L$_1$** ratio revealed a similar electrochemical behaviour to the one observed at pH 7.0, with a distinct irreversible cathodic wave being apparent at all pH values studied (**Figure 2.16**). The persistence of the voltammogram shape is indicative of the stability exhibited by the tetracoordinate **M$_1$:L$_1$** species under the experimental conditions employed. Changes in E_{pc} and i_{pc} values were minimal above pH 7.0 with a maximum E_p shift of -30 mV observed at pH 8.0. The difference is too modest to be attributed to any structural changes and presumably is a result of decreased competition between H$^+$ ions and iron(III) at higher pH levels. Contrastingly, although in agreement with the literature, both E_{pc} and i_{pc} values exhibited a significant shift as the solution pH was lowered. Minimal changes were observed at pH 6.5 and 6.75 with a

maximum peak potential shift of +80 mV in comparison to the E_{pc} measured at pH 7.0. Lowering the pH to 6.25 and consecutively to 6.0 evoked a positive E_p shift of 290 mV versus $\underline{E}_p$ at pH 7.0 which was additionally associated with an 86% decrease in the cathodic Faradaic current.
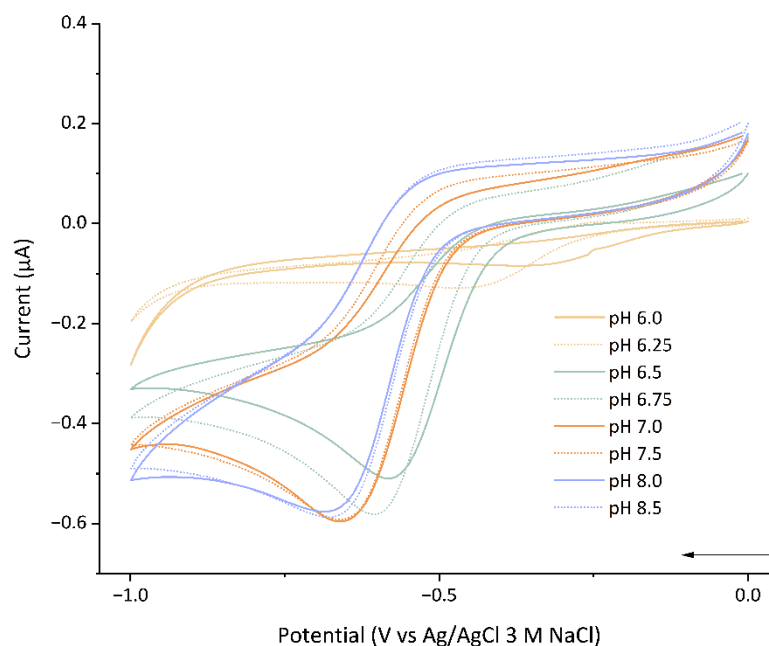
Figure 2.16 Cyclic voltammograms of iron(III) azotochelin solution prepared in an equimolar **M₁:L₁** ratio at different pH values, pH 6.0 − 8.50 in either 0.25 or 0.5 increments. Buffer composition comprises 5 mM Bis-TRIS and 100 mM NaCl; v = 10 mV s^{-1}; third scans are shown (**Figure A.5** includes first scans for reference).

The extent of the observed changes allows to hypothesise a change within the coordination environment of the redox iron(III) centre as more positive potential values suggest the presence of a complex with reduced stability. As the Faradaic current is proportionally related to the number of electrons transferred as defined by the Butler-Volmer theorem (**Equation 2.1**), a decrease in current flow frequently corresponds to a lower concentration of the redox species, however, all solutions were prepared equally. Therefore, it can be presumed that a change in current arises as a result of the shift from catecholate to salicylate-type coordination. The switch in

$$i = nFk_0 \left[c_O e^{\left\{ \frac{-\alpha nF}{RT}(E-E^\circ) \right\}} - c_R e^{\left\{ \frac{(1-\alpha)nF}{RT}(E-E^\circ) \right\}} \right]$$

Equation 2.1 The Butler-Volmer equation describing the current response of a redox system under kinetic control.[177,194,195] i = measured net current; n = number of electrons transferred; F = the Faraday constant; k_0 = the electron transfer rate constant; c_O = concentration of the oxidised species; c_R = concentration of the reduced species; α = the charge transfer coefficient; R = the molar gas constant; T = temperature; E = measured electrode potential; E° = formal electrode potential of the redox species.

coordination mode is associated with a charge change of the iron(III) azotochelin complex, from the negatively charged $[Fe^{3+} \ Azoto^{4-}]^-$ catecholate coordination mode to the singly positively charged $[Fe^{3+} \ H_2Azoto^{2-}]^+$ salicylate species. The resulting electrostatic repulsion between the latter complex and the inherent positively charged H-terminated surface of the BDD electrode is assumed to give rise to either a decreased local concentration of the complex at the electrode surface, or a change in the rate of electron transfer, k_0.[196] The relationship between the reduction potential of **M₁:L₁** iron azotochelin as a function of pH has been summarised in **Figure 2.17**.

To investigate the validity of the presumed coordination shift (rather than speciation change) for iron(III) azotochelin at pH levels below 6.5, further characterisation studies were performed. UV-vis measurements were acquired for equimolar iron(III) siderophore solutions in conditions analogous to the initial voltammetric study. Absorbance spectra were acquired at pH 6.0 and 6.50 (**Figure 2.18**) in an attempt to capture the composition of solutions for which the most significant changes in the electrochemical behaviour were observed. In comparison to the spectrum acquired at pH 7.0, the position of the LMCT band was mostly unaffected as surmised from the closely related λ_{max} values, 555 ± 9 nm, suggesting the **M₁:L₁** stoichiometry was preserved even at lower pH levels. In agreement with the voltammetric data, a reduced absorbance was noted at
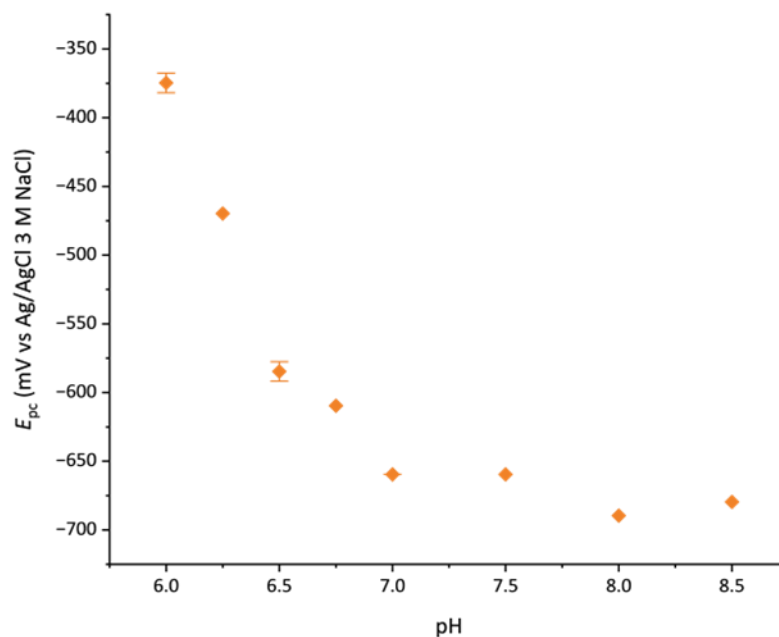
Figure 2.17 A plot illustrating the reduction potential (E_p) of iron(III) azotochelin solution prepared in an **M$_1$:L$_1$** ratio as a function of pH extracted from CVs shown in **Figure 2.16**. Standard deviation bars are shown for values measured at pH 6.0, 6.5 and 7.0.

pH 6.0 and 6.50 (**Figure 2.18**) in an attempt to capture the composition of solutions for which the most significant changes in the electrochemical behaviour were observed. In comparison to the spectrum acquired at pH 7.0, the position of the LMCT band was mostly unaffected as surmised from the closely related λ_{max} values, 555 ± 9 nm, suggesting the **M$_1$:L$_1$** stoichiometry was preserved even at lower pH levels. In agreement with the voltammetric data, a reduced absorbance was noted at pH 6.0 which is associated with a decline in the concentration of the complex comprising the iron(III) catecholate chromophore, [Fe^{3+} Azoto^{4-}]$^-$. This provides evidence for the presence of a secondary species, the formation of which results in the depletion of the catecholate-coordinated iron(III) azotochelin complex and the subsequent emergence of a mixture comprising both species. Thus, the complex formed as the pH levels were lowered must lack the iron catechol chromophore associated with the observed LMCT band, which has been demonstrated in the literature to be an iron(III) catecholate complex exhibiting salicylate coordination.[168]
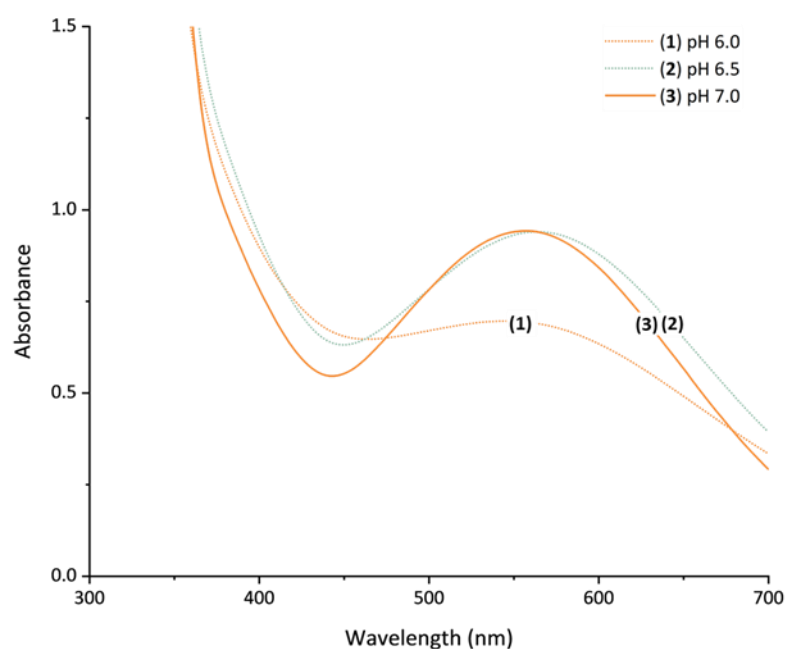
Figure 2.18 UV-vis absorption spectra acquired for an equimolar **M₁:L₁** solution of iron(III) azotochelin at varying pH levels; 6.0 (**1**), 6.5 (**2**) and 7.0 (**3**). All measurements were obtained in 5 mM Bis-TRIS, 100 mM NaCl buffer at pH 7.0 with both analyte concentrations equal to 0.45 mM.

Further investigation utilising ESI-MS was performed to validate the presence of the salicylate-coordinated iron(III) complex. In a similar manner to the previous study, peaks which could be ascribed to a $[Fe^{3+} H_2Azoto^{2-}]^+$ complex were observed in the positive ionisation mode for solutions prepared in both stoichiometric equivalents, **M₁:L₁** and **M₂:L₃**. However, as previously mentioned in **Section 2.2.3**, the NH_4OAc buffer employed in the study experiences acidification during the ionisation process in the positive mode which consequently lowers the solution pH. Thus, it would not be appropriate to consider these results as a reliable representation of the iron complexation at those pH levels.

The MS data alone cannot be considered as definitive proof; however, it can supplement the more definitive UV-vis and CV data. The results of those studies clearly demonstrate that as the pH of the solutions decreases below

pH 7.0, the concentration of the salicylate-coordinated complex, $[Fe^{3+} H_2Azoto^{2-}]^+$ increases. This concentration change is associated with a positive E_p shift reflecting the shift in the thermodynamic stability of the complexes in solution. As the pH drops below 6.25, a significant shift of 290 mV and a substantial decrease in the Faradaic current, suggest that the $[Fe^{3+} H_2Azoto^{2-}]^+$ complex becomes the prevailing species in the solution. This new insight allows us to postulate that the modulation of pH may be a feasible approach for controlling the release of the iron(III) azotochelin anchor from the ArM. Despite the coordination shift at lower pH, the retention of the **M₁:L₁** stoichiometry should not prevent the binding of the SidCat, however, the high reduction potential of the metal centre should facilitate easier disassembly of the ArM.

The inherent tendency for iron(III) azotochelin to form complexes in an **M₁:L₁** stoichiometry, rather than in a dimerised **M₂:L₃** form, results in an unsaturated coordination sphere which creates two vacant coordination sites at the metal centre. Those sites offer the potential for the binding of secondary molecules; the incorporation of these within the first coordination sphere would influence the thermodynamic stability and subsequently influence the reduction potentials of the Fe(III)/(II) redox couple. This can be utilised as a model to predict the effect of site-directed mutagenesis of the residues directly coordinating to the metal centre in the binding pocket of the ArM.[197–199] Thus, variations in buffer composition and the effect on the E_p of iron(III) azotochelin were investigated through CV studies at pH 7.0; the results are summarised in **Table 2.2**.

The most notable response to the change in buffer composition was observed for TES and TRIS buffers, with a positive E_p shift of 170 mV and 250 mV, respectively, in comparison to the value measured in the Bis-TRIS buffer. The observed values correspond to the reduced thermodynamic stability of the iron(III) azotochelin complex, indicating the presence of

Table 2.2 The tabulated values of the iron(III) azotochelin reduction potential (E_p) measured in solutions comprising different buffer salts, which exhibit varying iron(III) chelation abilities.

Buffer salt[a]	Structure	pK_a[b]	Fe(III) coordination[c]	E_p[d]
TRIS		8.06	Yes[200]	−410
TES		7.40	Yes[200]	−490
Bis-TRIS		6.46	No[171]	−660
HEPES		7.48	No[201]	−700
PIPES		6.76	No[202]	−710

[a] TRIS, 2-amino-2-(hydroxymethyl)-1,3-propanediol; TES, N-[tris(hydroxymethyl)methyl]-2-aminoethanesulfonic acid; Bis-TRIS, bis(2-hydroxyethyl)amino tris(hydroxymethyl) methane; HEPES, 4-(2-hydroxyethyl)piperazine-1-ethanesulfonic acid; PIPES, piperazine-1,4-bis(2-ethanesulfonic acid).

[b] At 25°C.

[c] This column represents the most prevailing conclusions from the literature, however, it must be acknowledged that these strongly depend on the experimental conditions employed. Consequently, variations and inconsistencies may exist among different reports, and thus, it is suggested that the above information should only be regarded as a guideline rather than an absolute reference.

[d] E_p (mV) vs Ag/AgCl 3 M NaCl; 5 mM buffer salt, 100 mM NaCl at pH 7.0; analyte concentrations of [Fe] = 0.45 mM and [Azoto] = 0.45 mM; v = 10 mV s^{-1}.

species formed exclusively in the presence of the two buffers. The primary and secondary nitrogen atoms within the TES and TRIS buffer molecules, respectively, possess the capability to coordinate iron(III). However, the inclusion of the soft/intermediate nitrogen donor atoms stabilises the

iron(II) oxidation state over iron(III), facilitating the electron transfer from the electrode to the metal centre, leading to an increase in the reduction potential. More in-depth speculation could be made into the effect of the different pK_a values for the nitrogen atoms and the effect of the sulfonic acid group in the TES buffer, however, the electrochemical data alone does not allow to reach any valid conclusions. Mass spectrometric investigations would provide valuable insight; however, these cannot be conducted due to the requirement for a volatile buffer, which neither TRIS nor TES fulfils.

An inverse trend was noted for the piperazine-containing buffers bearing tertiary amines, HEPES and PIPES, with negative E_p shifts of 40 mV and 50 mV, respectively, versus the E_p observed in the Bis-TRIS buffer. Nonetheless, it is challenging to establish the source of the changes as the fluctuations in the reduction potential values were minimal. Possible theories include the structural differences between the buffer molecules which may hinder the electron transfer upon chelation due to steric restrictions. Alternatively, the net charges of the molecules under the experimental conditions employed may result in electrostatic repulsion upon contact with the negatively charged iron(III) azotochelin complexes.

2.3.5 Extending the use of the BDD working electrode to other siderophores

The ability to perform voltammetric investigations of iron(III) siderophores on BDD working electrodes instead of mercury-based ones should be of interest to the wider siderophore research community engaged in studying newly discovered siderophores, or those interested in exploiting the iron(III) complexes of siderophores in alternative applications. Thus, deviating from the main ArM focus of the PhD project, voltammetric interrogation of the reduction potential on BDD working electrodes was performed on two tris(catecholate) siderophores, protochelin and enterobactin (**Figure 2.3**). Enterobactin was a gift from Prof. Alison Butler, whereas protochelin

[**NGB-09**] was synthesised according to the established protocol available in the literature (**Scheme 2.2**).[174]
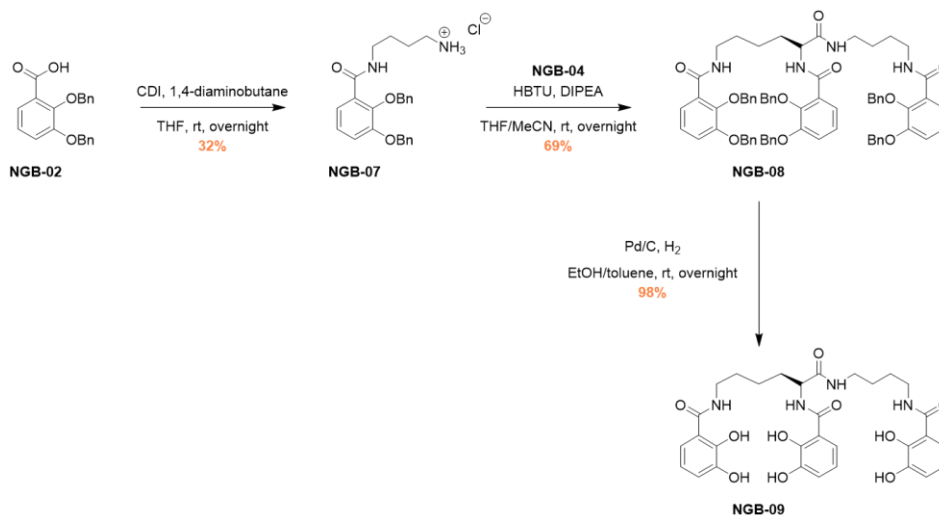
Scheme 2.2 Chemical strategy for the synthesis of the tris(catecholate) siderophore, protochelin [**NGB-09**] from the benzyl-protected analogue of azotochelin [**NGB-04**].

The benzyl-protected carboxylic acid [**NGB-02**] obtained during the preparation of azotochelin (**Scheme 2.1**), was reacted with 1,4-diaminobutane in the presence of a coupling reagent, CDI to achieve a mono substitution of the amine. The product [**NGB-07**] was recovered in a relatively poor yield in comparison to the 72% reported in the literature, thought to be associated with the formation of an emulsion, hindering layer separation during the aqueous workup.[174] Ensuring a complete removal of tetrahydrofuran, increasing waiting time before the removal of the bottom organic layer or the addition of more brine are a few examples of how the workup can be improved if the reaction was to be repeated. In the subsequent step, the previously synthesised benzylated azotochelin [**NGB-04**] was reacted with **NGB-07** in an amide bond formation reaction, facilitated by HBTU and DIPEA, acting as the coupling reagent and a comparable to that reported in a literature, following purification with column chromatography.[174] Protochelin [**NGB-09**] was isolated in a quantitative yield from its benzylated analogue [**NGB-08**] in a similar

manner to azotochelin; the protecting groups were cleaved in a hydrogenation reaction, ensuring the glassware was treated with 6 M HCl prior to the experiment.

An identical experimental procedure to the one employed in all previous voltammetric studies was implemented for the electrochemical investigation of enterobactin and protochelin. Unfortunately, the measurement of the reduction potentials for the two hexadentate catecholate siderophores was not feasible on a BDD working electrode. Solution conditions were employed to ensure the solubility of both iron(III) siderophore complexes, validated through the vibrant red colouration of the solutions, characteristic of iron(III) tris(catecholate) complexes. Thus, it is hypothesised that the E_p values were beyond the potential accessible to the electrode, as those two siderophores form iron(III) complexes of extremely high stability and subsequently very negative reduction potentials.

To confirm that the lack of success in obtaining voltammograms for iron(III) complexes of enterobactin and protochelin was indeed due to the values falling outside of the potential range of the BDD electrode, another hexadentate siderophore was investigated. A CV of ferricrocin (**Figure 2.19**), kindly donated by Prof. James Coulton, an iron(III) complex of a tris(hydroxamate) siderophore was acquired. As discussed throughout this chapter, iron(III) complexes formed with siderophores comprising hydroxamate chelating groups exhibit much lower stability and more positive reduction potentials in comparison to catecholate siderophores. This is exemplified by the pFe of 26.5 measured for ferricrocin, contrasting to the pFe of 35.6 reported for iron(III) enterobactin.[165,203] A quasi-reversible waveshape characterised by the presence of both reductive and oxidative peaks was observed; However, due to the significant ΔE value of 600 mV, the electrochemical reversibility of the Fe(III)/(II) redox couple could not be determined. The appearance of the anodic currents, not observed
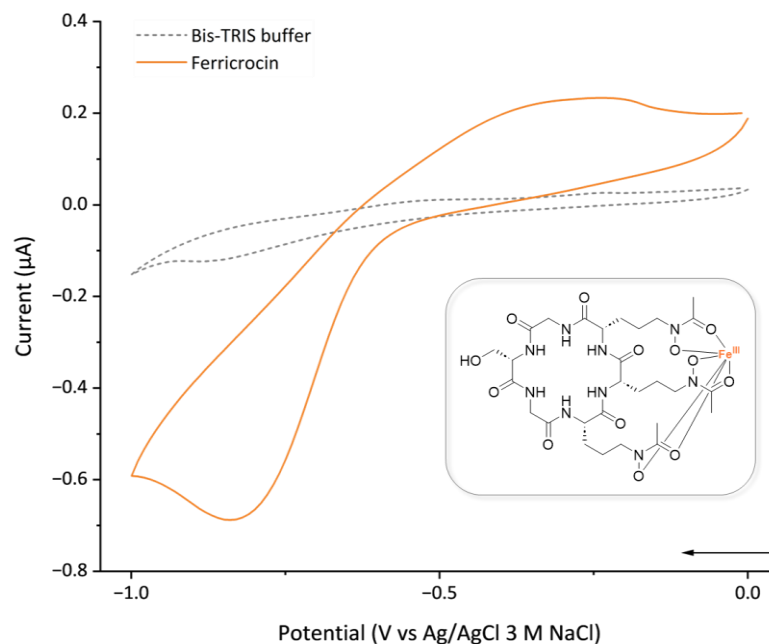
Figure 2.19 Cyclic voltammograms of ferricrocin (orange solid line) and a blank buffer solution (grey dotted line). Buffer composition comprises 5 mM Bis-TRIS and 100 mM NaCl at pH 7.0; [Ferricrocin] = 0.45 mM; v = 10 mV s^{-1}; third scans are shown (**Figure A.6** includes first scans for reference). The structure of ferricrocin, the iron(III) complex of the tris(hydroxamate) siderophore is shown in the indent.

previously in the voltammograms for iron(III) complexes of azotochelin and bisDHBS are presumed to be a result of the preorganised structure of the cyclic ferricrocin. This, along with the formation of a complex with a saturated coordination sphere can be presumed to limit the complex dissociation, allowing measurement of the reoxidation of the iron(II) centre. The $E_{1/2}$ for the Fe(III)/(II) redox couple was measured at −540 mV vs Ag/AgCl 3 M NaCl (−350 mV vs NHE); marginally higher than the literature value of −413 mV vs NHE with a ΔE of 60 − 69 mV.[203] While the voltammogram measured at the BDD electrode exhibited quasi-reversibility, the small ΔE value published in the literature is characteristic of an electrochemically reversible system. The reported CV was performed under different conditions; at a hanging mercury drop electrode in a buffer containing 100 mM phosphate and 1 M KCl (pH 8.0).[203] These discrepancies can be ascribed to the variation in experimental conditions,

however, they can also arise from the slower electron transfer kinetics exhibited by the BDD working electrode, as demonstrated in **Section 6.4.1**.

2.4 Summary and conclusions

The electrochemical study of iron(III) azotochelin, the anchoring motif of the Fe-PBP ArM, was successfully performed following the investigation of BDD as an alternative material to mercury-based working electrodes. The BBD working electrode was found to have a sufficiently wide potential window to enable the measurement of the reduction potential of low denticity catecholate siderophores, including azotochelin. Moreover, the electrochemical response of a high denticity hydroxamate siderophore, ferricrocin was successfully observed, illustrating the versatility of the electrode material. Unfortunately, it was found that the redox potentials of higher denticity catecholate siderophores, protochelin and enterobactin which exhibit high thermodynamic stability and thus very negative E_p values, were out of reach.

An irreversible electrochemical behaviour was observed in the cyclic voltammogram of iron(III) azotochelin, with the cathodic peak potential associated with the Fe(III)/(II) reduction at −660 mV vs Ag/AgCl 3 M NaCl (−470 mV vs NHE). The inability to detect the reoxidation of the metal centre due to the low stability of the complex is supported by UV-vis and native ESI-MS data which confirms the preferential formation of a coordinatively unsaturated species with a tetradentate coordination sphere, [Fe^{3+} Azoto^{4-}]$^-$. An identical speciation pattern is present in the binding pocket of CeuE, the PBP constituting the protein scaffold of the redox-reversible ArM, as revealed by its crystal structure.[54] Thus, the results acquired in this chapter provide evidence for the suitability of iron(III) azotochelin as the ArM anchor. The voltammetry data confirms the instability of the iron(III) azotochelin complex upon the reduction of the metal centre to iron(II) and its subsequent dissociation, in parallel to the

disassembly of the ArM upon the reduction of the metal centre within the anchor unit.[54]

The two studies exploring the reduction potential of iron(III) azotochelin as a function of buffer composition and pH indicated the feasibility of modifying either the primary or secondary coordination sphere of the metal to facilitate the release of the anchor. An increase in H^+ concentration was shown to exhibit a significant effect on the reduction potential, with a shift of +290 mV being observed at pH 6.0. Further characterisation through UV-Vis and native ESI-MS measurements unveiled that the **M_1:L_1** speciation of the complex was preserved under acidic conditions, while the shift from catecholate- to salicylate-type coordination mode was responsible for the change in reduction potential. It would be of interest to acquire the crystal structure of the iron(III) azotochelin complex bound to CeuE at varying pHs to determine whether such a coordination shift was possible within the protein binding pocket and measure the effect of salicylate coordination on the K_d value. A similar, although less extensive effect on E_p shift was noted in the presence of buffers constituting primary and secondary amines, TRIS and TES, respectively; the E_p values measured in the respective buffers were positively shifted by 250 mV and 170 mV. This is speculated to be a result of nitrogen coordination to the metal centre, and the subsequent stabilisation of iron(II) over iron(III) due to the soft donor atom character of nitrogen. The chelation of the metal centre by the buffer molecules and the subsequent effect on the reduction potential can serve as a model for predicting the effect of mutating the iron coordinating residues on the E_p value. Within the wild-type protein scaffold, iron(III) is coordinated by Y288 through the oxygen atom of the hydroxyl group (**Figure 2.20**) and thus mutation to a residue with a terminal primary amine, such as lysine, asparagine or glutamine may shift the reduction potential of the anchor to a more positive value which would facilitate its reduction and the subsequent disassembly of the ArM.
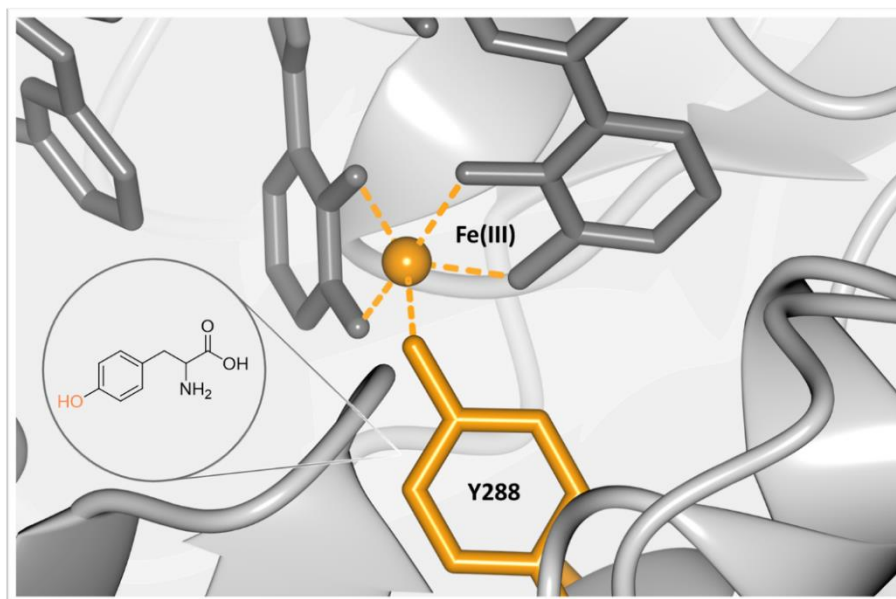
Figure 2.20 Crystal structure of the anchor binding pocket within the Fe-PBP ArM (PDOB: **5OD5**) illustrating the direct coordination between the hydroxy group of Y288 (orange cylinders) and the iron(III) centre (orange sphere) of the anchor motif (dark grey cylinder). The inset shows the structure of the tyrosine amino acid with the coordinating hydroxy group highlighted for reference.

***

Chapter 3 – ArM immobilisation on gold electrodes modified with nitriloacetic acid self-assembled monolayer

In parallel to research undertaken within the Duhme-Klair group, exploring anchoring the Fe-PBP ArM on immobilised-metal affinity chromatography (IMAC) columns, an approach for utilising IMAC strategies of binding the Fe-PBP ArM onto conducting supports has been investigated. The employment of affinity tags has been well established for the immobilisation of enzymes to improve their catalytic performance. The methodology has been also extended towards redox-active proteins, demonstrating feasibility for achieving their immobilisation in electroactive conformations on modified electrodes. However, such an approach has not been utilised for anchoring artificial metalloenzymes. Thus, this chapter evaluates two different approaches for modifying gold electrodes with nitrilotriacetic acid (NTA) functionalities through SAM formation, including a description of an alternative strategy for the synthesis of LA NTA. The efficiency of each modification method and subsequent ArM immobilisation is evaluated through electrochemical measurements, cyclic voltammetry (CV) and electrochemical impedance spectroscopy (EIS), as well as quartz crystal microbalance with dissipation (QCM-D) measurements.

3.1 Introduction

Immobilisation of enzymes for achieving efficient biocatalysis frequently relies on site-specific tethering approaches to ensure the catalytic site within the protein remains accessible for substrate binding.[204,205] Analogously, immobilisation of redox proteins on conducting surfaces

requires consideration of orientation for establishing an electrochemical connection between the redox centre and the electrode, as discussed in **Section 1.4.2**.[206,207] The immobilisation of redox enzymes therefore requires a combinatorial approach, since both substrate access and electroactive conformation must be considered in order to establish a successful system. Thus far, a plethora of immobilisation approaches is presently available, since a 'one approach fits all' methodology has not been yet developed to robustly resolve both considerations simultaneously. These various methodologies have been extensively reviewed in the literature and an interested reader is directed to these papers.[140,208–212]

Stable, site-specific approaches for covalent protein-electrode immobilisation are often complex as they frequently necessitate molecular biology manipulations to incorporate bioorthogonal handles which allow protein attachment to electrodes.[213–215] Covalent immobilisation often has an adverse effect on the protein structure, which has been shown to result in reduced catalytic activity within enzyme-electrode arrays.[216] Thus, non-covalent approaches are becoming increasingly more popular since most methods do not possess a prerequisite for protein modifications following their expression to achieve immobilisation. This aspect is also crucial from a commercialisation standpoint, as reducing the necessary steps for protein preparation to achieve an active molecule towards immobilisation is highly desirable. However, for a non-covalent protein-electrode immobilisation approach to be viable, the bonding strength of the non-covalent interaction must be comparable to that achieved through covalent methods, particularly for incorporation of enzymes on the surface where long-term stability is essential. The strength of the interaction between a divalent metal (M^{2+}) complex of nitriloacetic acid (NTA) and the imidazoles of a polyhistidine tag (6His), found to be 10^{-6} M, it was deemed feasible to explore this as a method for immobilisation the Fe-PBP ArM.[217]

3.1.1 Protein immobilisation via affinity polyhistidine tag

The 6His-tag is one of the most prominent affinity tags utilised within biochemistry, it being the core motif of protein purification through IMAC.[218,219] The technology relies on the ionic interaction between M^{2+} complex of a multidentate chelator, such as NTA, and the imidazole rings of the 6His-tag (**Figure 3.1**). Fundamentally the coordination chemistry drives the interaction; the chelating groups of NTA only fill four out of the six available metal ion coordination sites leaving an incomplete octahedral coordination sphere. Coordination of a 6His-tag through the binding of the two nitrogen atoms on the imidazole rings completes the coordination sphere of the divalent metal.[220]

Solid support   **M^{+2}-NTA**   **6His-tag**   Protein
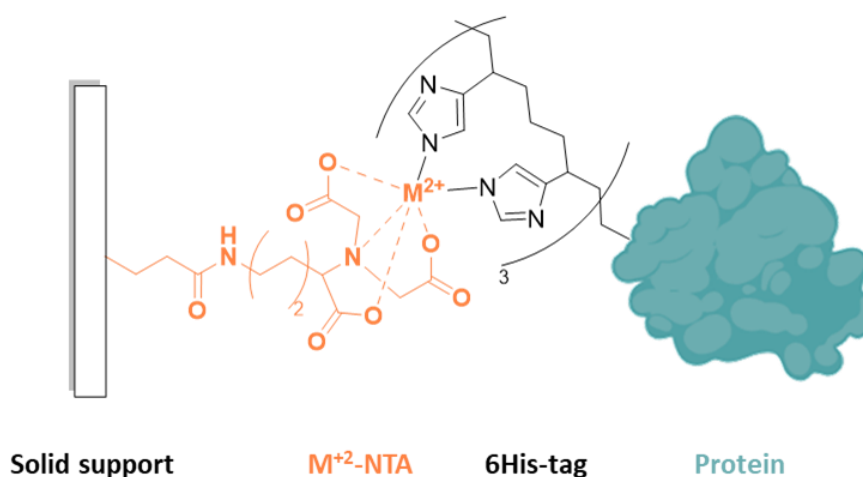
Figure 3.1 A schematic illustration of the interaction between the unsaturated M^{2+}-NTA complex and the imidazole rings of the 6His-tag. The attachment of the NTA to a support is not defined in the figure, as depending on the application, the support material may extensively vary; in IMAC applications the NTA ligand is covalently attached to cross-linked agarose beads.

In its early days, the immobilisation approach was limited to the use of nickel(II) and NTA, as the metal and chelating ligand pair, respectively. However, the metal choice has now been widely expanded (**Figure 3.2**), particularly as reports of nickel leaching have become more prominent.[221–223] The divalent metal at the centre of the immobilisation strategy has been

successfully varied to create immobilisation platforms exhibiting varying degrees of specificity and immobilisation strength. Compared to nickel(II), copper(II) has been shown to exhibit a higher affinity towards NTA. The surface coverage obtained with Fc(imd)$_2$, a ferrocene derivative bearing two imidazole (imd) rings employed as a model redox probe to mimic 6His-tag binding, was used to demonstrate the distinction between the two metal ions.[126] The anodic waves observed in CV obtained at functionalised carbon electrodes were integrated and the surface coverage (Γ) was calculated to be 16.6 x10^{-11} mol cm^{-2} and 8.2 x10^{-11} mol cm^{-2} for copper(II) and nickel(II) chelated NTA electrodes, respectively.[126] However, parallel studies have demonstrated copper(II) based surfaces exhibit much lower selectivity towards 6His-tagged molecules, resulting in a higher percentage of non-specific binding. Nonetheless, the redox-active enzyme horseradish peroxidase has been successfully immobilised in an electroactive configuration via a 6His-tag onto copper(II) modified NTA electrodes.[126] The reduction of copper(II) to copper(I) was observed at approximately −700 mV vs SCE (−459 vs NHE) in 20 mM phosphate, 50 mM NaCl buffer at pH 7.4. This suggests that the copper(II) based IMAC-derived approach would be unsuitable for stable immobilisation of redox proteins with highly negative $E°'$ values.[126] However, for some applications, the copper(II)/(I) redox chemistry can prove to be advantageous. One study demonstrated electrochemically-triggered release of an immobilised protein from a copper(II) NTA electrode through an application of a potential of −300 mV vs Ag/AgCl 3 M KCl.[224]

Instead of nickel or copper, some reports have investigated the utilisation of cobalt(II) ions for the immobilisation of 6His-tagged proteins on NTA functionalised surfaces. The literature on protein purification using IMAC columns strongly indicates a lower affinity of 6His-tagged proteins to cobalt(II), although with higher specificity.[225] An attractive solution to this problem has been to exploit the redox activity of cobalt(II); following immobilisation of a 6His-tagged green fluorescent protein on cobalt(II) NTA
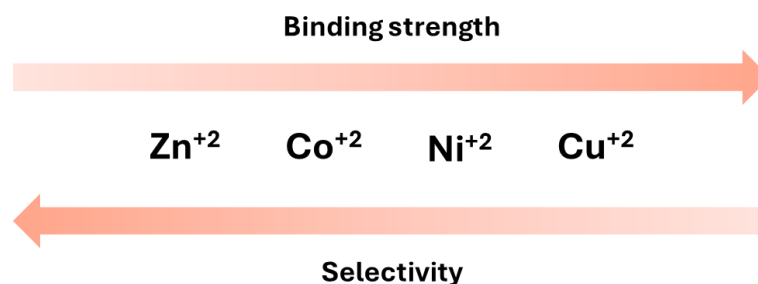
Figure 3.2 Illustrative representation of the metal(II) ions available for use in combination with NTA for the immobilisation of His-tagged proteins. The series is arranged based on the binding strength to the chelating ligand (top arrow) and selectivity towards His-tagged proteins which appear to have inversely proportional relationship.[226,227]

surface, the metal centre was oxidised to cobalt(III) using hydrogen peroxide.[228] Quartz crystal microbalance (QCM) measurements successfully demonstrated the higher stability of immobilised protein on the resulting surface in comparison to immobilisation on nickel(II) NTA. Following overnight incubation of 15 hours, 80% of protein remained on the cobalt(III) surfaces, in comparison to the 48% on the nickel(II) surface.[229] Moreover, the protein immobilised on the highly stable cobalt(III) surface was shown to be resistant to the presence of imidazole and EDTA, compounds which both normally compete with the binding of the 6His-tag to IMAC.[229] Indeed, the usual ability of small organic molecules to induce protein release can be a positive feature of IMAC inspired enzyme-electrode immobilisation strategies.

The possibility of triggered protein release, subsequent surface regeneration and protein re-immobilisation is particularly useful in situations where there is a necessity to employ a single immobilisation platform in multi-enzymatic cascades. Surface recycling contributes to the reduction of costs associated with manufacturing specific immobilisation platforms for each individual reaction. A balance must therefore be established between obtaining a highly stable protein immobilisation, while not precluding the ability to regenerate the surface.

In addition to substituting the metal ion to tune the strength and selectivity of the protein immobilisation, NTA can be substituted with an alternative metal chelating molecule to influence the stability of the metal complex.[126,230,231] This approach has not been explored within this work as ligand optimisation would require separate synthetic strategies which is beyond the scope of this project. Moreover, there are literature examples available exploring the use of longer His-tags to increase the strength of the protein immobilisation, with the most common approach being increasing the number of histidines twice fold to form a 12His-tag.[232] This was also investigated as it was presumed that such approach would result in a lower immobilisation yield, as one protein will likely become immobilised on multiple metal NTA sites, thus reducing the concentration of ArMs on the surface and making surface characterisation much more challenging.

Not all of the features associated with protein-electrode immobilisation via a polyhistidine affinity IMAC are advantageous. As described above, metal leaching is frequently noted as a major limitation. Additionally, Balland et al. described an incomplete saturation of immobilised NTA ligands with the metal cation, exposing the negatively NTA charged ligands to the enzyme.[233] The free ligands were hypothesised to interact with the positively charged residues on the protein surface, altering the orientation of the protein and subsequently bringing it into a closer proximity to the electrode surface. This resulted in multiple protein environments which were suggested to be responsible for the dispersion of the reduction potential exhibited by the redox-active cofactor, preventing its detection by voltammetric techniques.[233]

3.1.2 Self-assembled monolayer (SAM) formation

The introduction of NTA functionalities onto electrodes has been documented in the literature via a range of surface chemistries that are compatible with various electrode material types.[234] The wide variety of strategies enables the selection of one that is most appropriate for the

application of interest; for exploring the immobilisation of ArMs and the study of electrochemical disassembly a straightforward strategy on a surface compatible with a range of surface characterisation techniques to facilitate the validation of each modification step is of much interest, and therefore gold electrodes were targeted.

Formation of self-assembled monolayers (SAMs) on Au electrodes exploits the high affinity for Au-S bond formation between Au surfaces and derivatised thiol groups (R-SH) (**Figure 3.3**).[235,236] The mechanism via which chemical adsorption of these molecules generates well-ordered monolayers has been extensively studied and demonstrated to be highly reproducible.[237,238] The approach is characterised by minimal solution preparation requirements and easy (although somewhat laborious) surface regeneration procedures. Together, this ensures that screening and optimisation experiments can be performed in an efficient manner. The commercial availability of thiol alkyl molecules with a wide variety of terminating groups facilitates the use of SAMs for the introduction of various different functionalities onto Au electrodes. The use of dithiols, such as lipoic acid (LA) is becoming more prominent across the SAMs on Au literature.[146,239,240] Reductive desorption experiments performed in 0.5 M KOH have not shown significant variations in the E_{pc} values of monothiol versus dithiol analogues, indicating surfaces of similar stability.[241,242] However, there is an assumption for the two-point surface-molecule interaction exhibiting greater kinetic stability in comparison to the single-point attachment. The handling of dithiols is much easier as they are not characterised by a pungent smell, thus the utilisation of dithiols, if a suitable terminating group is available, is much more favourable.
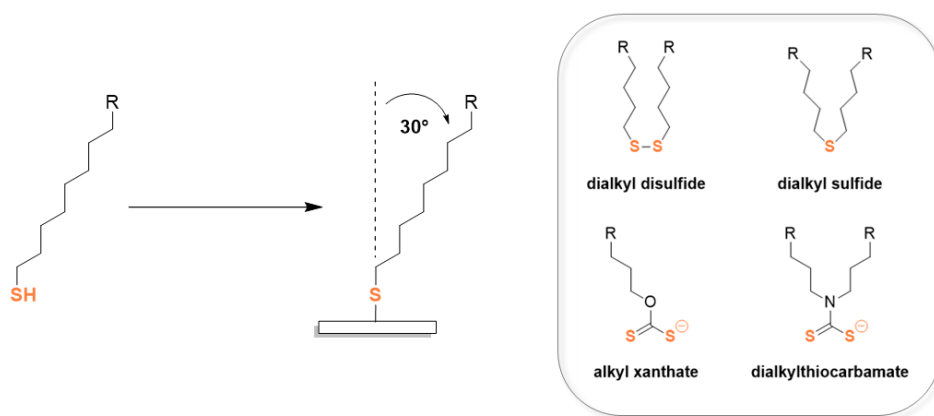
Figure 3.3 General scheme for the chemisorption of an alkyl thiol molecule onto a gold surface, illustrating the preferred orientation of the molecule which ensures a well-packed monolayer; the inset depicts the breadth of organosulfur functionalities capable of monolayer formation on gold.[243]

The phenomenon of thiol desorption from Au surfaces represents the most significant challenge to using SAMs on Au for long-term applications such as immobilisation of catalysts. Overtime, the loss of thiol molecules from gold surfaces is observed upon storage in aqueous media under ambient conditions. To demonstrate this, the electrochemical behaviour of $[Fe(CN)_6]^{3-}$ has been investigated at Au electrodes functionalised with an alkyl thiol as a function of storage time in PBS buffer.[244] Immediately after Au functionalisation, Faradaic peaks were not observable within the potential window studied, which supports the presence of a well-packed monolayer impeding electron transfer between the electrode and the redox couple in solution. However, a notable increase in the Faradic current and decrease in ΔE values corresponding to the Fe(III)/(II) couple was observed over a period over 35 days with near electrochemical reversibility being achieved by the end. Such results correspond to the loss of thiol molecules from the surface, this was supported by changes in surface IR spectra. In general, ambient degradation of Au-SAM surfaces is attributed to oxidative degradation, but SAMs also exhibit hight sensitivity to reducing conditions.[245]

Despite the challenges in using SAMs for protein immobilisation on Au electrodes, they remain the topic of many accounts across the literature. In terms of using them as the basis for functionalising Au with NTA functionalities, the most prominent example comes from the research group of Benoît Limoges. The researchers have successfully combined the formation of lipoic acid-based SAMs and NTA functionalities for the immobilisation of a variety of redox-active proteins via the 6His-tag. However, they report several limitations of the approach. During the study of human neuroglobin comprising a redox active iron(III) protoporphyrin IX complex at its centre, direct electrochemical interrogation of the protein was not achievable.[233] Neither Faradaic current corresponding to the iron(III)/(II) couple was observed, nor the catalytic current in the presence of O_2. However, surface-enhanced resonance Raman spectroscopy (SERR) was successful in establishing the feasibility of direct electron transfer.[233] The application of a reducing potential to the protein modified electrode was associated with a spectral shift characteristic of reduced hNB with an iron(II) centre.[233] The difficulties in employing cyclic voltammetry for characterising the protein was thus proposed to be associated with the presence of a heterogeneous surface. It was suggested that the incomplete metal chelation of NTA molecules gave rise to inconsistency in surfaces charges, thus generating multiple possible conformations of the immobilised proteins, with distinct E'° (Fe(III)/(II)) for each conformation. This dispersion of redox potentials resulted in peak broadening making it difficult to discern the presence of Faradaic currents. Similar LA NTA functionalised electrodes have also been employed for the immobilisation of laccase, exploiting copper(II) for the formation of the NTA complex.[125] To achieve an electrochemical connection, it was necessary to employ a soluble redox mediator, $[Os^{III}(bpy)_2pyCl]^{2+}$, to facilitate the electron transfer between the electrode and the copper redox centre of the metalloenzyme.[125] Kinetic analysis was performed which validated that the catalytic activity of the enzyme immobilised via the 6-His tag was not affected.

A study into the immobilisation of ferredoxin:NADP+ reductase which has been genetically modified to possess a pair of surface-exposed histidine residues was also successfully carried out on LA NTA functionalised electrodes using copper(II).[246] Catalytic currents for electrocatalytic oxidation of NADPH mediated with ferrocene (either solution free or surface tethered) were analysed. Moreover, specific and reversible immobilisation was concluded from the voltammetric data, where the catalytic current was absent without in the absence of histidine mutations or the metal.[246]

Collectively, the above literature analysis suggests that while employment of SAMs for electrode functionalisation with NTA might not be suitable for long-term applications, there is sufficient precedence to validate its employment in the initial validation of ArM immobilisation. The high efficiency of site-specific immobilisation and the ease of electrode functionalisation, as well as evidence of direct electron transfer (although not always detectable through CV) is beneficial for interrogating the feasibility of electrochemically triggered disassembly. Moreover, the ease with which the LA NTA SAM precursors can be synthesised, either through a two-step synthesis as established by B. Limoges and co-workers, or through on-surface EDC/NHS coupling further highlights the beneficial aspects of this immobilisation approach, especially for preliminary studies of the ArM.[125,247]

3.1.3 Protein-surface characterisation methods

Characterising on-surface synthesis poses one of the most significant challenges in surface chemistry. Presently there is a lack of methodologies enabling interrogation of surfaces structure with similar accuracy as that achieved in NMR for solution chemistry. Instead, most techniques rely on the changes the surface modification generates in the physical properties of the support. QCM technology is a surface characterisation technique that operates on the principle of piezoelectricity (**Figure 3.4**).[248,249] As mentioned above, while the technique does not provide precise identification of the

molecular structure of the species on the surface, it effectively detects mass changes on the surface by measuring frequency oscillation changes exhibited by the sensor crystal.
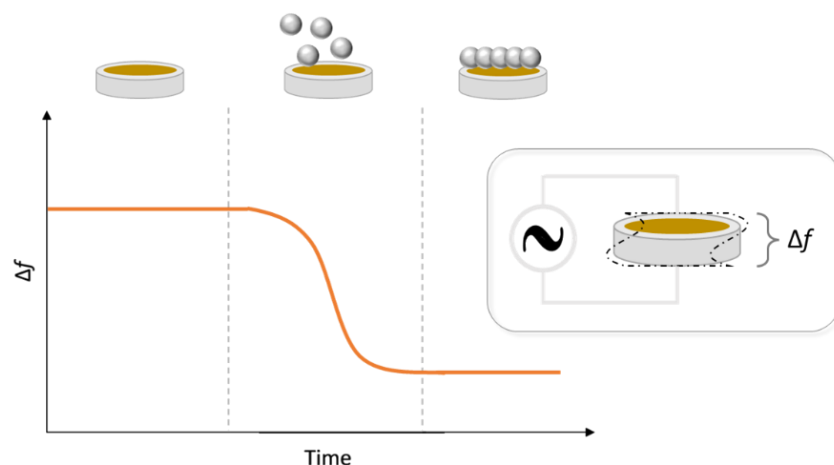
Figure 3.4 A schematic illustration of the typical plot acquired during the QCM experiments which represents the decrease in the resonance frequency of the sensor as the immobilised increases. The inset depicts the working principle of the technique which is based on the application of an alternative voltage to the quartz crystal causes it to oscillate in alternating directions; the change of the oscillation frequency is the measured parameter in QCM.

Electrochemical interrogation is also feasible. Electrochemical impedance spectroscopy (EIS) allows to characterise the extent of surface modification prior and after the functionalisation as a function of electron transfer resistance, also referred to as charge transfer resistance (R_{ct}) between a redox probe in solution, commonly potassium ferricyanide, $K_3[Fe(CN)_6]$ and the electrode (**Figure 3.5**).[250–252] While EIS does not provide real-time feedback response like QCM, it can prove to be more sensitive particularly when it comes to detecting surface changes that are not accompanied by significant mass differences, such as the incorporation of NTA functionality. The measure of impedance is more perceptive to subtle changes in surface properties, such as variations in charge density.
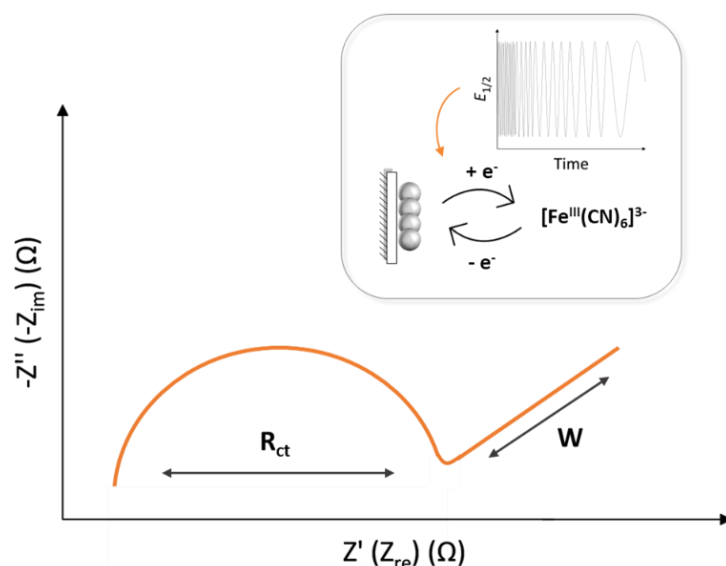
Figure 3.5 A schematic illustration of the Nyquist plot acquired during EIS measurements with a characteristic semicircle and a linear region. The size of the semicircle is proportional to the resistance of the electron transfer (R_{ct}) experienced by the redox probe, $[Fe(CN)_6]^{3-}$ which is the parameter of interest in EIS measurements. More extensive modifications of the surface result in higher R_{ct} values. The inset represents the working principle of the technique where a small amplitude potential perturbation at the $E_{1/2}$ of the redox probe for multiple frequencies.

3.1.4 Aims

The adaption of the affinity binding motif at the core of the IMAC technology for electrode functionalisation demonstrates an attractive strategy for immobilising redox proteins (**Figure 3.6**) on conducting, supported by its extensive utilisation across literature. Crucially, the employment of a 6His-tag offers the advantage of minimal requirement for protein manipulation as this functionality is incorporated regardless in majority of proteins due to its importance in protein purification. Its favourable terminal position minimises the risk of protein misfolding and interference with catalytic activity due to its presence. Among the extensive approaches for incorporation of NTA functionalities on electrode surfaces, the combination of sulfur-based SAMs and Au surfaces through the employment of a LA NTA molecule (**Figure 3.6**) stands out as an appealing approach. Despite the stability concerns associated with the usage of SAMs, especially in highly

reducing conditions, such as those required for the reduction of the iron(III) azotochelin anchor, their efficient installation onto Au makes them highly suitable for preliminary testing of the immobilised ArM system.
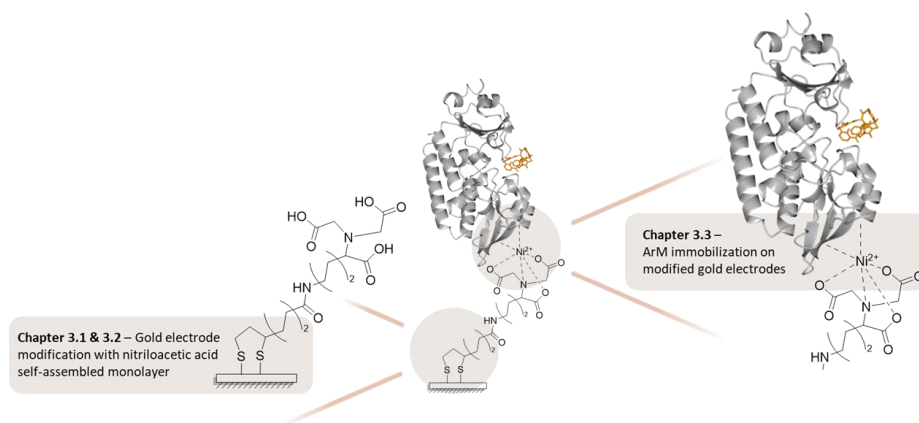
Figure 3.6 A scheme adapted from **Figure 1.13**, illustrating the focus of the work described in **Chapter 3**, the SAM modification of the surface and CeuE-6His immobilisation via the 6His-tag, and where it fits within the proposed recycling platform.

The work described in this chapter can thus be divided into two sections focusing firstly on the modification of the Au electrode with LA NTA SAM and subsequent immobilisation of the ArM. The objectives required to achieve both steps can be defined as follows:

- The synthesis and isolation of the LA NTA conjugate in a sufficiently large yield to ensure it is not a limiting factor in surface modification experiments.
- Optimisation of a protocol for modification of Au electrodes with NTA functionalities which yields a highly homogeneous surface.
- Determine the surface coverage of the metallated NTA functionalities using a redox marker capable of binding in a manner similar to His-tagged proteins.
- Employ multiples surface characterisation techniques to ensure the successful immobilisation of the ArM on modified gold electrodes.

- Develop an experimental methodology for assessing the extent of site-specific immobilisation of the ArM via the 6His-tag versus non-specific immobilisation.

3.2 Results and discussion

3.2.1 Lipoic acid-nitrilotriacetic acid conjugate: on-surface synthesis and SAM characterisation

The synthesis of the lipoic acid-nitriloacetic acid (LA NTA) conjugate has been pioneered in the group of Benoit Limoges, under the lead of Veronique Balland and reported to be achieved in a two-step procedure (**Scheme 3.1**).[125] The first step, the formation of an activated lipoic acid (LA NHS), through the installation of a *N*-hydroxysuccinimide functionality has been previously described in the literature to proceed through a relatively slow reaction although in a sufficiently high yield of 59%.[253] Subsequent conjugation of a lysine tethered NTA molecule to the LA NHS in the presence of triethylamine was shown to successfully form the desired dithiolane molecule, with minimal requirements for purification.[125]
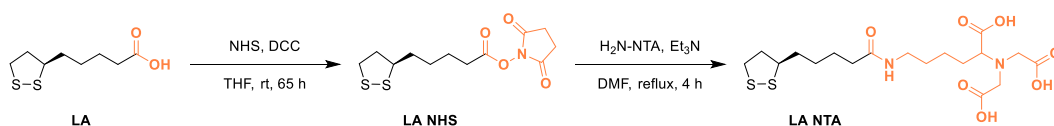
Scheme 3.1 A two-step synthetic strategy proposed for preparing a LA NTA conjugate for the functionalisation of gold surfaces as described in the literature by V. Balland et al.[125]

Inspired by the simplicity of the above methodology, an attempt was made to reproduce it for the synthesis of the LA NTA molecule. The derivatisation of the lipoic acid with an activated ester group, was performed in accordance with the literature.[253] Improving the recrystallisation conditions by substituting toluene with a mixture of ethyl acetate and hexane, the reaction time was able to be reduced from 65 to 48 hours while maintaining a comparable yield of 57%. However, the subsequent conjugation of the activated ester analogue to a NTA lysine derivative (H₂N-NTA) in

dimethylformamide did not yield the product as described in the literature. The primary limitation was suspected to be the inadequate solubility of the NTA molecule in the solvent employed, even with prolonged heating. Thin-layer chromatography (TLC) analysis indicated the conversion of the starting material to a species exhibiting a peak with m/z 503.23 as revealed by MS, however, the exact structure could not be determined. An alternative protocol was found employing a combination of methanol and tetrahydrofuran as the solvent system, which allowed the reaction to proceed at a milder temperature.[224] The improved solubility facilitated the formation of the desired product which corresponded to the most prominent peak in the negative ionisation mode of MS obtained on the crude reaction mixture (**Figure 3.7**). Isolating the desired product from the unreacted starting material proved to be challenging due to the hydrophilic nature of both molecules, which excluded the used of aqueous work-up or column chromatography. Multiple recrystallisation attempts were made, however, satisfactory results could not be achieved.
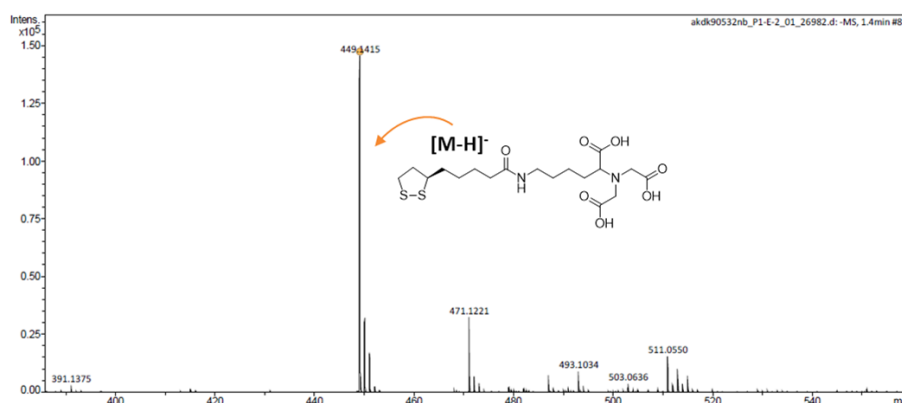
Figure 3.7 Mass spectrum (EIS) of the crude product from the synthesis of LA NTA in a mixture of methanol and tetrahydrofuran.

Multiple reports in the literature describe a simpler approach for the modification of surfaces with NTA moieties, which effectively circumvents the aforementioned challenges associated with the separation of H_2N-NTA from the desired product.[247,254,255] The initial surface functionalisation with a terminal carboxylic acid enables on-surface coupling with the amine of

the NTA precursor. As a result, the desired product remains adhered to the surface while the unreacted molecules and excess coupling reagents can be efficiently removed. The relatively low reactivity of carboxylic acids towards amide bond formation, particularly when they are immobilised on surfaces, is a well-known phenomenon.[256] To overcome this limitation, a commonly employed approach involves converting the functional group into a form that is more susceptible to nucleophilic attack by the amine. The formation of NHS-activated esters, in parallel to the methodology shown in the first step of **Scheme 3.1** appears to be the most favoured approach in the literature. [257–259]

It was anticipated that QCM-D could be employed to monitor the amide coupling reaction in situ and track the associated mass changes during the incorporation of the NTA moiety onto the surface, as well as assess the efficiency of subsequent nickel chelation. However, the incompatibility of the tubing material available with organic solvents, necessitates the amide conjugation to be performed in aqueous conditions. The high pH levels (pH > 7.5) required to facilitate the reaction, accelerate the rate of ester hydrolysis leading to lower NTA surface coverage.[260,261] Alternatively, the amide conjugation step can be carried out in an organic solvent and in the presence of a base, to minimise ester hydrolysis and enhance the conversion yield, mirroring solution conditions. However, this approach precludes the employment of QCM to monitor the progress of the reaction and determine the reaction yield.

Thus, the success of the SAM formation on Au (**SAM-02**) and subsequent modification of the head group to yield an NTA-terminated surface (**SAM-03**) was monitored through EIS measurements. Following overnight incubation of the gold electrodes in the solution of **NGB-10** to allow sufficient time for LA NTA to form well-packed monolayers, each electrode surface was washed and dried before being submerged in a 10 mM solution of $K_3[Fe(CN)_6]$, which was utilised as the redox probe. However, the use of

ferricyanide was approached with caution as multiple literature reports have been published discussing the adverse effect of the metal complex on Au electrodes.[262–265] The most prominent hypothesis is the degradation of the complex in aqueous conditions, resulting in the release of cyanide ions. These subsequently etch the gold causing the breaking of the Au-S bond, resulting in the detachment of the SAM molecules from the metal surface. Aside to employing dark conditions and short analysis time to minimise the degradation effect, further optimisation efforts were undertaken (not included within this thesis) to find conditions which will enhance the stability of the ferricyanide complex. However, the work remains ongoing and is currently being continued by other members of the research group.
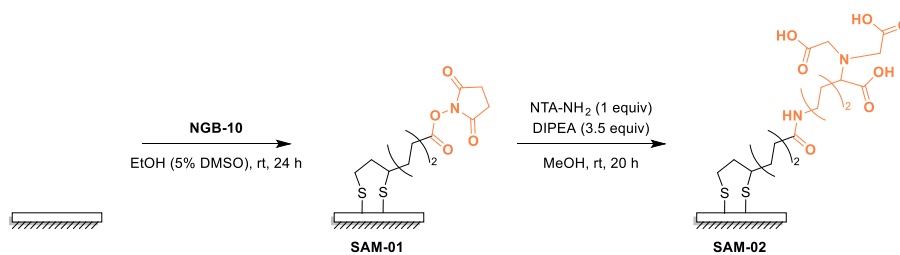
Scheme 3.2 The protocol employed for the 'on surface' synthesis of LA NTA on Au electrodes (**SAM-02**) in a parallel manner to the synthetic protocol employed in **Scheme 3.1**. The conditions for the amide bond formation were optimised for a heterogenous reaction and thus differ from those employed in solution chemistry.

Figure 3.8 A depicts the overlay of the Nyquist plots obtained at each modification stage, with the change in plot shape and subsequent R_{ct} values being clearly demonstrated. Whereas **Figure 3.8 B** illustrates the measured phase angle (ϕ) for each electrode surface, providing a summary of the observed monolayer quality, where the theoretical maximum value for a well-packed monolayer is 90°. The Nyquist plot acquired for the bare Au electrode is in reasonable agreement in the literature, indicating the electron transfer between the redox probe and the electrode being predominantly under diffusion control as evidenced by the significant linear region which can be modelled as Warburg impedance. Upon incubation of the electrode in the **NGB-10** SAM solution, the resulting surface (**SAM-01**) displayed a

significantly higher charge transfer resistance, reflected in the larger diameter of the semicircle on the plot and indicative of a modification of the bare Au surface. However, the observed change in plot shape was not anticipated. The enlarged Nyquist plot can be considered as an additive combination of two smaller semicircles, both exhibiting similar capacitance values, although with significantly different resistance as indicated by the asymmetric shape of the plot. This observation is associated with two different electron transfer processes occurring as the electrode surface, each governed by unique kinetic control. The data provides support for the existence of a heterogeneous surface, which can be attributed to partial hydrolysis of the NHS ester groups during the measurements in aqueous conditions and thus giving rise to a mixed monolayer. Following the amide conjugation step, the **SAM-02** surface gave rise to a much smaller Nyquist plot corresponding to lower electron transfer resistance, which was accompanied by a decrease in the phase angle value to 70°. Initially, this observation may raise concerns regarding the stability of the formed SAM and suggest the deterioration of the film, rather than the successful
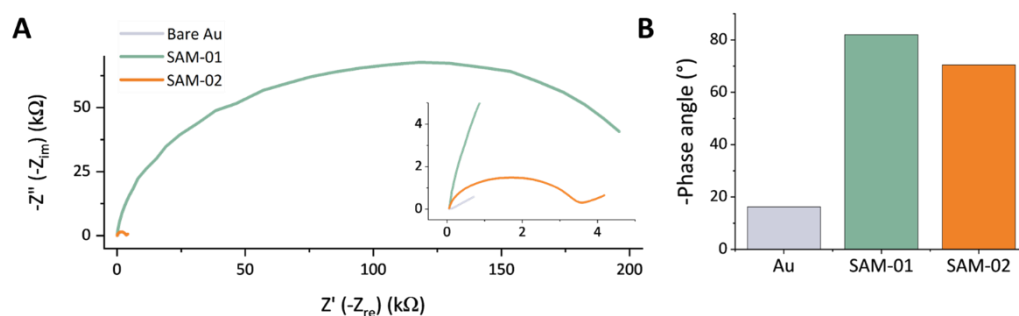
Figure 3.8 A Nyquist plots obtained at each stage of functionalisation of a polished Au disk electrode (bare Au) to yield an LA NTA capped (**SAM-02**) through 'on surface' synthesis from a LA NHS terminated surface (**SAM-01**). The measurements were performed in the presence of 10 mM $K_3[Fe(CN)_6]$ in 100 mM phosphate buffer, 233 mM NaCl at pH 7.0. $t_{(equilibration)}$ = 300 s, E_{dc} = 0.230 V, E_{ac} = 10 mV, f = 0.1 Hz − 10 kHz. The inset provides a zoomed in view of the Nyquist plot of **SAM-02**. **B** A graphical representation of maximum phase angle obtained for each surface modification step extracted from Bode plots, where the maximum theoretical value is 90°. The two types of plots were obtained simultaneously within a single measurement.

modification of the electrode with NTA functionalities. Particularly, the successful conversion of the surface termination should result in a surface bearing deprotonated carboxylic acids. Due to the electrostatic repulsion between these negatively charged functional groups and the negatively charged redox probe, an increase in charge transfer resistance would be anticipated.

An indirect approach can be undertaken to establish the success of the amide bond formation with the NTA derivative by performing a voltammetric investigation to determine the surface coverage of the available nickel(II) NTA sites. However, as documented across the literature, the redox silence of the nickel(II) NTA complex prevents from direct investigation of the nickel(II)/(I) redox couples. Thus, R. Blankespoor et al. developed a redox probe based on ferrocene, $Fc(imd)_2$, which exhibits a well-defined one-electron redox chemistry for the iron(III)/(II) couples.[126] The ferrocene was derivatised with two imidazole rings to mimic the binding of proteins through the 6His-tag in a 1:1 ratio, which should facilitate the calculation of the number of metal NTA sites through integrating the area under the Faradaic peaks. The published protocol for the synthesis of the $Fc(imd)_2$ complex [**NGB-17**] comprised the use of an alcohol ferrocene derivative [**NGB-15**] at the starting material, which was not commercially viable. Instead, a synthetic route was devised to form the **NGB-15** in a two-step protocol from a dicarboxylic acid form of ferrocene, as illustrated in **Scheme 3.3**. The first step, the conversion of the starting material to the methyl ester derivative was achieved with a satisfactory yield of 51% under acidic conditions, employing a standard esterification protocol. However, the subsequent step for reduction of the ester functionalities to the corresponding alcohol groups did not yield the desired product. Despite using an excess of the reducing agent, lithium aluminium hydride, no observable reaction occurred.
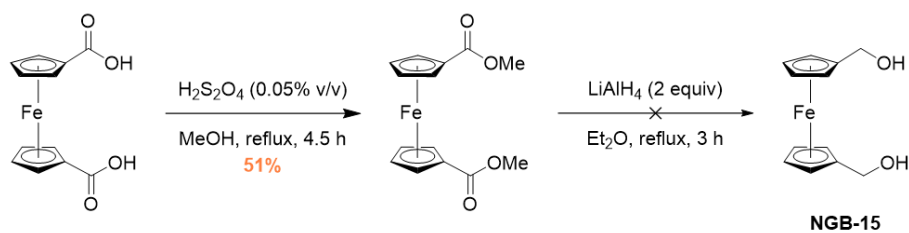
Scheme 3.3 Proposed synthetic strategy for the preparation of **NGB-15**, the starting material for the synthesis of the 6His-tag mimicking redox probe, **NGB-17**.

An alternative synthetic pathway was devised utilising a dialdehyde ferrocene derivative as the starting material, generously provided by Dr Luke Wilkinson.[266] The reduction of the aldehyde functional groups employing sodium borohydride proved to be significantly more successful than reduction of the methyl ester functionalities, achieving **NGB-15** in a 64% yield following the optimisation of the column chromatography conditions. The remaining synthetic steps were performed in accordance with the literature (**Scheme 3.4**), resulting in the successful formation of the $Fc(imd)_2$ redox probe, **NGB-17**; the characterisation data was consistent with the literature.[126,267]
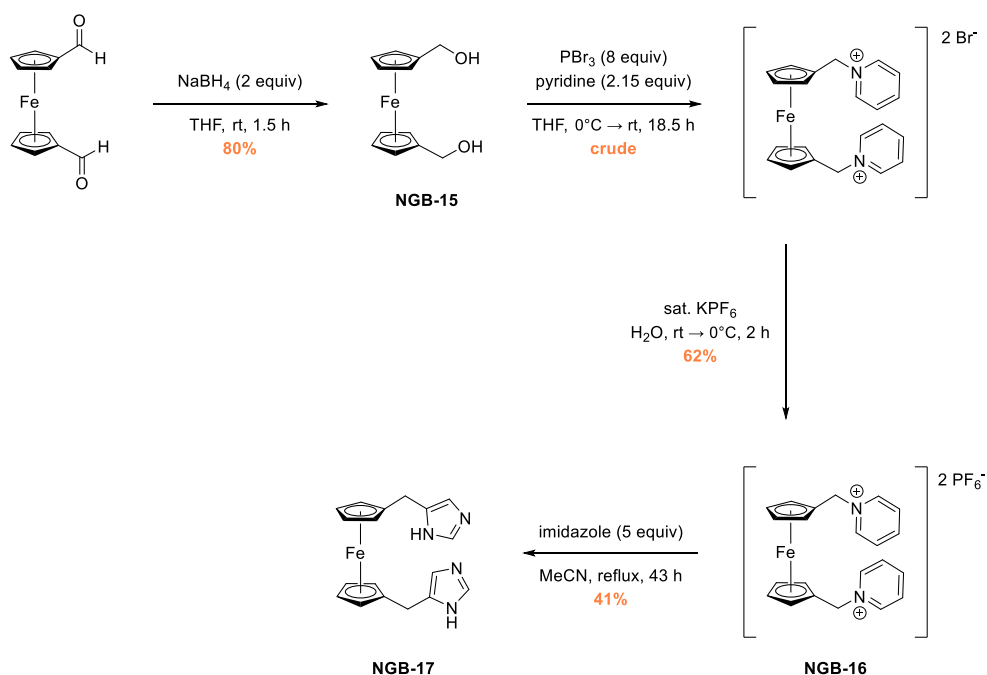
Scheme 3.4 The synthetic route for the formation of a $Fc(imd)_2$ complex [**NGB-17**], a redox probe capable of mimicking the 6His-tag binding of proteins. The final steps were performed according to the literature protocol described by R. Blankespoor et al.[126]

In preparation for the immobilisation of the **NGB-17** redox probe, a Au disk electrode was functionalised in parallel manner to the one described in **Scheme 3.2**, although omitting the EIS characterisation step of the **SAM-01** surface which was proposed to accelerate the hydrolysis of the NHS ester. To facilitate the binding of the ferrocene derivative, the **SAM-02** surface was treated with a 10 mM aqueous solution of $NiCl_2$ for 30 minutes to form a tetracoordinate nickel(II) NTA complexes on the electrode [**SAM-03**]. CV measurements were performed in a 1 µM **NGB-17** solution prepared in 100 mM phosphate buffer containing 250 mM NaCl, pH 7.0. The low concentration of the probe was anticipated to minimise Faradaic contribution from the solution dissolved species, with predominant response being observed from the surface confined ferrocene.
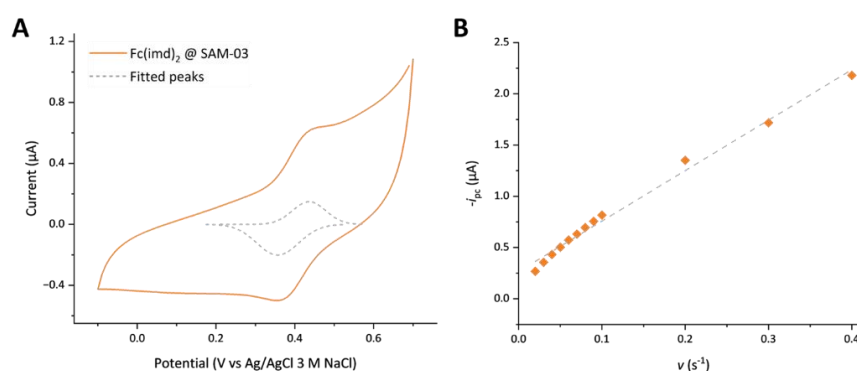
Figure 3.9 A Cyclic voltammogram (at 50 mV s^{-1}) indicative of a successful formation of a NTA film on the electrode surface through the conjugation of NTA-NH$_2$ to NHS ester terminated surface. Following the conjugation, the electrode was immersed in a 10 mM NiCl$_2$ solution and placed for measurement in a 100 mM phosphate, 250 mM NaCl buffer, pH 7.0 containing 1 µM of **NGB-17** (orange solid line). The peaks associated with Faradaic current were extracted through manual peak fitting (grey dashed line). **B** A linear plot (R^2 = 0.991) of peak current (i_{pc}) versus scan rate (v) illustrating the surface-confinement of **NGB-17** on the **SAM-03** electrode. The values were extracted from cyclic voltammograms of a 1 µM solution in 100 mM phosphate buffer, containing 250 mM NaCl at pH 7.0.

The voltammogram shown in **Figure 3.9 A** displays broad Faradaic peaks indicative of a surface confined species. Further confirmation was obtained through the analysis of the current peak (i_{pc}) as a function of scan rate (v),

which when plotted gave a linear correlation as depicted in **Figure 3.9 B**. This subsequently validates the successful formation of the NTA functionalised electrode through the 'on surface' approach as unsuccessful conjugation of the NTA derivative to the **SAM-01** surface would either lead to the absence of Faradic peaks or a nonlinear relationship in the plot of current peak versus scan rate. The surface coverage of the surface confined **NGB-17** can be determined using **Equation 3.1**, thus enabling the quantification of the available protein binding sites. The surface area of the electrode (A) used in the equation was determined as the electroactive area, calculated by integrating the reductive peak observed in the 50th scan of the electrochemical polish in acidic solution, performed prior to SAM formation.

$$i_p = \frac{n^2 F^2 A \Gamma v}{4RT}$$

Equation 3.1 An equation describing the relationship between peak current (i_{pc}) and the surface concentration of a redox species (Γ). n = number of electrons transferred; F = the Faraday constant; A = electroactive surface area of the electrode; v = scan rate; R = the molar gas constant; T = temperature.

The calculated surface coverage (Γ) of **NGB-17** was determined to be 9.7 x10^{-11} mol cm^{-2}. The value is notably lower than the 1.05 x10^{-10} mol cm^{-2} reported in the literature for Fc(imd)$_2$ immobilised on a LA NTA functionalised Au electrode, prepared from a synthesised LA NTA SAM molecule as described in **Scheme 3.1**. The lower surface coverage could be attributed to a low reaction yield during the NTA conjugation step, as steric hindrance and reduced reaction kinetics pose significant challenges in heterogenous reactions.

As explained in **Section 3.1.1**, incomplete metal chelation is often observed for NTA terminated surfaces as a result of electrostatic repulsion between the head groups. It can be hypothesised, that the presence of both metal-chelated, and non-chelated complexes can balance out the surface charges, leading to a more thermodynamically stable surface. Given that the number

of available protein binding sites is already reduced due to incomplete saturation of the NTA groups with nickel(II), it is crucial for the NTA functionalisation step to be high yielding, ensuring the maximum number of NTA head groups are made available. The challenge associated with an accurate determination of the reaction yield for 'on surface' synthesis, coupled with lower yields, suggests that developing and alternative synthetic route to the one outlined in **Scheme 3.1** might be worth pursuing to ensure high immobilisation yield of the ArM.

3.2.2 Lipoic acid-nitrilotriacetic acid conjugate: solution synthesis and SAM characterisation

The difficulties encountered in obtaining **NGB-14** following the synthetic procedure described in **Scheme 3.1** were concluded to result from the residual presence of the starting material in the reaction mixture. Due to the highly polar nature of the NTA functionality present in both molecules made, it posed a challenge to determine a suitable method for isolating the product, when attempts at recrystallisation were unsuccessful. Increasing the hydrophobicity of NTA through the introduction of bulky protecting groups was proposed to facilitate purification through column chromatography. The *tert*-butyl (*t*Bu) moiety represents one of the protecting groups frequently employed in amino acid synthesis, suitable for both primary amines and carboxylic acids either as *N-tert*-butyloxycarbonyl (Boc) or *t*Bu, respectively.[268] The selective addition of the *t*Bu group to the carboxylic acids necessitates initial protection of the amine with an orthogonal protecting group; the insensitivity of *t*Bu esters to the hydrogenation conditions required for removal of benzyloxycarbonyl (Cbz) prompted the selection of the latter as the NH$_2$ protecting group.
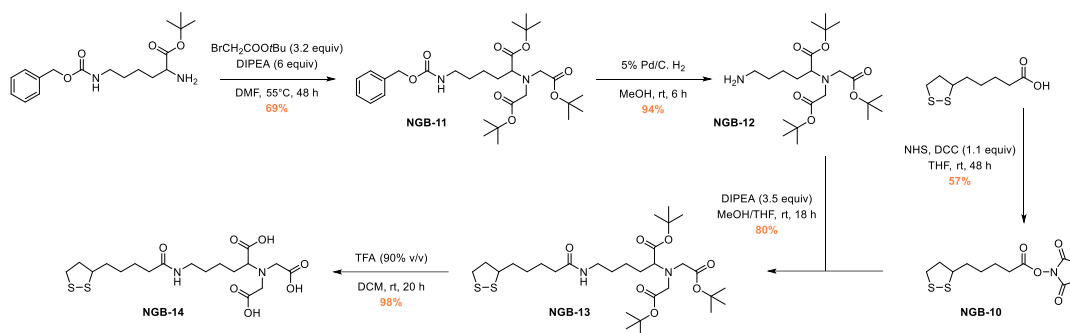
Scheme 3.5 The synthetic route developed for LA NTA [**NGB-14**] SAM molecule, as an alternative to the literature protocol outlined in **Scheme 3.1**; the utilisation of protecting group strategies aimed to eliminate the previously encountered issues with purification of the desired product.

Hence, an alternative synthetic route was developed for **NGB-14**, which involved incorporating protecting and subsequent deprotecting steps as depicted in **Scheme 3.5**. Through modification of existing literature protocols to suit the substrates involved in the synthesis, the desired LA NTA product was obtained in a satisfactory yield, despite the increased number of steps compared to **Scheme 3.1**. Embracing the ethos of developing sustainable synthetic routes, the 'on surface' formation of NTA functionalised electrodes, the **SAM-02** surface protocol aligns more closely with the principles of green chemistry. Hence, it was crucial to assess whether the extended protocol could be justified by offering a higher quality of the resulting SAM. A polished Au disk electrode was submerged in a 1 mM ethanol solution of **NGB-14** for 24 hours to yield a **SAM-04** surface; in a parallel manner to the formation of **SAM-01**. The quality of resulting film was evaluated by employing EIS; once again $K_3[Fe(CN)_6]$ was utilised as the redox marker in solution and charge transfer resistance across the modified surface was measured. The resulting Nyquist plot and extracted phase angles from Bode plots are displayed in **Figure 3.10 A** and **Figure 3.10 B**, respectively, along with the data obtained for **SAM-02**, enabling a direct comparison between the two approaches.
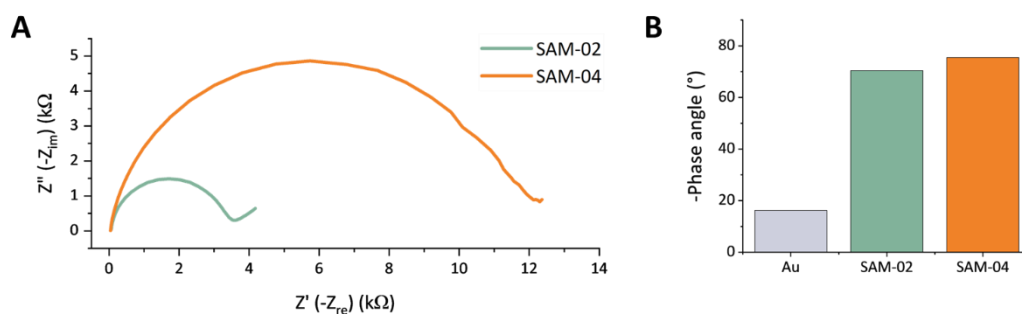
Figure 3.10 Comparison for two methods of functionalising Au electrodes with NTA functionalities through SAM formation; **A** Nyquist plots, **B** phase angles extracted from Bode plots. **SAM-02** is prepared through on surface conjugation of NTA molecule to NHS ester terminated surface (**SAM-01**); **SAM-04** is prepared through the incubation of Au electrode with **NGB-14**. The measurements were performed in the presence of 10 mM $K_3[Fe(CN)_6]$ in 100 mM phosphate buffer, 233 mM NaCl at pH 7.0. $t_{(equilibration)}$ = 300 s, E_{dc} = 0.230 V, E_{ac} = 10 mV, f = 0.1 Hz − 10 kHz.

Analysis of the Nyquist plots reveals a significant difference between **SAM-02** and **SAM-04** surfaces; performing equivalent circuit fitting (**Section 6.2.6**) on the data revealed the R_{ct} value for the latter being 8.68 kΩ higher. This disparity can be attributed to various factors, such as the variation in the number of defects and pinholes within the monolayer. This is evident from the larger linear region observed in the **SAM-02** correlating to the Warburg impedance, indicating a greater contribution from diffusion. arising from the redox probe being able to approach the electrode surface to a greater extent. This is supported by the data presented in **Figure 3.10 B**, which shows a larger phase angle exhibited by the **SAM-04** surface reflecting a higher film quality characterised by a greater degree of packing. The EIS characterisation data suggests that one step functionalisation of the electrode surface offers better control over SAM formation. However, it is challenging to determine the specific factors responsible for the lower quality of **SAM-02**, whether it is associated with the SAM formation of **NGB-10** or the subsequent amide conjugation step.

Similar to the analysis performed on **SAM-02**, **NGB-17** was utilised to quantify the number of available protein binding sites present on **SAM-04**

and investigate whether the better SAM quality corresponds to a higher number of NTA functionalities on the surface. To facilitate the immobilisation of the ferrocene derivative, **SAM-04** was prepared as described earlier following treatment with a 10 mM aqueous solution of NiCl$_2$ for 30 minutes to form a tetracoordinate nickel(II) NTA complexes on the electrode [**SAM-05**]. CV measurements were in the presence of **NGB-17** were performed under identical conditions as those employed for the analysis of **SAM-03**; the results are presented in **Figure 3.11**.
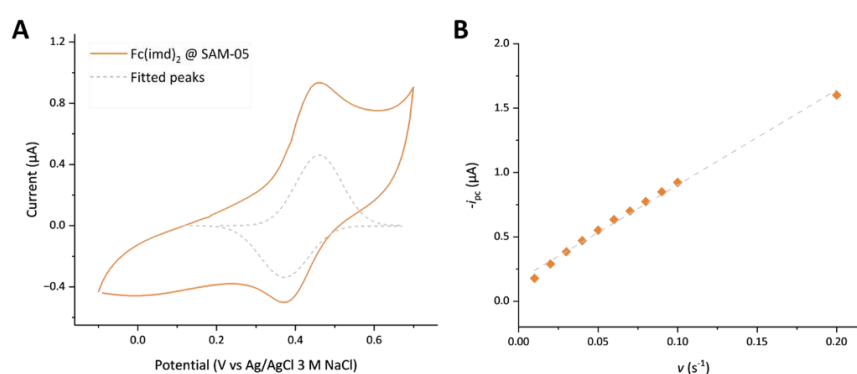
Figure 3.11 A Cyclic voltammogram (at 50 mV s^{-1}) indicative of a successful formation of a NTA film on the electrode surface through the incubation of the electrode in a 1 mM solution of **NGB-14**. Following the SAM formation, the electrode was immersed in a 10 mM NiCl$_2$ solution and placed for measurement in a 100 mM phosphate, 250 mM NaCl buffer, pH 7.0 containing 1 μM of **NGB-17** (orange solid line). The peaks associated with Faradaic current were extracted through manual peak fitting (grey dashed line). **B** A linear plot (R^2 = 0.994) of peak current (i_{pc}) versus scan rate (v) illustrating the surface-confinement of **NGB-17** on the **SAM-05** electrode. The values were extracted from cyclic voltammograms of a 1 μM solution in 100 mM phosphate buffer, containing 250 mM NaCl at pH 7.0.

Calculation of surface coverage for **SAM-05** was achieved by inputting the i_p value extracted from **Figure 3.7 A** into **Equation 3.1**; the remaining variables remain unchanged from the calculation performed for **SAM-03**. The obtained Γ value of ferrocene derivative immobilised on **SAM-05** was equal to 2.40 x10^{-10} mol cm^{-2}; much higher than the value achieved for **SAM-03**. The surface coverage obtained was twice the value reported in the literature by Balland et al. for a surface prepared similarly through direct

SAM formation of LA NTA, although prepared through a different synthetic pathway (**Scheme 3.1**).[125] Without further analysis, it is challenging to determine whether the increase from the literature value is a result of experimental error or if the conditions employed for SAM formation (such as room temperature versus 4°C and extended SAM incubation time) have influenced the outcome. Nevertheless, the significant enhancement in surface coverage observed in **SAM-05** compared to **SAM-03** serves as sufficiently conclusive evidence to justify the adoption of the strategy involving direct SAM formation of LA NTA, despite the lengthier synthesis.

3.2.3 Efficiency of CeuE-6His immobilisation on lipoic acid-nitrilotriacetic acid modified gold electrodes

EIS characterization has demonstrated its exceptional value in discerning subtle variations in the quality of SAMs formed on Au, even when the majority of surface moieties possess similar chemical functionalities. Thus, it is of great interest to explore whether similar sensitivity can be attained upon the immobilisation of a species with higher mass, enabling differentiation between the immobilised ArM and apo CeuE-6His. It is anticipated that this would be feasible, given that the presence of the SidCat which comprises redox-active metals imparts distinct chemical properties, particularly in the context of electrochemical arrays. The Au electrode was functionalised as before to yield a **SAM-05** surface following the immobilisation of either apo CeuE-6His (**SAM-06**) or ArM (**SAM-07**) as summarised in **Scheme 3.6**.

EIS measurements were conducted at each stage of functionalisation to validate the successful development of the immobilisation platform, following the previous concerns regarding the potential destructive effect of ferricyanide on the formed monolayer. However, it is crucial to approach the data analysis with vigilance since there is a possibility of variations
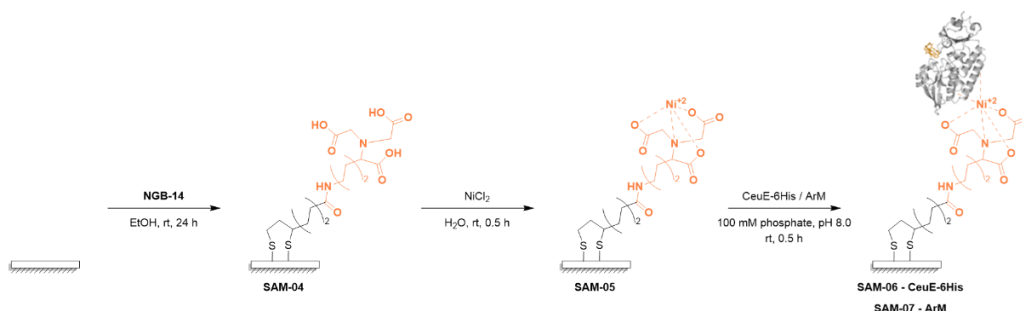
Scheme 3.6 The protocol employed for the preparation of **SAM-03**, NTA functionalised Au surface obtained through incubation in a 1mM **NGB-14** solution. The subsequent steps outline the conditions employed for the nickel chelation step (**SAM-05**) and the immobilisation of the protein on the modified electrode, either CeuE-6His (**SAM-06**) or ArM (**SAM-07**).

occurring in any of the steps across all the attempts, which may not be quantified. The acquired data represented as both Nyquist and Bode plots is shown in **Figure 3.12**. A direct comparison of the Nyquist plots enables the differentiation between each iteration of the surface, as the diameter of the circle changes distinctly with each subsequent step. This corresponds to an increase in the R_{ct} value with each subsequent modification step, which reflects the electron transfer becoming more challenging as the extent of surface functionalization increases. The distinction between the Nyquist plots was also possible between the two protein variants, although surprisingly the immobilised apo protein exhibited a higher R_{ct} value compared to the ArM. This is hypothesised to be a result of the SidCat's facilitation of electron transfer, as discussed earlier. The SidCat consists of two redox-active metal centres that possess the capability to exchange electrons, which could contribute to the observed difference in R_{ct} values. More in depth understanding behind the process underpinning the observed results was beyond the scope of the project.
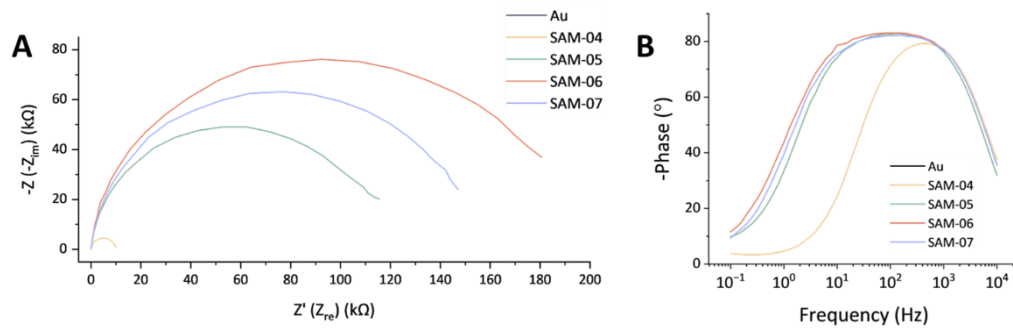
Figure 3.12 EIS measurements obtained for each step of surface characterisation to yield protein functionalised modified electrodes, with CeuE-6His (**SAM-06**) and ArM (**SAM-07**) as outlined in **Scheme 3.6**. Following each measurement, the surface was regenerated and further functionalised to minimise surface degradation effect of the measurements. The measurements were performed in the presence of 10 mM $K_3[Fe(CN)_6]$ in 100 mM phosphate buffer, 233 mM NaCl at pH 7.0. $t_{(equilibration)}$ = 300 s, E_{dc} = 0.230 V, E_{ac} = 10 mV, f = 0.1 Hz − 10 kHz. **A** Nyquist plot representation; **B** Simplified Bode plot representation.

However, a closer examination of the simplified Bode plot enables additional insights into the formation of the immobilisation platform. There is a significant difference, approximately a double increase, in the width of the plot between **SAM-04** and **SAM-05**, corresponding to the nickel chelation step. This observation suggests the cumulative addition of two plots with similar peak maxima, though these correspond to two distinct processes occurring at different frequencies. The implication of this data is that the metal chelation step was only partially successfully, leading to the presence of uncoordinated NTA functionalities on the surfaces and yielding a heterogenous surface, as previously speculated by Balland et al.[233] This highlights the need for caution when analysing data repeats, as the degree of incomplete NTA saturation with the divalent metal cation may vary across different experimental attempts. Consequently, different protein immobilisation patterns can arise with each iteration, illustrating the challenge of obtaining detailed characterisation data.

While EIS characterization can offer a breadth of information about the state of the electrode surface and enable tracking of the functionalisation

steps, it is challenging to utilise it for more in-depth analysis of the immobilized protein. Electrochemical analysis has confirmed the successful immobilisation of CeuE-6His based protein assemblies on the NTA-terminated Au electrodes and revealing a higher immobilisation yield on **SAM-04** compared to **SAM-02**. However, it does not provide the means to evaluate the orientation of the immobilised protein, which is a critical aspect of protein immobilisation to ensure the activity of the immobilised enzyme is preserved and the access to the catalytic site is not limited. The decision to use CeuE-6His as the scaffold for the NTA immobilised ArM was consciously made, as the immobilisation tag is located on the N-terminus, which is situated on the opposite side to the catalytic site. The reversibility of the affinity immobilisation strategy in the presence of imidazole, previously highlighted as advantageous for surface regeneration, can be exploited for assessing protein immobilisation.

QCM-D data was collected for the immobilisation of CeuE-6His on NTA functionalised surface, utilising for strategies for SAM formation explored within this chapter. The Au sensors were chemically polished using Piranha solution, and the **SAM-02** and **SAM-03** surfaces were prepared as outlined in **Scheme 3.2** and **Scheme 3.6**, respectively. The nickel chelation was carried out in situ, followed by immobilisation of the protein. Subsequently, imidazole washes of increasing concentration were performed. The immobilised mass on the sensors was determined by extraction from the raw data using the Sauerbrey equation (**Equation 3.2**); the results are shown in **Figure 3.13**.

$$\Delta m = -C \times \frac{\Delta f}{n}$$

Equation 3.2 The Sauerbrey equation illustrating the linear relationship between the change in resonance frequency (Δf) of a quartz crystal used in QCM measurements and the mass changes (Δm) on the surface. C = the sensitivity constant of the crystal; n = the odd harmonic.

The higher number of available protein binding sites established volumetrically for **SAM-04** in Section **3.2.2**, is validated by the significantly higher immobilisation mass achieved for the sensor in comparison to **SAM-02**. However, the most striking result is the minimal protein loss from the **SAM-02** surface even at a high concentration of imidazole, indicating a high degree of non-specific binding. Due to the limitation of available techniques, determining the exact composition of the terminal functionalities on the functionalised surface is challenging. As a result, the non-specific binding might be a result of multiple factors, however, the most viable explanation is a high level of electrostatic interactions between the surface and the
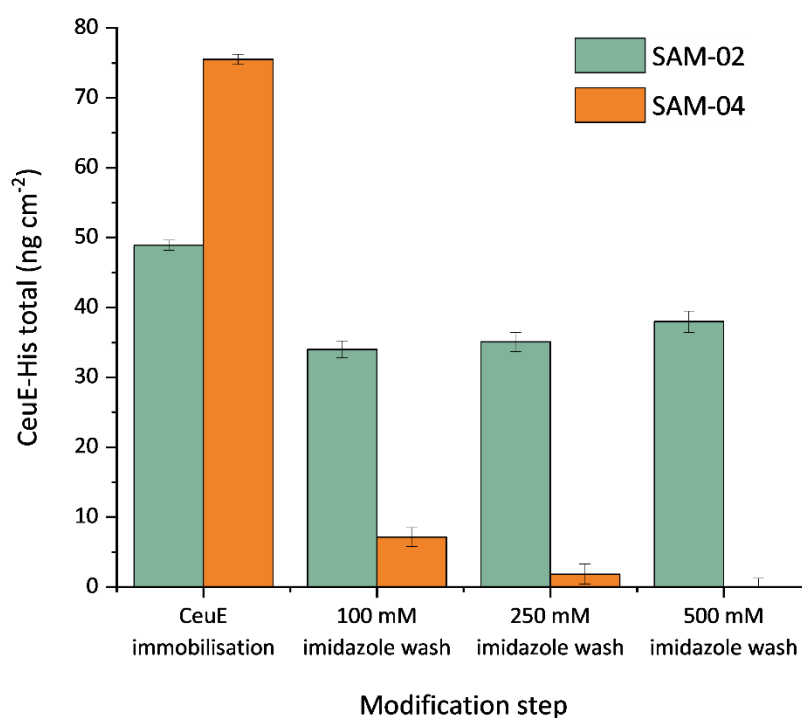
Figure 3.13 The comparison of immobilisation CeuE-6His mass between two NTA functionalised electrodes prepared via different approaches, **SAM-02** and **SAM-04**. The values were extracted from the raw QCM-D data (7th harmonic) and calculated using the Sauerbrey equation. The change in mass during the imidazole wash steps reflects the degree of non-specific adsorption. The nickel chelation step has been performed in situ prior to protein immobilisation. Buffer composition was 100 mM phosphate, 150 mM NaCl at pH 8.0; T = 21°C; flow rate = 70 µL min^{-1}; [protein] = 90 µg mL^{-1}.

protein. In contrast, the majority of the protein was lost from the **SAM-04** surface during the first imidazole wash, and complete removal was achieved at 500 mM. This highlights the potential for the complete regenerate the NTA functionalised surface, offering exciting prospects for recyclability and cascade development on a single platform.

3.3 Summary and conclusions

Achieving specific and site-oriented immobilisation of the Fe-PBP ArM is crucial for enabling substrate access to the catalytic site while ensuring proximity of the redox-active anchor to the electrode surface to facilitate an electrochemical connection between the ArM and the electrode. The strong affinity between the nickel(II) NTA complex and the imidazole rings of a protein polyhistidine tag was effectively utilised for immobilising an ArM comprising a CeuE-6His scaffold on an electrode surface. The Au support was chosen as it offered the highest compatibility with multiple surface characterisation techniques and ease of functionalisation. The incorporation of NTA functionalities onto the electrode surface was achieved by exploiting the high affinity between Au and thiols which results in the formation of SAMs using the corresponding SAM molecules. While the work described within this chapter is not the first example of utilising LA NTA derivatives for the formation of NTA-capped Au electrodes, it represents the first comprehensive investigation comparing two approaches for their assembly, focusing on the availability of protein binding sites obtained through each methodology.

The commonly employed 'on surface' approach comprises the conjugation of an amine derivative of NTA to a Au surface terminated with activated carboxylic acid functionalities (**SAM-01**). EIS was successfully utilised to confirm the successful formation of the SAM of **NGB-10** and subsequent NTA conjugation, as demonstrated by an observed increase in the charge transfer resistance compared to the bare Au surface. However, the data acquired for **SAM-01** revealed the rapid hydrolysis of the NHS ester

functionalities during the measurements conducted under aqueous conditions, thereby highlighting the limitation of the 'on surface' approach. Indirect quantification of the available protein binding sites was performed by voltammetric interrogation of a surface-confined redox probe, **NGB-17**. The results revealed that the surface coverage achieved using this approach was substantially lower than what has been reported in the literature for a direct formation of SAMs utilising LA NTA molecules. Therefore, a synthetic protocol was devised for LA NTA [**NGB-15**], addressing the purification challenges encountered when following the procedure described in the literature. Formation of NTA SAMs using **NGB-15** allowed for achieving higher surface coverage of the available protein binding sites, which is crucial for achieving a high immobilisation yield, validating the use of multistep synthesis over a two-step 'on surface' synthesis.

While EIS offers valuable insights into the extent of surface modification, it is limited in its ability to provide a detailed analysis of the orientation of the immobilised species immobilised on the surface. Thus, QCM-D was employed to investigate each method of surface functionalisation and evaluate the level of non-specific binding achieved, by taking advantage of the reversible interaction between the nickel(II) NTA and the 6His-tag in the presence of imidazole. The results showed a significant distinction between the two NTA-capped electrodes: **SAM-02** constructed using the 'on surface' approach and **SAM-03**, which was formed directly through the SAM formation of **NGB-15**. The mass of CeueE-6His remaining on the surface of **SAM-02** following imidazole wash was comparable to that observed on the control surface, comprising LA SAMs. Contrarily, the loss of all protein was detected on the **SAM-03** Au sensor, confirming that the immobilisation was primarily achieved through the 6His-tag in a homogenous manner with minimal non-specific binding. This outcome is crucial for the development of a biocatalytic immobilisation platform with the highest possible catalytic activity. However, for the successful utilisation of this platform for

electrochemical triggered disassembly, it is also necessary to be able to differentiate between the ArM before and after the SidCat release. Following the previous success of employing EIS for surface characterisation, it was subsequently used to assess the sensitivity of the technique to the presence of SidCat within the protein binding pocket. The acquired Nyquist plots for the ArM and the apo protein successfully showed different levels of charge transfer resistance on each surface.

While EIS has been demonstrated to be an extremely valuable technique for studying the surface changes occurring on the electrode surface, it must be noted that the technique still presents some challenges. Predominantly, in order to mitigate the influence of ferricyanide induced surface destruction on the acquired data, it is necessary to regenerate the surface prior to conducting subsequent measurements. This might present a problem for monitoring dynamic changes of the system, as only single point measurements can be taken with great certainty.

***

Chapter 4 – Exploring the redox-triggered disassembly of an immobilised ArM

To accomplish an electrochemically triggered release of the SidCat conjugate from an ArM immobilised on LA NTA functionalised gold, an electron transfer must occur from the electrode surface to the redox-active iron(III) centre. Limitations associated with the electron tunnelling distance frequently hinder direct electron transfer (DET), thus necessitating the employment of redox mediators. The feasibility of DET between the Au electrode and a redox-active molecule immobilised on the LA NTA surface was evaluated using a well-characterised fast-electron transfer metalloprotein, *Cj*X183. The lack of success prompted the search for a suitable redox mediator, capable of a reversible redox reaction within the potential range of the Fe(III)/(II) reduction exhibited by the iron(III) azotochelin anchor as determined in **Chapter 2**. Bioconjugation of the redox molecule to the protein scaffold was investigated as an approach for enhancing the electron transfer through CeuE, which does not possess inherent electron relay pathways.

Surface characterisation techniques, particularly to achieve the detection of small structural changes such as the presence or absence of a metal cofactor within the protein, present challenges due to intrinsic limits of detection (LOD). The work presented herein predominantly focuses on evaluating different techniques and methods for both direct and indirect characterisation of the ArM by determining either the presence or the absence of the SidCat conjugate. Attempts to overcome the LOD associated with the study of proteins immobilised on a planar surface are discussed, including the design of a new electrochemical cell with an increased surface area for enhancing signal amplitude.

Declaration

The cyclic voltammetry data for *Cj*X183 immobilised on both bare and LA NTA functionalised gold electrodes was acquired by Alice Hewson, a fellow PhD student in the research group who also expressed the protein studied. I conducted the subsequent data plotting, analysis, and fitting personally.

4.1 Introduction

Stimuli-responsive systems present an attractive pathway to attaining precise control over complex architectures, enabling selective changes to be induced. Most prevalent examples include conformational changes or destabilisations of the system leading to their breakdown.[269–273] Redox switches have acquired significant attention among the various investigated triggers, primarily due to the extensive range of structures capable of undergoing redox reactions. From organic supramolecular assemblies to metal coordination complexes, both chemical and electrochemical means have been utilised to trigger redox reactions. Given the redox gradient present in eukaryotic cells, the investigation of redox switches in proteins is an area that has surprisingly received comparatively less attention.[274] While disulfide bonds and cysteines are frequently targeted for intracellular reduction reactions, where their modifications often lead to significant structural and functional changes, their exploitation as artificial triggers has been relatively limited.[275–277] Metalloenzymes, despite comprising redox-active moieties that are crucial to their intrinsic properties, are often overlooked in the field of molecular switches for controlling their functionalities. However, the exploitation of the electron transfer properties for external applications is particularly challenging as within intracellular environments they are frequently integrated within complex electron transfer networks comprising multiple redox proteins and cofactors.[278]

4.1.1 Aims

Following on the successful immobilisation of the Fe-PBP ArM on LA NTA functionalised Au electrodes in a site-specific manner, the feasibility of establishing an electrochemical connection with the iron(III) redox centre must be explored (**Figure 4.1**). Results obtained from the characterisation of functionalised Au electrodes, outlined the previous chapter have demonstrated DET between the Au electrode and a small inorganic redox molecule. However, there is no certainty a comparable outcome will be achieved with a redox metalloprotein. Thus, extensive characterisation is required to confirm whether the application of a reductive potential causes the anticipated structural changes within the ArM. The release of the anchor-catalyst conjugate from the immobilised protein scaffold does not occur on the macromolecular scale and thus multiple approaches may have to be explored to identify a characterisation method with a sufficiently high sensitivity.
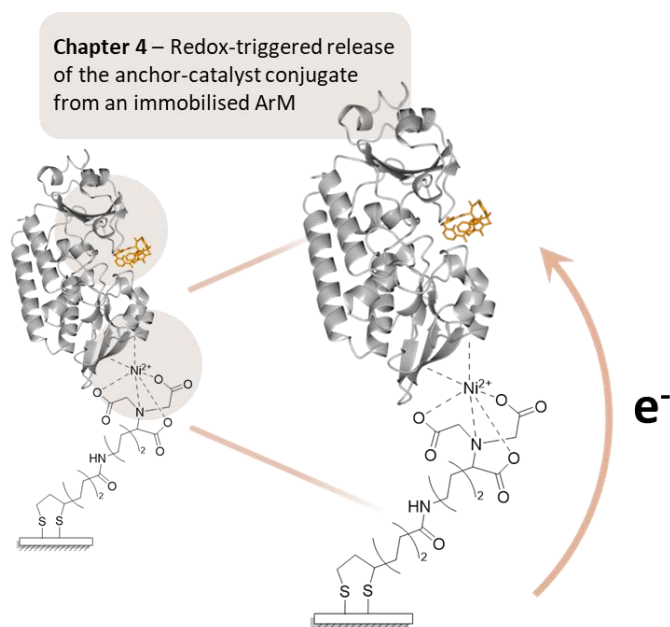
Figure 4.1 A scheme adapted from **Figure 1.13**, illustrating the focus of the work described in **Chapter 4** on investigating the redox-triggered release of the anchor-catalyst conjugate from an immobilised protein scaffold, and how it links the work described in the previous chapters.

The work described within this chapter brings together the results described in **Chapter 2** and **Chapter 3** on redox chemistry of iron(III) azotochelin, and ArM immobilised on NTA functionalised electrodes, respectively. To successfully established whether the methodologies described throughout this thesis yield an ArM recycling platform, several objectives must be met:

- Employment of a 'model' redox-active metalloprotein bearing a 6His-tag for immobilisation on the functionalised Au electrodes and interrogation of the redox-active centre through cyclic voltammetry.

- If successful, the same experimental results must be achieved when the model metalloprotein is substituted with the ArM of interest.

- If DET proves to not be a feasible approach, common redox mediators must be screened for their ability to reduce the iron(III) centre of the ArM. A suitable methodology must be developed to quantify the amount of released iron and thus anchor-catalyst conjugate through this approach.

- Electrochemical investigation of the chosen redox mediator to establish the required potential for the oxidation of the molecule and subsequent reduction of the iron(III) azotochelin anchor.

- Development of an experimental procedure for characterising the structure of the immobilised ArM before and after the application of reductive potential.

4.2 Results and discussion

4.2.1 Investigating the feasibility of DET for redox proteins immobilised on LA NTA functionalised gold electrodes

*Cj*X183 (**Figure 4.2**) is a small *c*-type cytochrome protein comprising a covalently-bound haem prosthetic group, naturally incorporated within Cbp2D, a protein found in *Cellvibrio japonicus*, a saprophytic bacterium.[279] A PFV study on the redox protein adsorbed onto the PGE electrode revealed a reversible one-electron electrochemical response with an $E_{1/2}$ value of 193

mV vs NHE measured at pH 7.0, assigned to the Fe(III)/(II) redox couple.[280] The presence of a reversible voltammogram is indicative of an efficient electron transfer, thus making *Cj*X183 a suitable candidate for assessing the potential of DET for redox proteins immobilised on the prepared LA NTA functionalised electrodes.
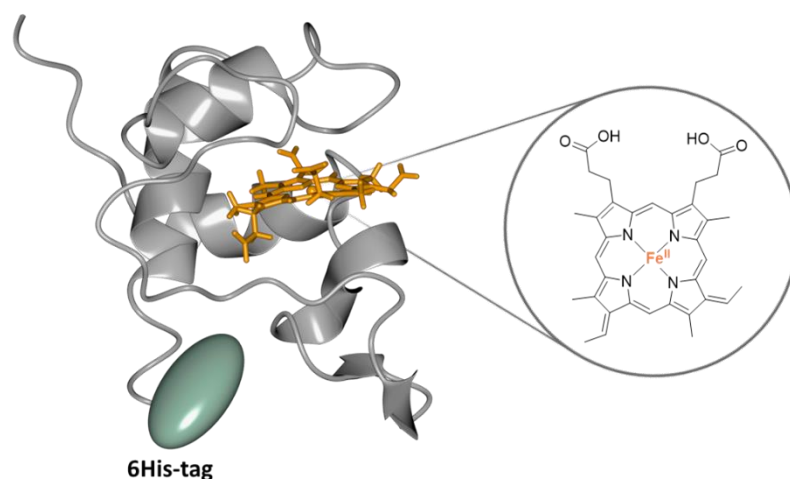
Figure 4.2 Crystal structure of *Cj*X183 (PDB: **7B21**), a *c*-type cytochrome protein (grey ribbon) encompassing a haem cofactor (orange cylinders); the chemical structure of the haem group is shown for clarity.[280] The location of the 6His-tag through which binding to the NTA occurs is highlighted in green.

A parallel PFV data was acquired for *Cj*X183 in buffer conditions analogous to those reported. However, instead of protein adsorption on the surface of a PGE electrode, a polished Au electrode was employed to establish a baseline electrochemical response for the comparison with LA NTA functionalised Au electrodes. The obtained voltammogram (**Figure 4.3 A**) revealed a pair of peaks correlating to the reversible Fe(II)/(III) redox couple within the haem group, which upon manual fitting was shown to exhibit a midpoint potential of −26 mV vs Ag/AgCl 3 M NaCl (+164 mV vs NHE). The peaks were not as well-defined as those reported in the literature which can be attributed to the lower protein adsorption of gold compared to PGE, subsequently resulting in reduced current intensity. Supplementary EIS data was collected to confirm the adsorption of the protein directly onto the electrode surface and allow differentiation from *Cj*X183 immobilised

through the affinity tag in subsequent experiments. Qualitative analysis of the Nyquist plots (**Figure 4.3 B**) before and after the introduction of the protein solution onto the electrode, evidently shows a significantly higher electron transfer resistance for the redox probe illustrated through a larger semicircle diameter and indicative of a successful protein film formation.
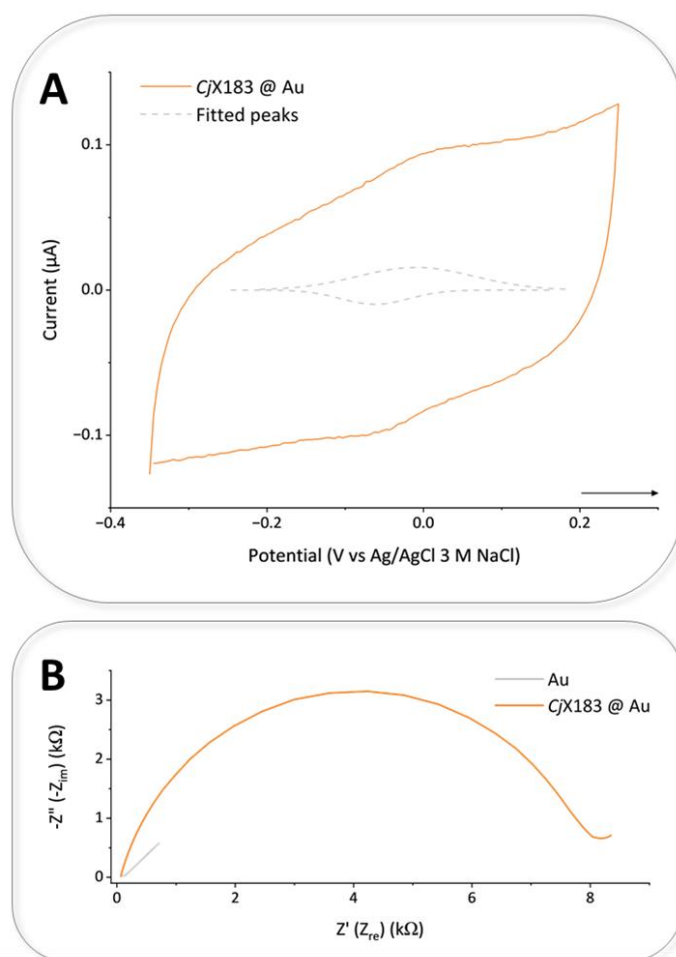
Figure 4.3 A Cyclic voltammogram of *Cj*X183 adsorbed onto a Au working electrode (orange solid line) and the associated potential peaks extracted through manual peak fitting (grey dashed line). The CV was acquired in 50 mM phosphate buffer, 150 mM NaCl at pH 7.0; v = 30 mV s^{-1}. **B** EIS Nyquist plots of a polished Au electrode (grey solid line) and *Cj*X183 adsorbed onto Au working electrode (orange solid line) recorded using 10 mM K$_3$[Fe(CN)$_6$] solution in 100 mM phosphate buffer, 233 mM NaCl at pH 7.0. $t_{(equilibration)}$ = 300 s, E_{dc} = 0.230 V, E_{ac} = 10 mV, f = 0.1 Hz − 10 kHz.

In the subsequent PFV experiment, a cyclic voltammogram of *Cj*X183 immobilised on a LA NTA functionalised Au electrode, prepared as

described in **Section 3.2.3**, was obtained. Unfortunately, no discernible redox peaks were observed under analogous conditions to those employed in the initial PFV study. The acquired data, along with supporting evidence from the literature, has unequivocally demonstrated that the haem group of the *Cj*X183 protein is capable of undergoing efficient and reversible electron transfer. Thus, the inability to detect the peaks associated with the Fe(II)/(III) redox couple can be attributed to the modification of the electrode surface with the LA NTA linkers. To ascertain whether surface functionalisation impeded electron transfer by inhibiting protein binding or increasing the distance for electron transfer beyond the upper limit, surface characterisation EIS experiments were performed. **Figure 4.4** summarises the comparison of the R_{ct} values for the various types of surfaces investigated, which provide a direct and descriptive measure of the degree and the nature of either functionalisation or protein immobilisation.
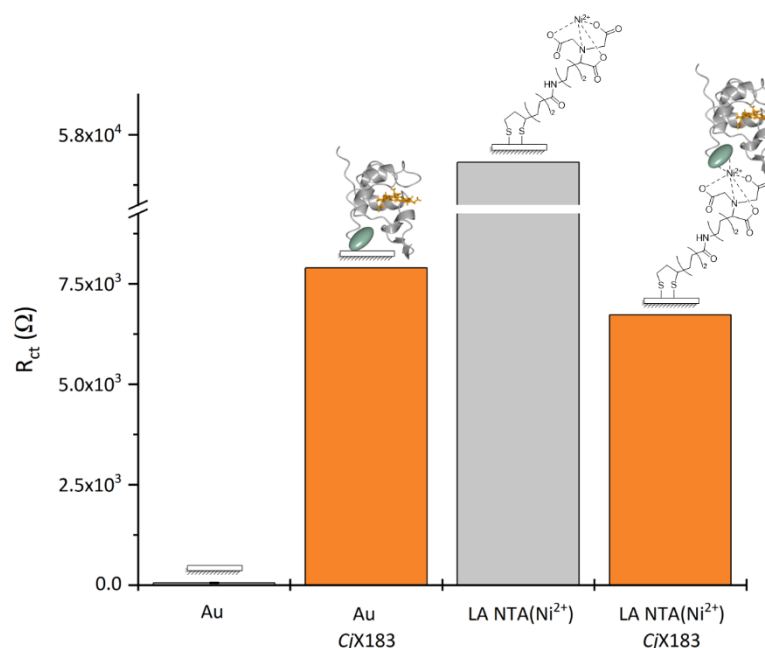
Figure 4.4 A comparison of the charge transfer resistance values (R_{ct}) for the immobilisation of *Cj*X183 on either an untreated gold surface or a LA NTA functionalised electrode. The numbers have been extracted from the circuit fitting of the relevant EIS Nyquist plots. Raw data was acquired in 10 mM $K_3[Fe(CN)_6]$ solution in 100 mM phosphate buffer, 233 mM NaCl at pH 7.0; $t_{(equilibration)}$ = 300 s, E_{dc} = 0.230 V, E_{ac} = 10 mV, f = 0.1 Hz – 10 kHz.

Initial analysis of **Figure 4.4** does not provide an obvious conclusion, as the charge transfer resistance observed upon the immobilisation of CjX183 on LA NTA(Ni^{2+}) functionalised electrode is significantly lower than the one for the modified surface prior to protein immobilisation. It could thus be questioned whether successful functionalisation of the electrode and protein immobilisation was achieved, however, the phase angle values of 78.7 ± 4.1° measured for both data sets, LA NTA(Ni^{2+}) and LA NTA(Ni^{2+}) CjX183, are indicative of a nearly well-packed monolayer. From the similarity of the R_{ct} values obtained for protein experiments on both unfunctionalised and functionalised surfaces, it could be postulated that for the latter CjX183 has directly immobilised onto the gold despite the presence of SAM. The absence of redox peaks and the characteristic large non-Faradic current observed for protein films in the voltammogram of CjX183 on LA NTA(Ni^{2+}) modified gold electrode excludes such a possibility. Thus, despite the unexpected decrease in the charge transfer value upon immobilisation of the cytochrome onto the functionalised surface, it can be inferred that the binding event was successful.

One plausible hypothesis may be that the measured charge transfer value reflects the electron transfer occurring between the $[Fe(CN)_6]^{3-}$ redox probe and the haem group within the cytochrome which is not affected by the presence of the LA NTA modification. The similarity between the R_{ct} values observed for the cytochrome immobilised directly on gold and the one bound to the modified electrode further supports the above theory. Consequently, the inability to detect the redox activity of the haem group can be attributed to the extended distance between the redox centre and the electrode surface caused by the formation of a self-assembled monolayer (SAM), surpassing the permissible limit for efficient electron transfer.

The difference in molecular weights between the CjX183 protein and CeuE, the ArM scaffold, 11.4 kDa and 35.2 kDa, respectively, illustrates a

substantial size difference. Subsequently, it can be reasonably inferred that the immobilised ArM will not be capable of undergoing efficient direct electron transfer in a similar manner, as the distance between its redox centre and the electrode is even greater. Thus, to facilitate electron transfer, the employment of a suitable redox mediator will be necessary.

As discussed in **Section 4.1**, for a small molecule to be capable of reducing the iron(III) azotochelin anchor, it must exhibit redox potential more negative than that of the Fe(III)/(II) couple, −660 mV vs Ag/AgCl 3 M NaCl (−470 mV vs NHE). The redox irreversibility of $Na_2S_2O_4$, the reducing agent employed in the original literature report precludes it from utilisation as a redox mediator, necessitating a search for an alternative. Among the reported classes of biochemically-relevant reversible redox mediators, viologen and its derivatives stand out as the sole family of compounds which possess adequately negative redox potentials.[281] Further modulation of the reduction potential can be achieved through functionalisation of the viologen core motif; more extensive *N*-alkylation gives rise to more negative $E_{1/2}$ values.[282–284] Consequently, an electrochemical investigation was performed with two symmetrical viologen molecules to ascertain their redox potentials relative to sodium dithionite. Solution CVs (**Figure 4.5**) were acquired in 100 mM MES, 500 mM NaCl buffer at pH 6.0. The electrochemical studies outlined in **Section 2.2.4** demonstrated a notably more positive reduction potential (−370 mV vs Ag/AgCl 3 M NaCl) for the iron(III) azotochelin anchor at such pH levels, indicating an easier reduction process, while maintaining the necessary $M_1:L_1$ stoichiometry for protein binding.

The electrochemical reversibility exhibited by the viologen derivatives, as indicated by the presence of both cathodic and anodic peaks with a ΔE of 70 mV, makes those compounds more suitable redox mediators than sodium dithionite. Despite the literature precedence on the extent of *N*-alkylation on the reduction potential values, both MV and EV exhibit an

identical $E_{1/2}$ value of −675 mV vs Ag/AgCl 3 M NaCl (−485 mV vs NHE), nonetheless, it exceeds the redox requirement for the reduction of iron(III) azotochelin. However, the increased current observed for EV compared to MV is indicative of a more efficient electron transfer with the Au electrode, thereby suggesting its better suitability as a redox mediator for electrochemically triggered ArM disassembly.
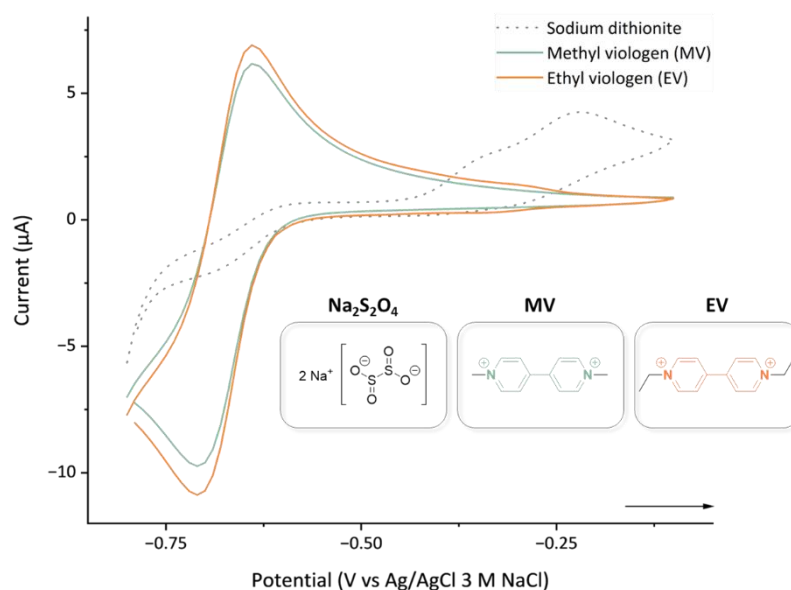
Figure 4.5 Cyclic voltammograms illustrating the difference in the reducing power of two viologen derivatives, methyl viologen (green solid line) and ethyl viologen (orange solid line) relative to sodium dithionite (grey dotted line). Measurements were acquired in 100 mM MES, 500 mM NaCl buffer, pH 6.0; [reducing agent] = 1.0 mM; v = 50 mV s^{-1}. The inset shows the structure of all the reducing agents investigated.

In order to validate the utilisation of ethyl viologen for the reduction of iron(III) azotochelin, especially in complexation with the protein scaffold, its reducing capacity was assessed through a ferrozine assay. Ferrozine is a bidentate ligand capable of forming a stable complex with iron(II) which exhibits a characteristic λ_{max} value of 562 nm.[285] Addition of the chelator to a reduced sample containing iron azotochelin, sequesters the iron(II) preventing its reoxidation and subsequently inhibiting the reformation of the anchor. The well-established Beer-Lambert Law, described the relationship between absorbance and analyte concentration, thus allowing the

quantification of each redox mediator. Both viologen derivatives, alongside sodium dithionite, were examined for the reduction of the isolated anchor (Sid), the anchor-catalyst conjugate (SidCat), and each one in complex with the protein scaffold, P-Sid and ArM, respectively. The apo protein has been employed as a negative control. In addition to CeuE, Gst, was examined as an alternative protein scaffold to investigate its effect on the ease with
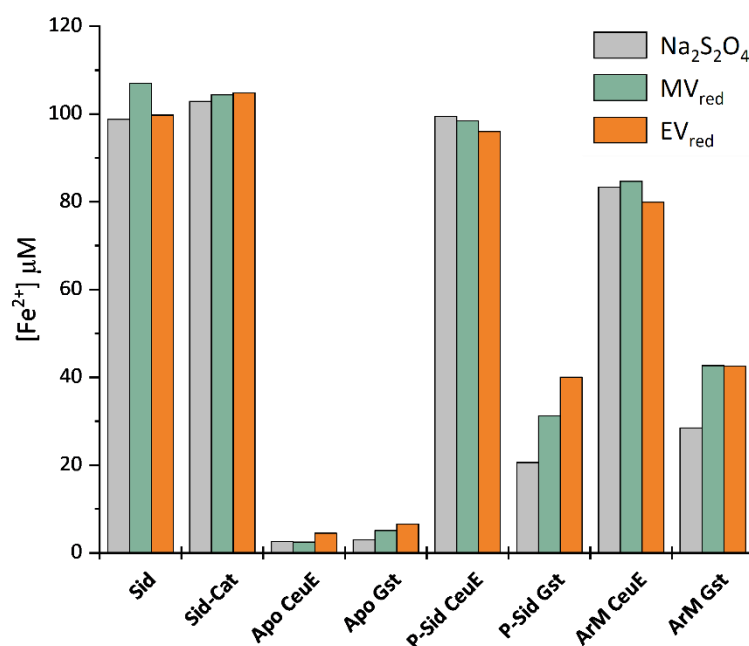
Figure 4.6 A plot of iron(II) concentration released from a series of samples containing the iron(III) azotochelin motif, as a result of iron(III) reduction by three reducing agents, sodium dithionite (grey), methyl viologen (green) and ethyl viologen (orange). The apo samples have been employed as negative controls as they do not contain iron(III) azotochelin. The iron(II) concentration has been measured from the absorbance at 562 nm, characteristic of the iron(II) ferrozine complex utilised in the assay as the indicator. Redox reaction was performed in 100 mM, 500 mM NaCl buffer at pH 6.0; [reducing agent] = 40-fold excess; [ferrozine] = 4-fold excess. Iron(II) concentration has been calculated using the linear regression equation obtained from a calibration curve. Sid, iron(III) azotochelin; SidCat, iron(III) azotochelin catalyst conjugate; apo, protein without a cofactor present; P-Sid, iron(III) azotochelin in complex with the protein scaffold; ArM, iron(III) azotochelin catalyst conjugate in complex with the protein scaffold. Even though it was not reflected in the sample nomenclature, all protein scaffolds employed comprised an N-terminal 6His-tag.

which the SidCat is released upon iron(III) reduction. Gst is a thermophilic homologue of CeuE found in *Geobacillus stearothermophilus,* currently investigated in the Duhme-Klair research group for improving the catalytic performance of the ArM.[286,287] The results of the ferrozine assay are summarised in **Figure 4.6**, which depicts the dependence of the reduced iron concentration for each sample on the reducing agent employed.

Successful reduction of iron(III) in solution was achieved for all investigated samples with both viologen derivatives demonstrating a comparable reducing power to sodium dithionite. Isolated Sid and SidCat complexes achieved nearly 100% reduction yield, with the redox reaction yield decreasing as anticipated upon binding of the two complexes to the proteins due to anchor stabilisation within the protein binding pocket due to tyrosine coordination. Notably, the protein complexes of Sid and SidCat with the Gst scaffold exhibited increased difficulty in anchor reduction as evidenced by the considerably lower iron(II) concentrations observed across all reducing agents. This could be partly attributed to the smaller K_d values observed for Gst complexes, corresponding to stronger cofactor binding, relative to those formed with the CeuE scaffold (**Table 4.1**).[286] Alternatively, the narrower opening of the binding pocket in Gst as shown by its crystal structure may limit the accessibility of the reducing agents, hindering the necessary proximity for efficient electron transfer to occur.[287] Nonetheless, the data obtained from the reduction assay confirms the suitability of EV as a potential redox mediator in its reduced form (EV$_{red}$) whose formation can be triggered through either electrochemical or chemical methods.

Table 4.1 Dissociation constant (K_d) values measured by Dr A. Miller for different protein complexes comprising the iron(III) azotochelin motif. Additionally, the concentration of reduced iron using ethyl viologen as the reducing agent is shown for each complex.

Protein scaffold	Cofactor	K_d / nM[286]	Reduced [Fe] / µM
CeuE	Sid	4.9 ± 0.7	96.0
	SidCat (ArM)	23.4 ± 3.2	79.9
Gst	Sid	3.5 ± 0.7	40.0
	SidCat (ArM)	9.9 ± 0.9	42.5

4.2.2 Direct detection of SidCat release from the Fe-PBP ArM

Direct electrochemical interrogation of immobilised redox proteins is the default technique of choice for studying the effect of changes in the oxidation of states occurring within the metalloprotein. In instances when it is not possible, alternative techniques can be employed. However, these predominantly focus on detecting global changes to the protein structure and may overlook more subtle changes. As the loss of the SidCat cofactor from the protein scaffold is only associated with a change of 1.06 kDa versus 34.2 kDa of CeuE-6His it was of concern that the dynamic reduction process would not be detectable.

Building on the successful utilisation of QCM-D for observing the dynamic binding and release events for P-Sid(CeuE-6His) on LA NTA functionalised Au sensors, further investigation was performed to determine its suitability for detecting and monitoring the release of the SidCat from an immobilised protein scaffold. An acidic Piranha solution was employed to polish the Au sensors, prior to their functionalisation with the **NGB-14** linker, parallel to the protocol utilised for the modification of Au electrodes. The chelation of nickel to the immobilised NTA groups was conducted in situ to prepare the surface for protein binding. The successful formation of NTA(Ni^{2+}) complexes was confirmed through the decrease in surface dissipation with an average of 0.33 ± 0.01 x10^{-6} ppm, attributed to the increased surface rigidity upon chelation of the carboxylic acids to the metal centre in a

defined coordination geometry. Following the immobilisation of both ArM and CeuE(6His), with the latter employed as a negative control, the sensors were exposed to an increasing gradient of $Na_2S_2O_4$, incorporating buffer washes between each gradient step (**Figure 4.7**). Sodium dithionite was chosen for this experiment due to the simplicity associated with its employment, as it does not require an initial reduction step to trigger the disassembly of the ArM.
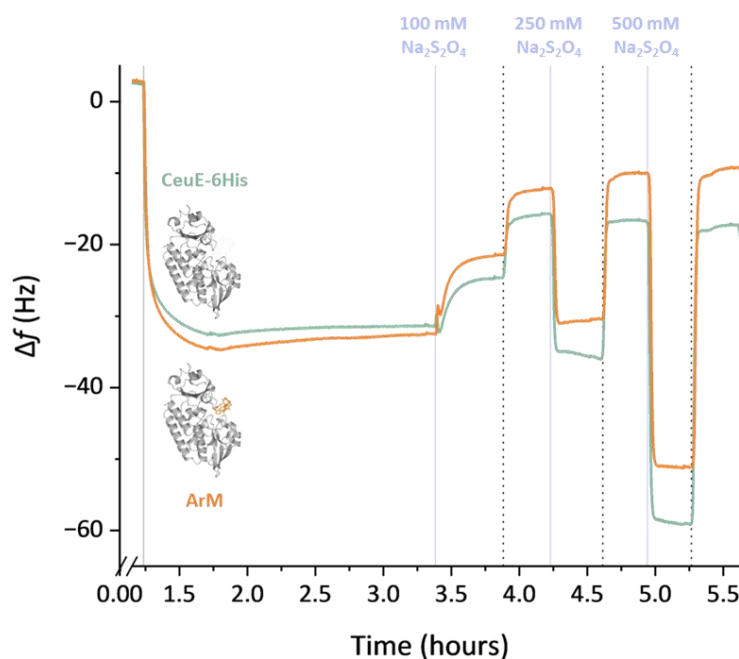
Figure 4.7 Plot of frequency changes (7th harmonic) as a function of time and the composition of the flowing solution over LA NTA functionalised Au sensors obtained during QCM-D experiments. The nickel chelation step has been performed prior to protein immobilisation; however, it has been omitted for clarity. Buffer composition was 100 mM phosphate, 150 mM NaCl at pH 8.0; T = 21°C; flow rate = 70 µL min^{-1}; [protein] = 90 µg mL^{-1}. The stamp points of each step are indicated with vertical lines, buffer was carried out between each reagent (grey dotted line) to equilibrate the surface.

Upon immobilization of the protein samples, as anticipated, a substantial negative shift in Δf was observed, indicating the immobilisation of mass onto the sensor surface. The shift displayed a noteworthy disparity between the CeuE-6His and the ArM, enabling differentiation of the mass change associated with the presence of the SidCat. Unfortunately, both surfaces

(apo CeuE and ArM) displayed a similar pattern of frequency changes upon exposure to the reducing agent, although to varying extents, indicating that these changes were unrelated to the presence of SidCat. Previous studies have shown the structural integrity of the protein scaffold remains unaffected in the presence of $Na_2S_2O_4$ and thus the control sensor, which lacks the SidCat conjugate, should not have exhibited a change in frequency correlating to a reduced immobilised mass. As described in **Chapter 3**, frequency and mass changes exhibit a linear relationship as described by the Sauerbrey equation which allows to surmise that the Δf of 25.1 correlates to a mass change of 63.4 ng cm^{-2}, a disproportionately large value to correspond to the loss of a 1.06 kDa molecule for each immobilised protein. A more plausible hypothesis would attribute the observed mass change to the removal of the ArMs from the surface, as a result of perturbation to the affinity binding between the 6His-tags and NTA(Ni^{2+}) groups. However, parallel studies performed in the Duhme-Klair research group on anchor release from ArMs immobilised on commercial supports, have failed to provide evidence for nickel(II) reduction by $Na_2S_2O_4$, which would have led to the loss of protein from the surface.

The oscillations experienced by the sensor are known to be particularly sensitive to solution changes, including fluctuations in pH and viscosity, which occur upon the dissolution of $Na_2S_2O_4$. Thus, control QCM-D experiments were performed to investigate the effect of the reducing agent concentration on the extent of the frequency shift for both CeuE-6His and ArM surfaces. In combination with the above study, sodium dithionite in concentrations of 50 mM, 100 mM and 1 M were explored. The difference in the change of frequency prior to protein immobilisation and following a buffer was calculated and plotted in **Figure 4.8**. At first glance, a pseudo-linear relationship can be assumed for the relationship between the mass lost from the surface and the concentration of the reducing agents. However, the large and overlapping standard deviation values, particularly at higher $Na_2S_2O_4$ concentrations, present a challenge for drawing definitive

conclusions. The observed frequency changes for both ArM and CeuE-6His comprising experiments, allow to speculate the existence of surface processes occurring in addition to the disassembly within the timescale of the experiments, which obscures the detection of SidCat release.

It would be of interest to explore whether the observed phenomenon is specific to $Na_2S_2O_4$ or if it can be circumvented by employing an alternative reducing agent, such as ethyl viologen. However, the need for an initial reduction step on viologen derivatives poses a challenge when one wants to avoid the addition of an extra chemical reducing agent. Although an application of a reducing electrochemical potential can be employed for the same effect, the unavailability of the electrochemistry module precluded this study from being carried out. Performing a control study in the presence of a non-reduced ethyl viologen would have provided valuable insights, into evaluating whether the frequency remains stable in its presence when no redox processes should be occurring. However, the limited access to the instrument has served as a motivation to explore an alternative technique.

EIS has proven to be a valuable approach for characterising the immobilisation of proteins on LA NTA functionalised gold electrodes, demonstrating the ability to distinguish between the CeuE-6His and the ArM based distinct charge transfer resistance values, as described in **Section 3.2.3**. Those measurements were obtained as discrete data points, with each modification step being studied on a separate electrode. Thus, before assessing the capability of EIS for detecting SidCat release and subsequently ArM disassembly, it was investigated whether it could be employed for monitoring dynamic changes occurring on the surface. To complement the successful QCM-D study to monitor the imidazole-triggered release of CeuE-6His from the LA NTA functionalised surface, an attempt was made to replicate the results using EIS.
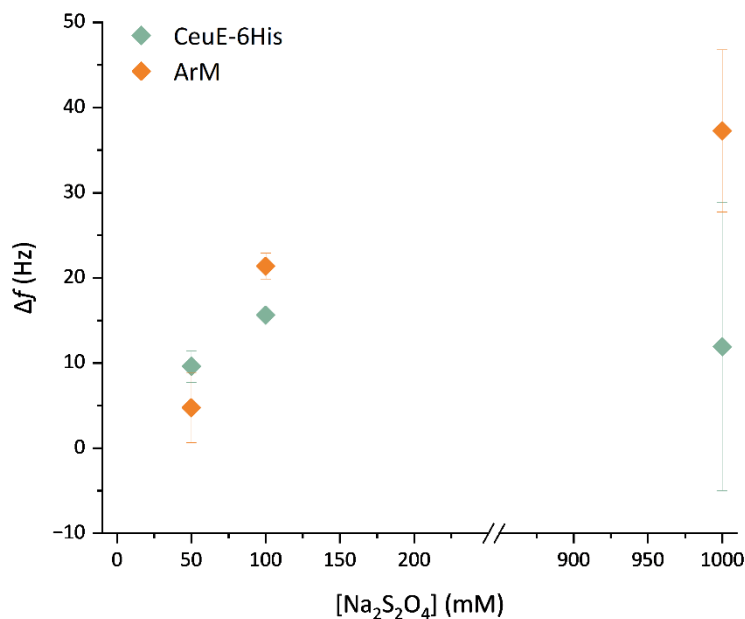
Figure 4.8 A plot illustrating the variations in the frequency change prior to and following the addition of a reducing agent, as a function of sodium dithionite concentration. values were extracted from QCM-D experiments performed in a parallel manner to those represented in **Figure 4.7**. The data has been collected for surfaces where either the apo CeuE-6His, anticipated to act as a negative control, or ArM samples were immobilised of LA NTA functionalised Au sensor, with nickel chelation performed in situ, prior to protein immobilisation.

The preparation of the LA NTA(Ni^{2+}) electrodes was performed as per the approach employed in the EIS studies reported in **Chapter 3**. Following the immobilisation of CeuE-6His, the modified electrode was characterised with EIS, washed with an excess of buffer and immediately incubated in an imidazole (imd) solution, prior to taking a final EIS measurement. The acquired data, represented as Nyquist and Bode plots are shown in **Figure 4.9**.

As outlined in **Chapter 3** high concentrations of imidazole are capable of displacing the 6His-tag within the coordination sphere of nickel(II), resulting in the loss of protein from the surface.[217] The charge transfer values, represented by the diameter of the semicircle in the Nyquist plots (**Figure 4.9 A**), provide valuable insight into such process as they report on the

extent of surface modification. Upon the loss of molecules from the surface, the R_{ct} value is expected to reduce as a thinner layer exhibits a smaller resistance towards electron transfer between the electrode and the redox-active probe in the solution. Thus, the significant shift in the size of the Nyquist plots observed after incubation of the electrode in the imidazole solution is consistent with the release of the protein from the surface. Examination of the simplified Bode plots before and after incubation with imidazole (**Figure 4.9 B**) confirms that the integrity of the surface was preserved as the phase angle was relatively unaffected, remaining at the experimentally achieved maximum value of 80.4 ± 0.1°, indicating a well-packed monolayer remaining on the surface. However, the R_{ct} value of 20.8 kΩ for the electrode surface exposed to the imidazole solution is not directly comparable to the 56.79 kΩ value obtained for a LA NTA(Ni^{2+}) during the characterisation study reported in **Section 3.2.3**. As both measurements are assumed to be conducted on surfaces with identical modifications, they should ideally yield identical results within experimental error. The discrepancy in the R_{ct} values does not necessarily imply that the imidazole release was unsuccessful but rather reflects inherent issues associated with the study of SAM functionalised electrodes using EIS, detailed further at the end of this section.
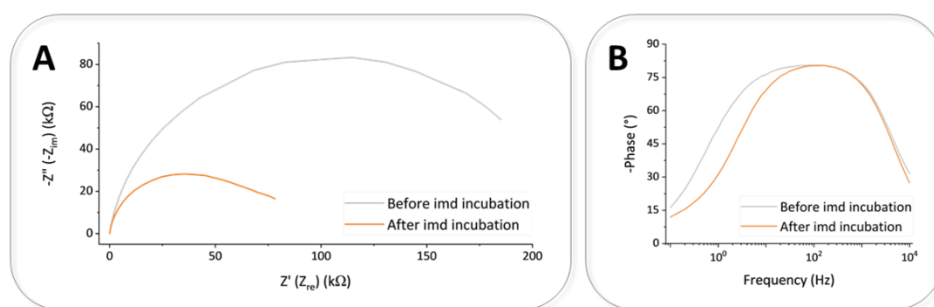
Figure 4.9 EIS data obtained for an electrode functionalised with LA NTA(Ni^{2+}) SAMs and immobilised CeuE-6His. The measurements were taken on an assembled electrode (grey solid line) and after incubation in a 500 mM imidazole (imd) solution in 100 mM phosphate, 150 mM NaCl (pH 8.0) for 60 seconds (orange solid line). Data was acquired in 10 mM $K_3[Fe(CN)_6]$ solution in 100 mM phosphate buffer, 233 mM NaCl at pH 7.0; $t_{(equilibration)}$ = 300 s, E_{dc} = 0.230 V, E_{ac} = 10 mV, f = 0.1 Hz − 10 kHz. **A** Nyquist plot data representation; **B** Bode plot data representation.

The previous results obtained for the characterisation of the functionalised Au electrode, as presented in **Chapter 3**, have provided valuable insight into the expected changes in the Nyquist plots upon the disassembly of the ArM. The release of the SidCat is anticipated to lead to a decrease in the charge transfer resistance value, which would be reflected in a smaller diameter of the semicircle. While accurate quantitative analysis may not be possible, qualitative comparison should still allow to evaluate the feasibility of using EIS for studying the release of SidCat. Thus, a Au electrode was functionalised with LA NTA SAM molecules, and following the chelation of nickel, the Fe-PBP ArM was immobilised on the surface. Subsequently, the electrode was immersed in a solution of $Na_2S_2O_4$ to trigger the disassembly of the ArM and following a wash with excess buffer, immersed in a solution of SidCat to initiate the reassembly of the ArM. EIS characterisation was performed at each step, and the obtained Nyquist plots are shown in **Figure 4.10 A**. The reduction step resulted in a significant decrease in the size of the Nyquist plot, indicating a substantial decrease in charge transfer resistance. However, the extent of the shift was far more substantial than anticipated in the characterisation studies and more resembles the change associated with the loss of protein from the surfaces as observed in **Figure 4.9**. Therefore, it was not unexpected that after immersing the electrode in the solution of SidCat which was intended to induce the reassembly of the ArM and revert the Nyquist plot to its pre-reduction shape, a further decrease in the semicircle size was observed.

To elucidate whether the obtained results obtained were specifically attributed to the presence of the chemical species, a control experiment was performed. The Fe-PBP ArM was immobilised on a freshly functionalised Au electrode and was subjected to the same treatment as before, with the exception that the buffer solutions did not contain the reducing agent nor the SidCat. As in the previous experiment, the electrode was characterised using EIS after each immersion in the buffer solutions (**Figure 4.10 B**). A similar pattern to the one observed in **Figure 4.10 A** was

recorded, with a decrease in the size of the semicircle size decreasing following each step. The presence of changes in the Nyquist plots, regardless of whether the intended chemical species were present, highlights one of the major challenges encountered when using EIS to monitor dynamic changes on the electrode surface.
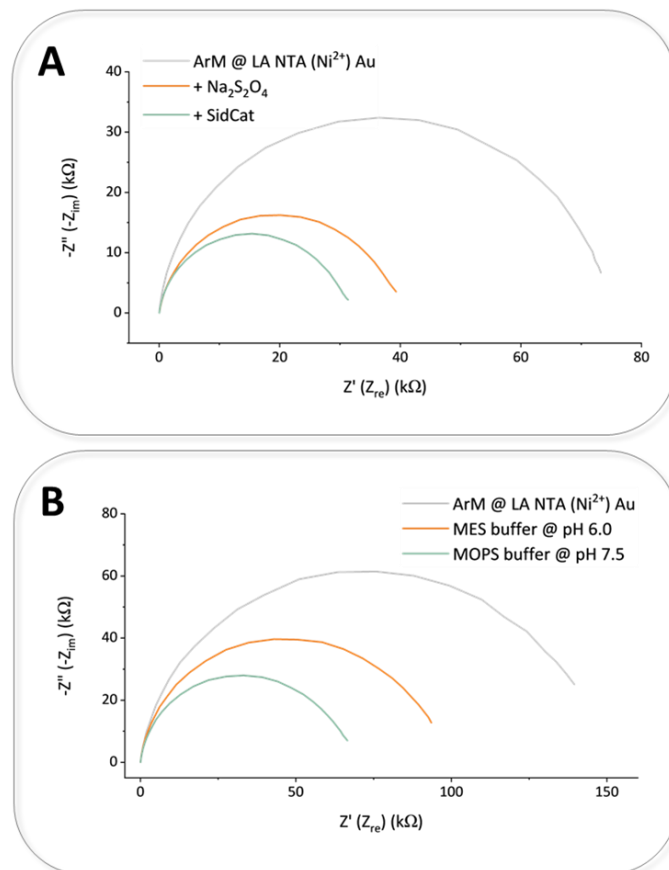
Figure 4.10 EIS Nyquist plots for an electrode functionalised with LA NTA(Ni^{2+}) SAMs and immobilised ArM monitoring the reversible disassembly of the ArM. **A** The electrode was exposed to a solution of a reducing agent, $Na_2S_2O_4$, followed by a solution of SidCat; **B** The electrode was immersed in a 100 mM MES, 500 mM NaCl buffer (pH 6.0), followed by 200 mM MOPS, 150 mM NaCl buffer (pH 7.5). Data was acquired in 10 mM $K_3[Fe(CN)_6]$ solution in 100 mM phosphate buffer, 233 mM NaCl at pH 7.0; $t_{(equilibration)}$ = 300 s, E_{dc} = 0.230 V, E_{ac} = 10 mV, f = 0.1 Hz – 10 kHz.

It is believed that exposure of SAMs to different solution compositions, including variations in pH levels, can induce changes that affect the resistance of electron transfer between the electrode and the $[Fe(CN)_6]^{3-}$ redox probe, without affecting the structural integrity of the monolayer.

Unfortunately, no suitable techniques were available to directly interrogate the structure of the surface and confirm the specific changes associated with the observed EIS drifts under identical experimental conditions.

Work performed within the Parkin research group by myself and other researchers has highlighted the sensitivity of EIS to even minor variations within the monolayer. These are frequently not structural, yet lead to significant differences in the acquired data, manifesting as high amplitude signal variations. The phenomenon of EIS signal drifts has been documented in isolated literature reports, although not as extensively as may be expected.[265] Those findings preclude the use of EIS as a quantitative technique, as demonstrated above by the discrepancies in R_{ct} values between the two surfaces that were expected to exhibit identical functionalisation. The fluctuations observed in acquired EIS data can be attributed to several factors, including the adverse interaction between $[Fe(CN)_6]^{3-}$ and the gold electrode surface resulting in decreased stability of the SAM over time (**Figure 4.11**).[263,264] Dynamic reorganisation and redistribution of the monolayer which gives rise to pinholes and defects, facilitating electron transfer has also been shown to contribute to EIS drifts.[288] The latter can occur in response to changes in potential, leading to charge redistribution, or changes to solution composition, as demonstrated by the control experiment performed in the ArM reduction study (**Figure 4.10 B**).

Several attempts have been made to stabilise the signal and enhance the reproducibility of the acquired data. Ruthenium(III) hexammine chloride, $[Ru(NH_3)_6]Cl_3$ has been investigated as an alternative redox probe in solution, due to its reported non-adverse interaction with gold in the literature.[262,289,290] However, low amplitude signals were observed, posing a challenge in distinguishing between different modification steps, which could be attributed to the differences in complex charges and electron transfer mechanism exhibited by the two probes. Some progress has been

made towards achieving more stable results through a combination of buffer composition changes and pre-treatment strategies to stabilise the monolayer prior to protein immobilisation.[263,291] However, the obtained results have not been fully supportive of the success for those approaches to support their utilisation for this project. The limited timeframe of this project has thus required to search for alternative methods, not relying on the direct characterisation of the immobilised molecule for detecting the release of the SidCat conjugate from the protein scaffold.
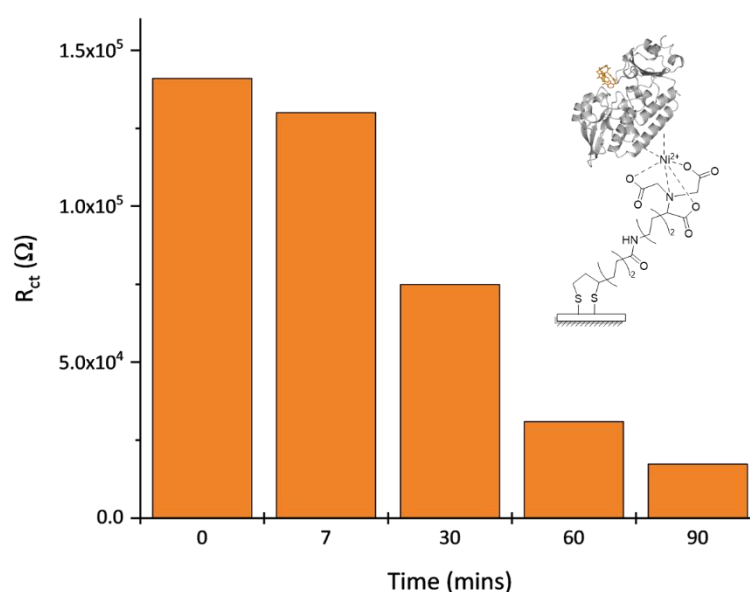
Figure 4.11 A plot of R_{ct} values as a function of time for an electrode functionalised with LA NTA(Ni^{2+}) SAMs and immobilised ArM. The R_{ct} values were extracted from EIS Nyquist plots following a circuit fitting. Raw data was acquired in 10 mM $K_3[Fe(CN)_6]$ the solution in 100 mM phosphate buffer, 233 mM NaCl at pH 7.0; $t_{(equilibration)}$ = 300 s, E_{dc} = 0.230 V, E_{ac} = 10 mV, f = 0.1 Hz − 10 kHz.

4.2.3 Indirect detection of SidCat release from the Fe-PBP ArM

The measurement of catalytic performance is an effective tool for assessing the activity of an immobilised enzyme, as long as the catalytic response is above the limit of detection (LOD) for the chosen detection technique. The notable difference in the enantioselectivity of the imine reduction reaction between the ArM and isolated SidCat, 35.4 ± 0.1% ee

versus < 3% *ee* respectively, provides a reliable metric for distinguishing between the assembled and disassembled states of the ArM.[54] However, the determination of the reaction enantioselectivity requires the employment of high-performance liquid chromatography (HPLC), which does not facilitate a streamlined monitoring process. The catalytic rate of the imine reduction can serve as another distinguishing parameter between the ArM and the SidCat, with the isolated catalyst exhibiting much faster reaction kinetics as demonstrated by a TOF value of 6.0 ± 0.3 min^{-1} in comparison to the ArM, which was shown to have a TOF of 0.30 ± 0.01 min^{-1}.[54] If either the substrate or product exhibits favourable fluorescence or absorbance, the determination of the catalytic conversion yield over time, and consequently the reaction rate, can be easily performed in situ.

To verify the feasibility of using the catalytic rate for distinguishing the ArM before and after disassembly, a control experiment was conducted under the conditions relevant for ArM immobilisation. However, due to the already low catalytic rate of the Fe-PBB ArM and the commonly encountered reduced rate upon enzyme immobilisation, it was of concern that the conversion rate would be below the LOD. Previous QCM (**Section 3.2.3**) and EIS (**Section 4.2.2**) experiments have demonstrated the efficiency of imidazole stripping as a reliable method for releasing the protein from the surface with a quantitative yield. The ability to recover the immobilised ArM from the NTA surface introduces new possibilities for protein characterisation, particularly as sample concentration can be easily increased for proteins in solution.

Unfortunately, the commonly used substrate for assessing the catalytic activity of ATHases, 6,7-dimethoxy-1-methyl-3,4-dihydroisoquinoline (**Figure 4.12**) is not suitable for either fluorescence or absorbance measurements. Similarly, the reaction product, salsolidine does not exhibit the necessary physical properties. However, harmaline (**Figure 4.12**) a naturally occurring alkaloid containing an imine functionality, can serve as

a viable alternative for the reaction substrate. The imine has been demonstrated to exhibit suitably high fluorescence, with an excitation wavelength of 380 nm and emission wavelength of 486 nm in the catalytic buffer, 0.6 M MES and 3 M sodium formate at pH 7.0.[286]
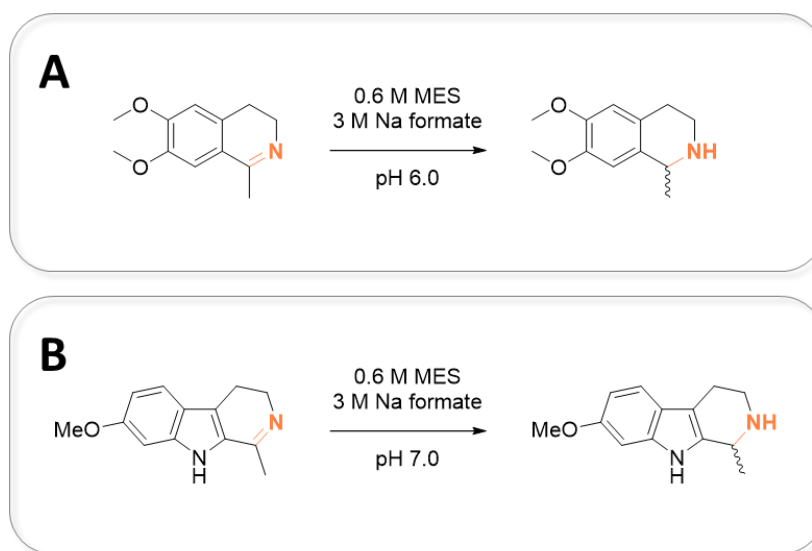
Figure 4.12 Reaction schemes for the imine reduction catalysed by ATHase ArM. **A** Conversion of 6,7-dimethoxy-1-methyl-3,4-dihydroisoquinoline to the corresponding secondary amine product, however, neither are suitable for fluorescence measurements in situ; **B** Conversion of harmaline to the corresponding secondary amine product, suitable for fluorescence measurements in situ.

Prior to commencing the experiment, a calibration plot was constructed by measuring the fluorescence of harmaline as a function of concentration (11 μm to 100 μm) using an automated plate reader. Regrettably, it was not possible to obtain a linear relationship within the concentration range of interest which was attributed to the phenomenon known as the inner filter effect.[292] This frequently occurring problem in fluorescence spectroscopy is associated with the substrate possessing a chromophore absorbing at the wavelength equivalent to the excitation wavelength resulting in the absorption of the excitation energy. Efforts are underway to develop methods for the correction of the fluorescence response; however, the presence of a chromophore within the molecule offers an alternative detection method. The calibration curve constructed from the absorbance

measurements successfully exhibited a linear relationship within the concentration range from 10 µm to 276 µm with an R^2 value of 0.998.

Following multiple iterations of condition optimisations, an absorbance assay was performed for the imine reduction of harmaline. The catalyst activity was measured as the function of decreasing substrate concentration in 0.6 M MES, 3 M sodium formate buffer, pH 7.0 at 25°C. The reactions were performed with 0.25% catalytic loading for both SidCat and the ArM; parallel negative controls were prepared where no catalyst was added. The absorbance was measured at 405 nm every 15 minutes for 73 cycles and the substrate concentration was subsequently calculated from the linear calibration equation and plotted as a function of time in **Figure 4.13**. As anticipated, the reaction rate recorded for the SidCat was much higher compared to that observed for the ArM, evident from the steeper gradient in the kinetic profile.[54] However, the rate catalyst exhibited by the ArM at a catalyst concentration of 0.92 µM was unexpectedly slow to the extent that it remained undetectable within the timescale of the experiment. This issue would be readily resolved by employing a higher concentration of the ArM. However, calculations based on the theoretical maximum concentration that can be release from the surface of an electrode indicate a maximum value of 0.013 µM. Consequently, this implies an alternative detection method needs to be developed or an electrode with a larger surface area is required. If the latter approach is employed and the concentration parallel to the tested was attained following ArM release from the surface, the successful determination of ArM disassembly would be indicated by the lack of a catalytic turnover. As the absence of a signal can be attributed to multiple factors it does not represent the most accurate way of determining the success of the SidCat release.
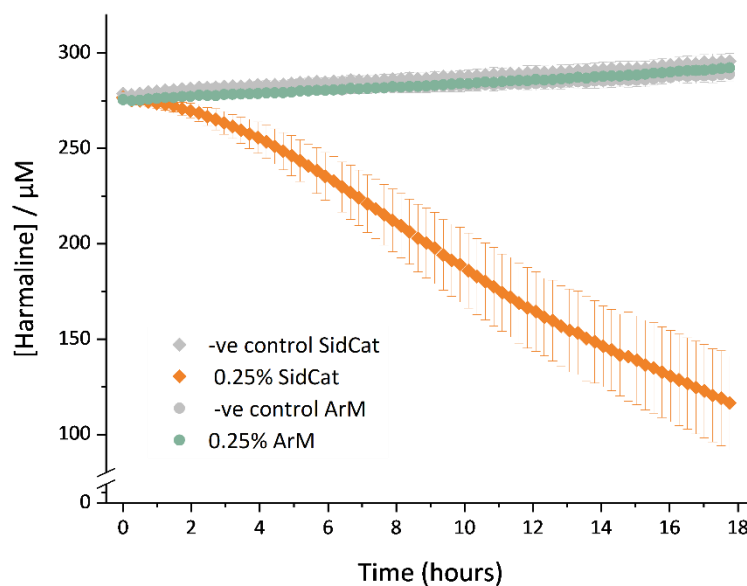
Figure 4.13 Kinetic profile for the imine reduction of harmaline catalysed by either SidCat (orange diamond points) or ArM (green circle points) as a function of decreasing substrate concentration. The controlled reactions in the absence of the catalyst are shown in grey. The harmaline concentration was calculated using the linear relationship obtained from the calibration plot; the absorbance was measured at 405 nm. The reaction was performed in 0.6 M MES, 3 M Na formate buffer at pH 7.0 (25°C); [harmaline]$_{start}$ = 368 µM; [catalyst] = 0.92 µM (0.25% catalyst loading).

The possibility of the ArM release from the surface following the disassembly and performing the subsequent characterisation of the obtained solution, presents an opportunity for exploring other commonly employed and reliable protein characterisation techniques. MS spectroscopy of biomolecules provides the advantage of accurately determining the molecular mass of the samples under investigation. The 1 kDa mass difference between the apo CeuE-6His and the corresponding ArM means it should be feasible to readily determined whether the SidCat cofactor is incorporated within the binding pocket.

A control experiments was conducted to establish the correct measurement conditions to facilitate the ionisation of the protein sample. Mass spectra were acquired for solution containing 1 µM of either the CeuE-6His or the ArM prepared in the standard MS solvent constituting a 1:1

mixture of H_2O and MeCN in the presence of 0.1% formic acid. After performing spectrum deconvolution, a high intensity peak corresponding to an m/z of 34079.40 was observed for the apo protein sample. The value was found to be 107.89 lower than the expected molecular peak with an m/z of 34187.29. The two subsequent peaks were separated by approximately 23.0, suggesting they corresponded to the sodium salts of the species associated with the peak at 34079.40. However, several literature reports describe the truncation of the N-terminal methionine residue during protein expression in eukaryotic cells.[293,294] The absence of methionine (C_5H_9NOS) would result in a new molecular weight of 34056.10 for the the CeuE-6His protein, corresponding to the molecular formula of $C_{1540}H_{2474}N_{404}O_{457}S_3$. The peak of interest has an m/z only 23.0 higher than the new predicted mass of the $[M-MET]^+$ protein, which allows to assign the peak as the $[M-MET-Na]^+$ species. However, the predicted mass of the molecular ion peak for the ArM comprising the truncated CeuE-6His protein scaffold is 35112.10. In the spectrum measured for the ArM sample, the highest intensity corresponds to the m/z of 34057.36; the mass difference of 1056 corresponding to the SidCat conjugate. The sodium ionisation pattern observed is also identical to the one present in the spectrum of CeuE-6His. It can thus be concluded that either the integrity of the ArM was not preserved during the ionisation or the solution conditions, which included 50% of organic solvent, had a denaturing effect on the protein. The subsequent unfolding of the protein compromised the binding between the CeuE-6His and the iron(III) azotochelin anchor.

In **Chapter 2**, native ESI-MS was utilised to analyse a complex of iron(III) azotochelin as it was necessary to preserve the non-covalent interactions within the complex upon entry of the analyte into the gas phase. The same approach can be employed for preserving the non-covalent interaction of a protein, which play a crucial role in the maintaining correct folding of the tertiary structure and any non-covalent interactions with small molecules. Thus, 10 µM samples of both CeuE-6His and the ArM (**Figure 4.14**) were

prepared in a 10 mM NH$_4$OAc solution, and the spectra were acquired with the assistance of Dr A. Dowle, who aided in finding optimal operating parameters for acquiring well-resolved spectra. Similarly, to the spectra obtained under denaturing conditions, a high intensity peak was observed at an m/z of 34079.28. Consistent with previous observations, the peak was attributed to a [M-MET+Na]$^+$ species as anticipated. As the ionisation of molecules is more extensive under native conditions due to presence of charged buffer species in the sample, a more extensive sodium salt ionisation pattern was observed.
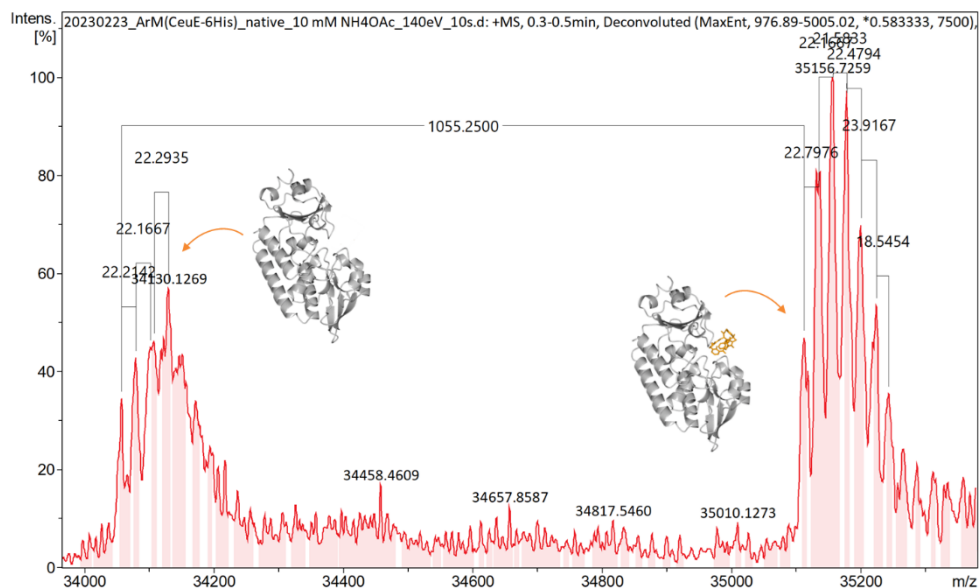
Figure 4.14 The deconvoluted mass spectrum acquired under native conditions for the sample containing 10 µM of the ArM. The peaks for both CeuE-6His and the ArM are observed with the separation distances being in agreement with the mass of the SidCat.

Employing native conditions for acquiring the spectrum of the ArM sample, allowed to observance a new peak corresponding to an m/z of 35113.50, in addition to the peak at m/z 34057.67 associated with the apoprotein. The mass difference of 1055.25 between the two peaks corresponds precisely to the mass of SidCat, allowing to conclude that the SidCat remained bound to the CeuE-6His during the ionisation process, and the intact ArM was successfully detected. Testing several sample concentrations allowed to determine that a minimum sample concentration of 10 µM, with a minimum

volume of 25 μL, was necessary to achieve a successful acquisition. The MS analysis requires a higher sample concentration in comparison to the catalyst assays. However, it provides a positive signal response in the presence of the ArM, offering a high level certainty on the species present as compared to the absence of a response.

4.2.4 The design and development of a new electrochemical cell

The availability of sample for characterisation studies, following ArM reduction is limited by the amount of protein that can be immobilised on the electrode surface. Theoretical surface coverage calculations assume maximum protein packing within homogenous layer and do not take into consideration the effectiveness of the immobilisation approach. However, under experimental conditions, the immobilisation efficiency is extensively influenced by both steric hindrance and electrostatic repulsion, as well as the availability of NTA(Ni^{2+}) sites. The immobilisation of proteins on NTA(Ni^{2+}) functionalised surfaces has been modelled by V. Balland et al., illustrating the variations in surface terminations which adversely impacts the protein immobilisation yield.[233]

To compensate for the immobilised protein concentration being lower than predicted by theoretical calculations, an alternative electrochemical set-up was designed and made in collaboration with technical workshops. Standard disk working electrodes tend to be only available in diameter size of 1.5 mm and 3.0 mm. Thus, an increased surface area was achieved by employing a Au-coated silicon wafer (Ø 10 cm) as the working electrode. However, such wafers do not possess inherent connections required for their incorporation into electrical circuits, necessitating the construction of a connection between the wafer and the potentiostat cable. It was proposed that a platinum wire, coiled within a glass rod, would allow for the current to pass through and transform the Au wafer into a working electrode upon contact with the platinum. The remaining two electrodes, reference and

counter electrodes, were analogous to those used in the electrochemical setups throughout this thesis. The bespoke electrochemical cell was constructed in two detachable parts: a nylon base with an engraved slow to allow for a close fit of the wafer electrode and a glass lid, containing multiple ports for the electrodes and gas lines. The fragility of the wafer necessitated the employment of a nylon ring to be situated between the two parts for additional cushioning and protection of the wafer during the assembly of the whole cell. Regrettably, the presence of the protective ring resulted in the effective surface area of the electrode being reduced to 38.5 cm^2 (Ø 7 cm) from 78.5 cm^2 (Ø 10 cm).

Preliminary CV measurements were performed in 0.6 M MES, 3 M Na formate buffer, pH 7.0, to assess the functionality of the design above as a viable electrochemical cell. In the absence of redox-active species, significant background noise was observed, with sufficiently high amplitude to obscure any iron(III)/(II) Faradaic peaks from an immobilised ArM. Further interrogation concluded the source of the non-Faradaic signal to be the connection between the 'bridging' platinum wire and the Au wafer. Thus, invalidating the use of the cell without further development, which was not possible within the time constraints of the project.

Nonetheless, parallel to QCM-D and EIS experiments described in **Section 2.2.3** and **Section 4.3.2**, respectively, an imidazole triggered release experiment was performed to assess the suitability of the Au wafer to serve as the immobilisation support for the ArM. A chemically polished Au wafer was functionalised with LA NTA SAMs, as per standard protocol, and positioned within the nylon support. Following nickel chelation and ArM immobilisation, employing conditions established from previous QCM-D and EIS experiments, the modified Au surface was incubated with a 500 mM imidazole solution for 30 minutes. All three solutions were collected and subsequently concentrated: the nickel chelation solution served as a negative control (**-ve**), the ArM solution as a positive control (**+ve**), and the

imidazole wash as the experimental solution (**exp**). The three samples were processed through desalting columns, lyophilised, and dissolved in buffer suitable for native ESI-MS. The presence of the ArM was successfully identified in the **+ve** control, in parallel with the controlled MS studies described in **Section 4.2.3**. However, MS analysis of the **exp** sample was not possible due to high amplitude peaks corresponding to the presence of imidazole, obscuring any other signals, if present. Thus, before the Au wafer was validated as a suitable immobilisation surface, an alternative sample clean-up protocol, such as dialysis, would be necessary.

4.2.5 The redox 'hedgehog' variant of the Fe-PBP ArM

Utilisation of either the Au wafer or the platinum wire as the working electrode will be associated with similar challenges linked to the maximum distance for efficient electron transfer and mass transfer limitations. Incorporation of a redox mediator within the proximity of the protein and the redox centre of the anchor is hypothesised to circumvent those issues through localisation of the electron transfer. Multiple literature examples are available where the Au surface has been functionalised with a mixed SAM monolayer, comprising NTA terminated SAM molecules and either alkyl thiols or lipoic acid derivatives terminated with a redox mediator instead of NTA. However, the ratio of the two SAMs cannot be controlled with extreme precision, making it difficult to ensure a sufficient availability of redox mediator molecules per a molecule of an immobilised ArM. Alternatively, direct conjugation of the redox mediator to the protein backbone allows to reduce the electron transfer distance even further. However, such strategy must be approached with caution as bioconjugation methods may have a detrimental effect on structural stability of the protein.

The exploitation of surface exposed lysine residues, abundant on the CeuE protein scaffold, allows the utilisation of straightforward amide chemistry to increase the ratio of the redox mediator to protein. The decoration of the

protein with redox-active molecule, producing a 'hedgehog' CeuE derivative, it anticipated to create an efficient artificial electron relay pathway from the electrode, around the protein scaffold and towards the redox-active anchor.

In the redox assay described in **Section 4.2.1**, ethyl viologen emerged as the most promising candidate for mediating the reduction of the ArM based on the CeuE-6His scaffold. Thus, a synthetic pathway using viologen as the starting material was proposed to install an activated ester functionality, yielding a viologen derivative capable of selective conjugation to the surface exposed lysine residues. Monosubstituted ethyl viologen [**NGB-18**] was reacted with 6-bromohexanoic, to incorporate a linker with sufficient flexibility thus ensuring ensure an efficient connection between each viologen molecules in the artificial electron relay pathways. Consequently, the synthesis of **NGB-19** was achieved in reduced yield with significant higher reaction time, in comparison to 3-bromopropionic acid utilised in the literature.[295] This was hypothesised to be a direct consequence of increased steric hindrance. While isolation of the viologen intermediated was achieved in a straightforward manner through precipitation, the purification of the final compound, EV NHS [**NGB-20**] from the unreacted starting material was unsuccessful; integration of ^{1}H NMR peaks determined a 0.4:1 ratio of the desired product to starting material. Nonetheless, it was decided that the heterogeneity of the sample should not be an issue in further studies, as the carboxylic acid derivative should not exhibit any reactivity due to it lower electrophilic character. Even if the reaction between **NGB-19** and lysine residues would take place, the final product would not be distinguishable from the reaction of **NGB-20** with the protein scaffold.

To ensure the presence of the alkyl chain did not have an adverse effect on the reducing power of the viologen derivative, the redox behaviour of **NGB-19** was compared to that of EV using previously described (**Section 4.2.1**) electrochemical and chemical assays. As observed in the

voltammograms, the electrochemical reversibility of the redox mediator was unaffected by the presence of the carboxylic acid functionality as demonstrated by an identical $E_{1/2}$ for both EV and **NGB-19**. However, a 19% reduction in the oxidation current was observed. This had a subsequent effect on the rate of electron transfer, as a smaller amount of Fe^{2+} was detected for **NGB-19** in comparison to EV for protein samples in the ferrozine assay. However, the anticipated high ratio of redox mediator per protein molecule should compensate for the slightly lowered reducing power imposed through the mono modification of the *N*-position. Unfortunately, the conjugation of the **NGB-20** to CeuE-6His ended up being beyond the timeline of the project.

4.3 Summary and conclusions

The electrochemical reduction of the iron(III) azotochelin anchor located within the CeuE-6His protein scaffold shows promise as an alternative to chemical reduction. However, direct electron transfer between the Au electrode and the redox centre of the ArM was found to be infeasible upon voltammetric analysis of a small fast-electron transfer protein, *Cj*X183, on LA NTA functionalised electrodes. No redox activity was observed upon immobilisation. This led to the search for a reversible reducing agent that could act as a redox mediator within the potential range of the iron(III) azotochelin anchor. Both an electrochemical investigation and a ferrozine assay, with the latter detecting the amount of iron(III) released during sample reduction, identified ethyl viologen as the most suitable candidate. Ethyl viologen derivative exhibited a sufficiently negative $E_{1/2}$ to participate in the reduction of iron(III) azotochelin and demonstrated the highest current among the investigated the viologen derivatives investigated.

To overcome potential mass transfer limitations encountered by redox mediators in solution, an activated ester of ethyl viologen functionalised with a long linker was prepared for facilitating its bioconjugation to the

excess of lysine residues on the surface of CeuE-6His. The aim was to increase the ratio of the redox mediator within the vicinity of the ArM and create an artificial electron relay pathway to circumvent the issue. However, the conjugation of the redox mediator was not feasible within timeframe of this project. The subsequent future step would be to perform EIS- MS and trypsin digestion to confirm the efficiency of the bioconjugation process and the location of the viologen derivatives on the protein scaffold. As some of the surface exposed lysine residues lie within the proximity of the binding pocket, it might be necessary to investigate the bioconjugation before and after ArM assembly to assess its impact on the efficiency of the ArM assembly and catalytic activity.

Characterisation of heterogeneous surfaces is one of the most challenging aspects encountered in protein immobilisation. Techniques such as QCM-D and EIS, which are capable of directly interrogating the surface have been successfully employed for detecting binding events of biomacromolecules on solid surfaces. This has been demonstrated by imidazole stripping experiments of CeuE-6His immobilised on LA NTA(Ni^{2+}) gold surfaces and the associated decrease in the frequency signal. However, these techniques exhibit limitations in detecting more subtle changes within immobilised proteins, such as the loss of the SidCat upon the chemical reduction of iron(III) azotochelin conjugate. Various attempts have been made to optimise EIS have; while they have been unsuccessful in this regard, they have contributed to improving the understanding of the technique within the research group.

Access to alternative surface characterisation methods such as surface plasmon resonance was not possible, thus the reversibility of the 6His-tag immobilisation was utilised to remove the protein from the surface and analyse it in solution, which illustrates a more straightforward approach. Control studies measuring the absorbance associated the catalytic turnover of the substrate and native ESI-MS characterisation were able to

differentiate between the apo protein and the ArM up to 1 µM and 10 µM, respectively. However, the ArM concentrations obtained from immobilisation on Au disk electrodes were below the LOD. As a result, an alternative electrochemical cell was designed and produced to accommodate a ⌀ 10 cm Au wafer as a support for ArM immobilisation. Preliminary studies were conducted to assess the feasibility of using this electrode surface for electrochemical reduction, however, the results were inconclusive, requiring further optimisation.

Considering that the encountered issues primarily revolve around overcoming the LOD, it is reasonable to assume that a combination of the ArM-redox mediator conjugate, MS characterisation in native conditions, and the utilisation of the novel electrochemical cell, which allows for the use of electrodes with larger surface area, will facilitate the detection of successful electrochemical reduction and subsequent ArM disassembly.

***

Chapter 5 – Conclusions and future perspectives

5.1 Summary and conclusions

The research presented in this thesis builds upon the pioneering ArM design, which was the first to report the controlled disassembly of the hybrid catalyst. A redox switch was employed to trigger the release of the anchor-catalyst conjugate from the protein scaffold, thereby enabling the recycling of individual components. The proof of concept in initial solution studies was successfully demonstrated using sodium dithionite, utilised as the reducing agent for the iron(III) anchor which triggered the disassembly. The preliminary study identified several drawbacks, with particular emphasis on the challenging simultaneous separation of the components following the disassembly and the inability to recycle the reducing agent. Thus, the project aimed to target those limitations through two key approaches, ArM immobilisation and electrochemical reduction, respectively. In parallel with the work performed within the research group on utilising IMAC columns for flow biocatalysis, the immobilisation strategy central to purification, based on the affinity between nickel(II) complexes of NTA and the imidazole rings of the 6His-tag, was aimed to be adapted for a conducting surface. While the literature on introducing NTA functionalities onto electrodes is available, inducing an electrochemically triggered dissociation of only a metal cofactor from immobilised protein has not been previously reported.

In the initial investigation into the feasibility of achieving an electrochemical reduction, a gap in the literature regarding the redox properties of iron(III) azotochelin which served as the ArM anchor was found. Thus **Chapter 2** details the successful implementation of a novel electrochemical setup utilising a BDD working electrode for the electrochemical study of iron(III)

azotochelin, which has been expanded to iron(III) complexes of related siderophores. The investigation, supplemented by native ESI-MS data, yielded valuable insight into the relationship between the irreversible electrochemical behaviour and the $M_1:L_1$ speciation of the complex. The discovery of the preference for iron(III) azotochelin to form coordinatively unsaturated coordination complexes has provided compelling evidence supporting the suitability of iron(III) azotochelin as the anchor for the ArM. The metal centre of the azotochelin complex is more easily reduced compared to related siderophores, while still maintaining a stable complex with the protein scaffold. Moreover, by understanding the redox properties of the system, it was possible to make informed decisions regarding the methodology functionalisation of electrodes with NTA groups.

Chapter 3 explores the feasibility of transferring the IMAC chemistry onto Au electrodes in an efficient manner to support the subsequent optimisation of the electrochemical-triggered disassembly. Two approaches for the installation of NTA on Au through SAM formation were explored and compared for the number of available protein binding sites and the degree of non-specific binding. Unsurprisingly, the solution synthesis of LA NTA [**NGB-14**] prior to immobilisation was proved to be a superior approach compared to the on-surface synthesis from immobilised activated ester derivative of lipoic acid, as it offers greater control over NTA coverage. Multiple analytical methods were used in a complimentary manner to confirm the successive surface modifications (EIS), the nickel occupancy of the NTA head groups (surface-confined voltammetry of the ferrocene redox probe, **NGB-17**) and the extent of non-specific binding through imidazole competition experiments (QCM-D).

Detecting subtle changes within immobilised molecules poses a challenging task, as the loss of Sid-Cat and the disassembly of the ArM does not induce any significant structural changes to the protein and is only associated with an approximately 3% decrease in mass. **Chapter 4**

investigates the viability of employing either QCM or EIS for monitoring the disassembly of the ArM, initially using a chemical reducing agent for preliminary testing. Unfortunately, neither of the approaches yielded successful results. The protein film displayed instability under the experimental conditions during QCM measurements, making it impossible to observe the changes in frequency that would indicate the loss of SidCat. The acquired EIS data showed a noticeable drift, which was attributed to the technique's high sensitivity to the reorganisation of the monolayer over time, hindering the detection of dynamic changes within the protein film. Nevertheless, the efforts invested in troubleshooting EIS have proven valuable to the research group, enhancing the understanding of the technique. It has established a foundation and an initial starting point for addressing the observed issues and improving the reliability of the technique in future experiments.

Ultimately, it was concluded that the recovery of the protein from the surface after the disassembly is crucial in order to accurately characterise the structure of the ArM. Following optimisation, both measurement of catalytic activity and native EIS-MS characterisation were demonstrated to be suitable techniques, as long as LOD requirements were met. In an effort to overcome the limitation, a new electrochemical cell was designed and constructed, featuring a gold wafer, allowing it to obtain a much higher ArM concentration in comparison to immobilisation on a disk electrode. However, during the initial testing, connectivity issues were encountered when attempts were made to utilise the wafer as a working electrode.

The concluding work of **Chapter 4** addresses findings from the electrochemical studies conducted on a model redox-active protein, *Cj*X183. The experiments led to the conclusion that DET between the Au electrode and the iron(III) azotochelin anchor of the immobilised ArM would not be feasible. Among commonly utilised viologen derivatives, ethyl viologen was found to be a viable alternative to sodium dithionite and

capable of serving as a redox mediator in MET. Preliminary work has been conducted towards developing a protein derivative with an artificial electron relay pathway by conjugating the redox mediator to the protein scaffold; the synthesis of the ethyl viologen conjugate has been successfully achieved.

Considerable progress has been made towards the development of an ArM immobilisation platform, with an emphasis on attaining a high loading capacity of the catalyst in a correct orientation while minimising non-specific binding. The search for a suitable methodology to monitor the disassembly process led to the discovery of native ESI-MS as a reliable approach for effectively distinguishing between the apo protein and the ArM. An alternative to sodium dithionite has been successfully found; ethyl viologen demonstrated promising reducing power and electrochemical reversibility. Although further optimisation of the electrochemical cell is necessary, the new design offers considerable advantages not only for ArM immobilisation but also for the study of surface bound proteins. The versatility of the immobilisation approach only necessitates the protein of interest to possess a 6His-tag, which are frequently incorporated into plasmids as a standard protocol to facilitate protein purification.

5.2 Future perspectives

The ability for iron(III) azotochelin to modulate its reduction potential while maintaining the $M_1:L_1$ complex stoichiometry, as demonstrated in the buffer study outlined in **Chapter 1**, presents possibilities for developing multi enzyme reaction cascades with high temporal and spatial control. The envisioned approach comprises the creation of a single enzymatic array incorporating multiple ArMs, each comprising different catalyst derivatives and each exhibiting distinct reduction potentials. The selective control over the disassembly of each ArM, would enable the precise regulation of each catalysed step, providing fine control over the overall enzymatic process. Hence, it is of great interest to investigate whether the effects observed in the buffer study can be reproduced when the anchor is situated within the

binding pocket of the protein. To assess the feasibility of the approach site-selective mutation of the iron(III) coordinating tyrosine to a residue with a terminal amine would be required (**Figure 5.1**); the basic residues, arginine and lysine, would make suitable candidates. Concurrently, it would be necessary to assess whether the strength of the anchor binding would be preserved across the CeuE mutants.

However, a suitable electrochemical setup capable of directly interrogating the iron(III) azotochelin complex within the protein has not been found thus far. A viable alternative would be to perform model CV experiments which the buffer solution is supplemented with the amino acid of interest, and the reduction potential of the iron(III) azotochelin is measured at a BDD working electrode.

Y288   **Y288K**   **Y288R**
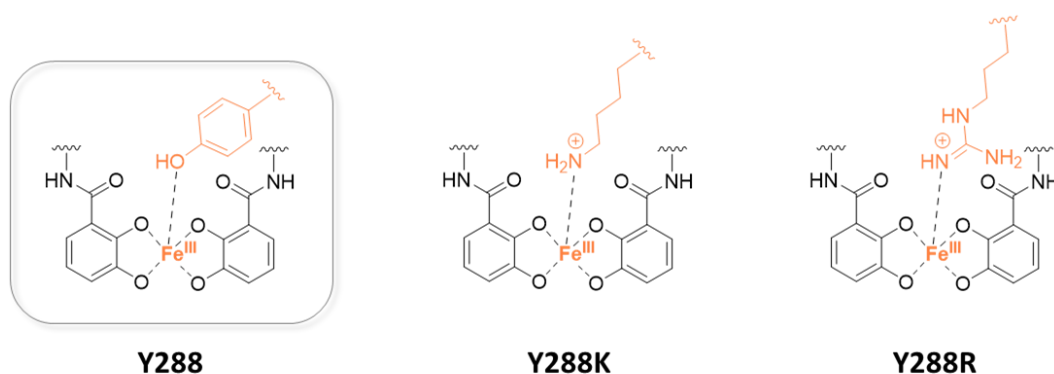
Figure 5.1 Schematic representations of the iron(III) coordination sphere within the ArM. The structure of the coordinating residue is shown in the native protein (Y288) and in the two possible mutation candidates to modulate the reduction potential of the iron(III).

Throughout the project, the functionalisation of Au electrodes has been achieved through the formation of SAMs, exploiting the spontaneous bond formation between thiols and Au. The selection of the SAM approach was primarily based on the ease with SAM formation occurs, which facilitates the screening and optimisation experiments. However, as demonstrated by the results of the EIS experiments, the surface modification did not exhibit high stability under all experimental conditions. As Au remains the most

compatible surface with most surface characterisation techniques, alternative approaches can be explored for installing NTA functionalities onto Au by employing more stable covalent bonding methods, such as diazonium electrografting (**Figure 5.2**).[296–298]
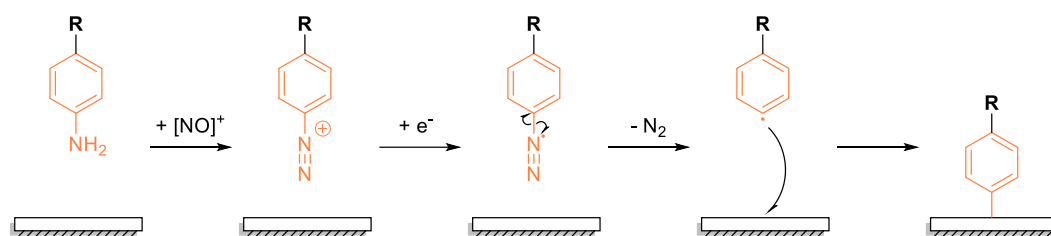
Figure 5.2 Stepwise protocol for the electrografting in situ generated diazonium salts on Au surfaces; the R group represents a handle for bioconjugation of proteins.

However, the most interesting future direction lies in the combination of all findings outlined in **Chapter 4** into one cohesive experiment, the multi-point ligation of the ethyl viologen conjugate [**NGB-20**] to the CeuE protein scaffold and subsequent immobilisation on the Au wafer. In its current state, the electrochemical cell would require optimisation and improvement of the connection between the connecting Pt wire and the Au wafer before it can be employed in electrochemical studies.

If resolving the connection issues proves to be more challenging than initially anticipated, an alternative approach would be to utilise the Au wafer solely as an immobilisation platform for the ArM and the Pt wire as the working electrode. While this electrode configuration would lead to an increased distance for electron transport, supplementing the buffer solution with viologen should allow to rely on the electrons between the working electrode and the 'artificial wire' of the immobilised ArM (**Figure 5.3**). The approach should prove viable as long as the viologen concentration in solution remains sufficiently high.

In the event of all previous approaches not being viable, Au NPs can be employed as an alternative immobilisation support. Entrapment of NPs within a three-dimensional network would ensure high loading capacity of ArMs and facilitate efficient electron transfer.[299] The inclusion of NPs within a microfluidic device featuring a gold surface would allow to create a sustainable bioreactor for flow biocatalysis capable of component recycling without having to replace the whole system.
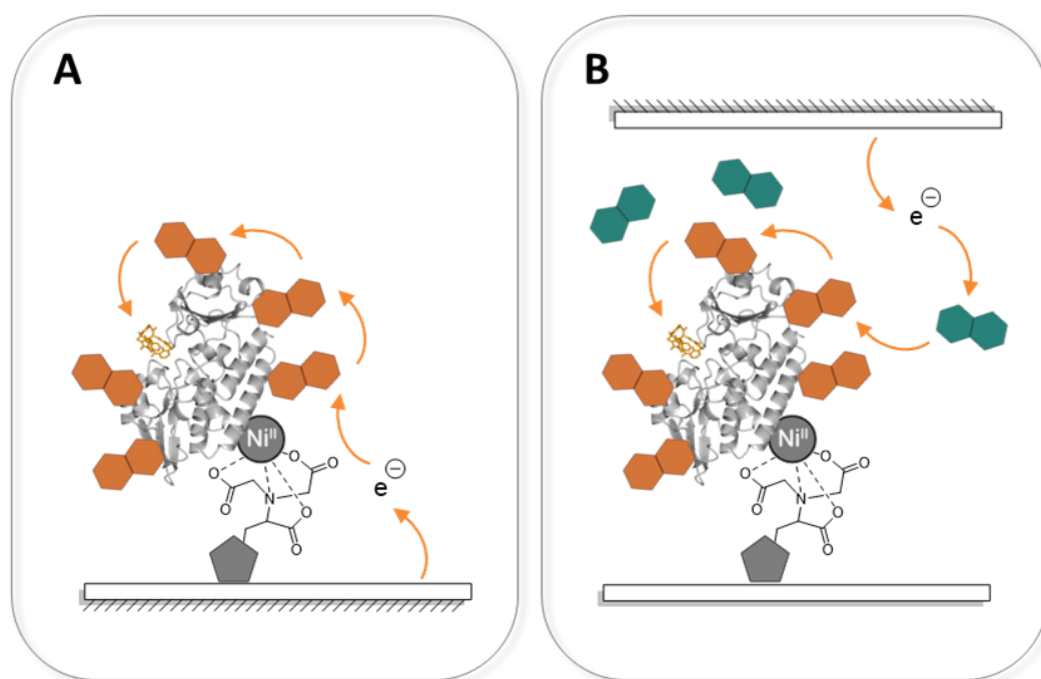
Figure 5.3 Schematic illustration comparing the electron transfer pathway for the two electrochemical setup options; the naphthalene rings are representative of viologen based redox mediator. **A** The Au wafer serves as the working electrode without the need for mediating viologen molecules in solution; **B** The Pt wire (top surface) serves as a working electrode with viologen molecules in solution acting as the secondary redox mediator while the Au wafer is acting purely as an immobilisation support.

***

Chapter 6 – Experimental

6.1 Synthesis

6.1.1 Materials

All chemical reagents and solvents were obtained from commercial suppliers (Fisher Scientific, Fluka Chemicals, Fluorochem, Sigma-Aldrich, Thermo Scientific, Tokyo Chemical Industry) and used as supplied unless otherwise stated. When required, solvents were either dried over heat-activated 4 Å molecular sieves or obtained from the Prosolv MD 7 solvent purification system, which involves the passage of the solvent through two columns packed with molecular sieves.

Bn$_4$-bisDHBS was obtained from Dr Daniel J. Raines (Department of Chemistry, University of York). **Enterobactin** was obtained from Professor Alison Butler and her graduate student Parker Stow (Department of Chemistry, University of California, Santa Barbara). **Ferricrocin** was obtained from Emeritus Professor James W. Coulton (Department of Microbiology and Immunology, McGill University, Montreal). **1,1'-Ferrocene-dicarboxaldehyde** was a gift from Dr Luke Wilkinson (Department of Chemistry, University of York). **CeuE**, **Gst-6His** and **some CeuE-6His stocks** were obtained from Dr Elena V. Blagova (York Structural Biology Laboratory, University of York). **AzotoCat** and **[Cp*IrCl$_2$]$_2$** were obtained from Dr Benjamin Large (Department of Chemistry, University of York). *Cj*X183 stock was obtained from Alice Hewson.

6.1.2 Instrumentation

NMR characterisation consisting of ^{1}H, ^{13}C, COSY, DEPT135 and HMQC spectra were recorded on Joel ECS and Joel EXC 400 MHz instruments (^{1}H NMR at 400 MHz, ^{13}C NMR at 101 MHz) at ambient temperature. The ^{1}H data are reported as follows: chemical shift (multiplicity, coupling constant

(in Hz) if applicable, number of protons, assignment). The ^{13}C data are reported as follows: chemical shift (assignment). All chemical shifts are reported in parts per million (ppm), quoted to the nearest 0.01 ppm and relative to residual solvent peaks. Multiplicity has been abbreviated as follows: singlet (s), doublet (d), triplet (t), quartet (q), multiplet (m), broad (br). When required, NMR assignments were supported with COSY, DEPT135 and HMQC experiments. All spectra were processed using the MestReNova 14.0.0 software.

High resolution mass spectra (HRMS) of small molecules were recorded using the electrospray ionisation (ESI) technique on a Bruker compact MS-Agilent 1260 mass spectrometer by either Karl Heaton or Angelo Lopez. The measurement mean error is reported in ppm and indicates the closeness of the measured m/z value to that of the theoretical.

Infrared (IR) spectra were recorded on either Perkin Elmer Spectrum Two FT-IR spectrometer or Bruker ALPHA II spectrometer at ambient temperature. The data are reported as peaks of interest of relevant functional groups.

Analytical thin layer chromatography (TLC) was performed on Merck silica gel 60 F$_{254}$ aluminium backed plates, which were visualised either under a UVItec LF-204.S lamp or using a potassium permanganate stain.

6.1.3 Synthetic protocols

[**NGB-01**] 2,3-Bis(benzyloxy)benzaldehyde

$C_{21}H_{18}O_3$
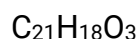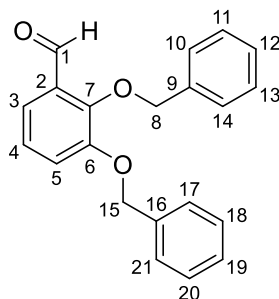
MW = 318.37 g mol^{-1}

The compound was prepared based on a procedure from the literature.[178]

2,3-Dihydroxybenzaldehyde (5.00 g, 36.2 mmol, 1.0 equiv) and benzyl chloride (10.0 mL, 86.9 mmol, 2.4 equiv) were dissolved in anhydrous ethanol (90 mL). Anhydrous potassium carbonate (6.25 g, 45.3 mmol, 1.25 equiv) was added to the stirring solution. The reaction mixture was refluxed under an inert atmosphere for 18 hours. The resulting precipitate was dissolved in diethyl ether (250 mL) and washed with deionised water (4 x 100 mL), followed by brine (100 mL). The solvent was removed *in vacuo* to yield a beige solid of the title compound which was used in the subsequent step without further purification; **11.0 g**, **34.5 mmol**, **95%**.

R$_f$: (petroleum ether:EtOAc, 8:2): 0.60.

HRMS: (EIS): Calcd. for $C_{21}H_{18}NaO_3$ [M+Na]$^+$ 341.1148; found 341.1143 (mean error 1.2 ppm).

^{1}H NMR: (400 MHz, CDCl$_3$): δ 10.19 (s, 1H, *H1*), 7.43 − 7.40 (m, 2H, *H10,17*), 7.37 − 7.27 (m, 8H, *H11-14,18-21*), 7.20 − 7.17 (m, 2H, *H3,5*), 7.05 (t, *J* = 7.9 Hz, 1H, *H4*), 5,14 (s, 2H, *H8*), 5.13 (s, 2H, *H15*).

^{13}C NMR: (101 MHz, CDCl$_3$): δ 190.38 (*C1*), 152.29 (*C7*), 151.67 (*C6*), 136.42 (*C2*), 130.63, 128.91, 128.85, 128.72, 128.68, 128.43, 127.69 (*C9-14,16-21*), 124.38 (*C3*), 120.05 (*C5*), 119.71 (*C4*), 76.21 (*C8*), 71.39 (*C15*).

IR (ATR) (cm^{-1}): 2875 (C-H), 1682 (C=O), 1579 (C=C aromatic).

Data consistent with literature values. [178]

[NGB-02] 2,3-Bis(benzyloxy)benzoic acid

$C_{21}H_{18}O_4$

MW = 334.37 g mol^{-1}
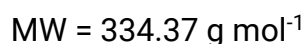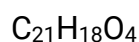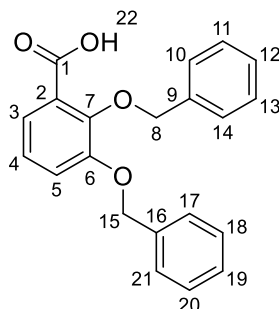
The compound was prepared based on a procedure from the literature.[178,179]

2,3-Bis(benzyloxy)benzaldehyde **[NGB-01]** (10.8 g, 33.9 mmol, 1.0 equiv) was dissolved in acetone (120 mL). Individual solutions of sulfamic acid (5.92 g, 61.0 mmol, 1.8 equiv) and sodium chlorite (3.68 g, 40.7 mmol, 1.2 equiv) in deionised water (40 mL and 30 mL, respectively) were prepared and added alternatingly to the reaction solution over 50 minutes. The resulting mixture was stirred for 3 hours in air at room temperature. Acetone was removed *in vacuo*, the solid collected and washed with deionised water. The crude product was recrystallised thrice in hot ethanol and dried in a desiccator for a fortnight to yield an off-white solid of the title compound; **7.44 g**, **22.2 mmol**, **66%**.

R$_f$: (chloroform:MeOH, 10:1): 0.68.

HRMS: (EIS): Calcd. for $C_{21}H_{18}NaO_4$ [M+Na]$^+$ 357.1097; found 357.1095 (mean error 1.0 ppm).

^{1}H NMR: (400 MHz, CDCl$_3$): δ 11.30 (s, 1H, *H22*), 7.67 (dd, *J* = 7.8, 1.8 Hz, 1H, *H3*), 7.42 − 7.27 (m, 10H, *H10-14,17-21*), 7.20 − 7.17 (m, 1H, *H5*), 7.12 (t, *J* = 8.0 Hz, 1H, *H4*), 5.19 (s, 2H, *H8*), 5.12 (s, 2H, *H15*).

^{13}C NMR: (101 MHz, CDCl$_3$): δ 165.58 (*C1*), 151.72 (*C7*), 147.48 (*C6*), 136.27 (*C2*), 135.02, 129.79, 129.32, 129.28, 129.03, 128.25, 125.33 (*C9-14,16-21*), 124.89 (*C3*), 123.40 (*C5*), 119.39 (*C4*), 77.60 (*C8*), 71.95 (*C15*).

IR (ATR) (cm⁻¹): 3031 (O-H), 2874 (C-H), 1683 (C=O), 1576 (C=C aromatic).

Data consistent with literature values. [178,179]

[NGB-03] 2,3-Bis(benzyloxy)benzoic acid-*N*-hydroxysuccinimide ester
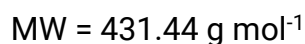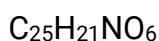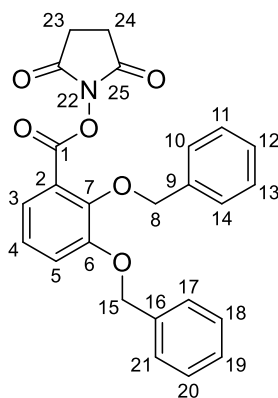
$C_{25}H_{21}NO_6$

MW = 431.44 g mol⁻¹

The compound was prepared based on a procedure from the literature.[180]

2,3-Bis(benzyloxy)benzoic acid **[NGB-02]** (5.00 g, 15.0 mmol, 1.0 equiv) and *N*-hydroxysuccinimide (1.89 g, 16.5 mmol, 1.1 equiv) were dissolved in anhydrous dioxane (40 mL) and the resulting solution was cooled down to 0°C. *N,N'*-Dicyclohexylcarbodiimide (3.40 g, 16.5 mmol, 1.1 equiv) was added and the reaction mixture was stirred on ice for further 10 minutes. The flask was allowed to warm up to room temperature and the suspension was stirred overnight under an inert atmosphere. The reaction mixture was filtered, and the bulk solvent was removed *in vacuo*. Isopropanol was added dropwise to the stirring oil until no more precipitate formed. The solid was collected and washed with a mixture of isopropanol and ethanol (1:1, v/v%). The crude product was recrystallised from hot ethyl acetate to yield a white crystalline solid of the title compound; **3.79 g**, **8.78 mmol**, **59%**.

R_f: (chloroform:MeOH, 10:1): 0.83.

HRMS: (EIS): Calcd. for $C_{25}H_{21}NNaO_6$ [M+Na]⁺ 454.1251; found 454.1259 (mean error 0.5 ppm).

¹H NMR: (400 MHz, CDCl₃): δ 7.58 (dd, *J* = 7.9, 1.6 Hz, 1H, *H3*), 7.43 − 7.27 (m, 10H, *H10-14,17-21*), 7.24 − 7.22 (m, 1H, *H5*), 7.12 (t, *J* = 8.0 Hz, 1H, *H4*), 5.13 (d, *J* = 1.6 Hz, 4H, *H8,15*).

¹³C NMR: (101 MHz, CDCl₃): δ 169.36 (*C22,25*), 160.80 (*C1*), 153.08 (*C7*), 149.95 (*C6*), 137.09 (*C2*), 136.33, 128.77, 128.37, 128.10, 127.72, 124.37, 123.86 (*C9-14, 16-21*), 121.13 (*C3*), 120.23 (*C5*) 75.98 (*C8*), 71.49 (*C15*), 25.83 (*C23,24*).

IR (ATR) (cm⁻¹): 3035 (C-H), 1764 (C=O ester), 1733 (C=O amide), 1578 (C=C aromatic), 1205 (C-O ester).

Data consistent with literature values. [180]

[NGB-04] *N²,N⁶*-Bis(2,3-dibenzyloxybenzoyl)-*L*-lysine (Bn₄-azotochelin)
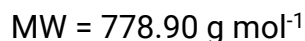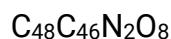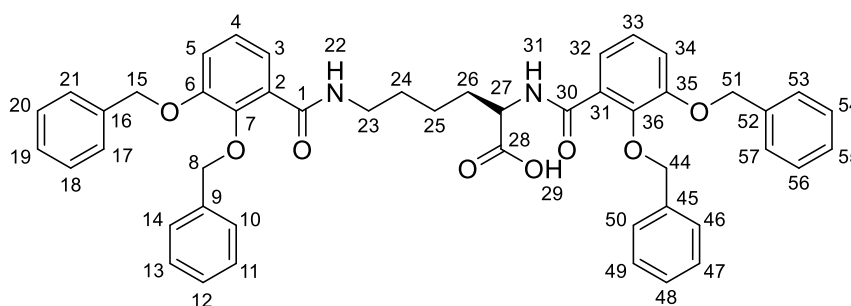
$C_{48}C_{46}N_2O_8$

MW = 778.90 g mol⁻¹

The compound was prepared based on a procedure from the literature.[180]

2,3-Bis(benzyloxy)benzoic acid-*N*-hydroxysuccinimide ester **[NGB-03]** (0.867 g, 2.01 mmol, 2.0 equiv) was dissolved in acetone (25 mL). A separate solution of *L*-lysine monohydrate (0.183 g, 1.00 mmol, 1.0 equiv) and triethylamine (0.9 mL, 6.46 mmol, 6.5 equiv) in deionised water (5 mL) was prepared and added to the acetone solution. The reaction mixture was stirred overnight at room temperature. The acetone was removed *in vacuo* to yield a yellow oil which was taken up in ethyl acetate (35 mL) and washed with 0.1 M HCl (4 x 30 mL). The solvent was removed *in vacuo* and the crude product was purified using flash column chromatography (chloroform:MeOH, 10:1) to yield an off-white crystalline solid of the title compound; **0.527 g**, **0.677 mmol**, **67%**.

R$_f$: (chloroform:MeOH, 10:1): 0.31.

HRMS: (EIS): Calcd. for $C_{48}H_{47}N_2O_8$ [M+H]$^+$ 779.3327; found 779.3325 (mean error 1.0 ppm). Calcd. for $C_{48}H_{46}N_2NaO_8$ [M+Na]$^+$ 801.3146; found 801.3165 (mean error -0.4 ppm).

^{1}H NMR: (400 MHz, CDCl$_3$): δ 8.51 (d, *J* = 7.0 Hz, 1H, *H31*), 7.89 (t, *J* = 5.5 Hz, 1H, *H22*), 7.71 − 7.66 (m, 2H, *H3,32*), 7.43 − 7.29 (m, 16H, *H11-14,18-21,46-49,53-56*), 7.22 − 7.20 (m, 4H, *H10,17,50,57*), 7.12 − 7.08 (m, 4H, *H4,5,33,44*), 5.10 − 5.09 (m, 6H, *H8,44,51*), 5.01 (s, 2H, *H15*), 4.47 (td, *J* = 7.4, 5.5 Hz, 1H, *H27*), 3.11 − 3.06 (m, 2H, *H23*), 1.70 − 1.61 (m, 1H, *H26$_a$*), 1.39 − 1.29 (m, 1H, *H26$_b$*), 1.15 − 1.08 (m, 4H, *H24,25*).

^{13}C NMR: (101 MHz, CDCl$_3$): δ 174.05 (*C28*), 166.24 (*C30*), 165.34 (*C1*), 151.87 (*C36*), 151.79 (*C7*), 147.32 (*C35*), 146.97 (C6), 136.55, 136.44, 136.38, 136.22 (*C9,16,45,52*), 129.06, 128.85, 128.75, 128.45, 128.40, 127.91, 127.80 (*C10-14,17-21,46-50,53-57*), 127.26 (*C31*), 126.14 (*C2*), 124.58 (*C32*), 124.55 (*C3*), 123.49 (*C34*), 123.42 (*C5*), 117.70 (*C33*), 117.14 (*C4*), 76.56 (*C51*), 76.47 (*C15*), 71.47 (*C44*), 71.42 (*C8*), 53.10 (*C27*), 39.46 (*C23*), 30.88 (*C26*), 28.87 (*C25*), 23.05 (*C24*).

IR (ATR) (cm^{-1}): 3361 (O-H), 2934 (C-H), 1733 (C=O acid), 1650 (C=O amide), 1572 (C=C aromatic), 1521 (N-H).

Data consistent with literature values. [180]

[NGB-05] *N^2,N^6*-Bis(2,3-dihydroxybenzoyl)-*L*-lysine (azotochelin)

$C_{20}H_{22}N_2O_8$

MW = 418.40 g mol^{-1}
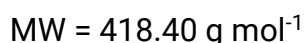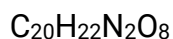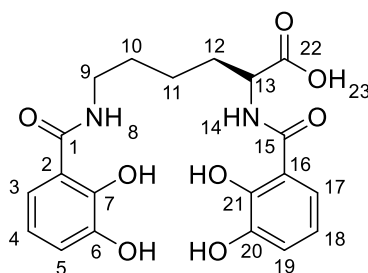
The compound was prepared based on a modified procedure from the literature.[180]

The glassware was soaked overnight in 6 M HCl and rinsed with deionised water and acetone. *N^2,N^6*-Bis(2,3-dibnzyloxybenzoyl)-*L*-lysine **[NGB-04]** (0.407 g, 0.523 mmol, 1.0 equiv) was dissolved in anhydrous mixture of

ethanol and toluene (40 mL) (28:1, v/v%) to which palladium on carbon (10%) (0.106 g, 0.25 equiv, w/w%) was added. The reaction mixture was stirred overnight at room temperature under a positive hydrogen atmosphere. The solution was filtered through Whatman (GF/F) glass microfiber filter and the solvent removed *in vacuo* to yield a white amorphous solid of the title compound; **0.210 g, 0.601 mmol, 96%**.

R_f: (chloroform:MeOH, 95:5): 0.0.

HRMS: (EIS): Calcd. for $C_{20}H_{21}N_2O_8$ $[M-H]^-$ 417.1303; found 417.1304 (mean error -1.0 ppm).

^{1}H NMR: (400 MHz, CD$_3$OD): δ 7.32 (d, *J* = 8.0 Hz, 1H, *H17*), 7.18 (d, *J* = 8.1 Hz, 1H, *H3*), 6.92 (dd, *J* = 12.2, 7.7 Hz, 2H, *H5,19*), 6.70 (dt, *J* = 15.4, 8.0 Hz, 2H, *H4,18*), 4.62 (dd, *J* = 8.8, 4.9 Hz, 1H, *H13*), 3.39 (t, *J* = 7.0 Hz, 2H, *H9*), 2.09 − 2.00 (m, 1H, *H12$_a$*), 1.96 − 1.87 (m, 1H, *H12$_b$*), 1.75 − 1.63 (m, 2H, *H10*), 1.57 − 1.50 (m, 2H, *H11*).

^{13}C NMR: (101 MHz, CD$_3$OD): δ 175.30 (*C22*), 171.33 (*C15*), 170.76 (*C1*), 150.06 (*C7,21*), 149.52 (*C6,20*), 147.10 (*C16*), 147.01 (*C2*), 119.54, 119.33 (*C5,19*), 119.26, 118.38 (*C3,17*), 116.78, 116.55 (*C4,18*), 52.90 (*C13*), 39.99 (*C9*), 32.43 (*C12*), 30.55 (*C10*), 24.80 (*C11*).

IR (ATR) (cm^{-1}): 3307 (O-H), 2936 (C-H), 1723 (C=O acid), 1636 (C=O amide), 1585 (C=C), 1539 (N-H).

Data consistent with literature values. [180]

[NGB-06] N^2,N^6-Bis(2,3-dihydroxybenzoyl-*L*-serine) (bisDHBS)

$C_{20}H_{20}N_2O_{11}$

MW = 464.38 g mol^{-1}
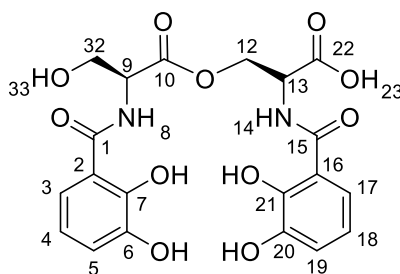
The compound was prepared based on a procedure from the literature.[300]

The glassware was soaked overnight in 6 M HCl and rinsed with deionised water and acetone. N^2,N^6-Bis(2,3-dibenzyloxybenzoyl)-*L*-serine (0.177 g, 0.176 mmol, 1.0 equiv) was dissolved in anhydrous mixture of ethanol and toluene (25 mL) (95:5, v/v%) to which palladium on carbon (10%) (46.1 mg, 0.26 equiv, w/w%) was added. The reaction mixture was stirred overnight at room temperature under a positive hydrogen atmosphere. The solution was filtered through Whatman (GF/F) glass microfiber filter and the solvent removed *in vacuo* to yield a white amorphous solid of the title compound; **81.7 mg**, **0.176 mmol**, **100%**.

R_f: (DCM:MeCN, 9:1): 0.0.

HRMS: (EIS): Calcd. for $C_{20}H_{19}N_2O_{11}$ [M-H]$^-$ 463.0994; found 463.0986 (mean error 2.6 ppm).

^{1}H NMR: (400 MHz, (CD$_3$)$_2$SO): δ 11.70 (s, 1H, *H23*), 9.80 (s, 1H, *H33*), 9.00 (d, *J* = 7.6 Hz, 1H, *H8*), 8.94 (d, *J* = 7.3 Hz, 1H, *H14*), 7.37 (dd, *J* = 8.1, 1.5 Hz, 1H, *H17*), 7.34 (dd, *J* = 8.1, 1.5 Hz, 1H, *H3*), 6.96 − 6.92 (m, 2H, *H5,19*), 6.71 (q, *J* = 7.7 Hz, 2H, *H4,18*), 4.81 (q, *J* = 5.8 Hz, 1H, *H9*), 4.62 − 4.55 (m, 2H, *H12a,32*), 4.41 (dd, *J* = 11.2, 6.5 Hz, 1H, *H13*) 3.84 − 3.75 (m, 2H, *H12b*).

^{13}C NMR: (101 MHz, (CD$_3$)$_2$SO): δ 170.32 (*C10*), 169.93 (*C22*), 168.83 (C*15*), 168.52 (*C1*), 148.69, 148.26 (*C7,21*), 146.14, 146.04 (*C6,20*), 119.01, 118.86 (*C2,16*), 118.60, 118.31 (*C5,19*), 118.27, 118.16 (*C3,17*), 115.91, 115.52 (*C4,18*), 64.93 (*C12*), 63.61 (*C32*), 55.23 (*C13*), 51.55 (*C9*).

IR (ATR) (cm^{-1}): 3367 (O-H), 2969 (C-H), 1739 (C=O acid, ester), 1638 (C=O amide), 1585 (C=C), 1533 (N-H), 1172 (C-O ester).

Data consistent with literature values. [300]

[NGB-07] *N*-(2,3-Dibenzyloxybenzoyl)-diaminobutane hydrochloride

(Bn$_2$-aminochelin)

$C_{25}H_{29}N_2O_3Cl$

MW = 440.97 g mol^{-1}
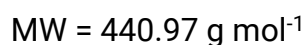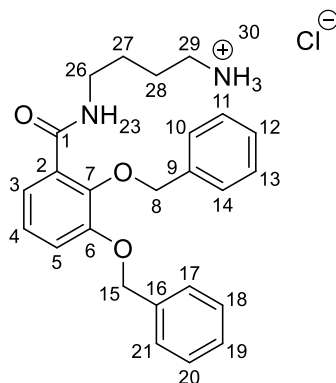
The compound was prepared based on a procedure from the literature.[174]

2,3-Bis(benzyloxy)benzoic acid **[NGB-02]** (0.501 g, 1.50 mmol, 1.0 equiv) and *N,N'*-carbonyldiimidazole (0.244 g, 1.50 mmol, 1.0 equiv) were dissolved in anhydrous tetrahydrofuran (12 mL). The resulting solution was added dropwise over 30 minutes to 1,4-diaminobutane (0.15 mL, 1.50 mmol, 1.0 equiv) in anhydrous tetrahydrofuran (20 mL). The reaction mixture was stirred overnight at room temperature under an inert atmosphere. The solvent was removed *in vacuo* and the solid was redissolved in chloroform (25 mL). The organic layer was washed with NaHCO$_3$ (2 x 20 mL), brine (1 x 20 mL), 2 M HCl (2 x 20 mL) and brine (1 x 20 mL). The solvent was partly removed *in vacuo* and ethyl acetate was added (30 mL). The solvent was removed *in vacuo* until a white precipitate formed. The solid was collected and washed with ethyl acetate (2 x 20 mL), yielding white solid granules of the title compound; **0.212 g**, **0.48 mmol**, **32%**.

HRMS: (EIS): Calcd. for $C_{25}H_{29}N_2O_3$ [M-Cl]$^+$ 405.2173; found 405.2184 (mean error -2.5 ppm). Calcd. for $C_{25}H_{28}N_2NaO_3$ [M-Cl-H+Na]$^+$ 427.1992; found 427.2002 (mean

error -3.0 ppm). Calcd. for $C_{25}H_{28}N_2KO_3$ $[M-Cl-H+K]^+$ 443.1723; found 443.1744 (mean error -2.2 ppm).

^{1}H NMR: (400 MHz, D$_2$O): δ 7.18 – 7.04 (m, 8H, *H10-14,H17-21*), 7.00 – 6.94 (m, 2H, *H3,5*), 6.83 (dd, *J* = 8.3, 1.5 Hz, 1H, *H4*), 4.66 (s, 2H, *H8*), 4.65 (s, 2H, *H15*), 3.03 (t, *J* = 7.3 Hz, 2H, *H26*), 2.79 (t, *J* = 7.7 Hz, 2H, *H29*), 1.51 – 1.44 (m, 2H, *H27*), 1.29 – 1.21 (m, 2H, *H28*).

^{13}C NMR: (101 MHz, D$_2$O): δ 167.73 (*C1*), 151.28 (*C2*), 145.05 (*C3*), 136.89 (*C7*), 136.00 (*C6*), 128.82, 128.73, 128.58, 128.47, 128.05, 127.81 (*C9-14,16-21*), 124.96 (*C5*), 121.41 (*C4*), 116.81 (*C29*), 75.90 (*C8*), 70.50 (*C15*), 38.95 (*C26*), 25.44 (*C27*), 24.25 (*C28*).

IR (ATR) (cm^{-1}): 3365 (N-H secondary), 3080 (C-H), 2804 (N-H cation), 1640 (C=O), 1570 (C=C aromatic).

Data consistent with literature values. [174]

[NGB-08] *N^1*-[*N^2,N^6*-Bis(2,3-dibenzyloxybenzoyl)-*L*-lysyl]-*N^4*-(2,3-di-benzyloxyenzoyl) -1,4-diaminobutane (Bn$_6$-protochelin)

$C_{73}H_{72}N_4O_{10}$

MW = 1165.40 g mol^{-1}
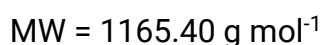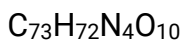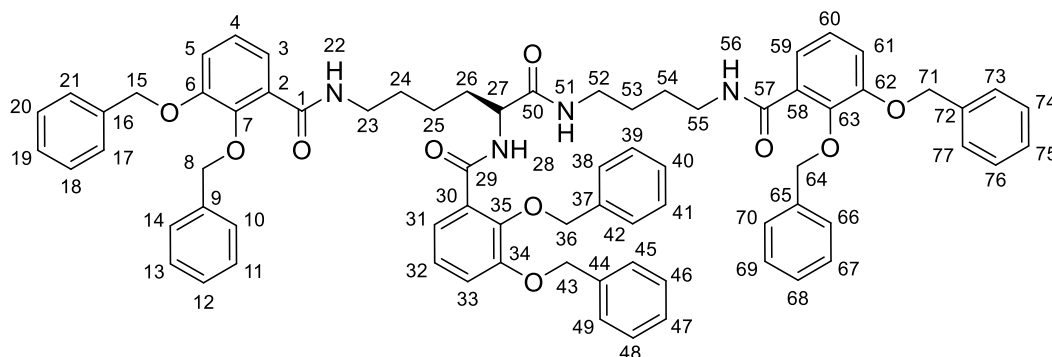
The compound was prepared based on a procedure from the literature.[174]

N^2,N^6-Bis(2,3-dibenzyloxybenzoyl)-*L*-lysine **[NGB-04]** (0.252 g, 0.324 mmol, 1.0 equiv) and *N,N,N',N'*-tetramethyl-*O*-(1H-benzotriazol-1-yl)uronium hexa-fluorophosphate (0.122 g, 0.322 mmol, 1.0 equiv) were dissolved in anhydrous tetrahydrofuran (6 mL) and anhydrous acetonitrile (4 mL). *N,N*-Diisopropylethylamine (0.15 mL, 0.861 mmol, 2.0 equiv) and *N*-(2,3-

dibenzyloxybenzoyl)-diaminobutane hydrochloride **[NGB-07]** (0.140 g, 0.317 mmol, 1.0 equiv) were added and the reaction mixture was stirred overnight at room temperature under an inert atmosphere. The solvent was removed *in vacuo* and brine was added (20 mL). The product was extracted with EtOAc (3 x 20 mL) and washed with 2 M HCl (10 mL), brine (10 mL), 5% $NaHCO_3$ (10 mL) and brine (10 mL). The solvent was removed *in vacuo* and the crude product was purified using flash column chromatography (EtOAc) to yield an off-white crystalline solid of the title compound; **0.254 g**, **0.218 mmol**, **69%**.

Rf: (EtOAc): 0.67.

HRMS: (EIS): Calcd. for $C_{73}H_{72}N_4NaO_{10}$ [M+Na]$^+$ 1187.51; found 1187.51 (mean error 1.8 ppm).

¹H NMR: (400 MHz, CDCl₃): δ 8.29 (d, *J* = 7.2 Hz, 1H, *H28*), 7.87 (t, *J* = 5.7 Hz, 1H, *H22*), 7.84 (t, *J* = 5.7 Hz, 1H, *H56*) 7.41 − 7.19 (m, 33H, *H10-14,17-21,31-33,38-42,45-49,66-70,73-77*), 7.07 − 7.04 (m, 6H, *H3-5,59-61*), 6.52 (br s, 1H, *H51*), 5.08 − 4.98 (m, 12H, *H8,15,36,43,64,71*), 4.30 (q, *J* = 7.3 Hz, 1H, *H27*), 3.16 (q, *J* = 6.3 Hz, 2H, *H52*), 3.11 − 3.03 (m, 4H, *H23,55*), 1.65 − 1.57 (m, 2H, *H26*), 1.33 − 1.23, 1.11 − 1.05, (m, 8H, *H24-25,53-54*).

¹³C NMR: (101 MHz, CDCl₃): δ 174.18 (*C50*), 171.47 (*C29*), 151.56 (*C57*), 151.50 (*C1*), 146.70, 146.58 (*C2,30,72*), 136.25, 136.20, 136.15, 136.11, 135.91 (*C6-7, 34-35,62-63*), 128.74, 128.57, 128.54, 128.51, 128.46, 128.12, 128.08, 127.60, 127.49, 127.48, 127.15 (*C9-14,16-21,37-42,44-49,65-70,72-77*), 124.20, 123.11, 122.94, 117.36, 116.72 (*C3-5,31-33,59-61*), 77.04 (*C36*), 76.69 (*C43*), 76.21 (*C64*), 75.96 (*C8*), 71.17 (*C71*), 71.08 (*C15*), 53.47 (*C27*), 39.02 (*C52*), 39.01 (*C55*), 38.96 (*C23*), 30.86 (*C26*), 28.70 (*C53*), 26.62 (*C54*), 26.48 (*C24*), 23.00 (*C25*).

Data consistent with literature values. [174]

[NGB-09] N^1-[N^2,N^6-Bis(2,3-dihydroxybenzoyl)-*L*-lysyl]-N^4-(2,3-dihydroxybenzoyl)-1,4-diaminobutane (protochelin)

$C_{31}H_{36}N_4O_{10}$
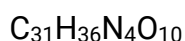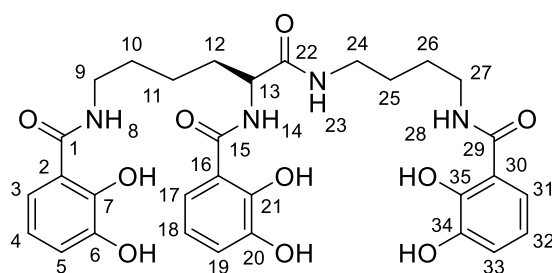
MW = 624.65 g mol^{-1}

The compound was prepared based on a modified procedure from the literature.[174]

The glassware was soaked overnight in 6 M HCl and rinsed with deionised water and acetone. N^1-[N^2,N^6-Bis(2,3-dibenzyloxybenzoyl)-*L*-lysyl]-N^4-(2,3-dibenzyloxybenzoyl)-1,4-diaminobutane **[NGB-09]** (0.152 g, 0.130 mmol, 1.0 equiv) was dissolved in anhydrous mixture of ethanol and toluene (25 mL) (95:5, v/v%) to which palladium on carbon (10%) (38.7 mg, 0.25 equiv, w/w%) was added. The reaction mixture was stirred for overnight at room temperature under a positive hydrogen atmosphere. The solution was filtered through Whatman (GF/F) glass microfiber filter and the solvent removed *in vacuo* to yield a white amorphous solid of the title compound; **79.9 mg**, **0.128 mmol**, **98%**.

R$_f$: (EtOAc): 0.0.

HRMS: (EIS): Calcd. for $C_{31}H_{37}N_4O_{10}$ [M+H]$^+$ 625.2504; found 625.2515 (mean error -2.1 ppm). Calcd. for $C_{31}H_{36}N_4NaO_{10}$ [M+Na]$^+$ 647.2324; found 647.2317 (mean error 1.9 ppm).

^{1}H NMR: (400 MHz, CD$_3$OD): δ 7.42 (dd, *J* = 8.2, 1.5 Hz, 1H, *H17*), 7.30 (t, *J* = 7.1 Hz, 2H, *H3,31*), 7.03 (t, *J* = 7.3 Hz, 3H, *H5,19,33*), 6.81 (q, *J* = 7.8 Hz, 3H, *H4,18,32*), 4.64 (dd, *J* = 8.4, 5.8 Hz, 1H, *H13*), 3.40 − 3.36 (m, 4H, *H9,27*), 3.25 (q, *J* = 6.9 Hz, 2H, *H24*), 1.94 − 1.83 (m, 2H, *H12*), 1.69 − 1.56 (m, 6H, *H10,25,26*), 1.54 − 1.46 (m, 2H, *H11*).

^{13}C NMR: (101 MHz, CD$_3$OD): δ 174.39 (*C22*), 171.53 (*C15*), 170.50 (*C1,29*), 150.32, 150.08, 149.47, 147.32, 147.17 (*C6-7,20-21,34-35*), 119.80, 119.70, 119.63, 119.54, 118.60, 117.28, 116.77, 116.71 (*C3-5,17-19,31-33*), 55.58 (*C13*), 40.14 (*C24*), 40.06 (*C9,27*), 32.98 (*C12*), 30.05 (*C10*), 27.79 (*C26*), 27.75 (*C25*), 25.09 (*C11*).

IR (ATR) (cm^{-1}): 3330 (O-H), 2930 (C-H), 1636 (C=O amide), 1585 (C=C), 1537 (N-H).

Data consistent with literature values. [174]

[NGB-10] α-Lipoic acid *N*-hydroxysuccinimide ester (LA NHS)

C$_{12}$H$_{17}$NO$_4$S$_2$

MW = 303.39 g mol^{-1}
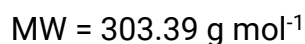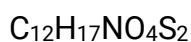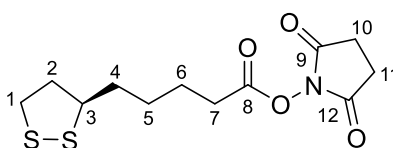
The compound was prepared based on a modified procedure from the literature.[301]

α-Lipoic acid (0.500 g, 2.42 mmol, 1.0 equiv) and *N*-hydroxysuccinimide (0.307 g, 2.67 mmol, 1.1 equiv) were dissolved in anhydrous tetrahydrofuran (20 mL) and the resulting solution was cooled down to 0°C. *N,N'*-Dicyclohexyl carbodiimide (0.550 g, 2.67 mmol, 1.1 equiv) dissolved in anhydrous tetrahydrofuran (5 mL) was added dropwise and the reaction mixture was left to stir for 10 minutes. The flask was allowed to warm up to room temperature and the reaction was stirred for 48 hours under an inert atmosphere. The resulting suspension was filtered through Celite™, and the bulk solvent was removed *in vacuo*. The solid was dissolved in ethyl acetate (20 mL), cooled down in an ice bath and filtrated through Celite™. The filtrate was collected and concentrated *in vacuo*. The crude product was recrystallised from ethyl acetate and hexane to yield a yellow crystalline solid of the title compound; **0.418 g**, **1.38 mmol**, **57%**.

R_f: (EtOAc): 0.64.

HRMS: (EIS): Calcd. for $C_{12}H_{18}NO_4S_2$ [M+H]$^+$ 304.0672; found 304.0671 (mean error - 1.4 ppm). Calcd. for $C_{12}H_{17}NNaO_4S_2$ [M+Na]$^+$ 326.0491; found 326.0487 (mean error 0.9 ppm).

¹H NMR: (400 MHz, CDCl₃): δ 3.61 − 3.55 (m, 1H, *H3*), 3.22 − 3.09 (m, 2H, *H1*), 2.84 (d, *J* = 4.1 Hz, 4H, *H10,11*), 2.63 (t, *J* = 7.3 Hz, 2H, *H7*), 2.51 − 2.43 (m, 1H, *H2_a*), 1.97 − 1.88 (m, 1H, *H2_b*), 1.79 (p, *J* = 7.6 Hz, 2H, *H6*), 1.74 − 1.68 (m, 2H, *H4*), 1.62 − 1.57 (m, 2H, *H5*).

¹³C NMR: (101 MHz, CDCl₃): δ 168.97 (*C8*), 168.25 (*C9,12*), 55.90 (*C3*), 39.98 (*C1*), 38.34 (*C2*), 34.24 (*C7*), 30.60 (*C4*), 28.14 (*C5*), 25.40 (*C10,11*), 24.17 (*C6*).

IR (ATR) (cm⁻¹): 2938 (C-H), 1809, 1778 (C=O amide), 1729 (C=O ester), 1203 (C-O).

Data consistent with literature values. [301]

[NGB-11] *N_α,N_α*-Bis[(*tert*-butyloxycarbonyl)methyl]-*N_ε*-(benzyloxy carbonyl)-*L*-lysine *tert*-butyl ester

$C_{30}H_{48}N_2O_8$

MW = 564.72 g mol⁻¹
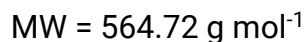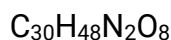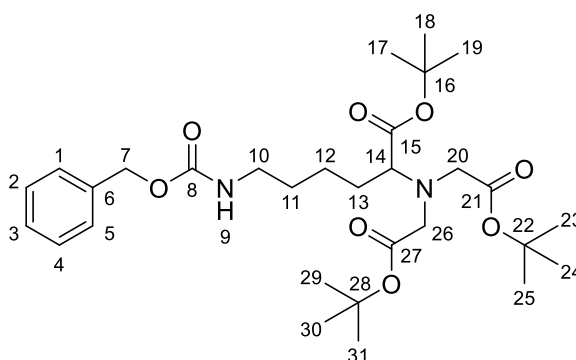
The compound was prepared based on a modified procedure from the literature.[302]

2-Amino-6-benzyloxycarbonylaminohexanoic acid *tert*-butyl ester (1.00 g, 2.68 mmol, 1.0 equiv) was dissolved in dimethylformamide (30 mL). *N,N*-Diisopropylethylamine (2.80 mL, 16.1 mmol, 6.0 equiv) and *tert*-butyl bromoacetate (1.30 mL, 8.81 mmol, 3.2 equiv) were added to the stirring

solution and the reaction was heated at 55°C for 51 hours under an inert atmosphere. The solvent was removed *in vacuo* and the crude product was dissolved in dichloromethane (100 mL) and washed with 1 M HCl (2 x 100 mL), saturated NaHCO$_3$ (2 x 100 mL) and brine (1 x 100 mL). The solvent was removed in vacuo and the crude product was purified using purified using flash column chromatography (petroleum ether:EtOAc, 7:3) to yield yellow oil of the title compound; **1.10 g, 1.95 mmol, 73%.**

R$_f$: (petroleum ether:EtOAc, 7:3): 0.39.

HRMS: (EIS): Calcd. for C$_{30}$H$_{49}$N$_2$O$_8$ [M+H]$^+$ 565.3483; found 565.3501 (mean error -3.4 ppm). Calcd. for C$_{30}$H$_{48}$N$_2$NaO$_8$ [M+Na]$^+$ 587.3303; found 587.3321 (mean error -3.6 ppm).

^{1}H NMR: (400 MHz, CDCl$_3$): δ 7.35 − 7.30 (m, 5H, *H1-5*), 5.08 (s, 2H, *H7*), 3.44 (d, *J* = 8.6 Hz, 4H, *H20,26*), 3.29 (t, *J* = 7.5 Hz, 1H, *H14*), 3.23 − 3.15 (m, 2H, *H10*), 1.57 − 1.48 (m, 4H, *H11,13*), 1.45 (s, 9H, *H17-19*), 1.43 (s, 18H, *H23-25,29-31*), 1.29 − 1.24 (m, 2H, *H12*).

^{13}C NMR: (101 MHz, CDCl$_3$): δ 172.56 (*C15*), 170.86 (*C21,27*), 156.42 (*C8*), 136.74 (*C6*), 128.59, 128.23, 128.10 (*C2-5*), 81.27 (*C16*), 80.87 (*C22,28*), 67.06 (*C7*), 65.21 (*C14*), 54.04 (*C20,26*), 41.50 (*C10*), 30.25 (*C13*) , 29.37 (*C11*), 28.36 (*C17-19*), 28.24 (*C23-25,29-31*), 23.14 (*C12*).

IR (ATR) (cm^{-1}): 3383 (N-H amide), 2977 (C-H), 1721 (C=O), 1526 (C=C), 1138 (C-O).

Data consistent with literature values. [302]

[NGB-12] N_a,N_α-Bis[(*tert*-butyloxycarbonyl)methyl]-*L*-lysine *tert*-butyl ester

$C_{22}H_{42}N_2O_6$
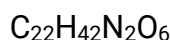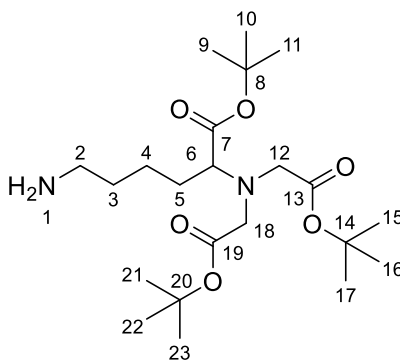
MW = 430.59 g mol^{-1}

The compound was prepared based on a procedure from the literature.[302]

N_a,N_α-Bis[(*tert*-butyloxycarbonyl)methyl]-N_ε-(benzyloxycarbonyl)-*L*-lysine *tert*-butyl ester **[NGB-12]** (0.502 g, 0.889 mmol, 1.0 equiv), was dissolved in anhydrous methanol (15 mL) to which palladium on carbon (5%) (53.0 mg, 0.10 equiv, w/w%) was added. The reaction mixture was stirred for 6 hours at room temperature under a positive hydrogen atmosphere. The solution was filtered through Whatman (GF/F) glass microfiber filter and the solvent removed *in vacuo* to yield a colourless oil of the title compound; **0.360 g, 0.836 mmol, 94%.**

R$_f$: (petroleum ether:EtOAc, 7:3): 0.12.

HRMS: (EIS): Calcd. for $C_{22}H_{43}N_2O_6$ [M+H]$^+$ 431.3116; found 431.3115 (mean error -0.4 ppm). Calcd. for $C_{22}H_{42}N_2NaO_6$ [M+Na]$^+$ 453.2935; found 453.2939 (mean error -0.8 ppm).

^{1}H NMR: (400 MHz, CD$_3$OD): δ 3.46 (q, *J* = 17.2, 12.7 Hz, 5H, *H6,12,18*), 2.65 (t, *J* = 6.9 Hz, 2H, *H2*), 1.66 – 1.62 (m, 2H, *H5*), 1.54 – 1.49 (m, 4H, *H3,4*), 1.47 (s, 9H, *H9-11*), 1.46 (s, 18H, *H15-17,21-23*).

^{13}C NMR: (101 MHz, CD$_3$OD): δ 173.87 (*C7*), 172.44 (*C13,19*), 82.44 (*C8*), 82.04 (*C14,20*), 66.73 (*C6*), 54.82 (*C12,18*), 42.25 (*C2*), 33.10 (*C5*), 31.44 (*C3*), 28.48 (*C9-11*), 28.39 (*C15-17,21-23*), 24.38 (*C3*).

IR (ATR) (cm^{-1}): 3411 (N-H amine), 2977 (C-H), 1724 (C=O), 1144 (C-O).

Data consistent with literature values. [302]

[NGB-13] *N*-[5-(1,2-Dithiolan-3-ylpentanoyl-amino)-1-(*tert*-butylcarboxy pentyl]imino-bis(tert-butyl ester) (LA NTA(*t*Bu))

$C_{30}H_{54}N_2O_7S_2$
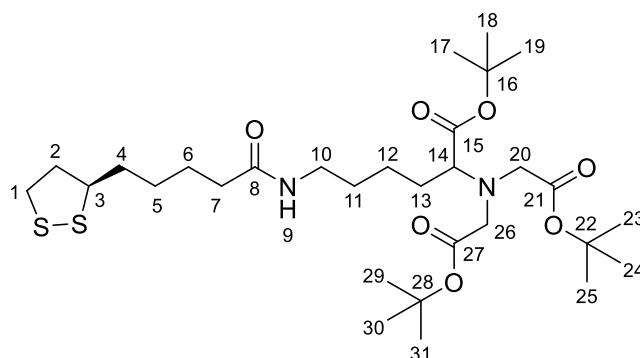
MW = 618.89 g mol^{-1}

N_α,N_α-Bis[(*tert*-butyloxycarbonyl)methyl]-*L*-lysine *tert*-butyl ester **[NGB-13]** (0.336 g, 0.781 mmol, 1.0 equiv) and *N*,*N*-diisopropylethylamine (0.5 mL, 2.87 mmol, 3.7 equiv) were dissolved in methanol (5 mL). A solution of α-lipoic acid *N*-hydroxysuccinimide ester **[NGB-11]** (0.237 g, 0.781 mmol, 1.0 equiv) in tetrahydrofuran (5 mL) was added and the resulting solution was stirred overnight at room temperature. The reaction mixture was concentrated, taken up in ethyl acetate (40 mL) and washed with 1 M HCl (2 x 40 mL), saturated NaHCO$_3$ (2 x 40 mL) and brine (2 x 40 mL). The solvent was removed *in vacuo* and the crude product was purified using flash column chromatography (DCM:MeOH:TEA, 93:6:1) to yield a yellow oil of the title compound; **0.388 g**, **0.627 g**, **80%**.

R$_f$: (DCM:MeOH, 95:5): 0.65.

HRMS: (EIS): Calcd. for $C_{30}H_{55}N_2O_7S_2$ [M+H]$^+$ 619.3445; found 619.3460 (mean error -3.1 ppm). Calcd. for $C_{30}H_{54}N_2NaO_7S_2$ [M+Na]$^+$ 641.3265; found 641.3274 (mean error -2.0 ppm).

^{1}H NMR: (400 MHz, CD$_3$OD): δ 3.58 (dq, *J* = 8.8, 6.3 Hz, 1H, *H3*), 3.48 (q, *J* = 17.3, 12.9 Hz, 4H, *H20,26*), 3.32 (t, *J* = 9.8 Hz, 2H, *H10*), 3.19 − 3.15 (m, 2H, *H1*), 3.13 − 3.07 (m, 1H, *H14*), 2.41 (dq, *J* = 12.5, 6.6 Hz, 1H, *H2$_a$*), 2.20 (t, *J* = 7.4 Hz, 2H, *H7*), 1.89 (dq, *J* = 13.5, 6.8 Hz, 1H, *H2$_b$*), 1.76 − 1.60 (m, 8H, *H4,6,11,13*), 1.57 − 1.50 (m, 4H, *H5,12*), 1.47 (s, 9H, *H17-19*), 1.46 (s, 18H, *H23-25,H29-31*).

¹³C NMR: (101 MHz, CD₃OD): δ 176.01 (*C8*), 173.73 (*C15*), 172.37 (*C21,27*), 82.49 (*C16*), 82.10 (*C22,28*), 66.22 (*C1*), 57.58 (*C3*), 54.85 (*C20,26*), 41.73 (*C2*), 40.19 (*C10*), 39.35 (*C14*), 36.95 (*C7*), 35.77 (*C4*), 31.26 (*C5*), 29.94, 29.91 (*C11,13*), 28.49 (*C17-19*), 28.42 (*C23-25,29-31*), 26.81 (*C6*), 24.43 (*C12*).

IR (ATR) (cm⁻¹): 2930 (C-H), 1723 (C=O ester), 1645 (C=O amide), 1142 (C-O).

Data consistent with literature values. [302]

[**NGB-14**] *N*-[5-(1,2-Dithiolan-3-ylpentanoylamino)-1-carboxypentyl] iminodiacetic acid (LA NTA)

$C_{18}H_{30}N_2O_7S_2$

MW = 450.57 g mol⁻¹
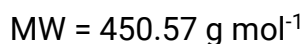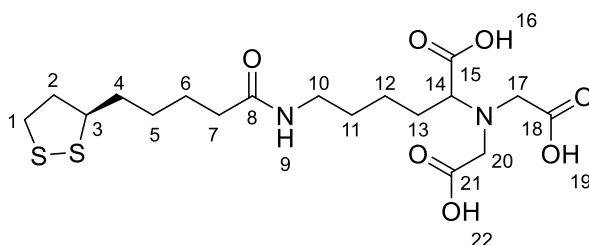
The compound was prepared based on a modified procedure from the literature.[302]

N-[5-(1,2-Dithiolan-3-ylpentanoyl-amino)-1-(*tert*-butylcarboxypentyl]imino-bis(tert-butyl ester) [**NGB-14**] (0.847 g, 1.37 mmol, 1.0 equiv) was dissolved in trifluoroacetic acid, diluted in dichloromethane (10 mL, 0.9, v/v%) and stirred overnight at room temperature. The solvent was removed *in vacuo* to give a yellow crystalline solid of the title compound; **0.560 g, 1.24 mmol, 91%.**

Rf: (DCM:MeOH, 9:1): 0.0.

HRMS: (EIS): Calcd. for $C_{18}H_{29}N_2O_7S_2$ [M-H]⁻ 449.1422; found 449.1429 (mean error -1.3 ppm).

¹H NMR: (400 MHz, CD₃OD): δ 3.70 − 3.67 (m, 4H, *H17,20*), 3.60 − 3.56 (m, 1H, *H3*), 3.21 − 3.17 (m, 4H, *H1,10*), 3.13 − 3.07 (m, 1H, *H14*), 2.46 (dq, *J* = 12.5, 6.6 Hz, 1H, *H2a*),

2.20 (t, *J* = 7.4 Hz, 2H, *H7*), 1.88 (dq, *J* = 13.5, 6.8 Hz, 1H, *H2$_b$*), 1.74 − 1.62 (m, 12H, *H4-6,11-13*).

^{13}**C NMR: (101 MHz, CD$_3$OD:(CD$_3$)$_2$SO, 99:1):** δ 175.77 (*C8*), 174.77 (*C15*), 174.02, 173.43 (*C18,21*), 66.88 (*C1*), 66.30 (*C3*), 57.59, 55.21 (*C17,20*), 52.61 (*C10*), 52.02 (*C2*), 41.33 (*C14*), 36.90 (*C7*), 35.72 (*C4*), 35.05 (*C5*), 30.06, 30.00 (*C11,13*) 29.89 (*C6*), 26.75 (*C12*).

IR (ATR) (cm^{-1}): 3305 (O-H), 2932 (C-H), 1727 (C=O ester), 1609 (C=O amide), 1181 (C-O).

Data consistent with literature values. [302]

[**NGB-15**] 1,1'-Di(hydroxymethyl)ferrocene (Fc(OH)$_2$)

C$_{12}$H$_{14}$FeO$_2$

MW = 246.09 g mol^{-1}
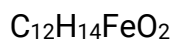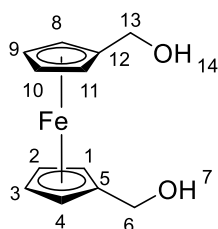
The compound was prepared based on a modified procedure from the literature.[303]

Sodium borohydride (0.138 g, 3.69 mmol, 2.2 equiv) was suspended in anhydrous tetrahydrofuran (5 mL) to which 1,1'-ferrocenedicarboxaldehyde (0.400 g, 1.65 mmol, 1.0 equiv) in anhydrous tetrahydrofuran (5 mL) was added dropwise. The reaction mixture was stirred at room temperature under an inert atmosphere for 1 hour. Sodium borohydride (0.162 g, 4.28 mmol, 2.6 equiv) was added in two portions within a 15-minute interval and the suspension was stirred for further 15 minutes. The reaction mixture was filtered through Celite™ and the residue was washed with tetrahydrofuran (3 x 20 mL). The reaction on Celite™ was suspended in tetrahydrofuran (50 mL), 1 M HCl was added until effervescence ceased followed by deionised water (5 mL) and the suspension was stirred for 15 minutes. The Celite™

was filtered off and the tetrahydrofuran was extracted with ethyl acetate (3 x 25 ml). The organic layer was washed brine (2 x 30 mL) and combined with tetrahydrofuran fractions. The solvent was removed *in vacuo* and the crude product was purified using flash column chromatography (DCM:MeOH, 95:5) to yield an orange crystalline solid of the title compound; **0.325 g**, **1.32 mmol**, **80%**.

HRMS: (EIS): Calcd. for $C_{12}H_{14}FeNaO_2$ [M+Na]$^+$ 269.0235; found 269.0233 (mean error 0.6 ppm).

¹H NMR: (400 MHz, CDCl₃): δ 4.38 (s, 4H, *H6,13*), 4.33 − 4.18 (m, 8H, *H1-4,8-11*), 2.44 (s, 2H, *H7,14*).

¹³C NMR: (101 MHz, CDCl₃): δ 91.29 (*C5,12*), 69.41, 69.03, 68.47, 68.03 (*C1-4,8-11*), 61.68 (*C6,13*).

IR (ATR) (cm⁻¹): 3275 (O-H), 2935 (C-H), 1050 (C-O).

Data consistent with literature values. [303]

[**NGB-16**] 1,1'-Bis(pyridiniomethyl)ferrocene bis(hexafluorophosphate) (Fc(py)₂)

$$C_{22}H_{22}FeN_2F_{12}P_2$$

MW = 660.20 g mol⁻¹
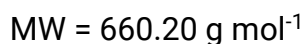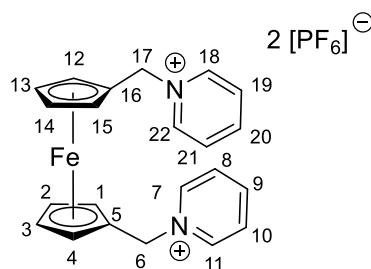
The compound was prepared based on a modified procedure from the literature.[126,267]

1,1'-Di(hydroxymethyl)ferrocene [**NGB-16**] (0.101 g, 0.410 mmol, 1.0 equiv) was dissolved in anhydrous tetrahydrofuran (8 mL) and anhydrous pyridine (0.15 mL, 1.85 mmol, 4.5 equiv) was added. The reaction was cooled down

to 0°C and a solution of phosphorus tribromide (0.31 mL, 3.30 mmol, 8.0 equiv) in anhydrous tetrahydrofuran (2 mL) was added dropwise. The resulting suspension was stirred for 1 hour, allowed to warm up to room temperature and stirred overnight under an inert atmosphere. The solid was collected, washed with a minimal amount of tetrahydrofuran, and dissolved in deionised water (10 mL). Potassium hexafluorophosphate (90.9 mg, 0.49 mmol) was added and the resulting suspension was stirred at 0°C for 2 hours. The yellow precipitate of the title compound was collected by filtration and allowed to dry; **0.168 g**, **0.254 mmol**, **62%**.

HRMS: (EIS): Calcd. for $C_{22}H_{22}FeN_2$ $[M]^{+2}$ 185.0561; found 185.0558 (mean error 0.4 ppm).

^{1}H NMR: (400 MHz, (CD$_3$)$_2$SO): δ 9.10 (d, *J* = 6.0 Hz, 4H, *H7,11,18,22*), 8.60 (t, *J* = 7.8 Hz, 2H, *H9,20*), 8.16 (t, *J* = 7.0 Hz, 4H, *H8,10,19,21*), 5.63 (s, 4H, *H6,17*), 4.65 (s, 4H, *H1,4,12,15*), 4.39 (s, 4H, *H2,3,13,14*).

^{13}C NMR: (101 MHz, (CD$_3$)$_2$SO): δ 145.70 (*C7,11,18,22*), 144.06 (*C8,10,19,21*), 128.39 (*C9,20*), 81.43 (*C5,16*), 70.68 (*C1,4,12,15*), 70.42 (*C2,3,13,14*), 59.38 (*C6,17*). **IR (ATR) (cm^{-1}):** 3094 (C-H), 1632 (C=N), 1142 (C-N).

Data consistent with literature values. [126,267]

[**NGB-17**] 1,1'-Bis(*N*-imidazolylmethyl)ferrocene (Fc(imd)$_2$)

$C_{18}H_{18}FeN_4$

MW = 346.22 g mol^{-1}
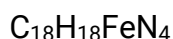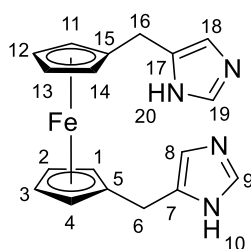
The compound was prepared based on a procedure from the literature.[126]

1,1'-Bis(pyridiniomethyl)ferrocene bis(hexafluorophosphate) [**NGB-17**] (0.132 g, 0.200 mmol, 1.0 equiv) and imidazole (67.8 mg, 0.996 mmol, 5.0

equiv) were dissolved in anhydrous acetonitrile (6 mL). The reaction solution was refluxed for 43 hours under an inert atmosphere. The solvent was removed *in vacuo*, and the residue was redissolved in deionised water (30 mL). An aqueous solution of 1 M HCl was added until a pH of 3 was reached and the solution was extracted with dichloromethane (2 x 30 mL). Concentrated NaOH was added to the aqueous layer, adjusting it to pH 10 and the solution was extracted with dichloromethane (2 x 30 mL). The organic fractions were combined, and the solvent was removed *in vacuo*. The crude product was purified using flash column chromatography (DCM:MeOH, 8:2) to yield an orange solid of the title compound; **37.2 mg, 0.107 mmol, 54%**.

HRMS: (EIS): Calcd. for $C_{18}H_{19}FeN_4$ [M+H]$^+$ 347.0954; found 347.0955 (mean error -0.6 ppm). Calcd. for $C_{18}H_{18}FeN_4Na$ [M+Na]$^+$ 369.0773; found 369.0771 (mean error 1.0 ppm).

^{1}H NMR: (400 MHz, CDCl$_3$): δ 7.51 (s, 2H, *H10,20*), 7.05 (s, 2H, *H9,19*), 6.91 (s, 2H, *H8,18*), 4.80 (s, 4H, *H6,16*), 4.19 (s, 8H, *H1-4,11-14*).

^{13}C NMR: (101 MHz, CDCl$_3$): δ 136.46 (*C9,19*), 133.05 (*C8,18*), 127.99 (*C7,17*), 83.74 (*C5,15*), 69.82 (*C1,4,11,14*), 69.37 (*C2,3,12,13*), 46.51 (*C6,16*).

IR (ATR) (cm^{-1}): 3097 (N-H), 2924 (C-H), 1681 (C=N), 1616 (C=C), 1222 (C-N).

Data consistent with literature values. [126]

[**NGB-18**] 1-Ethyl-4,4'-bipyridinyl iodide (EV)

$C_{12}H_{13}N_2I$

MW = 312.15 g mol^{-1}
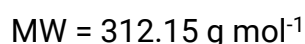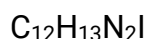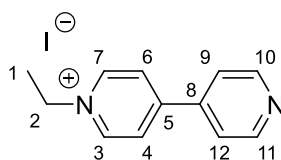
The compound was prepared based on a procedure from the literature.[304]

4,4'-Bipyridine (0.152 g, 0.973 mmol, 1.0 equiv) was dissolved in acetone (10 mL) and iodoethane (0.18 mL, 2.24 mmol, 2.3 equiv) was added dropwise to the stirring solution. The reaction was heated to reflux and stirred overnight under an inert atmosphere. The suspension was cooled down to room temperature and filtered to collect the orange solid of the title compound which was washed with excess acetone before drying; **0.147 g, 0.471 mmol**, **48%**.

HRMS: (EIS): Calcd. for $C_{12}H_{13}N_2$ $[M]^+$ 185.1073; found 185.1076 (mean error 0.6 ppm).

¹H NMR: (400 MHz, CDCl₃): δ 9.46 (dd, J = 6.8, 3.5 Hz, 2H, *H3,7*), 8.90 (dd, J = 6.2, 2.7 Hz, 2H, *H10,11*), 8.34 (dd, J = 6.8, 3.8 Hz, 2H, *H4,6*), 7.68 (dd, J = 6.20, 2.3 Hz, 2H, *H9,12*), 5.05 (q, J = 7.4 Hz, 2H, *H2*), 1.78 (t, J = 7.4 Hz, 3H, *H1*).

¹³C NMR: (101 MHz, CDCl₃): δ 162.69 (*C5*), 151.75 (C*3,7*), 145.28 (C*10,11*), 140.81 (*C8*), 126.18 (*C4,6*), 121.54 (*C9,12*), 57.66 (*C2*), 17.06 (*C1*).

IR (ATR) (cm⁻¹): 2969 (C-H), 1642 (C=N), 1174 (C-N).

Data consistent with literature values. [304]

[NGB-19] 1-(Carboxypentyl)-1'-ethyl-4,4'-bipyridinium dibromide

$C_{18}H_{24}N_2O_2Br_2$

MW = 460.21 g mol⁻¹
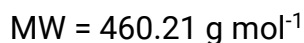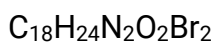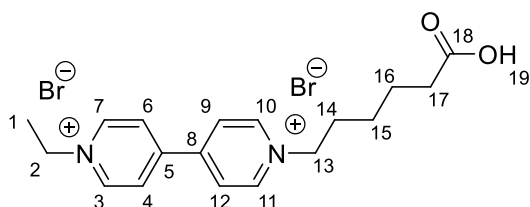
The compound was prepared based on a modified procedure from the literature.[305]

1-Ethyl-4,4'-bipyridinyl iodide **[NGB-19]** (0.500 g, 1.60 mmol, 1.0 equiv) was dissolved in anhydrous acetonitrile (5 mL). 6-Bromohexanoic acid (6.25 g, 32.0 mmol, excess) in anhydrous acetonitrile (15 mL) was added to the reaction and the resulting solution was refluxed under an inert atmosphere

for 70 hours. The solvent was removed *in vacuo* and the solid was suspend in a minimum volume of acetone. The suspension was filtered and the collected solid was washed with excess acetone. The crude product was recrystallised from hot ethanol and dissolved in deionised water. The suspension was filtered through Celite™, the filtrate flash-frozen and lyophilised overnight to yield a yellow solid of the title compound; **0.106 g, 0.230 mmol**, **14%**.

HRMS: (EIS): Calcd. for $C_{18}H_{23}N_2O_2$ [M-H]$^+$ 299.1754; found 299.1753 (mean error -4.7 ppm).

^{1}H NMR: (400 MHz, D$_2$O): δ 9.11 (t, *J* = 6.5 Hz, 4H, *H3,7,10,11*), 8.53 (d, *J* = 7.2 Hz, 4H, *H4,6,9,12*), 4.74 (q, *J* = 7.8, 7.3 Hz, 4H, *H2,13*), 2.37 (t, *J* = 7.3 Hz, 2H, *H17*), 2.10 (dt, *J* = 14.8, 7.0 Hz, 2H, *H14*), 1.71 − 1.62 (m, 5H, *H1,16*), 1.45 − 1.37 (m, 2H, *H15*).

^{13}C NMR: (101 MHz, D$_2$O): δ 179.34 (*C18*), 145.22 (*C3,7,10,11*), 126.99 (*C4,6,9,12*), 61.99 (*C13*), 57.16 (*C2*), 33.94 (*C17*), 30.28 (*C14*), 24.75 (*C15*), 23.75 (*C16*), 15.58 (*C1*).

IR (ATR) (cm^{-1}): 3338 (O-H), 2998 (C-H), 1704 (C=O), 1640 (C=N), 1178 (C-N).

[**NGB-20**] 1-(Carboxypentyl)-1‘-ethyl-4,4‘-bipyridinium *N*-hydroxy succinimide ester dibromide (EV NHS)

$C_{22}H_{27}Br_2N_3O_4$

MW = 555.04 g mol^{-1}
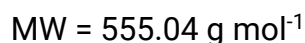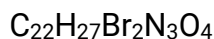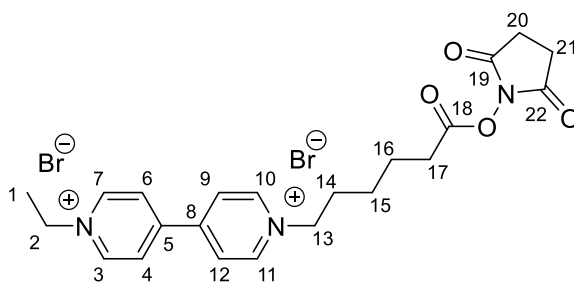
The compound was prepared based on a modified procedure from the literature.[306]

1-(Carboxypentyl)-1‘-ethyl-4,4‘-bipyridinium dibromide [**NGB-20**] (26.7 mg, 52.6 μmol, 1.0 equiv), *N*-hydroxysuccinimide (6.90 mg, 60.0 μmol, 1.1 equiv)

and *N,N'*-dicyclohexyl carbodiimide (12.8 mg, 62.0 μmol, 1.2 equiv) were dissolved in anhydrous dimethylformamide (10 mL). The solution was stirred overnight at room temperature under an inert atmosphere. The solvent was removed *in vacuo* and the solid was suspended in acetonitrile (20 mL). The suspension was filtered through Celite™ and the residue was washed with excess acetonitrile. The filtrate was concentrated to yield an orange solid which was a mixture of the title compound to starting material in a 0.4:1 ratio; **20.6 mg**, **37.2 μmol**, **71%**.

HRMS: (EIS): Calcd. for $C_{22}H_{27}N_3O_4$ $[M]^{2+}$ 198.5995; found 198.5984 (mean error 4.2 ppm).

^{1}H NMR: (400 MHz, CD$_3$CN): δ 9.13 − 9.10 (m, 4H, *H3,7,10,11*), 8.58 (d, *J* = 7.0 Hz, 4H, *H4,6,9,12*), 4.78 − 4.69 (m, 4H, *H2,13*), 2.75 (s, 2H, *H20*), 2.66 (t, *J* = 7.2 Hz, 2H, *H17*), 2.58 (s, 2H, *H21*), 2.12 − 2.02 (m, 2H, *H14*), 1.78 (p, *J* = 7.3 Hz, 2H, *H16*), 1.66 (t, *J* = 7.4 Hz, 3H, *H1*), 1.51 − 1.41 (m, 2H, *H15*).

^{13}C NMR: (101 MHz, CD$_3$CN): δ 171.21 (*C18*), 168.58 (*C19,22*), 145.18 (*C3,7,10,11*), 129.35 (*C4,6,9,12*), 62.49 (*C13*), 58.38 (*C2*), 31.28 (*C17*), 31.14 (*C14*), 26.40 (*C20*), 26.15 (*C21*), 25.45 (*C15*), 24.60 (*C16*), 16.25 (*C1*).

IR (ATR) (cm^{-1}): 2927 (C-H), 1731 (C=O), 1636 (C=N), 1206 (C-O), 1172 (C-N).

6.2 Electrochemical apparatus and methods

6.2.1 Instrumentation and set-up

All electrochemical experiments were conducted using a computer controlled PalmSens4 potentiostat (PalmSens BV) and the associated PSTrace 5 software for Windows. Unless otherwise stated, all experiments were performed at an ambient temperature inside an anaerobic glovebox (Mechanical Workshop, Department of Chemistry, University of York) which was maintained under a N_2 atmosphere ($O_2 \leq 2 − 8$ ppm). Solutions used in the experiments were deoxygenated with a stream of N_2 gas for at least 10 minutes prior to importing into the glovebox and then left overnight before using, allowing for the remaining O_2 to diffuse out.

6.2.2 Electrochemical cell

A conventional three-electrode set-up was used for all of the experiments; comprising a stationary working electrode, a Ag/AgCl (3 M NaCl) reference electrode (BASi) situated within a Luggin capillary and a platinum wire (Ø 0.2 mm) counter electrode (Electronics Workshop, Department of Chemistry, University of York). The type of the working electrode employed varied based on the nature of the experiment and the analyte of interest and was either a BDD disk (Ø 3 mm) electrode (BioLogic) (**Chapter 2**), a Au disk (Ø 3 mm) electrode (eDAQ, BASi) (**Chapter 3**) or a Au-coated silicon wafer (Ø 10 cm) electrode (Sigma Aldrich) (**Chapter 4**).

Experiments in **Chapter 2** utilising the BBD working electrode were conducted in a glass reaction vial, Reacti-Vial™ (Thermo Scientific). A custom-made PTFE lid (Mechanical Workshop, Department of Chemistry, University of York) was fitted on top and used to hold the three electrodes in place. In **Chapter 3**, a bespoke all-glass cell (Glassblowing Workshop, Department of Chemistry, University of York) made to accommodate a Au disk working electrode was employed. **Chapter 4** details experiments conducted on Au wafer electrodes which required the design and construction (Glassblowing, Mechanical and Electronic Workshops, Department of Chemistry, University of York) of a specialist electrochemical cell. A nylon 66 base was manufactured to house the working electrode with an all-glass reservoir position on top and held together by two acetal clamps; the design details are outlined in the relevant chapter.

6.2.3 Reference electrode calibration

All potentials in this thesis are quoted versus the reference electrode used, Ag/AgCl 3 M NaCl. The conversion factor (c.f.) between the reference electrode and the normal hydrogen electrode (NHE) was determined experimentally. The midpoint potential ($E_{1/2}$) value, calculated as the average of the cathodic (E_{pc}) and anodic (E_{pa}) peak positions for the

ferri/ferrocyanide redox couple was measured using cyclic voltammetry at a glassy carbon (GC) working electrode. The experimental $E_{1/2}$, 0.235 V vs Ag/AgCl 3 M NaCl was compared to the literature of 0.425 V vs NHE, to produce a c.f. of 0.190 V as described in **Equation 6.1**.[307]

$$Literature\ E_{1/2}\ (V\ vs\ NHE)$$
$$= Experimental\ E_{1/2}\ (V\ vs\ Ag/AgCl\ 3\ M\ NaCl) + c.f.$$

Equation 6.1 The relationship between literature and experimental $E_{1/2}$ values for a ferri/ferrocyanide redox couple for the determination of a conversion factor (c.f.) between the two reference electrodes. The experimental value was determined through cyclic voltammetry of 10 mM $K_3[Fe(CN)_6]$ in 100 mM phosphate buffer (I = 0.464 M, NaCl), pH 7.0.

6.2.4 Electrode preparation and modification protocols

Boron doped diamond disk electrodes comprise a very thin (*ca.* 500 μm) layer of the material adhered to a brass rod and thus abrasive mechanical polishing cannot be used. Sonication of the electrode in MilliQ water in three bursts of 15 seconds each after and before the experiment was used to remove any loosely adhered molecules and 'regenerate' the surface. BDD electrodes were used in experiments without further modification.

Gold disk electrodes were polished mechanically and electrochemically before being used either bare or for modification with SAM molecules. Mechanical polishing was performed on white felt polishing pads (Buehler) using aluminium oxide powder suspensions (MetPrep) of decreasing particle size, 1 (α), 0.3 (α) and 0.05 (γ) μm, for 1 minute per particle size. The electrodes were sonicated in MilliQ water for 3 minutes and ethanol for 3 minutes to remove any adhered aluminium particles before being dried under a stream of N_2. Cyclic voltammetry was used to electrochemically polish the electrodes; 50 scans at 100 mV s^{-1} were recorded in 0.5 M NaOH (from −1.25 to +0.65 V vs Ag/AgCl 3 M NaCl) before rinsing the electrodes in MilliQ H_2O and recording further 50 scans at 100 mV s^{-1} in 0.5 M H_2SO_4

(from −0.25 to +1.55 V vs Ag/AgCl 3 M NaCl). The above procedure was repeated until stable cyclic voltammograms was obtained with characteristic peak shape corresponding to a polished gold surface (**Figure 6.1**). The electrodes were thoroughly rinsed with MilliQ H$_2$O and dried under a stream of N$_2$ before being used, either bare or for SAM modification.
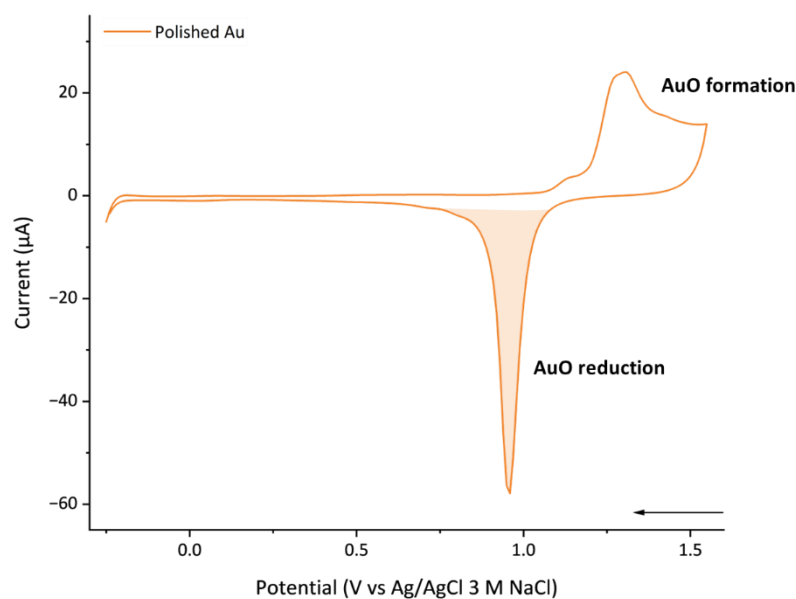
Figure 6.1 Representative cyclic voltammogram of a gold surface in 0.5 M H$_2$SO$_4$ recorded at 100 mV s^{-1}. Characteristic regions indicative of a polished electrode are highlighted; (**a**) minimum capacitive current is observed on a surface without any absorbed contaminants, (**b**) a single cathodic peak corresponds to the reduction of a single AuO monolayer.

Gold wafers were polished using an acidic Piranha solution, prepared by an addition of aqueous hydrogen peroxide 30% (Honeywell) to concentrated sulfuric acid (Fisher) in a 1:3 ratio. The substrates were immersed in the solution until the effervescence has ceased and rinsed thoroughly with MilliQ water before being dried under a stream of N$_2$ gas and used either bare or for SAM modification.

The same SAM assembly protocol was employed for both types of the Au surface. A polished and dry substrate was immersed in a 1 mM solution of the SAM molecule in ethanol, unless otherwise stated, for 24 hours at

ambient temperature. The surface was thoroughly washed with MilliQ water and ethanol alternatingly, before being dried under a stream of N_2 gas and used for electrochemical measurements or further modifications.

6.2.5 Cyclic voltammetry

The exact conditions under which cyclic voltammetry (CV) experiments were performed varied across the different studies and the details of those can be found under the relevant figure captions. In principle, the potential was cycled between the limiting potentials, starting at the most positive potential unless otherwise indicated by the arrow at the bottom right-hand corner of a voltammogram, at a potential step of 10 mV and a fixed scan rate. An equilibration period of 10 seconds was carried out prior to taking each measurement. Although multiple scans are recorded, only the third scan is presented unless disparate electrochemical behaviour is observed.

6.2.6 Electrochemical impedance spectroscopy

For all EIS experiments, the electrodes were immersed in a 10 mM $K_3[Fe(CN)_6]$ solution in 100 mM phosphate, 233 mM NaCl (I = 0.464) buffer, prepared at pH 7.0. An AC voltage input was applied equivalent to the $E_{1/2}$ of the redox probe, 230 mV vs Ag/AgCl 3 M NaCl for $K_3[Fe(CN)_6]$ with an oscillation amplitude of 10 mV in a current range of 100 µA. The $E_{1/2}$ of the redox probe was determined through cyclic voltammetry in 100 mM phosphate, 233 mM NaCl (I = 0.464) buffer, pH 7.0 on a bare Au electrode; calculated as the average of the cathodic (E_{pc}) and anodic (E_{pa}) peak positions. The system was equilibrated for 300 seconds prior to starting the measurement and the system was scanned in the range of 10 kHz to 0.1 Hz at 10 points per decade. Data sets were subsequently analysed using the PSTrace in-built circuit fitting programme, and equivalent circuit fitting was performed on Nyquist traces where applicable to the circuit shown in **Figure 6.2**.
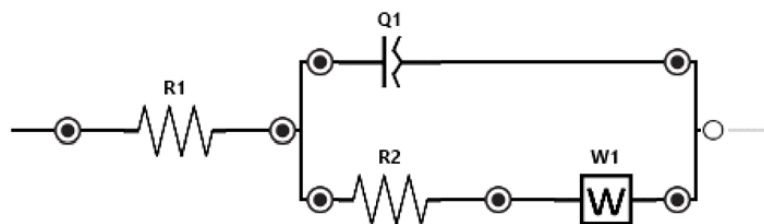
Figure 6.2 Theoretical electrical circuit (Randles circuit) for the fitting of gold electrodes modified with either small molecules or proteins, examined using a $[Fe(CN)_6]^{3-}$ redox probe in solution. **R1**, solution resistance (R_s); **Q1**, constant phase element modelling double layer capacitance (C_{dl}); **R2**, charge transfer resistance (R_{ct}); **W1**, Warburg element modelling diffusion (W) (in some cases substituted by Warburg open, W_O which describes finite-length diffusion with reflective boundary).

6.3 Protein related methods

6.3.1 Expression and purification of proteins

The CeuE protein and the the His-tagged version of Gst (Gst-6His) were expressed and purified by Dr Elena V. Blagova according to a published protocol.[85,287]

The His-tagged version of CeuE, CeuE-6His, was expressed and purified under the supervision of Dr Elena V. Blagova. The bacterial glycerol stock was provided by Dr Elena V. Blagova; the transformed plasmid contained the pET-YSBLIC3C vector encoding the protein of interest with an N-terminal hexa-histidine tag (6His) linked via a human rhinovirus 3C protease cleavage sequence. The protein was expressed in *E. coli* strain BL21(DE3) cells, grown in Luria-Bertani broth supplemented with 30 µg mL^{-1} of kanamycin. Protein expression was induced with 1 mM of isopropyl β-D-1-thiogalactopyranoside (IPTG) once an OD$_{600}$ of 0.6 – 0.8 was reached and the samples were incubated for 4 hours at 37°C before being harvested by centrifugation. The pellets were resuspended in 50 mM TRIS-HCl, 500 mM NaCl, 10 mM imidazole buffer, pH 7.5, in the presence of a protease inhibitor cocktail tablets, Complete Mini, EDTA-free and lysed by sonication on ice.

The supernatant was collected, and the soluble crude extract was purified in two steps. A His-Trap chelating column was charged with nickel and equilibrated with 50 mM TRIS-HCl, 500 mM NaCl, 10 mM imidazole buffer, pH 7.5. The crude sample was loaded, and the protein elution was achieved with 50 mM TRIS-HCl, 500 mM NaCl, 500 mM imidazole buffer, pH 7.5 over an imidazole gradient. The fractions containing the His-tagged CeuE protein were collected and further purified on a Superdex S200 size exclusion column using 20 mM TRIS-HCl, 150 mM NaCl, pH 7.5 elution buffer. The purified protein was concentrated using protein concentrator spin columns with a MW cut-off of 10 kDa (Amicon Ultra-15, Millipore) and the concentration was measured using the Bradford method (Coomassie Protein Assay Reagent, Thermo Scientific) before being aliquoted, flash-frozen and stored at −70°C.

The His-tagged version of CjX183 protein was expressed and purified by Alice Hewson; a previously published protocol was modified as described herein.[280] The construct containing residues 1408 − 1674 was incorporated into a pCW-LIC vector alongside with a C-terminal hexa-histidine tag (6His). The protein was expressed in $E.$ $coli$ strain BL21(DE3) competent cells, grown in 2x Yeast Extract Tryptone growth media supplemented with 1 µL mL^{-1} of ampicillin and chloramphenicol. Protein expression was induced with 1 mM of isopropyl β-D-1-thiogalactopyranoside (IPTG) once an OD$_{600}$ of 0.6 was reached and the samples were incubated overnight at 16°C before being harvested by centrifugation. The pellets were resuspended in 20 mM TRIS-HCl, 150 mM NaCl, 10% v/v glycerol buffer, pH 8.0, in the presence of a protease inhibitor cocktail tablets, Complete Mini, EDTA-free and benzonase, followed by lysis of the cells. The supernatant was collected, and 30 mM imidazole was added before the protein was purified in two steps. A His-Trap chelating column was charged with nickel and equilibrated with 20 mM TRIS-HCl, 200 mM NaCl, 30 mM imidazole buffer, pH 8.5. The crude sample was loaded, and the protein elution was achieved with 20 mM TRIS-HCl, 200 mM NaCl, 300 mM imidazole buffer, pH 8.5 over

an imidazole gradient. The protein containing fractions were pooled and further purified on a Superdex S75 size exclusion column using 20 mM TRIS-HCl, 200 mM NaCl, pH 8.0 elution buffer. The purified protein was concentrated using protein concentrator spin columns with a MW cut-off of 3 kDa (Vivaspin, Cytvia) and the concentration was measured using the absorbance at 410 nm (A_{410}) and calculated using the Beer-Lambert law and the corrected molar extinction coefficients for heme *c* before being flash-frozen and stored at −70°C.

6.3.2 Artificial metalloenzyme assembly

ArMs were prepared from three different protein scaffolds; a non-His-tagged version of CeuE and His-tagged versions of CeuE and Gst, abbreviated to CeuE-6His and Gst-6His, respectively. The absorbance at 280 nm (A_{280}) was measured for all protein stocks to calculate their concentrations using the Beer-Lambert law and the corrected molar extinction coefficients determined by Dr Alex H. Miller.[308,309]

A 2.174 mM stock of SidCat was prepared using a 10 mM (Fe)NTA$_{(aq)}$, stock prepared according to a literature procedure, 10 mM AzotoCat stock in DMF and a 5 mM [Cp*IrCl$_2$]$_2$ stock in DMF.[300] (Fe)NTA (75 μL) was added to 200 mM MOPS, 150 mM NaCl buffer, pH 7.5 (120 μL), followed by SidCat (75 μL) and [Cp*IrCl$_2$]$_2$ (75 μL). The solution was sonicated for 1 minute after each individual addition step.

The concentrated protein was diluted to a concentration of 50 − 100 μM in 200 mM MOPS, 150 mM NaCl buffer, pH 7.5 and the Sid-Cat stock was added in a 1:1 ratio in relation to the protein. The solution was left to equilibrate for 3 hours at 4°C before being washed twice with excess buffer to remove any unbound SidCat conjugate using protein concentrator spin columns with a MW cut-off of 10 kDa (Vivaspin, Cytvia). The samples were stored overnight at −18°C before being used.

The same procedure was followed to prepare protein–Sid conjugates. However, the SidCat stock was replaced with a 2.174 mM Sid stock; prepared by addition of (Fe)NTA (75 µL) to 200 mM MOPS, 150 mM NaCl buffer, pH 7.5 (195 µL), followed by a 10 mM of **NGB-05** in DMF (75 µL).

6.3.3 Dissociation constant measurements

The measurements and subsequent data fitting were performed by Dr Alex H. Miller according to the procedure described herein. Fluorescence spectroscopy was performed on a F-4500 Hitachi spectrophotometer at an ambient temperature with an excitation wavelength of 290 nm and an emission range of 295 – 410 nm, with a slit width of 10 nm and 20 nm for excitation and emission, respectively. DOSTAL DOSY liquid dispenser (Scientific Engineering Solutions) was used for ligand titrations.

The concentrated stock solutions of the proteins, CeuE and Gst, and the ligand Sid (prepared as described above in **Section 6.3.2**) were diluted in 40 mM TRIS-HCl, 150 mM NaCl buffer, pH 7.5, whereas the ligand SidCat (prepared as described above in **Section 6.3.2**) was diluted in dimethylformamide to overcome solubility issues. The stock concentrations were optimised individually for each combination of protein and ligand to reach homogenous data distribution. For each measurement, the ligand solution was titrated stepwise (1 µL per step) into the protein solution (2 mL) with continuous stirring. An equilibration period of 1 minute was set after each addition before the spectra was acquired. Each spectrum was buffer subtracted and integrated between 310 – 380 nm and the subsequent normalised peak area was plotted as the function of the ligand concentration. The dissociation constant values (K_d) were obtained following fitting of the plots to **Equation 6.2**, adapted from the literature, using a defined non-linear curve fitting analysis.[310]

$$Y = Y_0 + \left(\frac{B - Y_0}{2A} \left(A + X + K_d - \sqrt{(A + X + K_d)^2 - 4AX} \right) \right)$$

Equation 6.2 An equation for the fitting of fluorescence quenching data for calculating the dissociation constant values (K_d) to determine the binding affinity between protein and ligand pairs. Y = normalised fluorescence emission; Y_0 = initial normalised fluorescence emission, before ligand addition; B = the minimum normalised fluorescence emission, fully quenched state; A = protein concentration; X = ligand concentration.

6.4 Chapter specific experimental procedures

6.4.1 Experimental procedures for chapter 2

6.4.1.1 Characterisation of the BDD working electrode

The BDD working electrode was characterised electrochemically to establish its ability to efficiently facilitate electron transfer. Cyclic voltammetry measurements of a solution containing the potassium salt of ferricyanide, $K_3[Fe(CN)_6]$, were obtained at two different scan rates and compared to the values measured on the surface of a GC working electrode (**Table 6.1**).

Table 6.1 Electrochemical parameters extracted from cyclic voltammetry measurements of $K_3[Fe(CN)_6]$ performed at two different scan rates (v), for the comparison of electron transfer kinetics at boron-doped diamond (BDD) and glassy carbon (GC) working electrodes.

Working electrode	v / mV s^{-1}	$E_{1/2}$ / V[a]	ΔE / mV	i_{pa}/i_{pc}
GC	100	0.235	90	0.82
	50	0.235	90	0.81
BDD	100	0.230	120	0.78
	50	0.235	110	0.73

[a] $E_{1/2}$ vs Ag/AgCl 3 M NaCl; 100 mM phosphate buffer, 233 mM NaCl, pH 7.0.

From the CVs, the midpoint potential ($E_{1/2}$) and peak-to-peak separation (ΔE) values were extracted, as well as the ratio between the anodic (i_a) and

cathodic (i_c) currents to evaluate the electrochemical reversibility of the redox couple. For the GC electrode, all the parameters remained consistent at both scan rates with the ΔE being close to the theoretical value of 60 mV, characteristic of an electrochemical reversibility. However, the BDD working electrode exhibited an increase in ΔE with a further increase in the value at a higher scan rate, indicative of slower electron transfer kinetics.

The BDD electrode was further evaluated in different solution compositions, to determine the effect of buffer on the electrochemical behaviour of the ferricyanide redox couple. A significant shift in all extracted parameters, as shown in **Table 6.2**, was observed upon a change from phosphate to Bis-TRIS buffer and at a reduced concentration of the supporting electrolyte. In depth analysis was not performed, however, it served as evidence of the sensitivity of the BDD electrode to solution composition, highlighting the need for it to be carefully controlled.

Table 6.2 Electrochemical parameters extracted from cyclic voltammetry measurements of $K_3[Fe(CN)_6]$ at a BDD working electrode, where the solution composition was varied to evaluate the subsequent effect on the electrochemical behaviour of the redox species.

Buffer	$E_{1/2}$ / V[a]	ΔE / mV	i_{pa}/i_{pc}
Phosphate[b]	0.235	110	0.73
Bis-TRIS[c]	0.205[d]	90	1.22

[a] $E_{1/2}$ vs Ag/AgCl 3 M NaCl; v = 50 mV s^{-1}.

[b] 100 mM phosphate buffer, 233 mM NaCl, pH 7.0; $[K_3\{Fe(CN)_6\}^{3-}]$ = 10 mM.

[c] 5 mM Bis-TRIS buffer, 100 mM NaCl, pH 7.0; $[K_3\{Fe(CN)_6\}^{3-}]$ = 0.48 mM.

[d] Experimental value is comparable to the literature $E_{1/2}$ value of 0.206 V vs Ag/AgCl 3 M KCl obtained at a BDD working electrode in 100 mM sodium acetate buffer, pH 7.3.[311]

6.4.1.2 UV-vis measurements of iron(III) azotochelin complexes

UV-vis measurements were obtained on the UV-1800 Schimadzu spectrophotometer using Starna Scientific quartz cuvettes with a path

length of 10 cm. Prior to recording each spectrum, a blank measurement of the corresponding buffer, either Bis-TRIS or NH_4OAc, was taken. For spectra recorded in Bis-TRIS buffer, complex preparation was performed in situ, analogous to the procedure employed in cyclic voltammetry studies, as described in **Section 2.2.1**. Whereas for measurements made in NH_4OAc, the samples were prepared for native ESI-MS as described below, and were directly used for UV-vis.

6.4.1.3 Native ESI-MS of iron(III) azotochelin complexes

The samples for native ESI-MS experiments were prepared from 5 mM azotochelin$_{(MeOH)}$ [**NGB-05**] and 5 mM $FeCl_3$(aq) stocks. The two solutions were combined in 100 μL aliquots to produce **M_1:L_1** (200 μL total volume) and **M_2:L_3** (500 μL total volume) ratios. The resulting solutions were stirred for 3 hours at room temperature before the solvent was removed in vacuo. The purple residue was dissolved in 1 mL of 10 mM NH_4OAc buffer at either pH 6.0, 6.5 or 7.0; sonication for 10 minutes (at room temperature) was required to ensure full dissolution. Complex formation was confirmed through UV-vis spectroscopy and the presence of the characteristic λ_{max} value at 570 ± 2 nm. The mass spectra were acquired on a Bruker compact MS-Agilent 1260 mass spectrometer by Karl Heaton in both negative and positive ionisation modes.

***

Abbreviations

Ac	Acetyl
ArM	Artificial metalloenzyme
ATHase	Asymmetric transfer hydrogenase
AzotoCat	Azotochelin-catalyst conjugate
ATR	Attenuated total reflectance
A. vinelandii	*Azotobacter vinelandii*
BDD	Boron-doped diamond
bisDHBS	Bis(2,3-dihydroxybenzoyl-*L*-serine)
Bn	Benzyl
CA	Carbonic anhydrase
CAL-B	Lipase isolated from *Candida antarctica* B
CD	Circular dichroism
CDI	Carbonyldiimidazole
C. jejuni	*Campylobacter jejuni*
Cp	Cyclopentadienyl
CV	Cyclic voltammetry/voltammogram
DCM	Dichloromethane
DET	Direct electron transfer
DIPEA	*N,N*-Diisopropylethylamine
DMF	*N,N*-Dimethylformamide
$E°'$	Formal reduction potential
$E_{1/2}$	Midpoint potential

E_{pa}	Anodic peak potential
E_{pc}	Cathodic peak potential
E. coli	*Escherichia coli*
ee	Enantiomeric excess
EIS	Electrochemical impedance spectroscopy
ESI	Electrospray ionisation
EtOAc	Ethyl acetate
EV	Ethyl viologen
Fc	Ferrocene
GC	Glassy carbon
G. stearothermophilus	*Geobacillus stearothermophilus*
H	Histidine
6His	Polyhistidine tag
HBTU	Hexafluorophosphate benzotriazole tetramethyl uronium
HMDE	Hanging mercury drop electrode
HRMS	High resolution mass spectra
IMAC	Immobilised-metal affinity chromatography
imd	Imidazole
IR	Infrared
K_d	Dissociation constant
K_f	Formation constant
K_{sp}	Solubility product constant
LA	Lipoic acid
LMCT	Ligand-to-metal charge transfer

Mb	Myoglobin
MeOH	Methanol
MS	Mass spectrometry
NHE	Normal hydrogen electrode
NHS	*N*-Hydroxysuccinimide
NikA	Nickel binding periplasmic binding protein
NiRd	Nickel substituted rubredoxin
NMR	Nuclear magnetic resonance
NP	Nanoparticle
NTA	Nitrilotriacetic acid
PBP	Periplasmic binding protein
PCR	Polymerase chain reaction
PEG	Polyethylene glycol
PFV	Protein film voltammetry
PGE	Pyrolytic graphite edge
py	Pyridine
QCM-D	Quartz crystal microbalance with dissipation
SAM	Self-assembled monolayer
SCE	Saturated calomel electrode
SERR	Surface-enhanced resonance Raman
SHE	Standard hydrogen electrode
SidCat	Iron(III) azotochelin-catalyst conjugate
SPAAC	Strain-promoted azide-alkyne cycloaddition
*t*Bu	*tert*-Butyl

TEA	Triethylamine
TOF	Turnover frequency
TON	Turnover number
TLC	Thin layer chromatography
UV	Ultraviolet
vis	Visible
Y	Tyrosine

Appendix – Supplementary figures
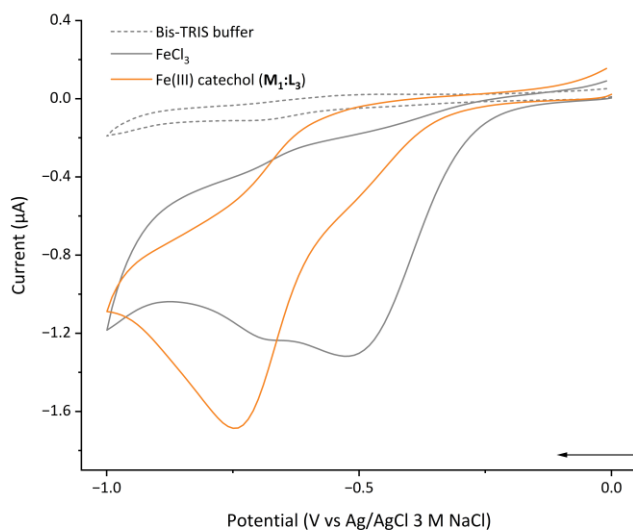
Figure A.1 Corresponding first scans of the cyclic voltammograms shown in **Figure 2.9**. Data was collected in 5 mM Bis-TRIS buffer, 100 mM NaCl at pH 7.0 (grey dashed line). Final analyte concentrations [Fe] = 0.48 mM (grey solid line), [Fe] : [cat] = 0.42 : 1.25 mM (orange solid line); v = 50 mV s^{-1}.
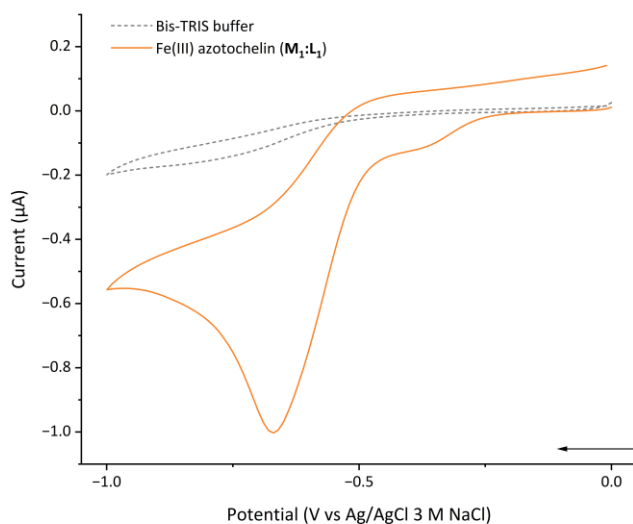
Figure A.2 Corresponding first scans of the cyclic voltammograms shown in **Figure 2.10**. Data was collected in 5 mM Bis-TRIS buffer, 100 mM NaCl at pH 7.0 (grey dashed line). Final analyte concentrations [Fe] : [Azoto] = 0.45 : 0.45 mM (orange solid line); v = 10 mV s^{-1}.
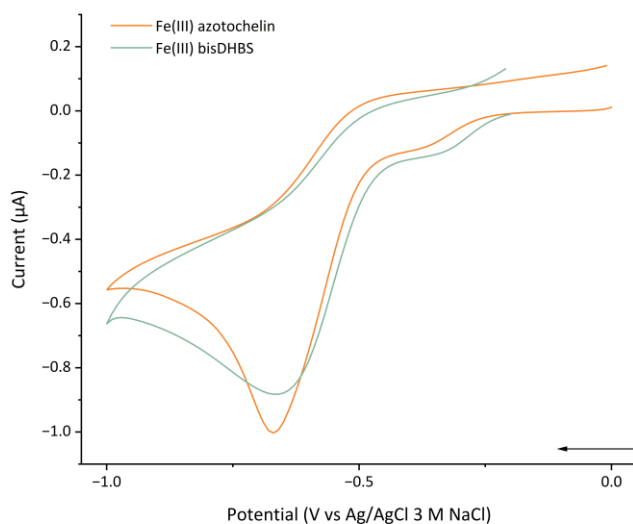
Figure A.3 Corresponding first scans of the cyclic voltammograms shown in **Figure 2.11**. Data was collected in 5 mM Bis-TRIS buffer, 100 mM NaCl at pH 7.0 for Fe(III) azotochelin (solid orange line) and Fe(III) bisDHBS (solid green line). Final analyte concentrations [Fe] = 0.45 and [siderophores] = 0.45 mM; v = 10 mV s^{-1}.
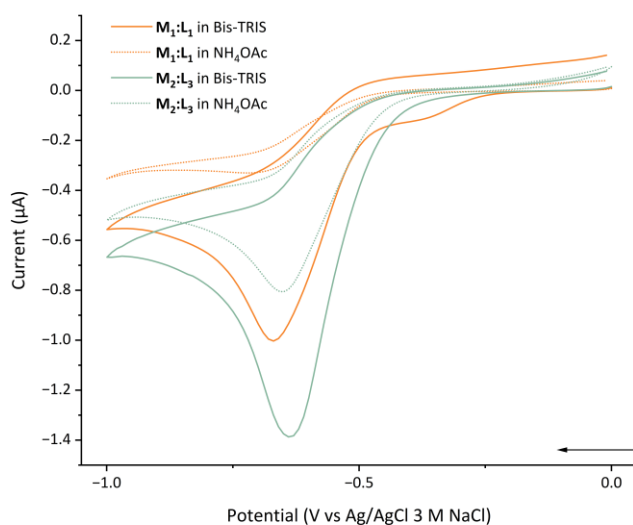
Figure A.4 Corresponding first scans of the cyclic voltammograms shown in **Figure 2.13**. Data was collected in solutions containing 5 mM buffer salt of either Bis-TRIS (electrochemistry buffer) or NH$_4$OAc (native ESI-MS buffer), 100 mM NaCl at pH 7.0 Final analyte concentrations at **M$_1$:L$_1$** ratio (solid and dotted orange lines), [Fe] = 0.45 mM and [Azoto] = 0.45 mM; at **M$_2$:L$_3$** ratio (solid and dotted green lines), [Fe] = 0.80 mM and [Azoto] = 1.20 mM; v = 10 mV s^{-1}.

221
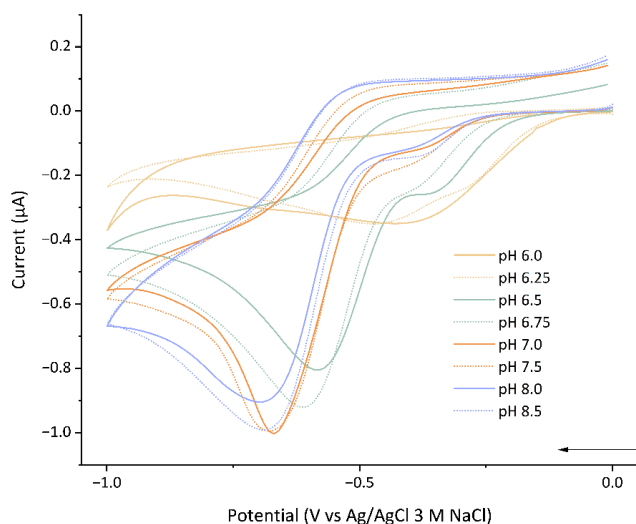
Figure A.5 Corresponding first scans of the cyclic voltammograms shown in **Figure 2.16**. Data was collected in 5 mM Bis-TRIS buffer, 100 mM NaCl at different pH values, pH 6.0 − 8.50 in either 0.25 or 0.5 increments. Iron(III) azotochelin was prepared in a **M_1:L_1** ratio where [Fe] = 0.45 and [siderophores] = 0.45 mM; v = 10 mV s^{-1}.
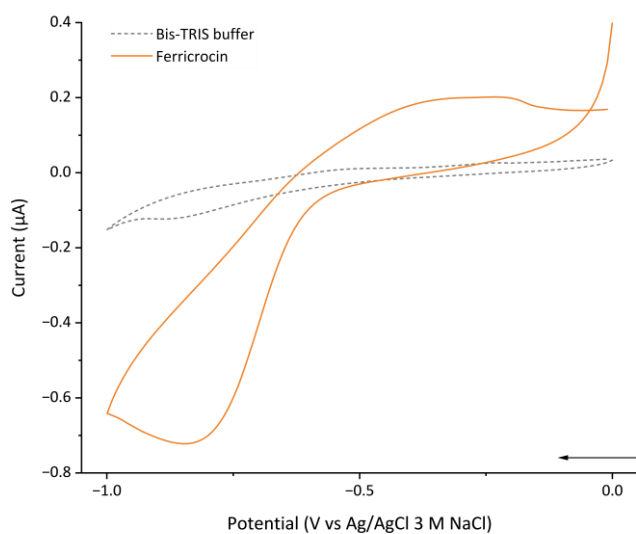
Figure A.6 Corresponding first scans of the cyclic voltammograms shown in **Figure 2.19**. Data was collected in 5 mM Bis-TRIS buffer, 100 mM NaCl at pH 7.0 (grey dotted line) for ferricrocin (solid orange line). Final analyte concentrations [Ferricrocin] = 0.45 mM; v = 10 mV s^{-1}.

References

1   United States Environmental Protection Agency, *2020 TRI National Analysis*, 2022.

2   J. M. Woodley, *Trends Biotechnol.*, 2008, **26**, 321–327.

3   J. M. Woodley, *Curr. Opin. Green Sustainable Chem.*, 2020, **21**, 22–26.

4   R. A. Sheldon and J. M. Woodley, *Chem. Rev.*, 2018, **118**, 801–838.

5   P. T. Anastas and J. C. Warner, *Green Chemistry: Theory and Practice*, Oxford University Press, Oxford, UK, 1998.

6   J. P. Adams, M. J. B. Brown, A. Diaz-Rodriguez, R. C. Lloyd and G. Roiban, *Adv. Synth. Catal.*, 2019, **361**, 2421–2432.

7   P. N. Devine, R. M. Howard, R. Kumar, M. P. Thompson, M. D. Truppo and N. J. Turner, *Nat. Rev. Chem.*, 2018, **2**, 409–421.

8   K. R. Campos, P. J. Coleman, J. C. Alvarez, S. D. Dreher, R. M. Garbaccio, N. K. Terrett, R. D. Tillyer, M. D. Truppo and E. R. Parmee, *Science (1979)*, 2019, **363**, eaat0805.

9   M. D. Truppo, *ACS Med. Chem. Lett.*, 2017, **8**, 476–480.

10   R. A. Sheldon and D. Brady, *Chem. Commun.*, 2018, **54**, 6088–6104.

11   N. J. Turner, *Nat. Chem. Biol.*, 2009, **5**, 567–573.

12   F. H. Arnold and A. A. Volkov, *Curr. Opin. Chem. Biol.*, 1999, **3**, 54–59.

13   A. Glieder, E. T. Farinas and F. H. Arnold, *Nat. Biotechnol.*, 2002, **20**, 1135–1139.

14   E. Arango Gutierrez, H. Mundhada, T. Meier, H. Duefel, M. Bocola and U. Schwaneberg, *Biosens. Bioelectron.*, 2013, **50**, 84–90.

15   P. S. Coelho, E. M. Brustad, A. Kannan and F. H. Arnold, *Science (1979)*, 2013, **339**, 307–310.

16   M. T. Reetz, J. D. Carballeira and A. Vogel, *Angew. Chem., Int. Ed.*, 2006, **45**, 7745–7751.

17   F. H. Arnold, *Acc. Chem. Res.*, 1998, **31**, 125–131.

18   M. B. Soellner, K. A. Dickson, B. L. Nilsson and R. T. Raines, *J. Am. Chem. Soc.*, 2003, **125**, 11790–11791.

19   S. Wu, Y. Zhou, T. Wang, H.-P. Too, D. I. C. Wang and Z. Li, *Nat. Commun.*, 2016, **7**, 11917.

20   A. Toscani, C. Risi, G. W. Black, N. L. Brown, A. Shaaban, N. J. Turner and D. Castagnolo, *ACS Catal.*, 2018, **8**, 8781–8787.

21   H. J. Davis and T. R. Ward, *ACS Cent. Sci.*, 2019, **5**, 1120–1136.

22   F. Yu, V. M. Cangelosi, M. L. Zastrow, M. Tegoni, J. S. Plegaria, A. G. Tebo, C. S. Mocny, L. Ruckthong, H. Qayyum and V. L. Pecoraro, *Chem. Rev.*, 2014, **114**, 3495–3578.

23   A. M. Knight, S. B. J. Kan, R. D. Lewis, O. F. Brandenberg, K. Chen and F. H. Arnold, *ACS Cent. Sci.*, 2018, **4**, 372–377.

24   S. B. J. Kan, R. D. Lewis, K. Chen and F. H. Arnold, *Science (1979)*, 2016, **354**, 1048–1051.

25   M. Jeschek, R. Reuter, T. Heinisch, C. Trindler, J. Klehr, S. Panke and T. R. Ward, *Nature*, 2016, **537**, 661–665.

26   S. I. Mann, T. Heinisch, T. R. Ward and A. S. Borovik, *Chem. Commun.*, 2018, **54**, 4413–4416.

27   J.-L. Zhang, D. K. Garner, L. Liang, D. A. Barrios and Y. Lu, *Chem. Eur. J.*, 2009, **15**, 7481–7489.

28   R. L. Shook and A. S. Borovik, *Inorg. Chem.*, 2010, **49**, 3646–3660.

29   S. Eda, I. Nasibullin, K. Vong, N. Kudo, M. Yoshida, A. Kurbangalieva and K. Tanaka, *Nat. Catal.*, 2019, **2**, 780–792.

30   K. Vong, S. Eda, Y. Kadota, I. Nasibullin, T. Wakatake, S. Yokoshima, K. Shirasu and K. Tanaka, *Nat. Comm.*, 2019, **10**, 5746.

31 A. Pordea and T. R. Ward, *Chem. Commun.*, 2008, 4239–4249.

32 U. Markel, D. F. Sauer, M. Wittwer, J. Schiffels, H. Cui, M. D. Davari, K. W. Kröckert, S. Herres-Pawlis, J. Okuda and U. Schwaneberg, *ACS Catal.*, 2021, **11**, 5079–5087.

33 Y. S. Zubi, B. Liu, Y. Gu, D. Sahoo and J. C. Lewis, *Chem. Sci.*, 2022, **13**, 1459–1468.

34 J. G. Rebelein, Y. Cotelle, B. Garabedian and T. R. Ward, *ACS Catal.*, 2019, **9**, 4173–4178.

35 M. M. Pellizzoni, F. Schwizer, C. W. Wood, V. Sabatino, Y. Cotelle, S. Matile, D. N. Woolfson and T. R. Ward, *ACS Catal.*, 2018, **8**, 1476–1484.

36 H. Yang, A. M. Swartz, H. J. Park, P. Srivastava, K. Ellis-Guardiola, D. M. Upp, G. Lee, K. Belsare, Y. Gu, C. Zhang, R. E. Moellering and J. C. Lewis, *Nat. Chem.*, 2018, **10**, 318–324.

37 R. F. Alford, A. Leaver-Fay, J. R. Jeliazkov, M. J. O'Meara, F. P. DiMaio, H. Park, M. V. Shapovalov, P. D. Renfrew, V. K. Mulligan, K. Kappel, J. W. Labonte, M. S. Pacella, R. Bonneau, P. Bradley, R. L. Dunbrack, R. Das, D. Baker, B. Kuhlman, T. Kortemme and J. J. Gray, *J. Chem. Theory Comput.*, 2017, **13**, 3031–3048.

38 L. Alonso-Cotchico, J. Rodríguez-Guerra, A. Lledós and J.-D. Maréchal, *Acc. Chem. Res.*, 2020, **53**, 896–905.

39 Z. Ke, S. Abe, T. Ueno and K. Morokuma, *J. Am. Chem. Soc.*, 2012, **134**, 15418–15429.

40 P. J. Deuss, R. den Heeten, W. Laan and P. C. J. Kamer, *Chem. Eur. J.*, 2011, **17**, 4680–4698.

41 F. Rosati and G. Roelfes, *ChemCatChem*, 2010, **2**, 916–927.

42 G. S. Biggs, O. J. Klein, S. R. Boss and P. D. Barker, *Johnson Matthey Technol. Rev.*, 2020, **64**, 407–418.

43   B. Large, N. G. Baranska, R. L. Booth, K. S. Wilson and A.-K. Duhme-Klair, *Curr. Opin. Green Sustainable Chem.*, 2021, **28**, 100420.

44   K. Okrasa and R. J. Kazlauskas, *Chem. Eur. J.*, 2006, **12**, 1587–1596.

45   Q. Jing, K. Okrasa and R. J. Kazlauskas, *Chem. Eur. J.*, 2009, **15**, 1370–1376.

46   K. Oohora, Y. Kihira, E. Mizohata, T. Inoue and T. Hayashi, *J. Am. Chem. Soc.*, 2013, **135**, 17282–17285.

47   M. L. Zastrow, A. F. A. Peacock, J. A. Stuckey and V. L. Pecoraro, *Nat. Chem.*, 2012, **4**, 118–123.

48   C. Esmieu, M. V. Cherrier, P. Amara, E. Girgenti, C. Marchi-Delapierre, F. Oddon, M. Iannello, A. Jorge-Robin, C. Cavazza and S. Ménage, *Angew. Chem. Int. Ed.*, 2013, **52**, 3922–3925.

49   J. Rittle, M. J. Field, M. T. Green and F. A. Tezcan, *Nat. Chem.*, 2019, **11**, 434–441.

50   V. M. Cangelosi, A. Deb, J. E. Penner-Hahn and V. L. Pecoraro, *Angew. Chem. Int. Ed.*, 2014, **53**, 7900–7903.

51   M. Tegoni, F. Yu, M. Bersellini, J. E. Penner-Hahn and V. L. Pecoraro, *Proc. Natl. Acad. Sci.*, 2012, **109**, 21234–21239.

52   C. M. Rufo, Y. S. Moroz, O. V. Moroz, J. Stöhr, T. A. Smith, X. Hu, W. F. DeGrado and I. V. Korendovych, *Nat. Chem.*, 2014, **6**, 303–309.

53   J. Collot, J. Gradinaru, N. Humbert, M. Skander, A. Zocchi and T. R. Ward, *J. Am. Chem. Soc.*, 2003, **125**, 9030–9031.

54   D. J. Raines, J. E. Clarke, E. V. Blagova, E. J. Dodson, K. S. Wilson and A.-K. Duhme-Klair, *Nat. Catal.*, 2018, **1**, 680–688.

55   A. G. Jarvis, L. Obrecht, P. J. Deuss, W. Laan, E. K. Gibson, P. P. Wells and P. C. J. Kamer, *Angew. Chem. Int. Ed.*, 2017, **129**, 13784–13788.

56   F. W. Monnard, E. S. Nogueira, T. Heinisch, T. Schirmer and T. R. Ward, *Chem. Sci.*, 2013, **4**, 3269–3274.

57   J. Bos, F. Fusetti, A. J. M. Driessen and G. Roelfes, *Angew. Chem., Int. Ed.*, 2012, **51**, 7472–7475.

58   M. V. Cherrier, E. Girgenti, P. Amara, M. Iannello, C. Marchi-Delapierre, J. C. Fontecilla-Camps, S. Ménage and C. Cavazza, *J. Biol. Inorg. Chem.*, 2012, **17**, 817–829.

59   N. M. Green, *Biochem, J.*, 1963, **89**, 585–591.

60   M. E. Wilson and G. M. Whitesides, *J. Am. Chem. Soc.*, 1978, **100**, 306–307.

61   M. Skander, N. Humbert, J. Collot, J. Gradinaru, G. Klein, A. Loosli, J. Sauser, A. Zocchi, F. Gilardoni and T. R. Ward, *J. Am. Chem. Soc.*, 2004, **126**, 14411–14418.

62   R. Noyori, T. Ohkuma, M. Kitamura, H. Takaya, N. Sayo, H. Kumobayashi and S. Akutagawa, *J. Am. Chem. Soc.*, 1987, **109**, 5856–5858.

63   A. Pordea, M. Creus, C. Letondor, A. Ivanova and T. R. Ward, *Inorg. Chim. Acta*, 2010, **363**, 601–604.

64   M. Dürrenberger, T. Heinisch, Y. M. Wilson, T. Rossel, E. Nogueira, L. Knörr, A. Mutschler, K. Kersten, M. J. Zimbron, J. Pierron, T. Schirmer and T. R. Ward, *Angew. Chem. Int. Ed.*, 2011, **50**, 3026–3029.

65   M. Creus, A. Pordea, T. Rossel, A. Sardo, C. Letondor, A. Ivanova, I. LeTrong, R. E. Stenkamp and T. R. Ward, *Angew. Chem. Int. Ed.*, 2008, **47**, 1400–1404.

66   T. Heinisch and T. R. Ward, *Acc. Chem. Res.*, 2016, **49**, 1711–1721.

67   S. Wu, Y. Zhou, J. G. Rebelein, M. Kuhn, H. Mallin, J. Zhao, N. V. Igareta and T. R. Ward, *J. Am. Chem. Soc.*, 2019, **141**, 15869–15878.

68   H. R. Nordlund, O. H. Laitinen, V. P. Hytönen, S. T. H. Uotila, E. Porkka and M. S. Kulomaa, *J. Biol. Chem.*, 2004, **279**, 36715–36719.

69   G. O. Reznik, S. Vajda, C. L. Smith, C. R. Cantor and T. Sano, *Nat. Biotechnol.*, 1996, **14**, 1007–1011.

70   J. M. Marangoni, S.-C. Wu, D. Fogen, S.-L. Wong and K. K. S. Ng, *Sci. Rep.*, 2020, **10**, 12483.

71   V. J. O'Sullivan, I. Barrette-Ng, E. Hommema, G. T. Hermanson, M. Schofield, S.-C. Wu, C. Honetschlaeger, K. K.-S. Ng and S.-L. Wong, *PLoS One*, 2012, **7**, e35203.

72   A. Pordea, M. Creus, J. Panek, C. Duboc, D. Mathis, M. Novic and T. R. Ward, *J. Am. Chem. Soc.*, 2008, **130**, 8085–8088.

73   C. Letondor, A. Pordea, N. Humbert, A. Ivanova, S. Mazurek, M. Novic and T. R. Ward, *J. Am. Chem. Soc.*, 2006, **128**, 8320–8.

74   J. B. Neilands, *J. Biol. Chem.*, 1995, **270**, 26723–26726.

75   C. Sprencel, Z. Cao, Z. Qi, D. C. Scott, M. A. Montague, N. Ivanoff, J. Xu, K. M. Raymond, S. M. C. Newton and P. E. Klebba, *J. Bacteriol.*, 2000, **182**, 5359–5364.

76   W. Köster and V. Braun, *J. Biol. Chem.*, 1990, **265**, 21407–21410.

77   X. Zeng, Y. Mo, F. Xu and J. Lin, *Mol. Microbiol.*, 2013, **87**, 594–608.

78   A. Bonneau, B. Roche and I. J. Schalk, *Sci Rep*, 2020, **10**, 120.

79   I. J. Schalk and L. Guillon, *Amino Acids*, 2013, **44**, 1267–1277.

80   B. F. Matzanke, S. Anemüller, V. Schünemann, A. X. Trautwein and K. Hantke, *Biochemistry*, 2004, **43**, 1386–1392.

81   M. Miethke, J. Hou and M. A. Marahiel, *Biochemistry*, 2011, **50**, 10951–10964.

82   S. Dhungana and A. L. Crumbliss, *Geomicrobiol. J.*, 2005, **22**, 87–98.

83   F. Imperi, F. Tiburzi and P. Visca, *Proc. Natl. Acad. Sci.*, 2009, **106**, 20440–20445.

84   M. Hannauer, Y. Barda, G. L. A. Mislin, A. Shanzer and I. J. Schalk, *J. Bacteriol.*, 2010, **192**, 1212–1220.

85   D. J. Raines, O. V. Moroz, K. S. Wilson and A. K. Duhme-Klair, *Angew. Chem. Int. Ed.*, 2013, **52**, 4595–4598.

86   E. J. Wilde, A. Hughes, E. V. Blagova, O. V. Moroz, R. P. Thomas, J. P. Turkenburg, D. J. Raines, A. K. Duhme-Klair and K. S. Wilson, *Sci. Rep.*, 2017, **7**, 45941.

87   S. Mortazavi and H. Aghaei, *Int. J. Biol. Macromol.*, 2020, **164**, 1–12.

88   T. C. Coutinho, J. O. D. Malafatti, E. C. Paris, P. W. Tardioli and C. S. Farinas, *ACS Appl. Nano Mater.*, 2020, **3**, 12334–12345.

89   J. M. Bolivar, L. Wilson, S. A. Ferrarotti, R. Fernandez-Lafuente, J. M. Guisan and C. Mateo, *Enzyme Microb. Technol.*, 2007, **40**, 540–546.

90   H. M. Abdel-Mageed, R. A. Radwan, N. Z. AbuelEzz, H. A. Nasser, A. A. El Shamy, R. M. Abdelnaby and N. A. EL Gohary, *Artif. Cells, Nanomed., Biotechnol.*, 2019, **47**, 2361–2368.

91   C. Zor, H. A. Reeve, J. Quinson, L. A. Thompson, T. H. Lonsdale, F. Dillon, N. Grobert and K. A. Vincent, *Chem. Commun.*, 2017, **53**, 9839–9841.

92   F. Subrizi, M. Crucianelli, V. Grossi, M. Passacantando, L. Pesci and R. Saladino, *ACS Catal*, 2014, **4**, 810–822.

93   A. Sethuraman and G. Belfort, *Biophys. J.*, 2005, **88**, 1322–1333.

94   D. N. Tran and K. J. Balkus, *ACS Catal.*, 2011, **1**, 956–968.

95   B. Zakeri, J. O. Fierer, E. Celik, E. C. Chittock, U. Schwarz-Linek, V. T. Moy and M. Howarth, *Proc. Natl. Acad. Sci.*, , DOI:10.1073/pnas.1115485109.

96   G. Zhang, T. Johnston, M. B. Quin and C. Schmidt-Dannert, *ACS Synth. Biol.*, 2019, **8**, 1867–1876.

97   T. Peschke, P. Bitterwolf, S. Gallus, Y. Hu, C. Oelschlaeger, N. Willenbacher, K. S. Rabe and C. M. Niemeyer, *Angew. Chem., Int. Ed.*, 2018, **57**, 17028–17032.

98   F. Peng, Q.-S. Chen, M.-H. Zong and W.-Y. Lou, *Mol. Catal.*, 2021, **510**, 111673.

99   F. A. Al-Lolage, M. Meneghello, S. Ma, R. Ludwig and P. N. Bartlett, *ChemElectroChem*, 2017, **4**, 1528–1534.

100 M. Meneghello, F. A. Al-Lolage, S. Ma, R. Ludwig and P. N. Bartlett, *ChemElectroChem*, 2019, **6**, 700–713.

101 F. A. Al-Lolage, P. N. Bartlett, S. Gounel, P. Staigre and N. Mano, *ACS Catal.*, 2019, **9**, 2068–2078.

102 L. Shen, M. Schroeder, T. L. Ogorzalek, P. Yang, F.-G. Wu, E. N. G. Marsh and Z. Chen, *Langmuir*, 2014, **30**, 5930–5938.

103 A. F. Chaparro Sosa, R. M. Bednar, R. A. Mehl, D. K. Schwartz and J. L. Kaar, *J. Am. Chem. Soc.*, 2021, **143**, 7154–7163.

104 J. Jasensky, K. Ferguson, M. Baria, X. Zou, R. McGinnis, A. Kaneshiro, S. Badieyan, S. Wei, E. Neil. G. Marsh and Z. Chen, *Langmuir*, 2018, **34**, 9133–9140.

105 B. Ge and F. Lisdat, *Anal. Chim. Acta*, 2002, **454**, 53–64.

106 K. A. Mahmoud, K. B. Male, S. Hrapovic and J. H. T. Luong, *ACS Appl. Mater. Interfaces*, 2009, **1**, 1383–1386.

107 K. Khaldi, S. Sam, A. Lounas, C. Yaddaden and N.-E. Gabouze, *Appl. Surf. Sci.*, 2017, **421**, 148–154.

108 X. Su, Y. Zong, R. Richter and W. Knoll, *J. Colloid Interface Sci.*, 2005, **287**, 35–42.

109 J. Kalia, N. L. Abbott and R. T. Raines, *Bioconjugate Chem.*, 2007, **18**, 1064–1069.

110 J. M. Abad, M. Vélez, C. Santamaría, J. M. Guisán, P. R. Matheus, L. Vázquez, I. Gazaryan, L. Gorton, T. Gibson and V. M. Fernández, *J. Am. Chem. Soc.*, 2002, **124**, 12845–12853.

111 K. Vasić, Ž. Knez and M. Leitgeb, *Sci. Rep.*, 2020, **10**, 19478.

112 R. Torres, C. Mateo, G. Fernandez-Lorente, C. Ortiz, M. Fuentes, J. M. Palomo, J. M. Guisan and R. Fernandez-Lafuente, *Biotechnol. Prog.*, 2003, **19**, 1056–1060.

113 C. Mateo, O. Abian, G. Fernandez-Lorente, J. Pedroche, R. Fernandez-Lafuente, J. M. Guisan, A. Tam and M. Daminati, *Biotechnol. Prog.*, 2002, **18**, 629–634.

114 M. L. Verma, M. Naebe, C. J. Barrow and M. Puri, *PLoS One*, 2013, **8**, e73642.

115 Y. S. Song, H. Y. Shin, J. Y. Lee, C. Park and S. W. Kim, *Food Chem*, 2012, **133**, 611–617.

116 H. Gröger, E. Capan, A. Barthuber and K.-D. Vorlop, *Org. Lett.*, 2001, **3**, 1969–1972.

117 P. Ye, Z.-K. Xu, A.-F. Che, J. Wu and P. Seta, *Biomaterials*, 2005, **26**, 6394–6403.

118 Y. Zhang, Z. Tang, J. Wang, H. Wu, C.-T. Lin and Y. Lin, *J. Mater. Chem.*, 2011, **21**, 17468–17475.

119 S. Vishwanath, D. Bhattacharyya, W. Huang and L. G. Bachas, *J. Membr. Sci.*, 1995, **108**, 1–13.

120 S. Fornera, T. E. Balmer, B. Zhang, A. D. Schlüter and P. Walde, *Macromol. Biosci.*, 2011, **11**, 1052–1067.

121 J. Coloma, T. Lugtenburg, M. Afendi, M. Lazzarotto, P. Bracco, P.-L. Hagedoorn, L. Gardossi and U. Hanefeld, *Catalysts*, 2020, **10**, 899.

122 S. Bormann, B. O. Burek, R. Ulber and D. Holtmann, *Mol. Catal.*, 2020, **492**, 110999.

123 M. Gand, C. Thöle, H. Müller, H. Brundiek, G. Bashiri and M. Höhne, *J. Biotechnol.*, 2016, **230**, 11–18.

124 W. Böhmer, T. Knaus, A. Volkov, T. K. Slot, N. R. Shiju, K. Engelmark Cassimjee and F. G. Mutti, *J. Biotechnol.*, 2019, **291**, 52–60.

125 V. Balland, C. Hureau, A. M. Cusano, Y. Liu, T. Tron and B. Limoges, *Chem. Eur. J.*, 2008, **14**, 7186–7192.

126 R. Blankespoor, B. Limoges, B. Schöllhorn, J. L. Syssa-Magalé and D. Yazidi, *Langmuir*, 2005, **21**, 3362–3375.

127   J. Patel, R. Cai, R. Milton, H. Chen and S. D. Minteer, *ChemBioChem*, 2020, **21**, 1729–1732.

128   L. Wang, R. Xu, Y. Chen and R. Jiang, *J. Mol. Catal. B: Enzym.*, 2011, **69**, 120–126.

129   M. Filice, O. Romero, A. Aires, J. M. Guisan, A. Rumbero and J. M. Palomo, *Adv. Synth. Catal.*, 2015, **357**, 2687–2696.

130   P. Wang, *Curr. Opin. Biotechnol.*, 2006, **17**, 574–579.

131   R. Ahmad and M. Sardar, *Biochem. Anal. Biochem.*, 2015, **4**, 1000178.

132   M. Hestericová, M. R. Correro, M. Lenz, P. F.-X. Corvini, P. Shahgaldian and T. R. Ward, *Chem. Commun.*, 2016, **52**, 9462–9465.

133   M. R. Correro, N. Moridi, H. Schützinger, S. Sykora, E. M. Ammann, E. H. Peters, Y. Dudal, P. F.-X. Corvini and P. Shahgaldian, *Angew. Chem., Int. Ed.*, 2016, **55**, 6285–6289.

134   A. Badia, S. Singh, L. Demers, L. Cuccia, G. R. Brown and R. B. Lennox, *Chem. Eur. J.*, 1996, **2**, 359–363.

135   G. Zambrano, M. Chino, E. Renzi, R. Di Girolamo, O. Maglio, V. Pavone, A. Lombardi and F. Nastri, *Biotechnol. Appl. Biochem.*, 2020, **67**, 549–562.

136   F. Nastri, L. Lista, P. Ringhieri, R. Vitale, M. Faiella, C. Andreozzi, P. Travascio, O. Maglio, A. Lombardi and V. Pavone, *Chem. Eur. J.*, 2011, **17**, 4444–4453.

137   C. C. Page, C. C. Moser, X. Chen and P. L. Dutton, *Nature*, 1999, **402**, 47–52.

138   J. R. Winkler and H. B. Gray, *Chem. Rev.*, 2014, **114**, 3369–3380.

139   J. E. Frew and H. A. O. Hill, *Eur. J. Biochem.*, 1988, **172**, 261–269.

140   N. D. J. Yates, M. A. Fascione and A. Parkin, *Chem. Eur. J.*, 2018, **24**, 12164–12182.

141　F. A. Armstrong, H. A. Heering and J. Hirst, *Chem. Soc. Rev.*, 1997, **26**, 169–179.

142　R. A. Clark and E. F. Bowden, *Langmuir*, 1997, **13**, 559–565.

143　A. Ranieri, S. Monari, M. Sola, M. Borsari, G. Battistuzzi, P. Ringhieri, F. Nastri, V. Pavone and A. Lombardi, *Langmuir*, 2010, **26**, 17831–17835.

144　M. Collinson, E. F. Bowden and M. J. Tarlov, *Langmuir*, 1992, **8**, 1247–1250.

145　P. A. Brooksby, K. H. Anderson, A. J. Downard and A. D. Abell, *Langmuir*, 2010, **26**, 1334–1339.

146　M. Akram, M. C. Stuart and D. K. Y. Wong, *Anal. Chim. Acta*, 2004, **504**, 243–251.

147　G. Zambrano, E. Ruggiero, A. Malafronte, M. Chino, O. Maglio, V. Pavone, F. Nastri and A. Lombardi, *Int. J. Mol. Sci.*, 2018, **19**, 2896.

148　F. A. Armstrong, P. Anthony Cox, H. A. O. Hill, V. J. Lowe and B. Nigel Oliver, *J. Electroanal. Chem. Interfacial Electrochem.*, 1987, **217**, 331–366.

149　C. F. Blanford and F. A. Armstrong, *J. Solid State Electrochem.*, 2006, **10**, 826–832.

150　J. Hirst and F. A. Armstrong, *Anal. Chem.*, 1998, **70**, 5062–5071.

151　R. E. Treviño, J. W. Slater and H. S. Shafaat, *ACS Appl. Energy Mater.*, 2020, **3**, 11099–11112.

152　J. W. Slater and H. S. Shafaat, *J. Phys. Chem. Lett.*, 2015, **6**, 3731–3736.

153　J. W. Slater, S. C. Marguet, M. E. Gray, H. A. Monaco, M. Sotomayor and H. S. Shafaat, *ACS Catal.*, 2019, **9**, 8928–8942.

154　N. G. Baranska, A. Parkin and A. K. Duhme-Klair, *Inorg. Chem.*, 2022, **61**, 19172–19182.

155 F. A. Armstrong, A. M. Bond, H. A. O. Hill, I. S. M. Psalti and C. G. Zoski, *J. Phys. Chem.*, 1989, **93**, 6485–6493.

156 L. J. Anderson, D. J. Richardson and J. N. Butt, *Biochemistry*, 2001, **40**, 11294–11307.

157 S. Wang, E. S. Humphreys, S.-Y. Chung, D. F. Delduco, S. R. Lustig, H. Wang, K. N. Parker, N. W. Rizzo, S. Subramoney, Y.-M. Chiang and A. Jagota, *Nat. Mater.*, 2003, **2**, 196–200.

158 T. Yu, Y. Gong, T. Lu, L. Wei, Y. Li, Y. Mu, Y. Chen and K. Liao, *RSC Adv.*, 2012, **2**, 1466–1476.

159 J. B. Neilands, in *Siderophores from Microorganisms and Plants. Structure and Bonding*, Springer, Berlin, Heidelberg, 1984, vol. 58, pp. 1–24.

160 M. Lou Guerinot, *Annu. Rev. Microbiol.*, 1994, **48**, 743–772.

161 H. Boukhalfa and A. L. Crumbliss, *BioMetals*, 2002, **15**, 325–339.

162 R. C. Hider and X. Kong, *Nat. Prod. Rep.*, 2010, **27**, 637–657.

163 R. L. Lundblad and F. M. Macdonald, *Handbook of Biochemistry and Molecular Biology*, CRC Press, Boca Roton, 4th edn., 2010.

164 J. M. Harrington and A. L. Crumbliss, *BioMetals*, 2009, **22**, 679–689.

165 W. R. Harris, C. J. Carrano, S. R. Cooper, S. R. Sofen, A. E. Avdeef, J. V. McArdle and K. N. Raymond, *J. Am. Chem. Soc.*, 1979, **101**, 6097–6104.

166 C.-W. Lee, D. J. Ecker and K. N. Raymond, *J. Am. Chem. Soc.*, 1985, **107**, 6920–6923.

167 S. R. Cooper, J. V McArdle and K. N. Raymond, *Proc. Natl. Acad. Sci. USA*, 1978, **75**, 3551–3554.

168 R. J. Abergel, J. A. Warner, D. K. Shuh and K. N. Raymond, *J. Am. Chem. Soc.*, 2006, **128**, 8920–8931.

169 L. D. Loomis and K. N. Raymond, *Inorg. Chem.*, 1991, **30**, 906–911.

170 I. Spasojević, S. K. Armstrong, T. J. Brickman and A. L. Crumbliss, *Inorg. Chem.*, 1999, **38**, 449–454.

171 S. W. Taylor, G. W. Luther and J. H. Waite, *Inorg. Chem.*, 1994, **33**, 5819–5824.

172 B. L. Lewis, P. D. Holt, S. W. Taylor, S. W. Wilhelm, C. G. Trick, A. Butler and G. W. Luther, *Mar. Chem.*, 1995, **50**, 179–188.

173 A. S. Cornish and W. J. Page, *Microbiology (N Y)*, 1998, **144**, 1747–1754.

174 A. Duhme, R. C. Hider and H. H. Khodr, *Chem. Ber.*, 1997, **130**, 969–973.

175 J. R. Telford and K. N. Raymond, *Inorg. Chem.*, 1998, **37**, 4578–4583.

176 I. Spasojević, H. Boukhalfa, R. D. Stevens and A. L. Crumbliss, *Inorg. Chem.*, 2001, **40**, 49–58.

177 A. J. Bard and L. R. Faulkner, *Electrochemical Methods: Fundamentals and Applications*, Wiley-Blackwell, Hamilton, 2nd edn., 2001.

178 W. H. Rastetter, T. J. Erickson and M. C. Venuti, *J. Org. Chem.*, 1981, **46**, 3579–3590.

179 B. O. Lindgren, T. Nilsson, S. Husebye, Ø. Mikalsen, K. Leander and C.-G. Swahn, *Acta Chem. Scand.*, 1973, **27**, 888–890.

180 A. Chimiak and J. B. Neilands, in *Siderophores from Microorganisms and Plants. Structure and Bonding*, Springer, Berlin, Heidelberg, 1984, vol. 58, pp. 89–96.

181 E. Dalcanale and F. Montanari, *J Org Chem*, 1986, **51**, 567–569.

182 R. C. Scarrow, D. J. Ecker, C. Ng, S. Liu and K. N. Raymond, *Inorg. Chem.*, 1991, **30**, 900–906.

183 C. J. Carrano, S. R. Cooper and K. N. Raymond, *J. Am. Chem. Soc.*, 1979, **101**, 599–604.

184 Z. Hou, K. N. Raymond, B. O'Sulliva, T. W. Esker and T. Nishio, *Inorg. Chem.*, 1998, **37**, 6630–6637.

185 R. Helman and G. D. Lawrence, *J. Electroanal. Chem. Interfacial Electrochem.*, 1989, **276**, 187–196.

186 M. Gledhill, *Analyst*, 2001, **126**, 1359–1362.

187 A.-K. Duhme, R. C. Hider and H. Khodr, *BioMetals*, 1996, **9**, 245–248.

188 J. A. Loo, *Int. J. Mass Spectrom.*, 2000, **200**, 175–186.

189 T. J. Sanderson, C. M. Black, J. W. Southwell, E. J. Wilde, A. Pandey, R. Herman, G. H. Thomas, E. Boros, A.-K. Duhme-Klair and A. Routledge, *ACS Infect. Dis.*, 2020, **6**, 2532–2541.

190 E. P. Storey, R. Boghozian, J. L. Little, D. W. Lowman and R. Chakraborty, *BioMetals*, 2006, **19**, 637–649.

191 L. Konermann, *J. Am. Soc. Mass Spectrom.*, 2017, **28**, 1827–1835.

192 V. Tomišić, S. Blanc, M. Elhabiri, D. Expert and A.-M. Albrecht-Gary, *Inorg. Chem.*, 2008, **47**, 9419–9430.

193 R. C. Hider, in *Siderophores from Microorganisms and Plants. Structure and Bonding*, Springer, Berlin, Heidelberg, 1984, vol. 58, pp. 25–87.

194 J. A. V. Butler, *Trans. Faraday Soc.*, 1924, **19**, 734–739.

195 T. Erdey-Grúz and M. Volmer, *J. Phys. Chem.*, 1930, **150A**, 203–213.

196 K. Muzyka, J. Sun, T. H. Fereja, Y. Lan, W. Zhang and G. Xu, *Anal. Methods*, 2019, **11**, 397–414.

197 M. Cascella, A. Magistrato, I. Tavernelli, P. Carloni and U. Rothlisberger, *Proc. Natl. Acad. Sci.*, 2006, **103**, 19641–19646.

198 J. F. Hall, L. D. Kanbi, I. Harvey, L. M. Murphy and S. S. Hasnain, *Biochemistry*, 1998, **37**, 11451–11458.

199 G. Battistuzzi, M. Borsari, J. A. Cowan, A. Ranieri and M. Sola, *J. Am. Chem. Soc.*, 2002, **124**, 5315–5324.

200   B. S. Gupta, M. Taha and M.-J. Lee, *J. Solution Chem.*, 2013, **42**, 2296–2309.

201   C. M. H. Ferreira, I. S. S. Pinto, E. V. Soares and H. M. V. M. Soares, *RSC Adv.*, 2015, **5**, 30989–31003.

202   Q. Yu, A. Kandegedara, Y. Xu and D. B. Rorabacher, *Anal. Biochem.*, 1997, **253**, 50–56.

203   G. B. Wong, M. J. Kappel, K. N. Raymond, B. Matzanke and G. Winkelmann, *J. Am. Chem. Soc.*, 1983, **105**, 810–815.

204   J. da N. Schöffer, C. R. Matte, D. S. Charqueiro, E. W. de Menezes, T. M. H. Costa, E. V. Benvenutti, R. C. Rodrigues and P. F. Hertz, *Process Biochem.*, 2017, **58**, 120–127.

205   K. Holland-Nell and A. G. Beck-Sickinger, *ChemBioChem*, 2007, **8**, 1071–1076.

206   N. Lalaoui, M. Holzinger, A. Le Goff and S. Cosnier, *Chem. Eur. J.*, 2016, **22**, 10494–10500.

207   C. Nowak, D. Schach, J. Gebert, M. Grosserueschkamp, R. B. Gennis, S. Ferguson-Miller, W. Knoll, D. Walz and R. L. C. Naumann, *J. Solid State Electrochem.*, 2011, **15**, 105–114.

208   C. D. Bostick, S. Mukhopadhyay, I. Pecht, M. Sheves, D. Cahen and D. Lederman, *Rep. Prog. Phys.*, 2018, **81**, 026601.

209   M. Frasconi, F. Mazzei and T. Ferri, *Anal. Bioanal. Chem.*, 2010, **398**, 1545–1564.

210   K. Hernandez and R. Fernandez-Lafuente, *Enzyme Microb. Technol.*, 2011, **48**, 107–122.

211   N. R. Mohamad, N. H. C. Marzuki, N. A. Buang, F. Huyop and R. A. Wahab, *Biotechnol. Biotechnol. Equip.*, 2015, **29**, 205–220.

212   V. Hitaishi, R. Clement, N. Bourassin, M. Baaden, A. De Poulpiquet, S. Sacquin-Mora, A. Ciaccafava and E. Lojou, *Catalysts*, 2018, **8**, 192.

213 D. Wasserberg, C. Nicosia, E. E. Tromp, V. Subramaniam, J. Huskens and P. Jonkheijm, *J. Am. Chem. Soc.*, 2013, **135**, 3104–3111.

214 J. C. Y. Wu, C. H. Hutchings, M. J. Lindsay, C. J. Werner and B. C. Bundy, *J. Biotechnol.*, 2015, **193**, 83–90.

215 B. K. Raliski, C. A. Howard and D. D. Young, *Bioconjugate Chem.*, 2014, **25**, 1916–1920.

216 L. Betancor, A. Hidalgo, G. Fernández-Lorente, C. Mateo, R. Fernández-Lafuente and J. M. Guisan, *Biotechnol Prog*, 2003, **19**, 763–767.

217 S. Knecht, D. Ricklin, A. N. Eberle and B. Ernst, *J. Mol. Recognit.*, 2009, **22**, 270–279.

218 J. Porath, *TrAC, Trends Anal. Chem.*, 1988, **7**, 254–259.

219 J. Porath, *Protein Expression Purif.*, 1992, **3**, 263–281.

220 E. Hochuli, H. Döbeli and A. Schacher, *J. Chromatogr. A*, 1987, **411**, 177–184.

221 W. H. Campbell, J. Henig and N. Plumeré, *Bioelectrochemistry*, 2013, **93**, 46–50.

222 V. Gaberc-Porekar and V. Menart, *J. Biochem. Biophys. Methods*, 2001, **49**, 335–360.

223 V. Gaberc-Porekar and V. Menart, *Chem. Eng. Technol.*, 2005, **28**, 1306–1314.

224 M. Bellare, V. K. Kadambar, P. Bollella, M. Gamella, E. Katz and A. Melman, *Electroanalysis*, 2019, **31**, 2274–2282.

225 J. A. Bornhorst and J. J. Falke, *Methods Enzymol.*, 2000, **326**, 245–254.

226 G. Owens, V. K. Ferguson, M. J. McLaughlin, I. Singleton, R. J. Reid and F. A. Smith, *Environ. Sci. Technol.*, 2000, **34**, 885–891.

227 N. Lingg, C. Öhlknecht, A. Fischer, M. Mozgovicz, T. Scharl, C. Oostenbrink and A. Jungbauer, *J. Chromatogr. A*, 2020, **1633**, 461649.

228 S. V. Wegner and J. P. Spatz, *Angew. Chem., Int. Ed.*, 2013, **52**, 7593–7596.

229 S. V. Wegner, F. C. Schenk and J. P. Spatz, *Chem. Eur. J.*, 2016, **22**, 3156–3162.

230 U. Contaldo, M. Curtil, J. Pérard, C. Cavazza and A. Le Goff, *Angew. Chem., Int. Ed.*, 2022, **61**, e202117212.

231 Y. Li, W. Zhang, J. Chang, J. Chen, G. Li and Y. Ju, *Macromol. Chem. Phys.*, 2008, **209**, 322–329.

232 F. Khan, M. He and M. J. Taussig, *Anal. Chem.*, 2006, **78**, 3072–3079.

233 V. Balland, S. Lecomte and B. Limoges, *Langmuir*, 2009, **25**, 6532–6542.

234 C. Ley, D. Holtmann, K.-M. Mangold and J. Schrader, *Colloids Surf., B*, 2011, **88**, 539–551.

235 C. D. Bain, J. Evall and G. M. Whitesides, *J. Am. Chem. Soc.*, 1989, **111**, 7155–7164.

236 K. L. Prime and G. M. Whitesides, *Science (1979)*, 1991, **252**, 1164–1167.

237 L. L. Rouhana, M. D. Moussallem and J. B. Schlenoff, *J. Am. Chem. Soc.*, 2011, **133**, 16080–16091.

238 Emmanuel. Delamarche, Bruno. Michel, H. A. Biebuyck and C. Gerber, *Adv. Mater.*, 1996, **8**, 719–729.

239 X. Ji, B. Jin, J. Jin and T. Nakamura, *J. Electroanal. Chem.*, 2006, **590**, 173–180.

240 R. K. Mendes, R. F. Carvalhal and L. T. Kubota, *J. Electroanal. Chem.*, 2008, **612**, 164–172.

241　Y. Dong, S. Abaci, C. Shannon and M. J. Bozack, *Langmuir*, 2003, **19**, 8922–8926.

242　A. Kolodziej, F. Fernandez-Trillo and P. Rodriguez, *J. Electroanal. Chem.*, 2018, **819**, 51–57.

243　A. Ulman, *Chem Rev*, 1996, **96**, 1533–1554.

244　N. T. Flynn, T. N. T. Tran, M. J. Cima and R. Langer, *Langmuir*, 2003, **19**, 10909–10915.

245　N. C. Ramos, J. W. Medlin and A. Holewinski, *ACS Appl. Mater. Interfaces*, 2023, **15**, 14470–14480.

246　J. Madoz-Gúrpide, J. M. Abad, J. Fernández-Recio, M. Vélez, L. Vázquez, C. Gómez-Moreno and V. M. Fernández, *J. Am. Chem. Soc.*, 2000, **122**, 9808–9817.

247　T. T. Le, C. P. Wilde, N. Grossman and A. E. G. Cass, *Phys. Chem. Chem. Phys.*, 2011, **13**, 5271.

248　A. R. Hillman, *J. Solid State Electrochem.*, 2011, **15**, 1647–1660.

249　M. C. Dixon, *J. Biomol. Tech.*, 2008, **19**, 151–158.

250　B.-Y. Chang and S.-M. Park, *Annu. Rev. Anal. Chem.*, 2010, **3**, 207–229.

251　H. S. Magar, R. Y. A. Hassan and A. Mulchandani, *Sensors*, 2021, **21**, 6578.

252　S. Wang, J. Zhang, O. Gharbi, V. Vivier, M. Gao and M. E. Orazem, *Nat. Rev. Methods Primers*, 2021, **1**, 41.

253　M. M. Ponpipom, R. L. Bugianesi and T. J. Blake, *J. Med. Chem.*, 1987, **30**, 705–710.

254　R. Vallina-García, M. del Mar García-Suárez, M. T. Fernández-Abedul, F. J. Méndez and A. Costa-García, *Biosens. Bioelectron.*, 2007, **23**, 210–217.

255　M. Sosna, H. Boer and P. N. Bartlett, *ChemPhysChem*, 2013, **14**, 2225–2231.

256 V. Leiro, P. Parreira, S. C. Freitas, M. C. L. Martins and A. P. Pêgo, in *Biomedical Applications of Functionalized Nanomaterials: Concepts, Development and Clinical Translation*, eds. B. Sarmento and J. das Neves, Elsevier, Netherlands, 2018, pp. 35–66.

257 S. Lata, M. Gavutis, R. Tampé and J. Piehler, *J. Am. Chem. Soc.*, 2006, **128**, 2365–2372.

258 C. R. Goldsmith, J. Jaworski, M. Sheng and S. J. Lippard, *J. Am. Chem. Soc.*, 2006, **128**, 418–419.

259 S. V. Wegner, O. I. Sentürk and J. P. Spatz, *Sci. Rep.*, 2016, **5**, 18309.

260 J. K. Lee, Y.-G. Kim, Y. S. Chi, W. S. Yun and I. S. Choi, *J. Phys. Chem. B*, 2004, **108**, 7665–7673.

261 C. Y. Lim, N. A. Owens, R. D. Wampler, Y. Ying, J. H. Granger, M. D. Porter, M. Takahashi and K. Shimazu, *Langmuir*, 2014, **30**, 12868–12878.

262 J. D. Schrattenecker, R. Heer, E. Melnik, T. Maier, G. Fafilek and R. Hainberger, *Biosens. Bioelectron.*, 2019, **127**, 25–30.

263 S. Lee, W. J. Kim and M. Chung, *Analyst*, 2021, **146**, 5236–5244.

264 J. Lazar, C. Schnelting, E. Slavcheva and U. Schnakenberg, *Anal. Chem.*, 2016, **88**, 682–687.

265 A. Bogomolova, E. Komarova, K. Reber, T. Gerasimov, O. Yavuz, S. Bhatt and M. Aldissi, *Anal. Chem.*, 2009, **81**, 3944–3949.

266 L. A. Wilkinson, T. T. C. Yue, E. Massey, A. J. P. White and N. J. Long, *Dalton Trans.*, 2019, **48**, 72–78.

267 A. S. Georgopoulou, D. Michael, P. Mingos, A. J. P. White, D. J. Williams, B. R. Horrocks' and A. Houlton, *J. Chem. Soc., Dalton Trans.*, 2000, 2969–2974.

268 A. Isidro-Llobet, M. Álvarez and F. Albericio, *Chem. Rev.*, 2009, **109**, 2455–2504.

269 S. Zahn and J. W. Canary, *Angew. Chem., Int. Ed.*, 1998, **37**, 305–307.

270   W. Ong, Y. Yang, A. C. Cruciano and R. L. McCarley, *J. Am. Chem. Soc.*, 2008, **130**, 14739–14744.

271   J. R. Kramer and T. J. Deming, *J Am Chem Soc*, 2012, **134**, 4112–4115.

272   C. Xiao, W. Wu, W. Liang, D. Zhou, K. Kanagaraj, G. Cheng, D. Su, Z. Zhong, J. J. Chruma and C. Yang, *Angew. Chem., Int. Ed.*, 2020, **59**, 8094–8098.

273   S.-H. Jung, S. Schneider, F. Plamper and A. Pich, *Macromolecules*, 2020, **53**, 1043–1053.

274   Y.-M. Go and D. P. Jones, *Biochim. Biophys. Acta*, 2008, **1780**, 1273–1290.

275   W. Chen, L. Li, Z. Du, J. Liu, J. N. Reitter, K. V. Mills, R. J. Linhardt and C. Wang, *J. Am. Chem. Soc.*, 2012, **134**, 2500–2503.

276   F. Rabe von Pappenheim, M. Wensien, J. Ye, J. Uranga, I. Irisarri, J. de Vries, L.-M. Funk, R. A. Mata and K. Tittmann, *Nat. Chem. Biol.*, 2022, **18**, 368–375.

277   T.-C. Meng, T. Fukada and N. K. Tonks, *Mol. Cell.*, 2002, **9**, 387–399.

278   M. Cordes and B. Giese, *Chem. Soc. Rev.*, 2009, **38**, 892.

279   J. G. Gardner, L. Crouch, A. Labourel, Z. Forsberg, Y. V. Bukhman, G. Vaaje-Kolstad, H. J. Gilbert and D. H. Keating, *Mol. Microbiol.*, 2014, **94**, 1121–1133.

280   J. Branch, B. S. Rajagopal, A. Paradisi, N. Yates, P. J. Lindley, J. Smith, K. Hollingsworth, W. B. Turnbull, B. Henrissat, A. Parkin, A. Berry and G. R. Hemsworth, *Biochem. J.*, 2021, **478**, 2927–2944.

281   M. Lou Fultz and R. A. Durst, *Anal. Chim. Acta*, 1982, **140**, 1–18.

282   S. Hardt, S. Stapf, D. T. Filmon, J. A. Birrell, O. Rüdiger, V. Fourmond, C. Léger and N. Plumeré, *Nat. Catal.*, 2021, **4**, 251–258.

283   Y. Liu, Y. Li, P. Zuo, Q. Chen, G. Tang, P. Sun, Z. Yang and T. Xu, *ChemSusChem*, 2020, **13**, 2245–2249.

284   J. Ding, C. Zheng, L. Wang, C. Lu, B. Zhang, Y. Chen, M. Li, G. Zhai and X. Zhuang, *J. Mater. Chem. A*, 2019, **7**, 23337–23360.

285   L. L. Stookey, *Anal. Chem.*, 1970, **42**, 779–781.

286   A. H. Miller, E. V. Blagova, B. Large, R. L. Booth, K. S. Wilson and A.-K. Duhme-Klair, *Under revision*.

287   E. V. Blagova, A. Miller, M. Bennet, R. Booth, E. J. Dodson, A.-K. Duhme-Klair and K. S. Wilson, *Acta Crystallogr., Sect. D: Struct. Biol.*

288   X. Xu, A. Makaraviciute, S. Kumar, C. Wen, M. Sjödin, E. Abdurakhmanov, U. H. Danielson, L. Nyholm and Z. Zhang, *Anal. Chem.*, 2019, **91**, 14697–14704.

289   A. Mehdinia, S. Habib Kazemi, S. Zahra Bathaie, A. Alizadeh, M. Shamsipur and M. F. Mousavi, *Anal. Biochem.*, 2008, **375**, 331–338.

290   V. Ganesh, S. K. Pal, S. Kumar and V. Lakshminarayanan, *J. Colloid Interface Sci.*, 2006, **296**, 195–203.

291   P. Kanyong and J. J. Davis, *J. Electroanal. Chem.*, 2020, **856**, 113675.

292   S. Kumar Panigrahi and A. Kumar Mishra, *J. Photochem. Photobiol., C*, 2019, **41**, 100318.

293   P. T. Wingfield, *Curr. Protoc. Protein Sci.*, 2017, **88**, 6.14.1-6.14.3.

294   C. Giglione, A. Boularot and T. Meinnel, *Cell. Mol. Life Sci.*, 2004, **61**, 1455–1474.

295   T. H. Dinh, S. C. Lee, C. Y. Hou and K. Won, *J. Electrochem. Soc.*, 2016, **163**, H440–H444.

296   L. Troian-Gautier, H. Valkenier, A. Mattiuzzi, I. Jabin, N. Van den Brande, B. Van Mele, J. Hubert, F. Reniers, G. Bruylants, C. Lagrost and Y. Leroux, *Chem. Commun.*, 2016, **52**, 10493–10496.

297   S. Kesavan and S. Abraham John, *J. Colloid Interface Sci.*, 2014, **428**, 84–94.

298   N. D. Yates, M. R. Dowsett, P. Bentley, J. A. Dickenson-Fogg, A. Pratt, C. F. Blanford, M. A. Fascione and A. Parkin, *Langmuir*, 2020, **36**, 5654–5664.

299   J. Jia, B. Wang, A. Wu, G. Cheng, Z. Li and S. Dong, *Anal. Chem.*, 2002, **74**, 2217–2223.

300   D. J. Raines, O. V. Moroz, E. V. Blagova, J. P. Turkenburg, K. S. Wilson and A. K. Duhme-Klair, *Proc. Natl. Acad. Sci. U. S. A.*, 2016, **113**, 5850–5855.

301   D. Benito-Alifonso, S. Tremel, B. Hou, H. Lockyear, J. Mantell, D. J. Fermin, P. Verkade, M. Berry and M. C. Galan, *Angew. Chem. Int. Ed.*, 2014, **53**, 810–814.

302   T. Hattori, K. Okitsu, N. Yamazaki, N. Ohoka, N. Shibata, T. Misawa, M. Kurihara, Y. Demizu and M. Naito, *Bioorg. Med. Chem. Lett.*, 2017, **27**, 4478–4481.

303   R. Claus, J. P. Lewtak, T. J. Muller and J. C. Swarts, *J. Organomet. Chem.*, 2013, **740**, 61–69.

304   T. H. Dinh, S. C. Lee, C. Y. Hou and K. Won, *J. Electrochem. Soc.*, 2016, **163**, H440–H444.

305   H. Yamaguchi and A. Harada, *Biomacromolecules*, 2002, **3**, 1163–1169.

306   W. S. Baker, B. I. Lemon and R. M. Crooks, *J. Phys. Chem. B*, 2001, **105**, 8885–8894.

307   J. E. O'Reilly, *Biochim. Biophys. Acta, Bioenerg.*, 1973, **292**, 509–515.

308   E. Layne, *Methods Enzymol.*, 1957, **3**, 447–454.

309   E. V. Blagova, A. Miller, M. Bennett, R. Booth, E. J. Dodson, A.-K. Duhme-Klair and K. S. Wilson, *Under revision*.

310   L. Jiang, Z. Xiong, Y. Song, Y. Lu, Y. Chen, J. S. Schultz, J. Li and J. Liao, *Sci. Rep.*, 2019, **9**, 2050.

311   G. Weber, N. von Wirén and H. Hayen, *BioMetals*, 2008, **21**, 503–513.